Low-Cost Magnesium Alloy Sheet Component Development and Demonstration Project

U.S. Department of Energy (DoE)

Final Closeout Technical Report

Cooperative Agreement DE-EE0007756

Project Duration: October 1, 2016 - July 31, 2021

DOE VTO Staff: S. Kleinbaum
DOE-NETL Staff: A. Yocum

October 19, 2021

This report does not contain any protected data.

Principal Investigator:
R. Gerken *(Stellantis, formerly FCA Automotive Group USA)*

United States Automotive Materials Partnership LLC
3000 Town Center Building, Suite 35
Southfield, MI 48075
USAMP DUNS Number: 826406808

Co-Authors / Leadership Team

Co-Investigators
A. Sachdev *(General Motors)*+
B. Ghaffari *(Ford Motor Co)*+

Task Leaders
M. Zaluzec*
(Ford Motor Company)

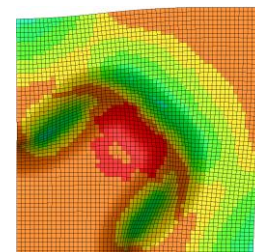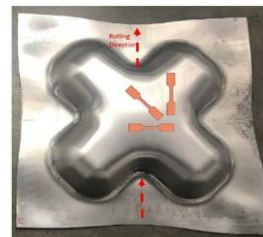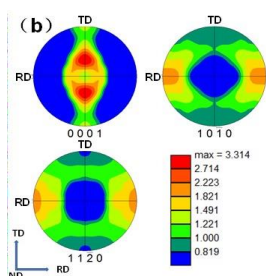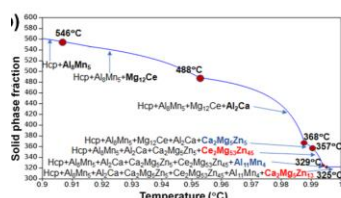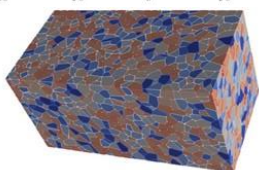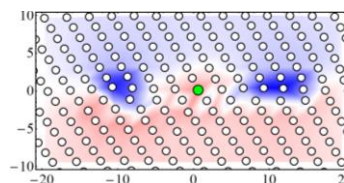L. Hector, Jr.+
R. Mishra*
A. Morales
(General Motors)

A. Adam+
L. Decker
S. Logan*
(Stellantis/FCA US LLC)

Project Managers
J. Carter+
M. Mehta+
(M-Tech International LLC)
E. McCarty*
(Materials Technologies Consulting LLC)

+ **Co-Author of this report**
* **Participated during early phases of the project.**

Acknowledgement and Disclaimers

Disclaimer: This report was prepared as an account of work sponsored by an agency of the United States Government. Neither the United States Government nor any agency thereof, nor any of their employees, makes any warranty, express or implied, or assumes any legal liability or responsibility for the accuracy, completeness, or usefulness of any information, apparatus, product, or process disclosed, or represents that its use would not infringe privately owned rights. Reference herein to any specific commercial product, process, or service by trade name, trademark, manufacturer, or otherwise does not necessarily constitute or imply its endorsement, recommendation, or favoring by the United States Government or any agency thereof. The views and opinions of authors expressed herein do not necessarily state or reflect those of the United States Government or any agency thereof.

Additional support for this project was provided to ORNL and PNNL from the LightMAT initiative.

This technical report does not contain any of the following: limited rights data (proprietary data), classified information, protected PII, information subject to export control classification, or other information not subject to release.

Table of Contents

Acronyms and Abbreviations

(See Table C1 for abbreviations of alloy names)

AET	AET Integration, Inc.		LT	Leadership Team
At.%	Atom percent		MFDC	Medium Frequency Direct Current
APS	Advanced Photon Source		MRD	Multi-Ring Domed (welding electrode)
BP	Budget Period		MWS	Minimum Weld Size
CAD	Computer-Aided Design		ND	Normal Direction
CAE	Computer-Aided Engineering		OEM	Original Equipment Manufacturer
COF	Coefficient of Friction		ORNL	Oak Ridge National Laboratory
CP	Crystal Plasticity		OSU	Ohio State University
CPFEM	Crystal Plasticity Finite Element Models		PM	Project Management
			PMP	Program Management Plan
CRS	Cold-Rolled Steel		PNNL	Pacific Northwest National Laboratory
CRSS	Critical Resolved Shear Stress		PPG	PPG Industries, Inc.
DC	Direct-Chill (a slab casting process)		PPM	Pinetree Pos Magnesium
DDRX	Discontinuous Dynamic Recrystallization		PSC	Plane Strain Compression
			RD	Rolling Direction
DFT	Density Functional Theory		RPW	Resistance Projection Welding (Arplas)
DIC	Digital Image Correlation		RSW	Resistance Spot Welding
DOE	Design of Experiment		RT	Room Temperature
EBSD	Electron Back Scatter Diffraction		RX	Recrystallization
EFP	E-Form Plus (Mg sheet alloy from POSCO)		SC	Steering Committee
			SEM	Scanning Electron Microscope
EWI	Edison Welding Institute		SOPO	Statement of Project Objectives
FEA	Finite Element Analysis		SRS	Strain Rate Sensitivity
FLC/FLD	Forming Limit Curve/Diagram		SRX	Static Recrystallization
FSW	Friction Stir Welding		TD	Transverse Direction
GAM	Grain Average Misorientation		TMP	Thermomechanical Processing
GD OES	Glow Discharge Optical Emission Spectroscopy		TRC	Twin Roll Casting
			UF	University of Florida
GOS	Grain Orientation Spread		UIUC	University of Illinois Urbana Champaign
HCP	Hexagonal Close Packed			
HDGS	Hot-Dip Galvanized Steel		UM	University of Michigan
ICME	Integrated Computational Materials Engineering		UMAT	User-defined Material Subroutine
			UPenn	University of Pennsylvania
IE	Index Erichsen		UTS	Ultimate Tensile Strength
IPF	Inverse Pole Figure		Wt.%	Weight percent
KMI	Korea Magnesium Industry		XRD	X-Ray Diffraction
LDH	Limiting Dome Height		YS	Yield Strength

Executive Summary

The overarching objective of this USAMP project was to develop and demonstrate door panels made from magnesium (Mg) sheet with a cost penalty over conventional steel stampings of no more than $5.50/kg saved. The technical approach integrated experiments with advanced computational tools based on Integrated Computational Materials Engineering (ICME) methods to develop new alloy chemistries and their thermomechanical processing that promise improved formability and lower forming temperatures. A penultimate task before finally forming the stampings was to incorporate actual microstructure into models that would enable formability simulations. This approach would, for the first time, account for individual magnesium grains moving in an anisotropic fashion unlike that for aluminum or steel that have isotropic properties upon which the current simulation tools are based. In separate activities, new coatings and lubricants to facilitate forming and improved corrosion protection and joining strategies, were developed to ensure that the door could be produced with stated product requirements. A technical cost model, which included parts production, assembly, and paint for a door specifically designed for Mg sheet, showed the cost penalty to be between $4.26 to $6.60/kg saved, which enveloped the project's cost targets. The cost of the coated Mg sheet was identified as the key driver for the cost penalty. The mass of the Mg-intensive door was 7.9 kg, which was 54% less than the baseline steel door.

A quintessential requirement of formability, a reflection of plasticity, is the ability of the individual grains to possess multiple slip systems as occurs in steel and aluminum. Mg instead has one basal slip system which is triggered at a much lower stress compared to the others such that deformation continues on this easy system till failure and before reasonable stampings can be formed. An important part of the project was to deconvolute the mechanisms that could promote multiple slip systems in Mg sheet to meet the project goals. Temperature is one variable that can trigger multiple slip but needs to be kept as low as possible for cost reasons, to be competitive with steel and aluminum that are formed at room temperature.

Atomistic calculations based on density functional theory (DFT), a pristine way to isolate the effect of individual atoms within grains and without other competing effects, demonstrated that the misfit strain from high atomic radius, low-cost, non-rare-earth elements like Ca, Mn, Zn, Li and Al, which have reasonable solubility in Mg, cause strong solute-dislocation core interaction that promotes non-basal slip. Thermodynamic calculations and detailed experiments showed that the combination of both Ca and Zn demonstrated dynamic strain aging due to negative strain rate sensitivity, which in turn nucleated desirable shear bands within a certain range of strain rates and temperatures during making of the sheet. It is on these bands that grains with a desirable weaker basal texture, and thus improved formability, form in the final recrystallized sheet ready for stamping. Moreover, a large database linking processing with microstructure and texture of Mg-Ca-Zn alloys was developed, revealing the significance of various processing steps. Combining these results led to the development of a new Mg-1Zn-1Al-0.5Ca-0.2Ce-0.4Mn alloy with a modified multi-stage homogenization process that demonstrated a high elongation of 31% and a stretched Erichsen cup height of 7.8 mm at room temperature, which values are very close to those of some automotive aluminum alloys. A pleasant outcome of the project was the development of the desirable weak texture when the sheets were rolled asymmetrically as opposed to when both rolls operate at the same surface speed.

Other than the challenges of obtaining a weak texture, Mg sheet does not have isotropically oriented grains as occurs generally in aluminum or steel. This anisotropy drives additional computational complexities when conducting formability simulation. This project, for the first time, initiated a multi-scale approach to incorporate the actual anisotropic microstructure obtained from electron back scatter diffraction (EBSD), which provides precise orientations of the individual grains. The evolution of the orientation of the grains with strain were coupled in a Crystal Plasticity (CP) model where each integration point accounts for the initial and evolving microstructure due to multiple slip, twinning and

texture evolution. Inputs to the model were obtained from high resolution tests to determine micro-yielding behavior and obtain strain-rate dependence of stress-strain behavior as function of temperature and sheet orientation along various strain paths. Indeed, CP simulation, based on the improved material card obtained from actual microstructure input, predicted strains in locations on stamped parts that were in agreement with actual experiments. These failure strains were not predicted by simulations based on averaged material information which do not include the evolving anisotropy.

A key endeavor of the project was to develop virtual microstructures in a quest to enable their manipulation in computational models to define those that could directionally be tailored towards multiple slip systems with less anisotropy in Mg alloys compared with pure Mg. To that end, 3D virtual microstructures based on experimental measurements of binary Mg alloys to represent key features of texture, grain size, grain orientation were developed. The critical stresses for slip on the various planes were calculated from DFT and, when input to crystal plasticity models, matched experimental measurements. Reducing grain size was shown to have a pronounced effect on increasing strength.

Confidence in the formability simulations were first validated in experimental symmetrical stampings and subsequently in actual door stampings. Successful stampings were obtained at temperatures between 200ºC-250ºC to meet the ultimate goals of the project with appropriate modification to the die originally designed for steel, as suggested by the simulation and preliminary stamping trials. The actual panels were scanned with light in 3D to validate the simulations. Although not tested, simulations of side pole intrusion test, as well as several other attribute tests, showed that the magnesium door met all engineering and performance requirements.

The paramount challenge for implementing Mg sheet cost effectively in automotive products is the ability to join and coat with lubricants and pretreatment for downstream stamping and paint processing without disrupting the large capital investments in place. Both resistance spot welding and laser welding in uncoated and pretreated conditions with and without forming lubes showed consistently good welds and thus not a limitation. A unique ester-based lubricant augmented with a superwetting agent provided uniform hydrophilic film coverage on the as-rolled sheet after drying. This lubricant eliminated carbonization at the elevated forming temperatures used. An oil-based lubricant was also developed as an alternative that met all tribological requirements for forming. Conversion coatings that passivate the intrinsic oxide film on magnesium obtained due to general oxidation of this reactive metal, just as for aluminum, were developed to prevent oxidation and corrosion of the sheet. One pretreatment developed removed the oxide layer to improve corrosion performance after e-coat (the first step in the paint process) which was followed by another pretreatment to form an insoluble protective coating when steel and aluminum in multi-material bodies are present in adjacence. A chrome-free conversion coating and a zinc plating were also developed that demonstrated good bonding with magnesium sheet and did not fracture during stamping. All coatings passed the required humidity tests and met the oxidation and corrosion requirement for warm forming. Neither lubricant needed to be washed off or cleaned in any way after forming for joining or adhesive bonding, and the lubricants and coatings were totally compatible with the typical automotive paint shop.

Although the various elements of the project like new alloys, rolling processes, and coatings could not be incorporated into the sheet that made the demonstration door, the overall project generously funded by DOE demonstrated immense strides towards bringing magnesium sheet closer to a viable structural automotive application. The research completed will hopefully spur future work in areas such as enhancements to the computational modeling tools for virtual development and characterization of new alloys with still more randomized texture and enhancements to direct crystal plasticity models better optimized for complex stampings. Larger efforts will still be needed to scale up the various promising technology components identified for high volume implementation.

Chapter A. Introduction

A1. Background and State of the Art

The "Low-Cost Mg Sheet Component Development and Demonstration Project" (LCMS) was awarded to the United States Automotive Materials Partnership, LLC (USAMP) effective October 1, 2016. This 60-month, approximately $8 million (including cost-share) project was organized to produce low-cost magnesium sheet products for automotive applications.

USAMP is 100% owned by the United States Council for Automotive Research (USCAR) whose members are U.S.-based automobile original equipment manufacturers (OEMs): FCA US LLC, Ford Motor Company, and General Motors Holdings LLC. Since its formation over two decades ago, USAMP has collaborated extensively with the U.S. Department of Energy to conduct precompetitive research and development aimed at reducing the mass of automobiles through strategic use of lightweight materials.

Most of the applications of magnesium (Mg) in cars and trucks are die castings rather than sheet metal. These include large parts such as radiator supports, liftgate inner panels, seat frames, and cross-car beams; and small parts such as roof handles, steering wheels, and shift levers. The main advantages of Mg are mass reduction, part consolidation, metallic "feel", accurate dimensions, and surface textures. Automotive applications of magnesium sheet have typically been experimental or low-volume serial production, including decklid inner panels, rear seatback panels, and roof panels. These are formed at elevated temperatures ranging up to 450°C, by either a blow forming process or a stamping process.

A2. Project Objectives

The objective of this project was to research, develop, and demonstrate at least one large, challenging magnesium sheet component on a model year 2013 (MY13) or newer vehicle at a manufacturing cost penalty of less than $2.50 per pound of weight saved ($5.50/kg saved) when compared to steel.

The baseline components evaluated in this project were inner and outer panels from the front doors of two mid-size sedans: Chrysler 200 and 2013 MY Ford Fusion. These components were selected due to the numerous challenges involved in producing large Mg alloy-based panels that would meet industry requirements for formability, durability, join-ability, stiffness, corrosion protection, and appearance. Whereas the Chrysler door was used for technical cost modelling, the Ford door was used for demonstration due to the ready availability of stamping tools. The proprietary Ford door design and the associated confidential CAD models prevented the Ford door from being used in the cost modelling, thus the Chrysler 200 door, being of similar design, was utilized as a surrogate.

A3. Technical Approach

USAMP implemented a technical approach that integrated experimental, computational and data tools that, through this project, have shown a pathway to accelerate the development and deployment cycle of low-cost Mg sheets. To accomplish the project objectives, USAMP organized a team of 22 sub-recipients, national laboratory partners and vendors to research, develop, test, and evaluate at least one Mg alloy and commensurate processing suitable for rolling automotive appearance grade sheet, and to demonstrate warm forming of inner and outer door panels based on the 2013 MY Ford Fusion to validate the results.

The USAMP's holistic approach included the following automotive sheet component technologies:
- Alloy chemistry and sheet rolling process development
- New coil-applied coatings and warm-forming lubricants
- Warm forming simulation, stamping and joining process development
- Paint shop pretreatment process developed to work with Mg, Al, and steel
- Final cost, weight, and performance evaluation at end of project.

This 60-month, approximately $8 million (including cost-share) project consisted of the following major activities conducted over seven technical tasks (see Figure A1): technical cost guidance to identify key cost drivers associated with current Mg component production; alloy and process optimization; material characterization and modeling studies; coil pretreatment studies, protective coating application and stamping lubrication developments; panel forming simulation studies and scaling to warm-forming demonstration of large components; corrosion protection; and sheet joining studies.
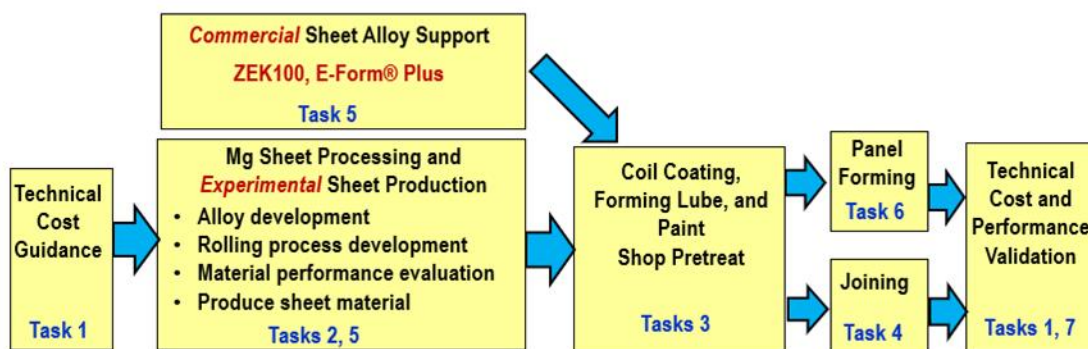

Figure A1: Project task interrelationships. (Source: USAMP)

The USAMP team accessed National Laboratory tools and expert researchers within the LightMAT Consortium – specifically Oak Ridge National Laboratory (ORNL) and Pacific Northwest National Laboratory (PNNL). Public data and code developed on the project were curated and hosted in the DataHUB repository established by LightMAT as part of USAMP's Data Management Plan (DMP).

The project encompassed two major aspects or thrust areas for research collaborations to achieve the objective of low-cost Mg sheet for automotive use:

1. Towards the first aspect, the USAMP's characterization of E-Form Plus Mg alloys has resulted in the development of detailed material property data for a new alloy at elevated temperatures, and facilitated its implementation in computational modeling tools, thereby spurring the virtual development and characterization of new Mg alloys better optimized for automotive manufacturing.

2. The second aspect focused on the improvement of rolling, forming and joining processes, pretreatments, high-temperature lubricants, and corrosion coatings to enable greater use of existing Mg sheet materials.

Due to this dual path, many of the technical sub-tasks were executed concurrently in order to achieve identified milestones over the three budget periods wherein the technical emphasis was as follows:

Budget Period 1 – Alloy Development, Process Cost Analysis and ICME Predictive Modeling.

Budget Period 2 – ICME Model Validation, Pretreatment/Coating/Lubricant Development, Alloy and Rolling Development, and Joining Processes Development.

Budget Period 3 – Large Sheet Production, Demonstration Component, and Cost/Weight Analysis.

During the project, several non-basal (randomized) textured Mg alloy sheet samples were designed and fabricated in academic laboratories, and their properties evaluated for potential in stamping panels at moderately elevated temperature (involving stretch as in outer panel and draw as in inner panel, besides other strain paths in between) to meet the quality, appearance, and corrosion/paint requirements. This

effort required the modelling, experimental, engineering and data tool teams to work in a seamless manner. Research teams from University of Florida (UF), University of Illinois Urbana Champaign (UIUC) and PNNL collaborated in developing microscale and atomic scale computational approaches, while the University of Pennsylvania (UPenn), InalTech, PNNL and Vehma teams focused on macroscale (i.e., Finite Element Analysis, FEA) model development, data fitting, and integration. They were supported in material characterization, experimental properties measurement, and thermomechanical processing approaches by Ohio State University (OSU), ORNL, UF and University of Michigan (UM) to provide composition and microstructure inputs as well as warm-forming inputs. Additional specialized strain path testing at elevated temperature was performed by FADI-AMT LLC in order to determine forming limit curves (FLC). The UPenn/InalTech team supplied constitutive information to the warm stamping participant, Vehma, and provided desired texture specifications and mechanical property specifications to the sheet supplier, POSCO. The labs involved in experimental work at UF, OSU, UM, and PNNL validated predictions from atomistic, thermodynamic, microscale and continuum scale models developed at UIUC, UF, OSU, InalTech/UPenn and PNNL. The knowledge obtained from the modeling suite was used for planning downstream part forming trials by both, Edison Welding Institute (EWI) (cup-draws and intermediate size and complexity cross-forms), and Vehma (inner and outer door panels). Selected data were validated in lab-scale experiments via coupon-level tests.

The industrial participants Henkel, Xtalic, Fuchs, Quaker, PPG and AET Integration collaborated on development of coil pretreatments, stamping lubricants, joining, and application of protective coatings to deliver Mg alloy sheet panels which met specified goals for automotive formability, join-ability, mechanical behavior, corrosion resistance, appearance, and cost. Initial experimental work on development of forming lubricants and anti-corrosion treatments began with the commercially available ZEK100 alloy sheet (a rare earth-containing alloy shown to be warm stampable at 250°C). For reasons documented in Chapter F, the USAMP then transitioned the team's focus at the end of BP1 to evaluation of E-Form Plus (AZXM2110) alloy for the remainder of the project. In addition to physical experiments, the industrial participants (primarily Vehma) conducted computer simulations in the areas of formability analysis and mechanical behavior of the door assembly.

Technical cost modeling activities were led by Camanoe Associates, and occurred both, early in the project to help identify the major cost drivers (BP1), and at the conclusion of the project (BP3) to quantify the overall success due to the technological advances demonstrated.

The academic and national laboratory participants and the suppliers integrated their respective activities under USAMP's oversight to meet the technical data requirements of the project.

A4. Project Management
The 22-organization project team comprised technical staff from the three USAMP-member automotive companies, academic researchers, selected automotive Tier 1 manufacturing suppliers, sheet material and coating suppliers, test laboratories, technical consultants and national laboratories. Twelve organizations were contracted as sub-recipients. The two national laboratories were separately engaged under a DOE-USAMP agreement with the LightMAT Consortium, and the remaining organizations were engaged as vendors under USAMP Purchase Orders (A full list is shown in Appendix 1).

The entire project was managed by a 12-member USAMP OEM-led Leadership Team (LT) appointed under the oversight of the USAMP Steering Committee of senior managers from the OEMs. The LT met weekly and comprised two or more Task Leaders from each USAMP member company, DOE-VTO Program Manager and NETL Project Manager (as non-voting members), and a third-party Technical Project Manager from M-Tech International LLC. M-Tech coordinated tasks per schedule, liaised with the sponsors, sub-recipients/vendors and USAMP management, and reported on research progress. USAMP's administrative, legal and financial staff participated as needed.

Regular task-level reviews were held by the OEM-based task leaders with each performing organization to ensure research activities were relevant to the project goals. Monthly reviews were held with LightMAT and DataHUB partners, and quarterly all-team meetings were held at USCAR in Southfield, MI – these meetings began with a Technical Kickoff in June 2017 and continued until January 2020. With the Covid-19 pandemic emergency in Spring 2020, mandatory office shutdowns and shelter-in-place directives issued by governments and USCAR necessitated all project task-level and team-level meetings to be held virtually using electronic collaboration tools. A Final Closeout Review was held virtually with the DOE and USAMP management in May 2021.

A5. Data Archiving in LightMAT DataHUB

The Data Management Plan involved USAMP collaborating with the LightMAT Consortium to develop and employ a project-specific data repository system known as DataHUB for the storage, curation, and dissemination of project experimental data and models. The objectives and functions of DataHUB are:

1. To enable review and certification of project experimental data;

2. To provide appropriate metadata to describe the sources and methodologies used to generate experimental data;

3. To facilitate transfer of experimental data between project participants;

4. To facilitate material model calibration and validation;

5. To provide an archival record of data and material models generated during the project;

6. To provide a reference source for project publications; and

7. To provide public access to project data and technical reports.

In addition to all experimental and modeling data being uploaded to DataHUB by all team members, each of the sub-recipients' final technical reports were uploaded as well and are publicly accessible (with account setup protocols) – these final sub-task reports provide far more detail than could be included in this technical report.

Each sub-task report is accessible at https://data.lightmat.org/project as explained in each chapter summary in this final report.

Chapter B. Task 1: Technical Cost Guidance
(Camanoe Associates – Principal Investigator: J. Gregory)

B1. SUMMARY

There were two objectives for Task 1 on technical cost guidance: (1) Identify and quantify the key cost drivers and obstacles associated with the current magnesium alloy sheet material and automotive component development process to understand the best opportunities to develop a low-cost alternative. (2) Compare the costs and weights of producing the lightweight magnesium door with a conventional steel door.

The initial analysis of cost drivers found that magnesium assemblies are more expensive because material and assembly costs relative to baseline steel designs outweigh gains from lower mass and part count reduction. The material costs are primarily driven by high raw material costs. Primary magnesium from China produced using the Pidgeon process is about half as expensive as that made in the US using the electrolytic process.

Camanoe's process-based cost modeling (PBCM) analysis of the magnesium door used both scenarios of producing the magnesium. Total costs included parts production, assembly, and paint. As shown in Figure B1, the comparison of producing the magnesium door to the steel door showed that the China-produced magnesium door's lightweighting cost of $4.26/kg saved was under the project target of $5.50, whereas the US-produced magnesium scenario had a lightweighting cost of $6.60. The cost of the coated magnesium alloy sheet is a key driver of the results. A 10% decrease in the cost of US magnesium would lead to it being within the project's lightweighting cost target. The mass of the magnesium-intensive door is 9.1 kg (54%) less than that of the steel door.

While the larger parts in the magnesium door design are cost competitive, the smaller parts have relatively high lightweighting costs, and the aluminum casting is heavier and significantly more expensive than the equivalent three steel parts. This indicates there is opportunity to optimize the magnesium door design. Detailed discussion of work on this Task may be found in Camanoe's final report at https://data.lightmat.org/project.
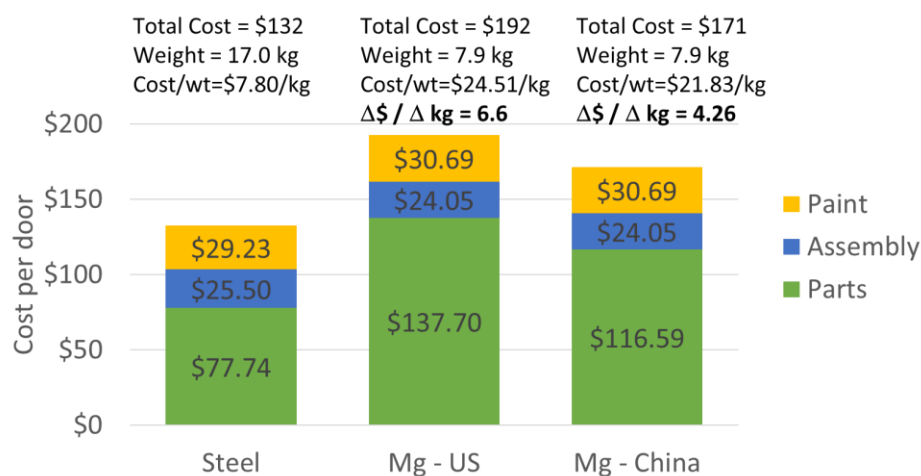

Figure B1: Total part fabrication, assembly, and paint costs per door (100,000 annual volume). (Source: Camanoe)

B2. ACCOMPLISHMENTS AND RESULTS

B2.1 Objectives
The objectives were accomplished through work in six sub-tasks, which were accomplished successfully without variances:

1. Provide summary of cost drivers.
2. Calculate cost of producing benchmark steel door.
3. Develop cost models of two coatings processes.
4. Modify existing Mg warm forming model.
5. Calculate cost of producing Mg door.
6. Compare weights and cost of Mg and steel door.

B2.2 Methodology

B2.2.1 Summary of Cost Drivers
The objective of this sub-task was to provide a summary of existing cost drivers of current magnesium sheet and automotive component production and assembly. The approach taken was to use information from the 2010 USAMP Automotive Metals Division (AMD) 603 project and publicly available literature. (Camanoe did the original analyses in AMD 603).

B2.2.2 Process-Based Cost Modeling
The approach for the other tasks involved the use of process-based cost modeling to quantify costs of parts production, coating, and assembly of the magnesium and steel doors. PBCMs combine engineering process models, operational models, and an economic framework to map from details of product and process to operating costs. Since PBCMs are built around technical details, they allow one to explore how cost evolves as a technology or operating conditions change.

The scope of the door production process for both the steel and magnesium designs is summarized in Figure B2. PBCMs of coil pretreatment, part production, assembly, and paint were used for both, the magnesium and steel doors. The lightweighting cost of the magnesium doors and parts was calculated by dividing the difference in cost between the magnesium and steel designs by the difference in weight.

All part and assembly data for both the steel and magnesium door designs was provided by FCA. Processing data were generated by Camanoe using existing PBCMs or were developed in consultation with other industrial partners on the project. The PBCMs include equipment and operational data such as equipment costs and capacities using information from Camanoe databases. Component-specific processing parameters were estimated using algorithms in the models including equipment size, line rate, tool cost, and number of workers.

The set of PBCMs used in the analysis include: Mg coil coating pretreatment; Component Production (stamping, warm forming, die casting); Body Shop Assembly Operations (including spot welding, adhesive bonding, fastening, laser welding, weld nuts, clinch nuts, self-pierce rivets and screws); and Paint Shop Operations (including cleaning, pretreatment, E-coat, paint).

B2.2.3 Model Input Data
General input data (wages, electricity cost, building cost, etc.) and steel material prices are based on proprietary Camanoe databases. Magnesium sheet prices were more difficult to estimate. While the USGS provides data on the price of primary magnesium, there is limited available data on alloy costs and sheet production. Alloy ingot prices were assumed to equal recent primary magnesium prices: $5.00/kg for US and $2.50/kg for Chinese. Data on the conversion cost of primary magnesium to sheet was also difficult to obtain. POSCO provided data on twin-roll cast aluminum sheet conversion costs of $2.13/kg, which is approximately $3.30/kg for magnesium when accounting for the density differences. A pretreatment price of $1.20/kg was used. A Mg scrap price of $1.50/kg (60% of Pidgeon price) was used.
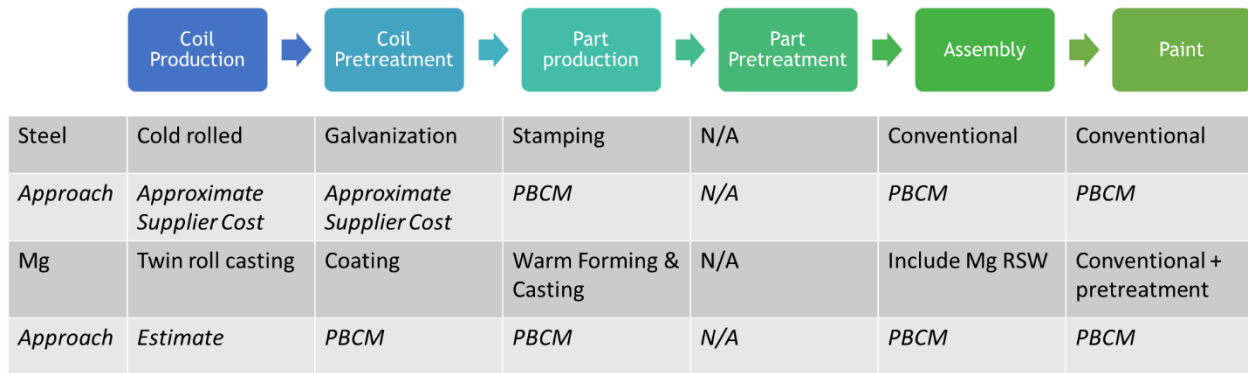
Figure B2: Comparative analysis scope and approach for modeling and cost estimation. (Source: Camanoe)

B2.2.4 Door Designs

The baseline steel door design (17.0 kg and 9 parts) from the Chrysler 200 is shown in Figure B3 and a lightweight magnesium-intensive Chrysler 200 door design (7.9 kg and 7 parts) developed in this project is shown in Figure B4. Additional details on the designs, processes, and assembly content are shown in Table B1.

Table B1: Number of parts, mass, and assembly content for two door designs.

Design Name	Parts (#)	Weight (kg)	Spot Welds (#)	Weld Nuts (#)	Adhesive Bonding (m)	Hems (#)	Laser Welds (m)	Clinch Nuts (#)	Self-Pierce Rivets (#)	Sealant (m)	Screws (#)
Steel Baseline	9	17.0	41	14	4.5	1	1.0				
Proposed Mg	7	7.9	13		4.5	1	1.0	18	16	0.9	4

B2.3 Results

B2.3.1 Magnesium Cost Drivers

Cost drivers were broken down by the key steps in the Mg door production process as follows: primary Mg production, sheet rolling, part forming, part surface treatment, and assembly.

Primary Magnesium Production

Camanoe had conducted a cost analysis of producing primary magnesium using both the US electrolytic and Chinese Pidgeon process as part of the AMD 603 project. Results were around $4.60 and $3.30/kg, respectively. Raw material prices are key cost drivers for both processes. Pidgeon process is sensitive to labor costs, whereas the electrolytic process is sensitive to equipment costs. Data availability was better for the Pidgeon process.

Magnesium Sheet Rolling

The main source of information was a study was conducted by the Aluminum Consultants Group and the Pacific Northwest National Laboratory in 2005 that analyzed the costs of twin-roll and twin-belt sheet production. Metal cost (AZ31 alloy) was found to be the primary cost driver in both cases. The total cost is highly sensitive to the raw metal price, but generally twin-roll casting was shown to have potential as a lower-cost alternative. Capital utilization is key for both processes, and rolling reduction per pass and recovery are also key cost drivers.

Part Forming

A preliminary cost modeling analysis of a magnesium door inner panel produced from sheet via warm forming was conducted using models and data from the AMD 603 project. That inner was assumed to be 3.3 kg (50% of the steel door design) with the same engineered scrap rate (55%), and the same magnesium alloy sheet prices as the AMD 603 study were used ($8.00/kg). Material cost accounted for 82% of the $52 total cost per door inner. This is due to both the high cost of the sheet and the relatively high engineered scrap rate for a door inner.

Part Surface Treatment and Assembly

Other cost drivers related to were summarized from experience gained from the AMD 603 project.
- Surface treatment of parts prior to assembly:
  - Added cost: no treatment required for steel parts.
  - Pretreatment required for individual parts. Conversion coating and top-coating required for complete assembly.
  - Opportunities to reduce treatment costs and/or change surface treatment approach.
- Assembly:
  - Despite parts consolidation, Mg front end assembly costs higher than steel.
  - Opportunities to reduce assembly content and/or reduce joining costs.

B2.3.2 Impacts on Mass and Cost

The calculated impacts on mass and cost for the steel scenario and two magnesium scenarios were shown in Figure B1 for complete door structures and are shown in detail in Figures B5 and B6 for three selected large panels. The latter show that material cost is approximately 50-70% of the panel cost.

B2.3.3 Sensitivity Analyses

There is uncertainty in several of the parameters used in the cost analysis, particularly annual production volume and material costs. The baseline annual production volume of 100,000 clearly assumes a long-range scenario. The cost per door is highest at low volumes and decreases as volumes increase, primarily driven by the fixed cost of tooling. Although the cost of each door is sensitive to the annual production volume, the steel door is always lower cost than the magnesium designs and the US magnesium scenario always has the highest cost.

The sensitivity of total door cost to material costs is high: A 10% change in material cost leads to approximately a 5% change in total door cost for all three scenarios, with the US magnesium scenario showing the largest impact because of it having the highest material cost. The US magnesium scenario can achieve the $5.50/kg project target with a 10% decrease in material costs. A 50% reduction of China magnesium price would likely be necessary in order to achieve cost parity with the steel design.
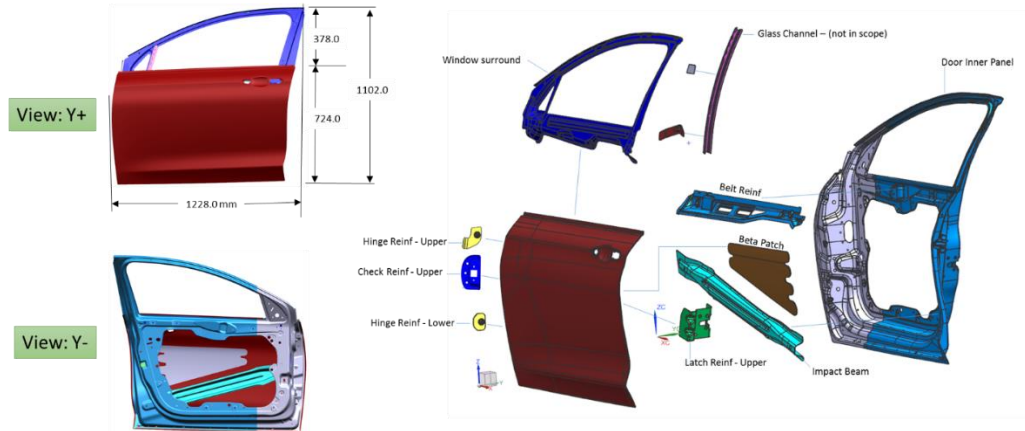
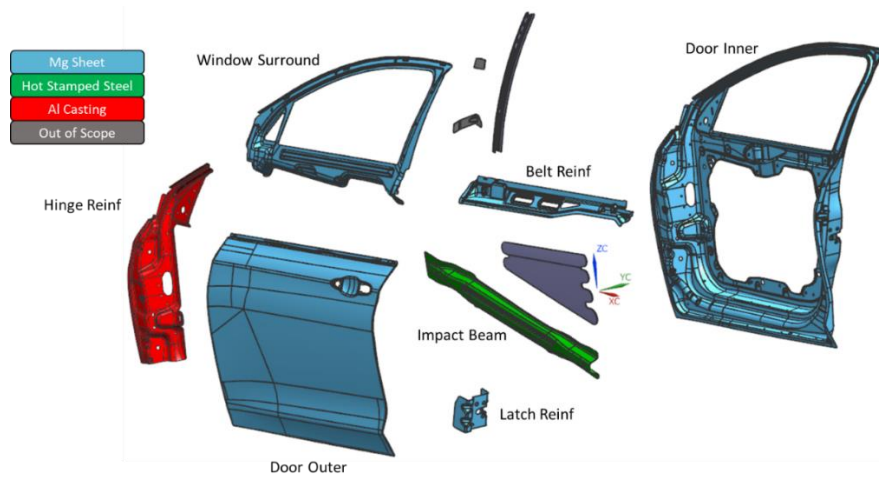Figure B3: Baseline steel door design from the Chrysler 200 (source: FCA).

Figure B4: Magnesium-intensive Chrysler 200 door design concept. (Source: FCA, for cost study only.)

B3. CONCLUSIONS AND RECOMMENDATIONS

1. The analysis of cost drivers found that automotive sheet magnesium assemblies are more expensive because material and assembly costs (relative to baseline steel designs) outweigh gains from lower mass and part count reduction. Material costs are primarily driven by high raw material costs. Primary magnesium (ingot) from China is about half as expensive as that produced in the US by a different process.

2. The magnesium door weighs 9.1 kg less than the baseline steel door. The cost of lightweighting is $4.26/kg saved if the sheet is from China, which is less than the target of $5.50. The cost is $6.60/kg saved if the sheet is sourced from the US.

3. While the larger parts in the magnesium door design are cost competitive, the smaller parts have relatively high lightweighting costs. This suggests opportunities for design optimization.

4. From a cost modeling standpoint, there are opportunities to improve the robustness. The highest priority should be the cost of the coated magnesium sheet given it is the largest cost driver. A better understanding of sheet pretreatment processes would lead to a better cost estimate as well.
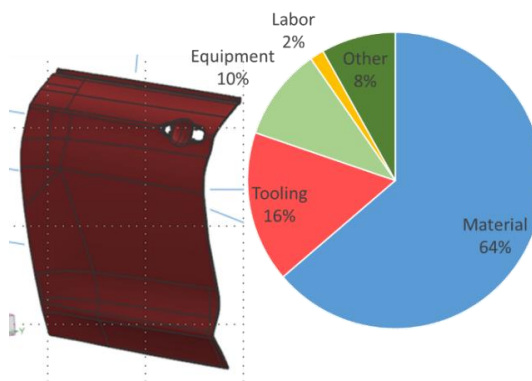
Door Inner Panel: $31.50
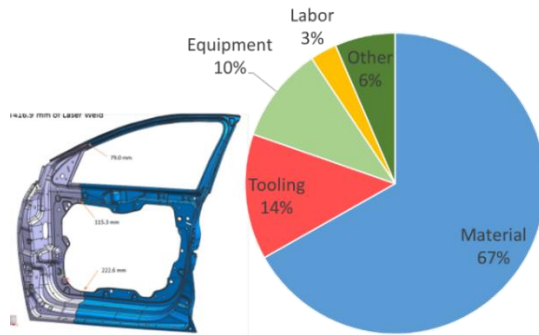
Material	Cold Rolled Mild Steel 140 Yield, 270 Tensile, hot-dipped galvanized
Thickness	1.5/0.75 mm (LWB)
Dimensions	1227 x 1102 x 32 mm
Blank Weight	15.5 kg (LWB)
Part Weight	6.63 kg
Eng. Scrap	57%

Tool Cost	$1,500,000
Press Line	4800 t Transfer
Line Rate	990 parts/hr
Workers	3

Door Outer Panel: $12.71

Material	Bake hardendable substrate steel 210MPa Yield, 310MPa Tensile, electrogalvanized coated
Thickness	0.65 mm
Dimensions	1102 x 724 x 111 mm
Blank Weight	13.6 kg (2 parts per blank)
Part Weight	4.52 kg
Eng. Scrap	34%

Tool Cost	$1,500,000
Press Line	6000 t Transfer
Line Rate	750 parts/hr
Workers	3

Window Surround: $11.93
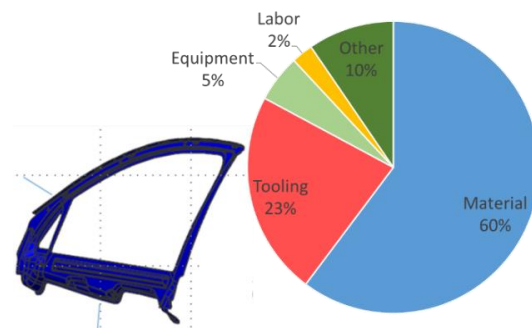
Material	Cold Rolled Mild Steel 140 Yield, 270 Tensile, hot-dipped galvanized
Thickness	0.85 mm
Dimensions	1161 x 526 x 81 mm
Blank Weight	5.41 kg
Part Weight	1.65 kg
Eng. Scrap	69%

Tool Cost	$1,000,000
Press Line	2400 t Transfer
Line Rate	1050 parts/hr
Workers	3

Figure B5: Steel door part processing parameters, assumptions, and costs. (Source: Camanoe)

Door Inner Panel: $34.94
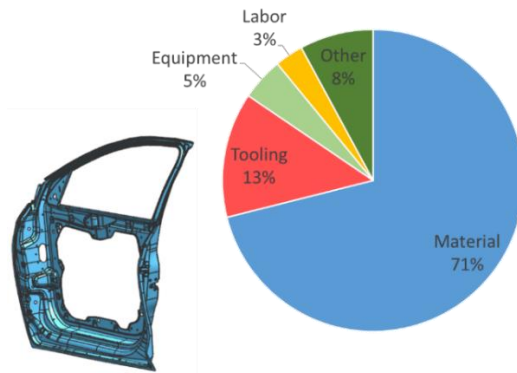
Material	Coated Mg sheet
Thickness	1.2 mm
Dimensions	1227 x 1102 x 326 mm
Blank Weight	3.95 kg
Part Weight	1.77 kg
Eng. Scrap	55%

Tool Cost	$1,800,000
Press Line	800 t Tandem
Line Rate	350 parts/hr
Workers	3

Door Outer Panel: $23.80
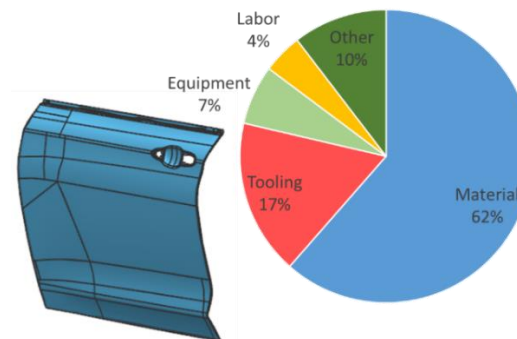
Material	Coated Mg sheet
Thickness	1.0 mm
Dimensions	1228 x 724 x 111 mm
Blank Weight	2.19 kg
Part Weight	1.54 kg
Eng. Scrap	30%

Tool Cost	$1,500,000
Press Line	750 t tandem
Line Rate	350 parts/hr
Workers	3

Window Surround: $16.34
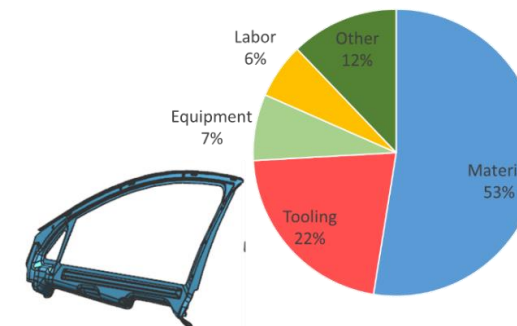
Material	Coated Mg sheet
Thickness	1.0 mm
Dimensions	1161 x 526 x 80 mm
Blank Weight	1.41 kg
Part Weight	0.43 kg
Eng. Scrap	70%

Tool Cost	$1,300,000
Press Line	750 t Tandem
Line Rate	350 parts/hr
Workers	3

Figure B6: Magnesium door part processing parameters, assumptions, and costs. (Source: Camanoe)

Chapter C. Task 2: Alloy and Sheet Processing Development

TASK INTRODUCTION

The research goals pursued in this broad-scope task were to use Integrated Computational Materials Engineering (ICME) methods to develop better fundamental understanding of the role of alloying elements in new Mg alloys and validate their material models, characterize key alloy properties needed to predict improved sheet alloy chemistries, and pursue thermomechanical process development to achieve the following objectives:

- Improved formability/reduced *rolling* temperatures and number of rolling passes required;
- Improved formability/reduced *forming* temperatures;
  - Goal: Reduce stamping temperature to below 250°C in a process in which the blank is heated but the tooling is not.
  - Stretch Goal: Room-temperature formability with "Class A" surface appearance (by stamping sheet in a stable soft temper, then hardening the part by a paint-bake-like heat treatment).
- Achieve randomized crystallographic texture sheet;
- Demonstrate mechanical properties in new Mg alloys sufficient to enable weight reduction opportunities greater than those of today's Mg sheet materials for the selected automotive components;
- Validate ICME predictions for formability and mechanical properties, including high strain rate properties compared to baseline material using test samples prepared in this project.

Figure C1 illustrates the types of data generated by each performing organization and its application in sample fabrication and characterization. The sub-task level final reports received from each contributing organization have been significantly condensed in this report to highlight accomplishments. Individual detailed sub-task final reports are accessible at the project's DataHUB folder.
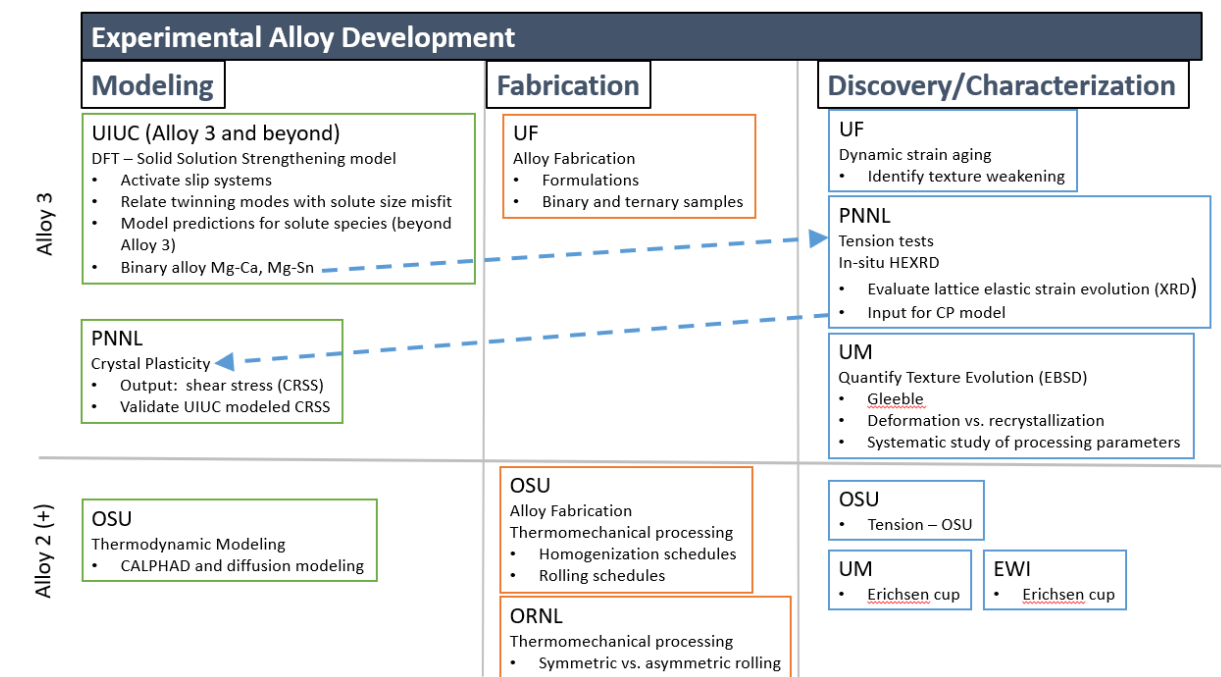

Figure C1: Task organization and data flows for the alloy development process. (Source: USAMP)

Table C1 lists several Mg alloys which were used and/or referenced in this project, together with their elemental compositions. Throughout this report, the alloys are referred to by their "Abbreviated Names" shown in this table, but the trade names and ASTM-like names are included for completeness.

Table C1: Names and compositions (wt. %) of Mg alloys used in this study.

Trade/Alloy Name	Abbrev. Name	ASTM-like name	%Al	%Zn	%Zr	%Ca	%Mn	%Sn	%RE	Notes
AZ31B		AZ31B	3	1	-	-		-	-	
ZEK100 (Elektron 717™)	ZEK	ZE10A	-	1.0-1.5	>0.2	-	-	-	0.12-0.22	1
E-Form Plus™	EFP	AZXM2110	1.5-2.5	0.6-1.4	-	<1.0	0.2-1.0	-	-	2
EFP batch 1	EFPb1	AZXM2110	1.94	0.89	-	0.71	0.30	-	-	3
EFP batch 2	EFPb2	AZXM2110	1.92	0.89	-	0.77	0.30	-	-	3
EFP batch 3	EFPb3	AZXM2110	1.97	0.91	-	0.85	0.36	-	-	3
EFP batch 4	EFPb4	AZXM2110	1.65	0.75	-	0.72	0.30	-	-	4
USAMP Alloy 1	Alloy 1	ATMZ3100	2.98	0.30	-	-	0.40	1.01	-	5
USAMP Alloy 2	Alloy 2	ZXME2100	0.011	2.10	-	0.52	0.42	-	0.209 Ce	6
USAMP Alloy 2 Plus	Alloy 2 Plus	ZAXME11000	1	1	-	0.5	0.4	-	0.2 Ce	
"Alloy 3"	Family of Mg-based binary and ternary alloys containing Ca, Zn.									

Notes in Table C1:
1. Luxferga.com/app/uploads/Luxfer-Elektron-717_2018.pdf
2. POSCO specification on Certificate No. 2981845
3. GM R&D Analytical Chemistry Certificate for EFP Batches 1-3.
4. GM R&D Analytical Chemistry Certificate for EFP Batch 4.
5. Korea Magnesium Industry Sample No: KS171215 41
6. Korea Magnesium Industry Lot No: KA180622 01

Abbreviations for elements in magnesium alloys (From ASTM B951-11 (2018))	
A	Aluminum
E	Rare earths
J	Strontium
K	Zirconium
M	Manganese
S	Silicon
T	Tin
X	Calcium
Z	Zinc

C1. Atomistic Modeling of Deformation Mechanisms in Magnesium
(University of Illinois Urbana-Champaign – Principal Investigator: D. Trinkle)

C1.1 SUMMARY
Atomistic simulations were utilized to develop predictive models for Mg alloy chemistries with increased isotropic deformation and greater ductility, stemming from solid solution strengthening. In general, solutes with large size mismatch with Mg (either undersized or oversized) are the most effective at strengthening the individual deformation modes and lowering the plastic anisotropy ratios for improved ductility. Specifically, the rare earth solutes Gd, Tb, Dy, Nd, Ho, Er, Tm, Yb, and Sm are the most promising for increasing the strength and ductility of HCP Mg, with the solutes listed here in decreasing order of effectiveness. Other solutes, Y, Sc, Pb, Ca, Ag, Bi, Tl, Zn, Li, Ga, Al, and Cd, may also increase strength and ductility of HCP Mg, with the solutes listed here in decreasing order of effectiveness. These elements would benefit the alloy formability only if they possess sufficient solubility in Mg. Accordingly, solubility analysis was extended to eight ternary Mg alloy systems utilizing the COST507 database. Solubility limits for Mg-Al-Cu, Mg-Al-Li, Mg-Al-Mn, Mg-Al-Si, Mg-Al-Zn, Mg-Cu-Si, Mg-Cu-Y, and Mg-Cu-Zn were determined by scanning the temperature-composition space to determine the maximum solubility of each solute in the HCP phase of Mg. Since large solutes are the most effective strengtheners in Mg, it is generally expected that in the most promising ternary alloys the smaller of the two solutes will increase the solubility of the larger solute. In the Mg-Al-Li system, Al increases the solubility of Li and Li increases the solubility of Al. Adding a small amount of Li to Mg-Al, can increase the yield stress of the non-basal deformation modes by up to 25% while reducing the ratios of the non-basal to basal yield stresses by up to 10%. For the other seven ternary systems, the addition of a second solute either has a negligible effect on the solubility of the second solute or reduces the solubility depending on the alloy. Detailed discussion of work on this Task may be found in UIUC's final report at https://data.lightmat.org/project.

C1.2 KEY ACCOMPLISHMENTS AND RESULTS

The approach to solute strengthening relied on Labusch-type solution models. Density-functional theory (DFT) computed the interactions of selected solute species with $\langle c + a \rangle$ edge, $(10\bar{1}2)$ tension twinning edge, and $(10\bar{1}1)$ tension twinning edge dislocations in Mg. These direct interaction calculations were then developed into approximate interaction models that combine geometric information from the dislocation cores in pure Mg with solute size and chemical misfits. The computed interaction energies parameterized the Labusch models which predict the strengthening potencies of 63 different solute species on these three different non-basal plastic deformation modes. Ratios of the solute-induced change in non-basal yield stresses to the solute-induced change in basal yield stress were computed. Promising solute candidates reduce these ratios at room temperature, thereby promoting dislocation slip on a larger number of slip systems required for generalized plastic deformation.

C1.2.1 Computational Methods
UIUC computed the strengthening potencies of 63 different substitutional solute species on $\langle c + a \rangle$ and twinning edge dislocations in Mg using Labusch-type solid solution strengthening models. The inputs to the strengthening models are dislocation core structures and solute-dislocation interaction energies, computed with DFT, and dislocation line tensions, computed using a classical potential.

C1.2.2 Solid-Solution Strengthening Models
Labusch-type weak pinning models gave the effects of solute concentration, temperature, and strain rate on the critical resolved shear stress (CRSS) in the examined dislocation cores. These models are based on previous work on solution strengthening of edge dislocations in Al and basal edge dislocations in Mg. Model input was the spatial distribution of solute-dislocation interaction energies in and around the

dislocation core, $U(x_i, y_j)$. UIUC optimized the dislocation and computed the interactions $U(x_i, y_j)$ of different solute species. This involved direct substitution of solutes into sites in the dislocation cores, and also for 63 different solute species. The size misfit quantifies the mismatch in volume between a solute and an HCP Mg atom, and the chemical misfits quantifies the interaction of a solute with stacking faults and twin boundaries in Mg.

C1.2.3 Plane Wave DFT in the VASP Code
The VASP DFT CODE enabled first principles calculations of solute-dislocation core energetics.

C1.2.4 Dislocation Core Optimization using First Principles Calculations
The $\langle c + a \rangle$ dislocation cores in Figure C1.1 were optimized using DFT with flexible boundary conditions (FBC). The edge dislocation splits into $\langle c + a \rangle/2$ partial edge dislocations. The screw dislocation also splits into partial dislocations but gets stuck in a local energy minimum where the partials are close together. Thus, the screw dislocation geometry is annealed using a modified embedded atom method (MEAM) potential which resulted in the proper dissociation of the perfect dislocation into $\langle c + a \rangle/2$ partial screw dislocations before starting the DFT FBC optimization.

C1.2.5 Twin Boundary Optimization
UIUC used DFT to optimize the geometries of the $(10\bar{1}1)$ and $(10\bar{1}2)$ twin boundaries in pure Mg as the first step in computing the interactions of solutes with these twin boundaries. The twin boundary geometries shown in Figure C1.2 mirror the atoms across the twin boundary planes represented by the dashed lines and them removing any duplicated atoms in the boundaries. Solutes are substituted into the sites labeled in the figure to directly compute solute-twin boundary interactions.

C1.2.6 Solute-Dislocation Interactions
Solutes that lower the difference in CRSS between basal and non-basal deformation modes to reduce plastic anisotropy, improving ductility and room-temperature formability, need to be identified. There are two approaches: (1) direct calculations or geometric interaction models parameterized with DFT data. (2) geometric interaction energy models that combine geometric information from the solute-free dislocation geometry with solute size and chemical misfits.

C1.2.7 Solute Interactions with Twinning Edge Dislocations
Solute-twin boundary interactions are used to compute a chemical misfit energy ΔB_{chem}^s that shifts the directly computed energies. The accuracy of the geometric model was validated by comparing predictions to direct calculations for Ca solutes in both twin cores.

C1.2.8 Solute Interactions with $\langle c + a \rangle$ Dislocations
For solute interactions with the $\langle c + a \rangle$ dislocations Al, Ca, Mn, Sn, or Zn solutes produce small changes in dislocation core structures. This can be captured using geometric models.

C1.2.9 Solute Size Misfits
Volumetric size misfits for 63 substitutional solutes in Mg were computed using the strain misfit tensor methodology. The strain misfit tensor ϵ_{ij}^s is the derivative of solute-induced strain $e_{ij}^{c_s}$ with respect to solute concentration c_s. To determine ϵ_{ij}^s, a single Mg atom is replaced with a substitutional solute in an HCP Mg supercell and then atomic positions are relaxed while fixing supercell lattice vectors. The strain ϵ_{ij}^s is computed from the solute's elastic dipole tensor P_{kl}^s and the DFT-computed elastic compliance tensor S_{ijkl}^0 of pure Mg.

C1.2.10 Solute Interactions with Twin Boundaries
Solutes interact with the dislocation core near the step as well as with the twin boundaries away from the

step, and both types of interactions contribute to solute-induced changes in the CRSS for twinning dislocation motion. The interaction energy of a solute s at site n near a twin boundary was computed. All eight sites shown in Figure C1.2 for the $(10\bar{1}2)$ and $(10\bar{1}1)$ twin boundaries are computed. Atomic relaxation is constrained so that atoms can only move perpendicular to the boundary.
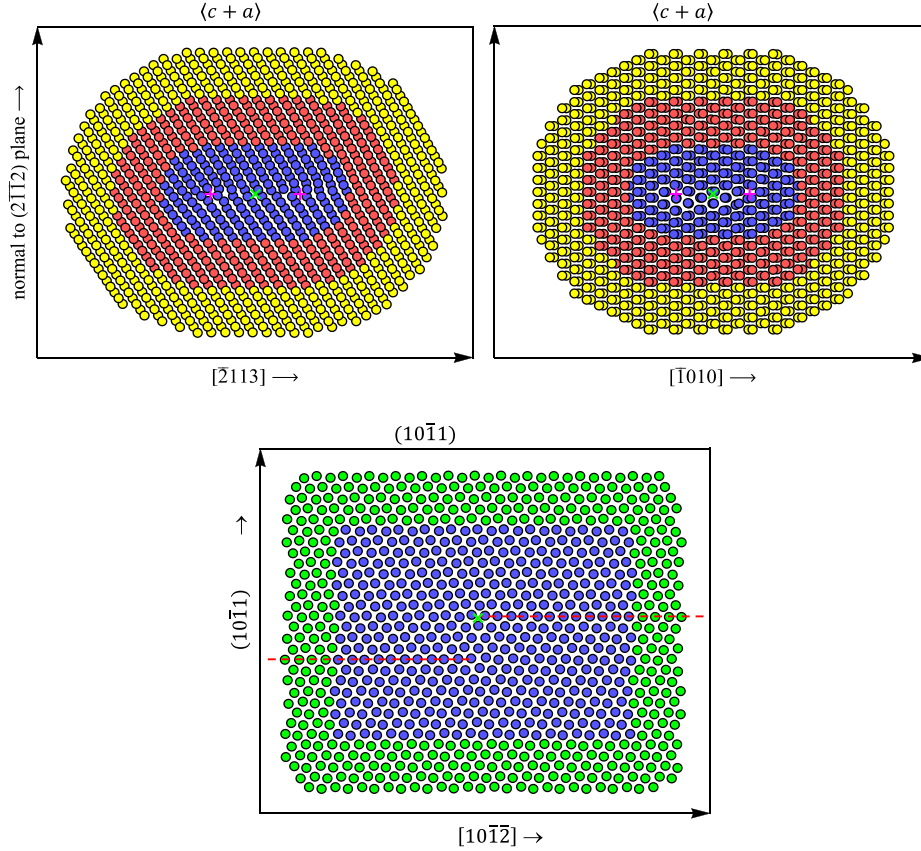

Figure C1.1: Initial DFT supercell geometries for the $\langle c + a \rangle$ edge, $\langle c + a \rangle$ screw, and $(10\bar{1}1)$ compression twinning edge dislocations in HCP Mg. The green "×"indicates the initial elastic center for the dislocation geometries. The initial $\langle c + a \rangle$ perfect dislocations dissociate into $1/2\langle c + a \rangle$ partial dislocations indicated by the magenta "+" symbols. The $\langle c + a \rangle$ dislocation geometries are divided into regions I (blue), II (red), and III (yellow) for subsequent relaxation using DFT with lattice Green's function (LGF)-based FBC. The twinning dislocation geometry is divided into a free region (blue), and a fixed region (green) for subsequent relaxation using DFT. The dashed red lines indicate the $(10\bar{1}1)$ twin boundary. Each supercell is subject to periodic boundary conditions along the threading direction which is out of the page. The $\langle c + a \rangle$ edge and screw dislocation slabs have thicknesses of 5.529 Å and 6.087 Å. The $(10\bar{1}1)$ twinning dislocation slab has a thickness of 3.192 Å. (Source: UIUC)
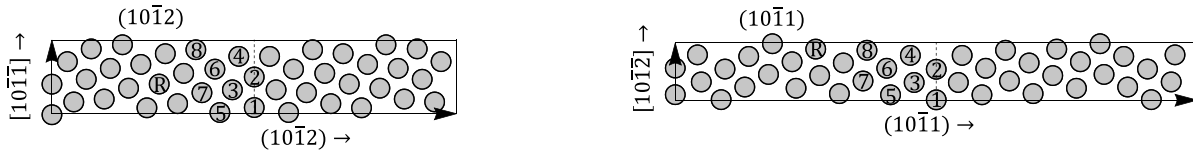

Figure C1.2: Supercell geometries of the relaxed $(10\bar{1}2)$ and $(10\bar{1}1)$ twin boundaries in Mg. (Source: UIUC)

C1.2.11 Dislocation Core Structures from First-Principles Calculations

The $\langle c + a \rangle$ edge and screw perfect dislocations dissociate into $1/2\langle c + a \rangle$ partial dislocations separated by a pyramidal 2 stacking fault. Figure C1.3 shows the dislocation geometries visualized using a combination of atomic positions and Nye tensor distributions.
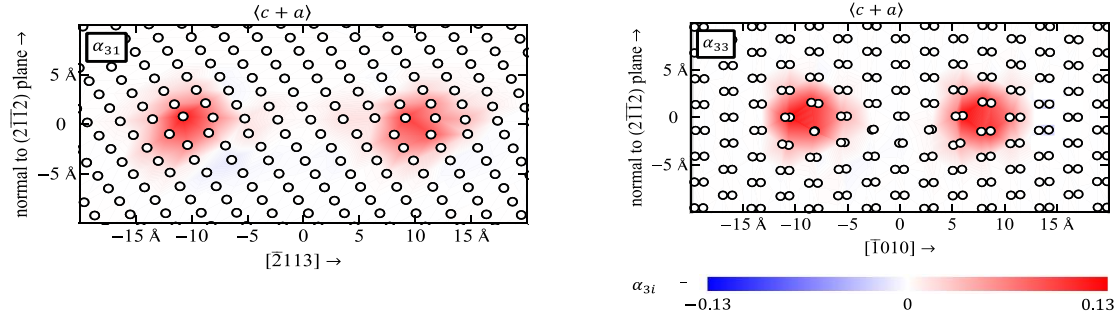

Figure C1.3: Core structures of the $\langle c + a \rangle$ edge and screw dislocations optimized using DFT with LGF-based FBC. The edge core is visualized using the α_{31} edge component of the Nye tensor distributions, and the screw core is visualized using the α_{33} screw component. The dislocations dissociate into $1/2\langle c + a \rangle$ partial edge or screw dislocations separated by a pyramidal 2 stacking fault. (Source: UIUC)

C1.2.12 Solute Interactions with the Pyramidal 2 Stacking Fault

The interaction of a solute s with the stacking fault region between the partial cores of $\langle c + a \rangle$ dislocations is determined by the local slip energy E_{slip} computed from the core geometry and the pyramidal 2 stable stacking fault energy γ_{p2}, and the solute's chemical misfit $\epsilon_{\text{p2}}^{s,n}$. The pyramidal 2 chemical misfits for Al, Ca, Cs, Ir, K, La, Li, Mn, Na, Os, Pr, Rb, Sn, Sr, Y, and Zn solutes were computed in all three layers. The volumetric size misfits ϵ_V^s of these solutes range from -1.31 for Os to 1.71 for Cs, and the chemical misfits for all three layers are described with second order polynomial in ϵ_V^s. However, for solutes with large $|\epsilon_V^s|$ the solute-dislocation interactions are dominated by the volumetric strain contributions, and the slip energy contributions have a negligible effect on the strengthening potency predictions. See Figure C1.4.

C1.2.13 Solute-Twin Boundary Interactions

The computed interactions of 18 solute species with the $(10\bar{1}1)$ and $(10\bar{1}2)$ twin boundaries showed that the interactions scale with the solute volumetric size misfit ϵ_V^s scale as $U_{n,\text{TB}}^{s,\text{fit}} \approx \alpha_n \epsilon_V^s + \beta_n \epsilon_V^{s\,2}$, where we treat α_n and β_n as empirical fitting parameters for each site type n. These scaling relations are used to predict the interactions of 45 other solute species with the twin boundaries. Chemical misfits for the twinning dislocations are given in Figure C1.5.

C1.2.14 Solute Size and Chemical Misfits

UIUC computed the volumetric size misfits ϵ_V^s of 63 different substitutional solute species in Mg using the strain misfit tensor approach. The misfit tensor method for computing volumetric size misfits is a robust approach that is also computationally efficient, since a single calculation is needed for each solute where only atomic coordinates are relaxed.

C1.2.15 Solute-Dislocation Interactions from Direct First-Principles Calculations

UIUC validated the approximate geometric models for solute-dislocation interactions for $(10\bar{1}1)$ twinning edge dislocations and for $\langle c + a \rangle$ edge dislocations by comparing the interactions for Ca solutes with direct interaction calculations. Figure C1.6 shows the agreement between the geometric and direct energy values for each dislocation. The geometric models were used to generate the interactions at all the core sites for input to the Labusch models.

C1.2.16 Solid-Solution Strengthening Predictions for Individual Deformation Modes

Accurate strengthening (i.e., increase in CRSS of the $(10\bar{1}2)$ twinning dislocation) predictions for any substitutional solute species can be made from ϵ_V^S as

$$\Delta\tau_y^s = \frac{603c_s/\text{at.}\%}{(T/300\text{K})\{\ln[10^8] - \ln[\dot{e}/(10^{-3}\text{s}^{-1})]\}}\epsilon_V^{s\,2}\ \text{MPa},$$

where T is the temperature and $\dot{e}$ is the strain rate. The solute-induced change in τ_y for (1011) compression twinning and $\langle c + a \rangle$ edge dislocations also varies quadratically with the volumetric size misfit, and may also be on the order of tens or hundreds of MPa per at.% solute. Note that the quadratic dependence means that both undersize and oversize solutes cause strengthening.
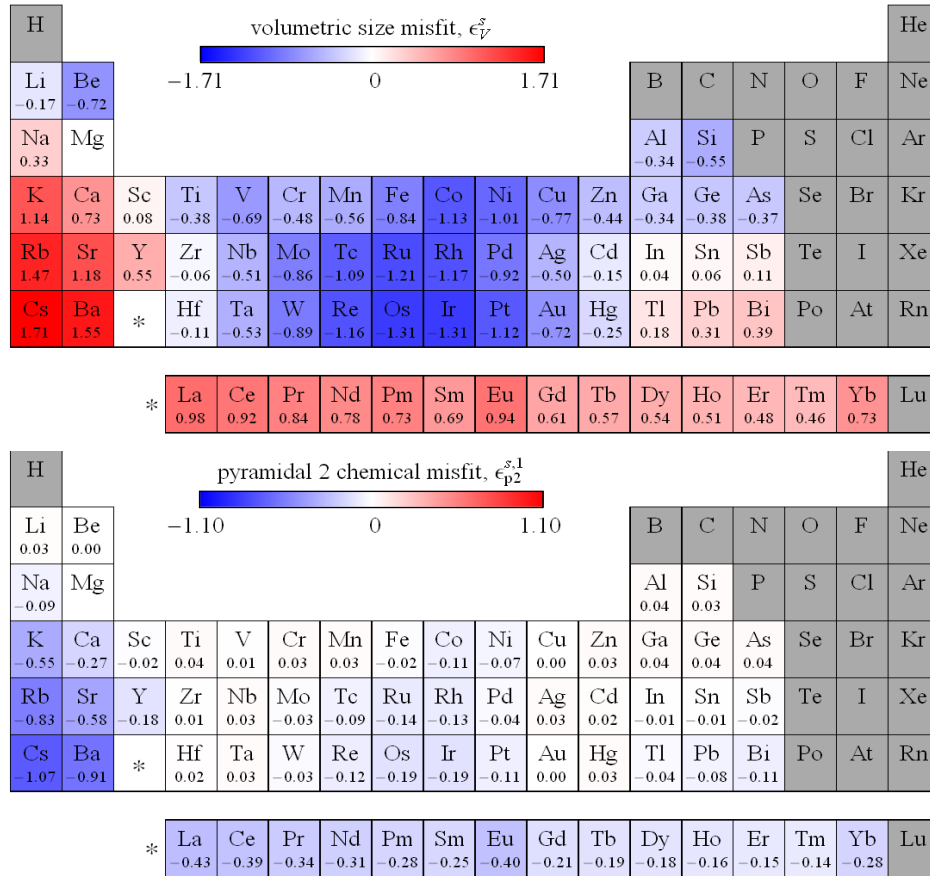

Figure C1.4: Size and stacking fault (chemical) misfits across the periodic table. (Source: UIUC)

C1.2.17 Strength and Ductility Predictions for Mg Alloys

In general, solutes with moderate size misfit values have a favorable combination of solubility and strengthening potency to potentially improve both the strength and ductility of Mg alloys. The rare earth solutes Gd, Tb, Dy, Nd, Ho, Er, Tm, and Yb show the greatest potential for strengthening the individual deformation modes, as well as for improving the plastic anisotropy of Mg by reducing the ratios of non-basal to basal yield stresses. The solutes Y, Sc, Pb, and Ca show the greatest potential for improving the mechanical properties out of the non-rare earth elements, approaching the improvements from the rare earths. It should be noted that the solubilities of Sc, Tl, Li, and Al are large, which may result in less accurate quantitative strength predictions compared to elements with lower solubilities, since the strengthening models do not account for the effects of solute-solute interactions on the motion of the dislocation cores.
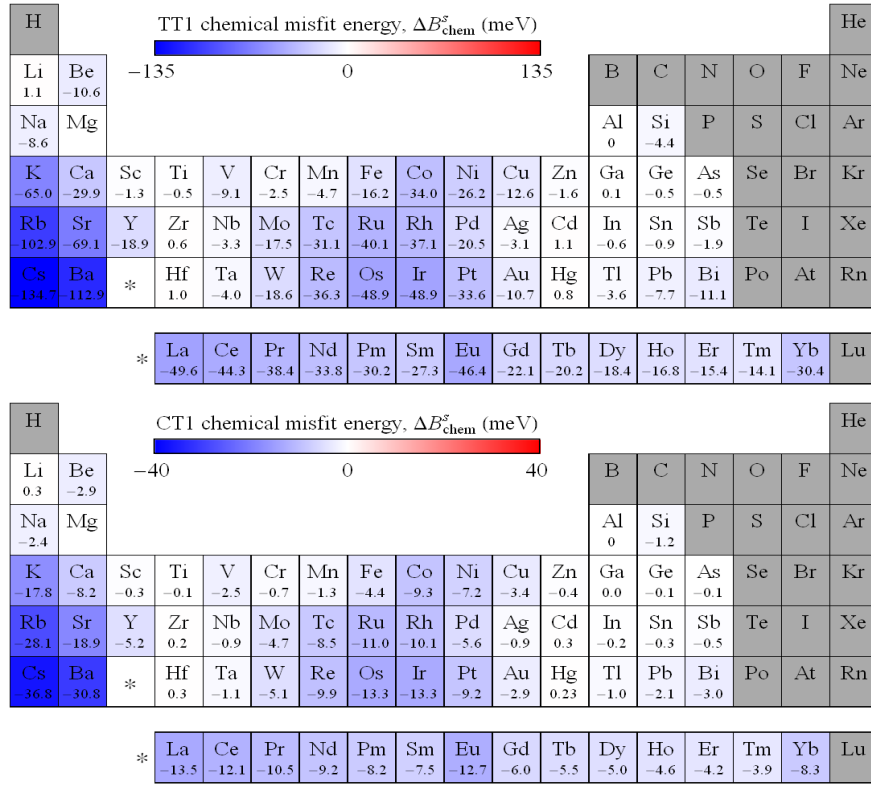
Figure C1.5: Chemical misfit energy for tension and compression twins across the periodic table. (Source: UIUC)
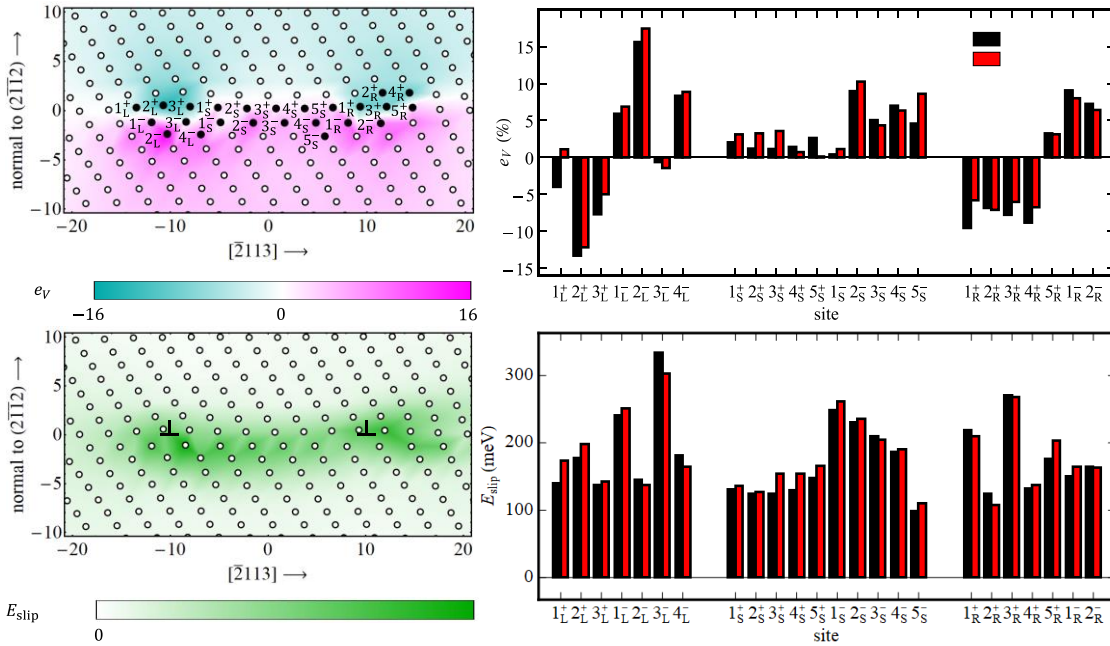
Figure C1.6: Local volumetric strain e_V and slip energy E_{slip} distributions in the $\langle c + a \rangle$ edge dislocation core (sorted by strain). The figures on the left show the distributions for the pure Mg dislocation core and label 24 different sites in the core for direct solute substitution. The bar charts on the right show there are minimal changes in the distributions after substituting solutes at the sites in the core. (Source: UIUC)

C1.3 CONCLUSIONS AND RECOMMENDATIONS

Strengthening predictions show that solutes with large positive or large negative size misfits are most effective at increasing the yield stress of the different deformation modes. However, these solutes generally have low solubilities in HCP Mg so their overall effectiveness at improving the mechanical properties of Mg alloys is limited. Solutes with small size misfits can have large solubilities in HCP Mg, but their strengthening potencies are small, so they are also ineffective. The most favorable combinations of strengthening potency and solubility for improving the strength and ductility of Mg alloys via solid solution strengthening are obtained with rare earth elements such as Gd, Tb, Dy, and Nd. Several non-rare earth elements, including Y, Sc, Pb, and Ca, are also promising alloying additions in Mg. Multi-component alloys can offer additional benefits over simple binary alloys.

C1.3.1 Contribution to the State-of-Art
The UIUC work has contributed in a variety of ways:
1. Development of predictive models of solute chemistry on deformation in magnesium;
2. Suggested routes for alloy chemistry of magnesium alloys with improved formability;
3. Increased computationally efficient routes to map out the solute energy landscape for other alloy systems.

Methodologies developed to efficiently and accurately predict solute-defect interactions from a smaller subset of calculations can be extended to other alloy systems in the future. The approach – combining accurate defect geometry calculations, solute misfits, and parameterized interaction models – permits the identification of chemical trends as well as the determination of energy landscapes with a fraction of computational effort needed for direct calculations. While elements of this approach have been used in the past, this is the first application for so many deformation modes and the majority of the periodic table.

C1.3.2 Technological Gaps
There are two issues to be tackled in future studies: (1) more complex interaction models, and (2) lack of thermodynamic data. In addition to developing new predictive strength models for combined solute chemistries, additional thermodynamic data is crucial. The approach developed here for considering binary alloys works in part because there is a large amount of binary phase diagram data available from which maximum solubilities can be extracted. However, when considering whether two solutes might promote higher solubility due to a "co-doping" effect, there is a lack of available thermodynamic data.

C2. Alloy 3 Design and Development
(University of Florida – Principal Investigator: M. Manuel)

C2.1 SUMMARY

A strong basal texture developed in magnesium sheet during rolling and recrystallization limits its formability. Select rare-earth (RE) alloying additions such as cerium (Ce) and neodymium (Nd) have been shown to enhance formability via texture modification when rolling is performed at certain temperature and strain rate conditions. A key mechanism identified for texture modification is dynamic strain aging (DSA), a diffusion-controlled process causing an increase in work hardening rate and negative strain rate sensitivity, relating to the pinning and unpinning of dislocations by solutes. Shear band nucleation, observed under conditions in which DSA occurs, has been reported to be responsible for texture weakening in dilute Mg–RE alloys. Calcium (Ca), a low-cost substitute for RE elements, with similar atomic size to Ce, has the potential to cause DSA and thereby modify texture in Mg-Ca alloys. Ca was also identified as a favorable alloying addition based on density functional theory calculations.

The sole addition of Ca to the α-Mg matrix did not, however, result in significant texture changes after deformation under DSA at 200°C. Nonetheless, the absence of RE-type texture in Mg-0.35Ca may be attributed to the absence of dynamic recrystallization which is considered necessary for the formation of the RE-texture component in extrusions of Mg-0.5Ca (wt.%) binary alloy. Additions of 0.5 wt.% Zn to Mg-0.35Ca decreased the recrystallization texture significantly after compression under DSA and non-DSA conditions and static recrystallization. However, no significant texture changes were observed between samples of Mg-0.35Ca-0.5Zn compressed under DSA and non-DSA conditions. Additions of 0.5 wt.% Zn to Mg-0.35Ca reduced the recrystallization texture intensity significantly by ~49% after compression under DSA and by ~54% after compression under non-DSA conditions, water-quenching, and then static recrystallization. A higher area fraction (~ 12% more) of recrystallized grains with weak (RE-type) texture was observed after static recrystallization of Mg-0.35Ca-0.5Zn previously deformed under DSA, in contrast with the sample deformed under non-DSA conditions. Combinations of both Ca and Zn in solution reduce Mg basal texture intensity after deformation and static recrystallization and enhance formability when processed inside the DSA regime. Detailed discussion of the UF's work may be found at https://data.lightmat.org/project/.

C2.2 KEY ACCOMPLISHMENTS AND RESULTS

C2.2.1 Experimental Methods and Procedures
All of the alloys in this research program were cast from elemental sources using a resistance furnace in a glovebox with a high-purity argon atmosphere. Melting was performed at 750°C in a BN-coated graphite crucible covered with a BN coated graphite lid and then the molten metal was poured into a BN-coated graphite mold. Castings were approximately 200 grams (g) with dimensions 82 x 20 x 84 mm, and 60 g with dimensions 45 x 16 x 48 mm. All castings were sectioned and encapsulated in a Pyrex tube sealed under vacuum for subsequent homogenization or annealing treatment, followed by water quenching. All testing methods followed ASTM E9-09 for compression testing of machined cylindrical samples measuring 16 mm in diameter and 24 mm in height.

C2.2.2 Results
The key outcomes of UF's experiments on development of binary and ternary Mg alloys are summarized in the sections below.

Alloy Selection
Thermodynamic calculations were performed using ThermoCalc and the associated TCMG4 database to

identify solid solution composition limits. Figure C2.1a illustrates the maximum solubility of Ca in Mg as a function of temperature. Figure C2.1b illustrates the effect of Zn additions on a Mg-0.35Ca, wt.% alloy. Table C2.1 shows the nominal and measured compositions of the alloys used in this research program. After casting, ingots were homogenized at 475°C for 50 h.
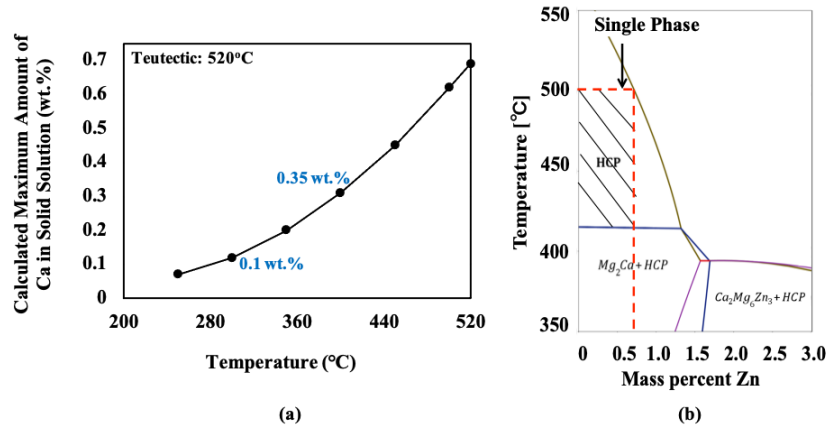

Figure C2.1: (a) Maximum amount of Ca in solid solution as a function of temperature in Mg, and (b) phase diagram of Mg-0.35 wt.% Ca as a function of Zn composition. (Source: UF)

Table C2.1: Nominal and measured compositions (wt.%) using ICP-OES of selected alloys.

Alloy	Nominal Compositions			Measured Compositions		
	Ca	Zn	Mg	Ca	Zn	Mg
Mg-0.1Ca	0.10	-	Bal.	0.07 ± 0.00	-	Bal.
Mg-0.35Ca	0.35	-	Bal.	0.34 ± 0.00	-	Bal.
Mg-0.1Ca-0.5Zn	0.10	0.50	Bal.	0.08 ± 0.01	0.43 ± 0.03	Bal.
Mg-0.35Ca-0.5Zn	0.35	0.50	Bal.	0.34 ± 0.00	0.45 ± 0.01	Bal.

Microstructural Characterization

Figure C2.2 shows XRD patterns from homogenized Mg-Ca and Mg-Ca-Zn alloys showed only the characteristic peaks of α-Mg. No peaks corresponding to Mg_2Ca secondary phase were detected. However, scanning electron microscopy (SEM) with energy dispersive spectroscopy (EDS) showed evidence of Mg_2Ca phase within grain boundaries with no secondary particles observed in the Mg α-matrix for all compositions (as shown in Figure C2.3). Table C2.2 summarizes the average Mg_2Ca particle size of homogenized alloys. Five particles were measured for size determination.

C2.2.3 Temperature and Strain-Dependent Mechanical Behavior

Figure C2.4 shows the stress versus strain curves of Mg–Ca binary and Mg–Ca–Zn ternary alloys compressed at 250 °C at strain rates of 10^{-3}, 10^{-2}, and 10^{-1}/s. Serrations, a macroscopic manifestation of DSA, were observed at 200° and 250°C at 10^{-3}/s in alloys of higher Ca composition. i.e., Mg–0.35Ca and Mg–0.35Ca–0.5Zn. However, no serrations were observed on samples compressed at 300°C and 10^{-1}/s.
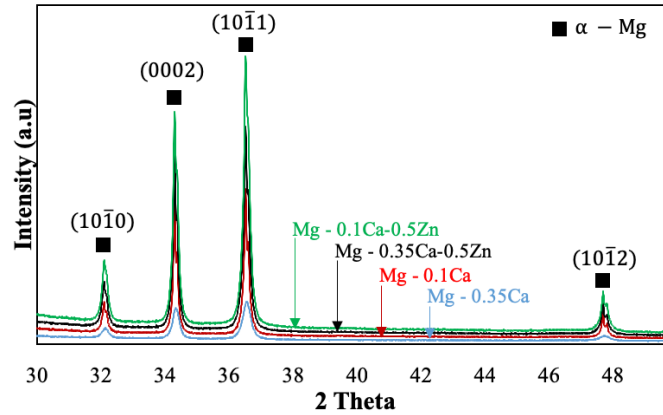
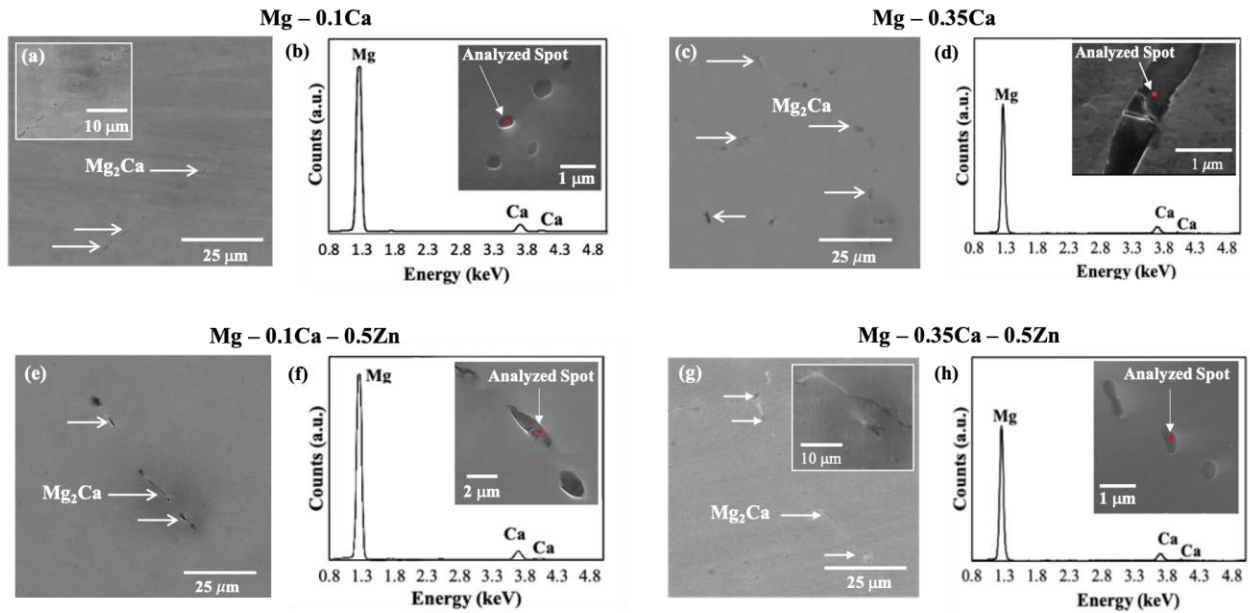Figure C2.2: XRD data obtained from homogenized (475°C /50 h) Mg –Ca and Mg–Ca-Zn alloys. (Source: UF)

Figure C2.3: Secondary electron images of homogenized alloys (a, c, e, and g) showing the distribution of the second phase, and (b, d, f, and h) EDS spectrum of the second phase indicating that it is Mg_2Ca. (Source: UF)

Table C2.2: Average Mg_2Ca particle size in homogenized alloys.

Composition (wt.%)	Average Mg_2Ca Particle size (µm)
Mg-0.1Ca	0.33 ± 0.06
Mg-0.35Ca	2.39 ± 0.7
Mg-0.1Ca-0.5Zn	$1.45 \pm 0.2l$
Mg-0.35Ca-0.5Zn	1.64 ± 0.50

Strain Rate Sensitivity (SRS) of Flow Stress

DSA is commonly observed under conditions at which the SRS is negative. SRS was calculated for all compositions using the 0.2% offset flow stress. Mg-0.1Ca and Mg-0.1Ca-0.5Zn were characterized by positive values of SRS, thus indicating the lack of DSA occurring at those test conditions as shown in

Figure C2.5. This can be related to the low amount of Ca in the Mg matrix of 0.1 wt.%. On the other hand, compositions of higher amounts of Ca, i.e., 0.35Ca wt.% were characterized by negative SRS at 200 and 250°C from 10^{-3} to 10^{-2}/s. These results correlate to findings that demonstrate that increasing the solute content broadens the range of conditions at which DSA occurs. All compositions were characterized by positive values of SRS at 300°C as shown in Figure C2.5, thus no DSA occurring.
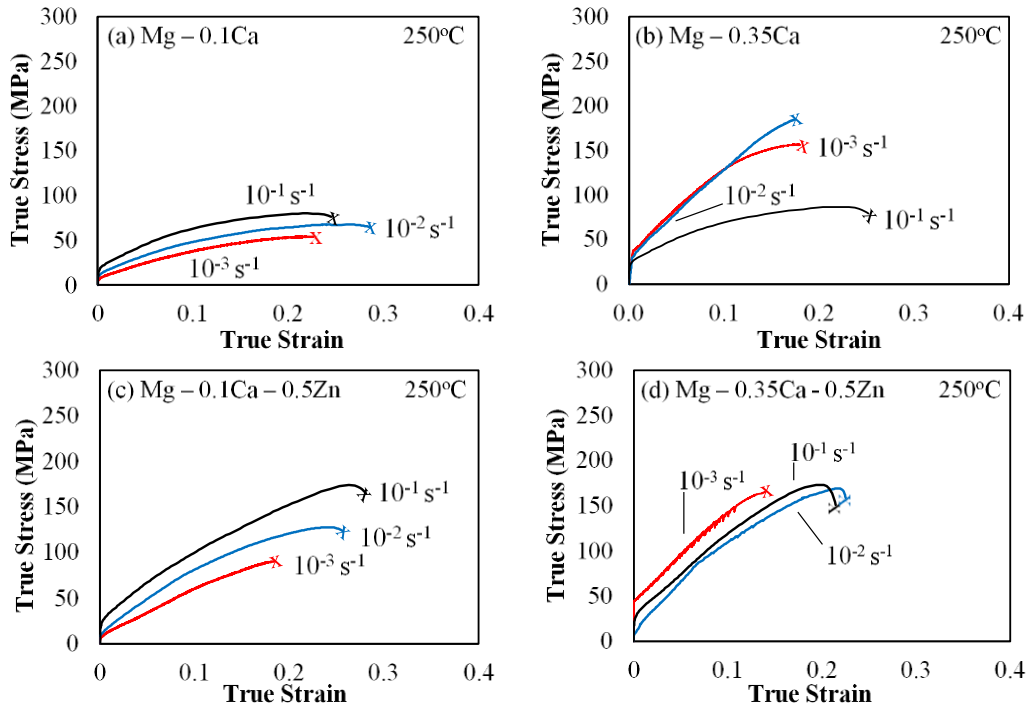

Figure C2.4: Compression stress-strain curves of Mg–Ca and Mg–Ca–Zn alloys at 250°C at strain rates of 10^{-3}, 10^{-2} and 10^{-1}/s. "X" represents the sample's fracture point. (Source: UF)
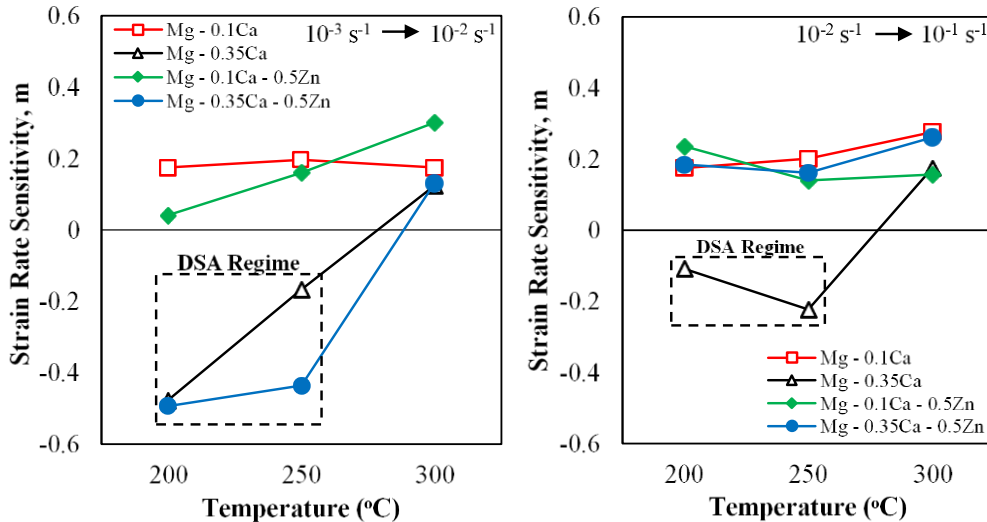
Figure C2.5: Strain rate sensitivity as a function of temperature showing the DSA regime from (left) 10^{-3} to 10^{-2}/s and (right) 10^{-2} to 10^{-1}/s for Mg–Ca binary and Mg–Ca–Zn ternary alloys. (Source: UF)

Static Recrystallization

To determine the effect of processing in the DSA regime on sample texture, Mg-0.35Ca and Mg-0.35Ca-0.5Zn samples were compressed up to 15% strain under DSA and non-DSA conditions, heat-treated at

450°C for various times, and water-quenched. Representative optical micrographs in Figure C2.6, show a mixture of recrystallized grains and regions of abnormal grain growth after 30 minutes of heat treatment.
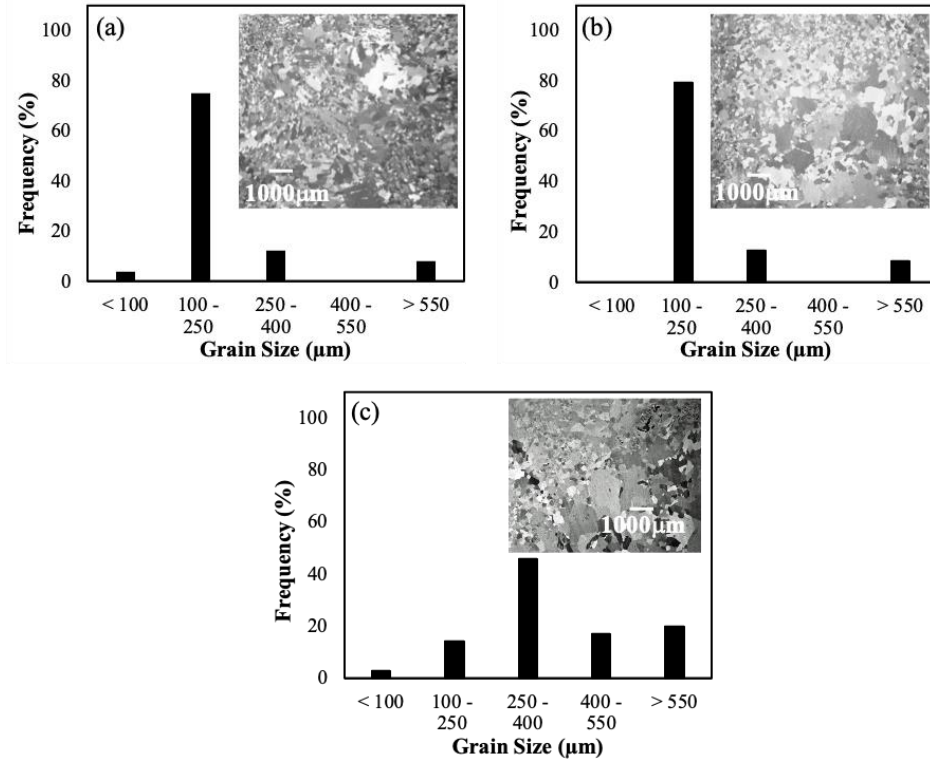

Figure C2.6: Representative optical micrographs normal to compression direction of (a) Mg-0.35Ca and (b) Mg-0.35Ca-0.5Zn cylinders compressed under DSA at 200°C and (c) non-DSA at 300°C conditions, then annealed at 450°C for 30 minutes. (Source: UF)

C2.2.4 Texture Analysis

Texture analysis was performed on two DSA and one non-DSA sample at PNNL. A Mg-0.35Ca and a Mg-0.35Ca-0.5Zn alloy compressed under DSA at 200°C-10^{-3}/s and Mg-0.35Ca-0.5Zn under non-DSA at 300°C–10^{-3}/s (all compressed up to 15% strain). Before texture analysis, all samples were recrystallized at 450°C for 30 minutes. The average grain size of these fine-grained regions was 100 ± 80, 127 ± 80, and 138 ± 103 μm for Mg-0.35Ca and Mg-0.35Ca-0.5Zn compressed under DSA and Mg-0.35Ca-0.5Zn compressed under non-DSA conditions, respectively. Texture analysis of Mg-0.35Ca compressed under DSA at 200°C-10^{-3}/s annealed at 450°C for 30 minutes showed a slightly decreased basal texture with the basal pole tilted 15° towards the transverse direction (TD) with a maximum intensity of 12.40 multiples of random distribution (MRD). This particular recrystallized texture differs from statically recrystallized textures of previously cold and hot rolled Mg-Ca binary alloy sheets which are characterized by strong basal components with c-axis parallel to the normal direction (ND). On the other hand, a significantly weaker texture characterized by a two-peaked TD-split texture (characteristic RE-texture) about 45 degrees away from ND was observed in Mg-0.35Ca-0.5Zn processed under similar conditions with a maximum intensity of 6.27 MRD as shown in Figure C2.7b (compare to Mg-0.35Ca binary shown in Figure C2.7a). Similarly, the texture of Mg-0.35Ca-0.5Zn compressed under non-DSA at 300°C (Figure C2.7c) was characterized by TD-split texture with basal poles about 30° away from ND with a maximum intensity of 5.68 MRD. Nonetheless, texture weakening of the Mg-Ca-Zn ternary alloys is strongly influenced by alloy composition, deformation processes, and annealing temperatures.

The total scanned area for EBSD was ~ 10 and 20 mm^2 for Mg-0.35Ca-0.5Zn compressed under DSA and non-DSA conditions, respectively. A higher area fraction (~ 30%) of weak (non-basal) textured grains

with an average grain size of 159 ± 61 μm was observed in the Mg-0.35Ca-0.5Zn after compression under DSA conditions and static recrystallization as shown in Figure C2.7b, while the sample compressed under non-DSA conditions was characterized by an area fraction of ~18% of weak textured grains with an average grain size of 143 ± 73 μm after static recrystallization (Figure C2.7c). Thus, it is evident that deformation of Mg-0.35Ca-0.5Zn under DSA conditions increased the average area fraction of weaker textured grains by about ~ 12% after static recrystallization compared to the sample compressed under non-DSA conditions. According to previous studies, deformation under DSA conditions promotes shear band nucleation attributed to being responsible for texture weakening in Mg-RE based alloys.
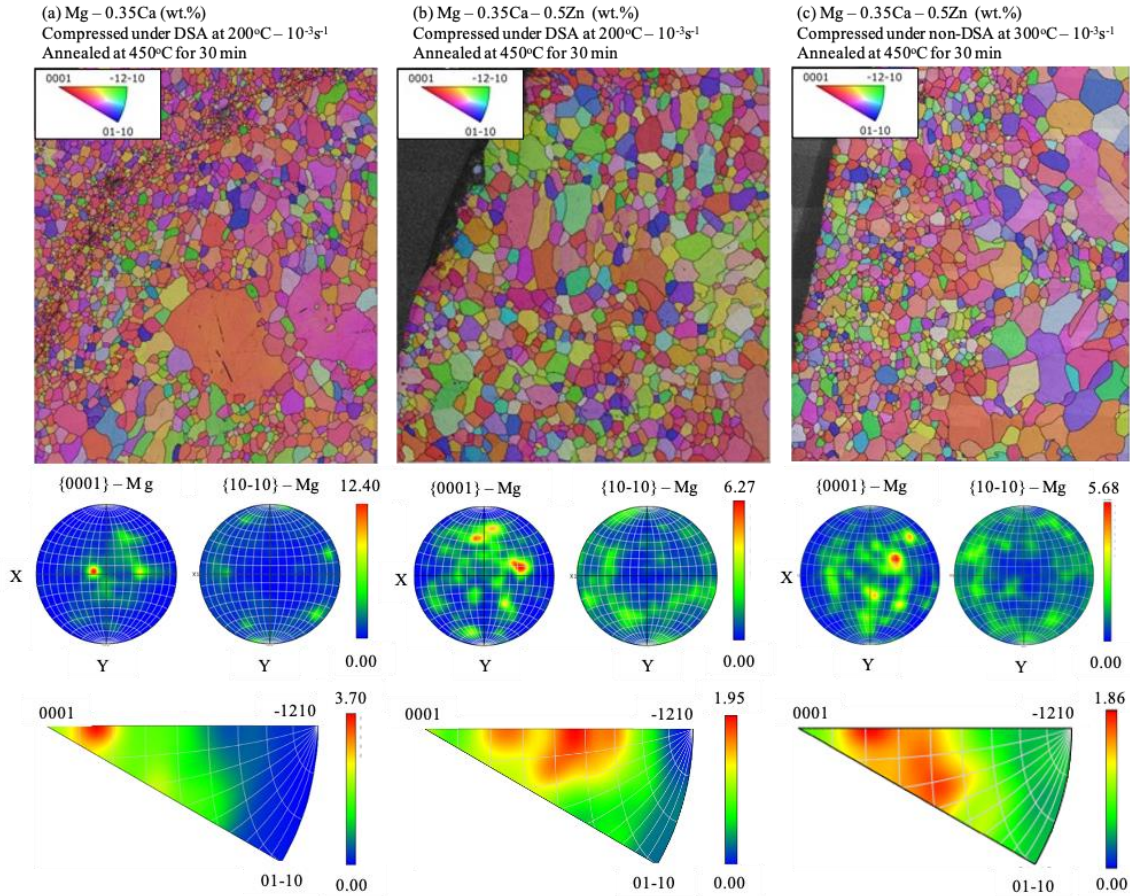

Figure C2.7: EBSD orientation maps and corresponding pole and inverse pole figures sets of (a) Mg-0.35Ca and (b and c) Mg-0.35Ca-0.5Zn compressed under DSA at 200°C -10^{-3}/s and under non-DSA at 300°C, all statically recrystallized at 450°C for 30 minutes. EBSD scans were performed by PNNL. (Source: UF)

C2.3 CONCLUSIONS AND RECOMMENDATIONS

1. Mg-0.1Ca and Mg-0.1Ca-0.5Zn wt.% were characterized by positive values of SRS, thus no DSA occurred at 200° and 250°C from 10^{-3} to 10^{-1}/s. This can be related to the low amount of Ca in the Mg matrix of 0.1 wt.%. On the other hand, compositions of higher amounts of Ca, i.e., 0.35Ca wt.% were characterized by negative SRS at 200° and 250°C from 10^{-3} to 10^{-2}/s. These results correlate to findings that demonstrate that increasing the solute content, broadens the range of conditions at which DSA occurs.

2. The addition of 0.5 wt.% Zn to Mg-0.35Ca reduced the average grain size, which in turn increased the critical stress for twinning and subsequently reduced the volume fraction of twins after deformation.

3. The sole addition of Ca to the α-Mg matrix does not result in significant texture changes after deformation under DSA at 200°C. Nonetheless, the absence of RE-type texture in Mg-0.35Ca may be attributed to the absence of dynamic recrystallization which is considered necessary for the formation of the RE-texture component in extrusions of Mg-0.5Ca (wt.%) binary alloy.

4. Additions of 0.5 wt.% Zn to Mg-0.35Ca decreased the recrystallization texture significantly after compression under DSA and non-DSA conditions and static recrystallization. However, no significant texture changes were observed between samples of Mg-0.35Ca-0.5Zn compressed under DSA and non-DSA conditions.

5. A higher area fraction (~ 12% more) of recrystallized grains with weak (RE-type) texture was observed after static recrystallization of Mg-0.35Ca-0.5Zn previously deformed under DSA, in contrast with the sample deformed under non-DSA conditions. These results partially support our hypothesis that processing dilute Mg-Ca-Zn alloys inside the DSA regime will lead to RE-texture components that enhance formability.

6. It is evident from these results and the literature, that combinations of both Ca and Zn in solution reduce Mg basal texture intensity after deformation and static recrystallization. Therefore, Mg-Ca-Zn alloys represent promising RE-free alloys for production of low-cost Mg sheets for the automotive industry.

C3. Modelling Alloy 3
(PNNL – Principal Investigator: E. Barker)

C3.1 SUMMARY

The activities at PNNL aimed to investigate the fundamental relationships between alloy composition and microstructural attributes with the deformation mechanisms of the different slip and twin systems for select Mg alloys. The deformation mechanisms of the binary alloys Mg-0.2at.%Ca (0.33 wt.%Ca) and Mg-1.5at.% Sn (6.92 wt.% Sn) were studied by in-situ neutron diffraction and synchrotron XRD and SEM/EDS/EBSD, providing detailed information about the microstructure and the available slip and twin deformations that are activated at room temperature under tensile load.

Furthermore, room-temperature tensile deformation mechanisms and texture evolution of E-Form Plus (EFP) were investigated by the above techniques, to better understand and characterize the alloy that was prominently utilized by the other Tasks in this project. Notably, the much smaller grain size and higher ductility of EFP, compared to the binary alloys, allowed the in-situ experiments to provide valuable inputs for the modeling efforts, for which the binary alloy results were not sufficient.

The above experimental information, as well as first-principles calculations from University of Illinois Urbana-Champaign, were used to inform Crystal Plasticity Finite Element Models (CPFEM) for these alloys. Deformation of the binary alloys under tensile loading was modeled and favorably compared with experimental results, providing validation for the first-principles calculations. This work was funded through the DOE-VTO LightMAT program. Detailed discussion of this work may be found in the sub-task final report at https://data.lightmat.org/project/.

C3.2 KEY ACCOMPLISHMENTS AND RESULTS

C3.2.1 Experimental Investigations

Two sets of binary Mg alloys, Mg-0.2at.%Ca and Mg-1.5at.%Sn, were cast and rolled (~1.2 mm thick) for this study by University of Florida. Additionally, 1.2-mm thick sheets of EFP Batch #2 were studied. Tensile specimens were excised from these sheets along the rolling direction (RD), for in-situ experimentation. The interest in EFP stemmed from the expansive work on this alloy throughout the project, while the alloying elements Ca and Sn were selected based on experimental and first principles work that indicated these elements have widely differing effects on the Mg alloy texture and formability, that would allow robust testing of the UIUC calculations for these elements. The difficulties associated with producing these samples and achieving the needed compositions and microstructural features necessitated producing two sets of alloys, which were received and studied at different times. Furthermore, the complexity in scheduling X-ray and neutron beam times meant that the results from the different binary samples need to be considered in aggregate to provide a better understanding of the deformation mechanisms and other material properties. The full datasets and results are presented in the stand-alone sub-task final report from PNNL. The results and conclusions are summarized in this report.

Two samples cut from recrystallized binary Mg alloys (Sample Set # I) and the EFP sheets were used for in-situ neutron diffraction tensile test at the VULCAN Diffractometer of Spallation Neutron Source (SNS) at Oak Ridge National Laboratory. The tensile tests were carried out at room temperature with a strain rate of 10^{-6}/s. High-intensity X-rays at the Advanced Photon Source (APS) at Argonne National Laboratory were utilized to probe any fluctuations in XRD peak width during *in-situ* tensile deformation.

The neutron diffraction results for the recrystallized binary alloys Mg-0.2Ca and Mg-1.5Sn are displayed in Figure C3.1. In Figure C3.1a, the stress-strain curve indicates that the recrystallized Mg-0.2Ca sample

yielded at about 70 MPa. The sample fractured at about 10% engineering strain. In Figure C3.1b, the lattice strain evolution indicates that grains in {10-11} direction (red) yielded first by the activation of basal slip at the stress of 40 MPa. The red dotted line illustrates the deviation of lattice strain from linearity, and the increased slope indicates the grains in that direction release stress, that is the grains micro-yield. For the recrystallized Mg-1.5Sn sample, the stress-strain curve (Figure C3.1e) indicates yielding at about 80 MPa. The sample fractured at about 7% engineering strain. In Figure C3.1f, the slope of {10-11} lattice strain increased at about 38 MPa, indicating micro-yielding for also this sample. The plastic deformation was activated by basal slips in {10-11} grain, leading to the grains in {10-10} and {11-20} directions accommodating more stresses. The increased peak intensity of {10-10} and {10-11} diffraction after yielding implies that those grain reorientations lead to {10-10} and {10-11} planes gradually reorienting to loading direction (LD), which is the typical texture caused by dislocation slips in HCP materials in tensile deformation. The increase of FWHM (Figures C3.1d and C3.1h) is mainly induced by dislocations, but the magnitude of increase is not significant, which indicates that twinning might be an alternative deformation mechanism. In summary, the tensile deformation of both binary Mg alloys is dominated by the basal slip and extension twins. The increase in dislocation density was small and the twinning activity was limited due to low ductility.

EBSD was used to obtain microstructure information on these recrystallized alloys, and to measure the grain structure and texture before and after tensile deformation described above. The CPFEM models described below were built based on the following before-deformation measurements. The EBSD inverse pole figure (IPF) image of Mg-0.2Ca in Figure C3.2a shows nearly equiaxed grains with an average grain size of 48 µm after recrystallization. However, some grains are larger than 200 µm in diameter. After tensile deformation, deformation twins were observed (Figure C3.2c). Since the plastic strain was small, the change of pole figures is negligible as shown in Figures C3.2b and C3.2d.
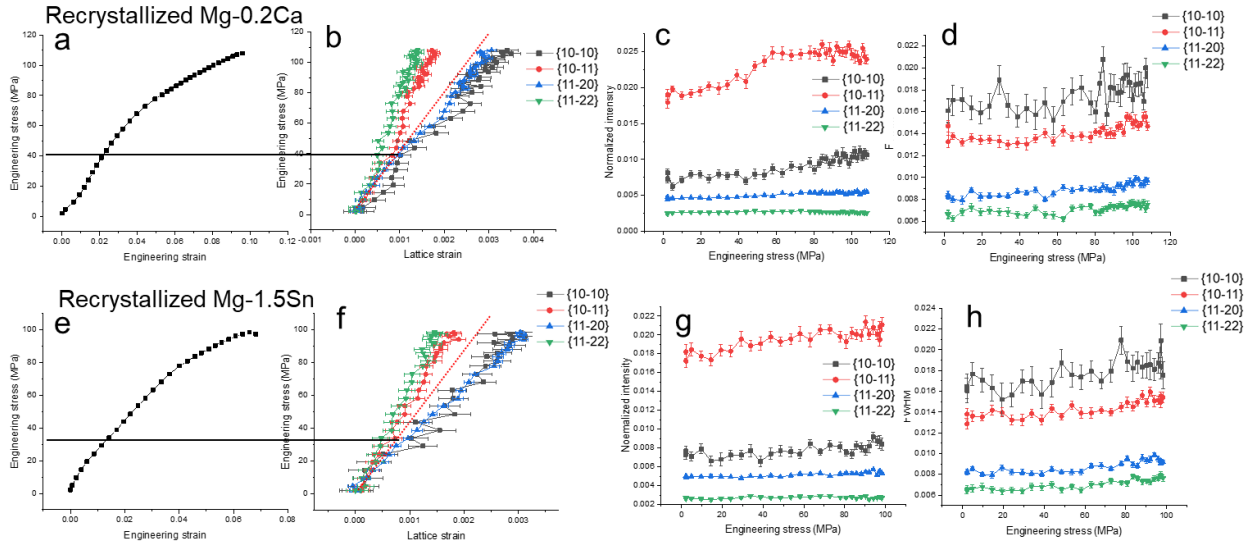

Figure C3.1: The results of in-situ neutron diffraction tensile tests of Mg-0.2Ca: (a) stress-strain curve and the evolution of (b) lattice strain (c) normalized peak intensity (d) FWHM; Mg-1.5Sn: (e) stress-strain curve (f) lattice strain (g) normalized peak intensity (h) FWHM. (Source: PNNL)

For recrystallized Mg-1.5Sn alloy, the IPF image in Figure C3.3a shows nearly-equiaxed grains with an average grain size of 67 µm. Some grains larger than 200 µm in diameter were also observed. The deformation twins were occasionally observed in some grains after tensile deformation (Figure C3.3c). After deformation, the intensity of basal texture decreased from 12 MRD to 6 MRD as shown in Figures C3.3b and C3.3d.
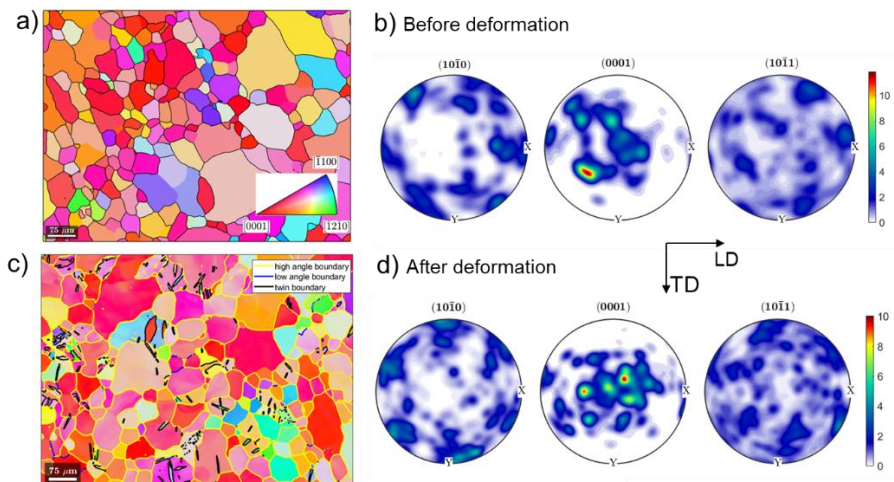
Figure C3.2: EBSD results of Mg-0.2Ca: (a) IPF image and (b) pole figures before tensile deformation; (c) IPF image and (d) pole figures after tensile deformation. (Source: PNNL)
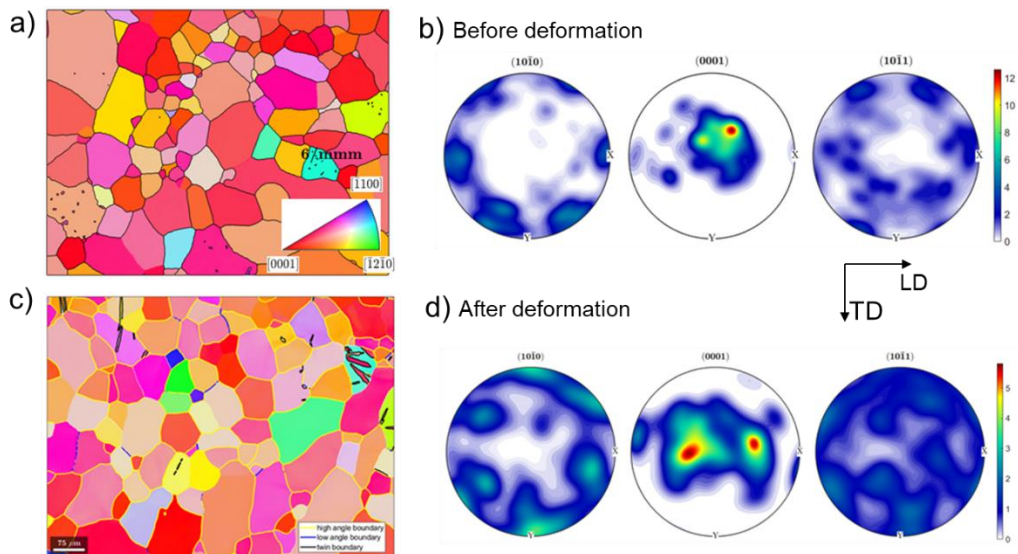

Figure C3.3: EBSD results of Mg-1.5Sn: (a) IPF image and (b) pole figures before tensile deformation; (c) IPF image and (d) pole figures after tensile deformation. (Source: PNNL)

The SEM images of the received EFP Batch #2 sheet display a uniform dispersion of 1-2 µm sized precipitates (Figure C3.4). The higher magnification SEM image also shows the extensive precipitation in this alloy. EDS mapping showed that the precipitates are predominantly rich in Ca and Al. The EBSD IPF map shown in Figure C3.5 corresponds to nearly-equiaxed grains, in a range from 5-35 µm with an average grain size of about 10 µm, with the c-axes of most grains being aligned along the normal direction (ND). The corresponding (0001) pole figure indicates the typical basal texture of a rolled Mg alloy sheet (different batches of EFP sheets displayed much different textures and deformation behaviors).
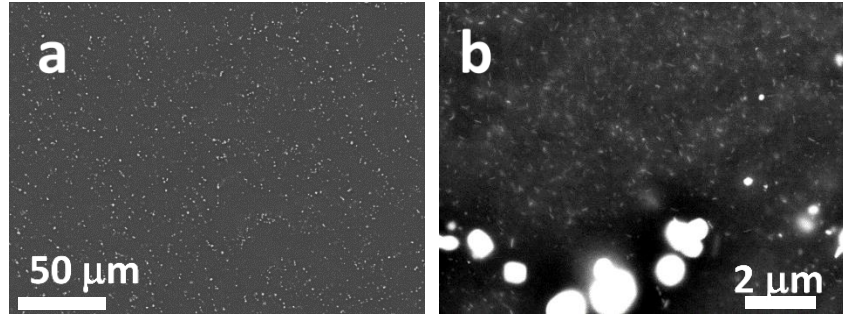
Figure C3.4: Backscattered electron SEM images of the microstructure of as-received EFP alloy: (a) low magnification showing the uniform dispersion of precipitates and (b) high magnification showing additional nano-scale precipitates. (Source: PNNL)

The in-situ time-of-flight neutron diffraction results for EFP are shown below. Figure C3.6a shows the lattice strain evolution versus true stresses for the four diffracting planes of Mg in the LD and two diffracting planes in the TD. It should be noted that no peaks of precipitates are observed from neutron diffraction. Initially, the sample undergoes elastic deformation, and the lattice strains increase linearly at nearly the same slope for all the grain orientations. The deviation from the linearity indicates the onset of yielding in 'soft' grains along with a stress redistribution among different grain orientations. The selective lattice strain of the soft orientations from $\{10\bar{1}1\}$ and $\{11\bar{2}2\}$ diffraction at the small strain in Figure C3.6b indicates micro-yielding occurred at about strain of 0.1% and stress of 50 MPa. However, the volume fraction of these yielded grains is small in this strongly textured sample, which results in a small effect on the overall deformation behavior. The soft grains yield first because the basal slip is easily activated in such orientations due to low critical resolved shear stress (CRSS).
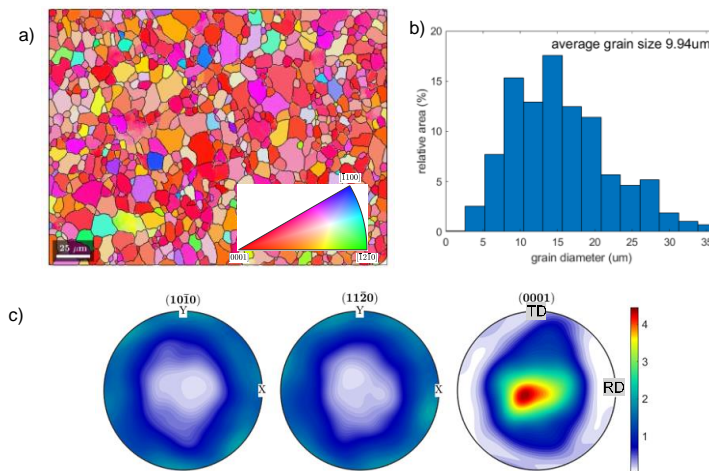
Figure C3.5: EBSD results of the EFP Batch #2 tensile sample before deformation: (a) the IPF map with the color code projected to RD; (b) grain size distribution showing average grain size about 10 mm; (c) the pole figure indicating a typical basal texture of the as-rolled alloy. Maximum of 4 MRD. (Source: PNNL)

Moreover, combining synchrotron XRD and in-situ uniaxial tensile testing, the development of texture induced by different deformation modes in EFP was determined by measuring pole figures. Similar to the EBSD results, the initial texture was typically characterized by the pole figure of the basal plane. The grain orientations were randomly distributed along RD and TD. The basal texture increased as the load was applied along RD. Then, increased $\langle 10\bar{1}0 \rangle$//RD texture component was observed as the plastic strain

accumulated. The tensile loading led the initial basal texture to slightly spread towards TD, which also agreed with EBSD results. More importantly, compared with EBSD, the in-situ results highlight the gradual texture development of the pole figures.
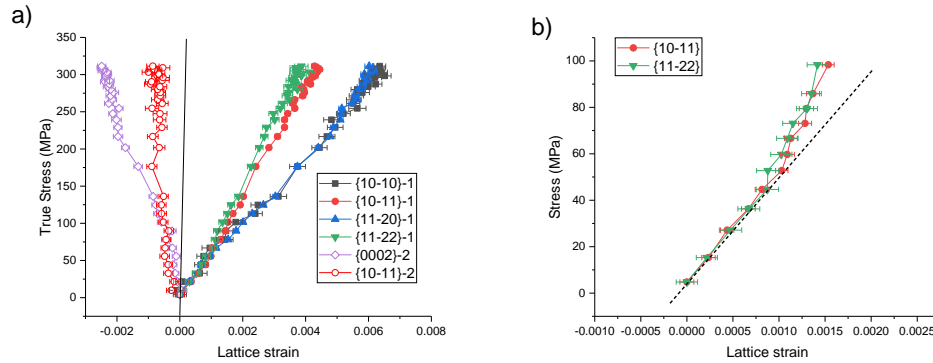

Figure C3.6: In-situ neutron diffraction results of EFP: (a) the evolution of the lattice strain; (b) selected lattice strain showing the micro-yielding during early deformation. (Source: PNNL)

The dependence of the activated deformation modes on the texture evolution in Mg alloys is understood by the simulation using the Taylor model. The classical Taylor model considers the homogeneous deformation of a polycrystal. The representative volume elements for EFP, including 5000 grains with initial basal texture, is created based on the EBSD and synchrotron XRD results. The CRSS values needed to activate certain slip systems for this simulation are summarized in Table C3.1. Extension twinning is excluded in the calculation because neither EBSD nor neutron diffraction showed evidence of twinning activities. These results serve as a starting point for the CP model described below.

Table C3.1: The activated slip systems and their CRSS values for the Taylor model.

Slip system	Plane	Direction	CRSS (MPa)
Basal <a>	$\{11\bar{2}0\}$	$\langle11\bar{2}0\rangle$	16
Prismatic <a>	$\{01\bar{1}0\}$	$\langle2\bar{1}\bar{1}0\rangle$	55
Pyramidal <c+a>	$\{2\bar{1}\bar{1}3\}$	$\langle\bar{1}101\rangle$	73

C3.2.2 Simulated Stress-Strain Response of the Alloys

The state and evolution of grain orientations, stress and strain states, CRSS values, and other microstructural details were modeled using the crystal plasticity finite element method as these simulations are able to investigate the impact of individual variables such as specific grain orientations, grain size, and CRSS value for each slip system where physical experiments cannot hold all other factors constant. For the current work, grain geometries representative of the binary Mg alloys, Mg-0.2Ca and Mg-1.5Sn were generated using the software package *Neper*. Corresponding finite element meshes were also generated using *Neper*. Crystal plasticity finite element simulations of the Mg alloy samples under tension were conducted using the software package *FEpX* which computes the elastoplastic deformations of polycrystalline solids.

For the recrystallized Mg-1.5Sn sample, the grains were observed to be equiaxed with an average grain size of 67 μm while for the recrystallized Mg-0.2Ca sample, the equiaxed grains were observed to have a smaller average grain size of 48 μm. For the current simulation study, polycrystal geometries were generated within a bounding box of 1mm x 1mm x 2mm to mimic the rectangular shape of the tensile specimen gage section (Figure C3.7). The average grain sizes of 48 and 67 μm were used to generate tessellations resembling the two alloys Mg-0.2Ca and Mg-1.5Sn, respectively. This resulted in 18,085

grains for the Mg-0.2Ca digital sample and the Mg-1.5Sn digital sample containing 6,650 grains. The resulting finite element meshes included 1,571,017 and 965,559 elements respectively.

<div align="center">(a)   (b)</div>
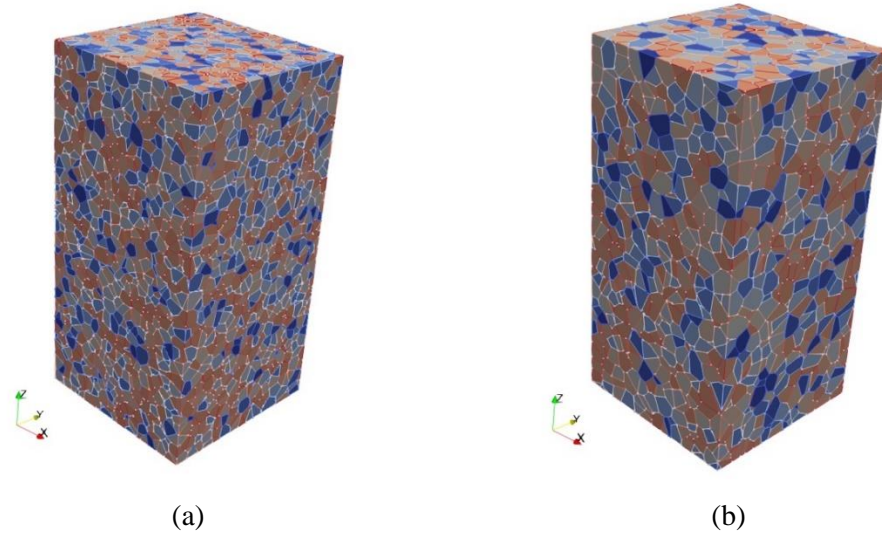
Figure C3.7: Polycrystal geometries generated using Neper to represent the (a) Mg-0.2 at.% Ca and (b) Mg-1.5 at.% Sn binary alloys. (Source: PNNL)

The elastic stiffness constants were calculated by UIUC using the modified embedded atom method (MEAM) with an interatomic potential for HCP Mg. The resulting values are C_{11} = 64.3 GPa, C_{33} = 70.9 GPa, C_{12} = 25.5 GPa, C_{13} = 20.3 GPa, and C_{44} = 18.0 GPa. The lattice constants used are a_0 = 3.187 Å and c_0 = 5.173 Å. The additional plasticity parameters required by *FEpX* for each binary alloy are listed in the full report.

Base values for the initial slip system strengths, calculated using the Taylor model, discussed previously, were set to 16, 55, and 73 MPa. Note that these values were measured for EFP, for which the small grain size allowed robust measurement. Those values were then augmented following the UIUC work calculating the changes in CRSS due to the concentration of different solute species. The UIUC task directly calculated the changes in CRSS for the optimal concentration of Ca, 0.40 at.%, being dissolved in the Mg matrix. The current material only contains 0.2 at.% of Ca. Therefore, the values reported by UIUC were modified. The UIUC work does not specifically calculate the ratio for prismatic/basal. For the current work, since the basal slip is the weakest, the pyramidal changes are also used for prismatic. Following their procedure, values were also calculated for Sn. Using the samples and material parameters described above, a series of simulations were conducted to compare the impact of grain orientations, average grain size, and differences in material parameters. Finally, simulation results were compared to the strain-stress in-situ measurements.

EBSD measurements of the texture of the two binary alloys captured very similar off-center basal textures. To isolate the impact of the minor changes seen in textures, simulations were conducted using the geometry and mesh representing the Mg-1.5Sn alloy and the corresponding material properties. The results indicated that utilizing the only slightly varying texture observed for the Mg-0.2Ca alloy did not result in visible changes to the stress-strain response.

The difference in average grain size between the two alloys may seem small. However, it results in 2.7 times as many grains in the 1 x 1 x 2 mm Mg-0.2Ca model versus the Mg-1.5Sn model. To demonstrate

the impact of this grain size difference, the material properties for Mg-1.5Sn and the same orientation distribution were assigned to both geometries. The orientation input for the Mg-1.5Sn geometry only contains 6,650 orientations. This set of orientations was repeated to reach the necessary 18,085 orientations needed for the Mg-0.2Ca geometry. As Figure C3.8 shows, the smaller grains allow for additional hardening to occur given the same material model properties, clarifying the relatively large difference seen for the two different grain sizes, 48 µm and 67 µm.
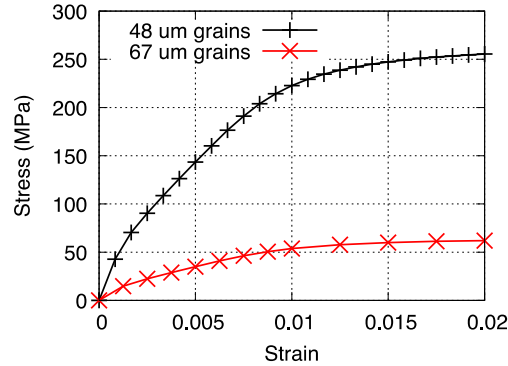

Figure C3.8: Stress-strain response for samples with the same material model properties and grain orientations. The black line corresponds to response from the geometry representing Mg-0.2Ca with smaller grains while the red line is the Mg-1.5Sn geometry. (Source: PNNL)

Given the large impact of average grain size on the bulk response of the models, simulations were conducted to compare the difference in the material model parameters for the Mg-0.2Ca and Mg-1.5Sn using the same geometry and mesh. For this comparison the larger grain size model representing Mg-1.5Sn was selected. The CRSS values for Mg-1.5Sn are higher. This results in the higher hardening seen in Figure C3.9 when the average grain size is controlled for. However, when the higher CRSS values compete with the smaller average grain size, the grain size effect results in the Mg-0.2Ca sample having higher strength as observed in the in-situ tensile tests.
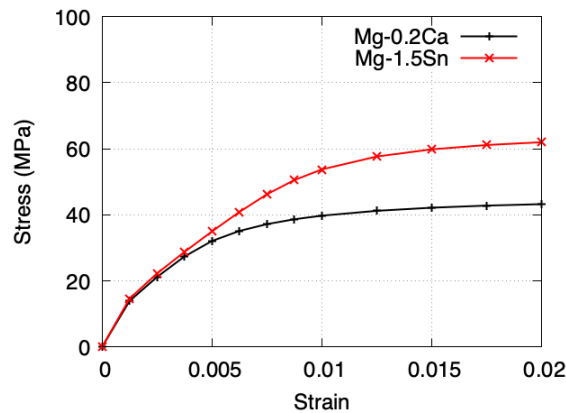
Figure C3.9: Stress-strain comparison of material properties holding geometry, mesh, and orientation constant. (Source: PNNL)

Figure C3.10 shows results for the Mg-1.5Sn sample loaded in uniaxial tension to 2% strain. This simulation is best compared to the in-situ tensile results for the recrystallized Mg-1.5Sn sample. The experimental stress-strain curve shows micro-yielding at approximately 16 MPa compared to 19 MPa for the simulated results, with a yield of 62 MPa compared to 61 MPa observed. The main deviation between the experiments and simulations is the strain levels at which the stress values are reached. The simulation shows the yielding occurring at significantly lower strains. This may be due to the smaller model size

compared to the full gage size of the experimental sample. Additional impacts may also come from crystal plasticity model parameters that were not calibrated to UIUC Density Functional Theory (DFT) results and affect the slope of the stress-strain curve inordinately. However, the current results do indicate that the changes made to the CRSS values calculated by DFT do result in corresponding stress values.
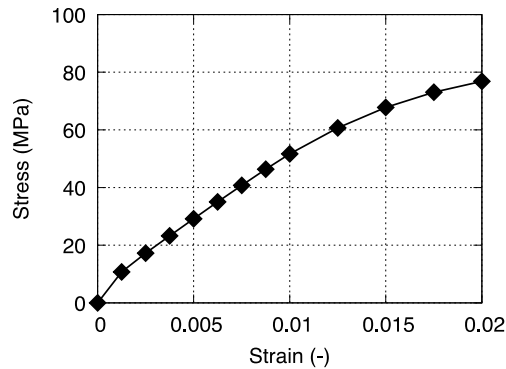

Figure C3.10: Simulated stress-strain response for Mg-1.5Sn loaded in uniaxial tension. (Source: PNNL)

C3.3 CONCLUSIONS AND RECOMMENDATIONS

CPFEM samples representative of the microstructure and texture of two binary Mg alloys, Mg-0.2at.%Ca and Mg-1.5at.%Sn were modeled using crystal plasticity parameters from literature values for pure Mg, Taylor model values for EFP, and modified using the change in CRSS calculated by UIUC using DFT simulations. The first goal of the CPFEM simulations was to understand the impact of individual microstructure features and parameters on the bulk behavior. The study demonstrated the large impact of what might seem to be a small difference in grain size (67 µm to 48 µm between the two binary alloys) on the bulk behavior of the sample. The second goal was to determine if incorporating the changes in CRSS values calculated by DFT resulted in stress-strain response that matched the in-situ measurements. While using the CRSS values from DFT did match the stress levels of micro-yield, yield, and ultimate stress measured, the strain values were lower. The micro-yield stress value was most impacted by the changes in CRSS for the basal slip systems. This is to be expected as deformation is dominated by basal slip. The changes in CRSS values for the prismatic and pyramidal could be seen in changes to the yield and ultimate stress values. Additional investigation needs to be conducted to determine appropriate model parameters to capture the strain levels observed experimentally.

C4. Alloy 3 Parallel Development, Processing, and Recrystallization
(University of Michigan – Principal Investigator: J. Allison)

C4.1 SUMMARY

It has been previously established that the RE-like textures associated with improved formability in Mg alloy sheets can also be produced using Mg-Zn-Ca alloys, but the roles of the Zn and Ca solutes and associated mechanisms responsible are still not fully understood, although they have been shown to drive negative strain rate sensitivity and dynamic strain aging that helps promote recrystallized grains with non-basal texture (see Chapter C2). Producing formable Mg alloy sheets requires having both the correct alloy chemistry and the correct thermomechanical processing (TMP) route for that alloy. Improper processing can result in the strong basal texture known to be detrimental to sheet formability. Of all the alloy and TMP routine combinations used in this work, the Mg-3.2Zn-Ca alloys (in wt.%) exhibited the weakest textures with an annular structure in the basal pole figures. To achieve the desirable texture, the alloy must contain at least 0.1 weight percent Ca. However, Ca content above this level had little effect on the texture in the alloys explored in this study. Processing Mg-2.1Zn-0.1Ca was also optimized to produce the desirable texture, as described below.

For both alloys, the processing schedule that produced the most desirable texture consisted of ten passes with a constant true strain of 0.2 per pass at a strain rate of 0.5/s. Between passes the specimens were held at 350ºC for 10 minutes, a step which is referred to as the "intermediate anneal" throughout this work. A final post-deformation annealing treatment of 30 minutes at 350ºC resulted in complete recrystallization in these alloys. The mechanisms behind each of these processing steps, which play crucial roles in the developed texture, will be discussed.

It should be noted that not all alloys studied demonstrated texture improvement during the final annealing treatment. In the unalloyed Mg, the Mg-Ca binaries, and the Mg-0.5Zn-0.1Ca ternary (the ternary with the lowest Zn content in this study) the strong (> 12 MRD) basal texture in the as-deformed state was unchanged after annealing at 350ºC for 30 minutes. These alloys showed no evidence of discontinuous dynamic recrystallization (DDRX). A population of randomly-oriented RX grains did not exist after ten deformation passes in these alloys, resulting in a strong texture in the as-deformed condition. With no mechanism for introducing randomly oriented grains during the final annealing treatment, the strong basal texture was retained. This lack of texture evolution is consistent with literature on conventional Mg alloys such as AZ31. Detailed discussion of this work may be found in the sub-task report at https://data.lightmat.org/project/.

C4.2 KEY ACCOMPLISHMENTS AND RESULTS

C4.2.1 Materials and Experimental Approach
Cast ingots with dimensions of approximately 80 x 80 x 20 mm were received from the University of Florida. A summary of the compositions studied is shown in Table C4.1. The binary ingots were solution treated for 24 h at 500ºC, while the ternary ingots were solution treated for 24 h at 350ºC. The unalloyed Mg was used in the as-cast condition. Plane strain compression (PSC) samples with dimensions of 20 x 15 x 10 mm were extracted from the center regions of the ingots. The grain size of the initial microstructure in the PSC samples is on the order of mm and some porosity was present. Samples obviously containing porosity were discarded.

Table C4.1: Alloy designation and composition as measured using OES at Ford Motor Co.

Alloy name	Zn content (wt. %)	Ca content (wt. %)
Unalloyed	0	0
X0	0	0.1
X1	0	0.3
ZX0p50	0.5	0.1
ZX10	1	0.1
ZX21	1.9	0.3
ZX30	3.2	0.1
ZX31	3.2	0.3

Testing was conducted using a Gleeble Model 3500 thermomechanical simulator, Table C4.2. For all TMP schedules, the samples were heated up to 350°C at a rate of 5°C/s and then held at 350°C for 10 minutes before the first compressive hit. Optical microscopy and electron backscatter diffraction (EBSD) mapping were used for characterization.

Table C4.2: Summary of Gleeble PSC TMP routines used in this work.

Process Name	# of passes	Temp (ºC)	Strain Rate (/s)	Strain per Pass	Duration of intermediate anneal (s)
10-pass	10	350	0.5	0.2	600
1-pass	1	350	0.5	0.2	600
3-pass	3	350	0.5	0.2	600
5-pass	5	350	0.5	0.2	600
10-pass (15s)	10	350	0.5	0.2	15
10-pass (5min)	10	350	0.5	0.2	300
10-pass (30min)	10	350	0.5	0.3	1800
Ramp	12	350 to 325	0.5	0.5 to 0.25	300
20-pass	20	350	1	0.03 to 0.4	300
20-pass (15s)	20	350	1	0.03 to 0.4	15
10-pass (0.1/s)	10	350	0.1	0.2	600
10-pass (0.25/s)	10	350	0.25	0.2	600
10-pass (1/s)	10	350	1	0.2	600

C4.2.2 Effect of Alloying

The Gleeble true stress-true strain responses for all alloys are presented in Figure C4.1 which shows that the ternary alloys exhibit a higher stress during compression than the dilute alloys. After deformation, the unalloyed Mg, binary alloys, and the low Zn ternary have an inhomogeneous microstructure consisting of bands of finer grains surrounded by larger grains. In contrast, the higher-Zn ternary alloys have a finer and more consistent grain size through the reduced section, with a mean grain diameter of approximately 20 µm. As processing for all alloys was fixed, the grain refinement and more homogenous as-deformed microstructure must be an effect of the addition of 3.2 wt.% Zn to Mg-0.1Ca.

Higher magnification microscopy reveals a second difference in the deformed condition; the three higher-Zn ternary alloys exhibit serrated grain boundaries, evidence of grain boundary bulging, and sub-µm grains decorating the boundaries of some of the larger grains. These features are considered characteristics of DDRX. The grain boundary structures in the other alloys and in unalloyed Mg are fairly straight, even in the finer-grained regions. The EBSD grain orientation spread (GOS) maps illustrate differing amounts of recrystallization in the as-deformed state.

The post-deformation annealing treatment of 30 minutes at 350ºC resulted in the average grain diameter (as measured from the EBSD maps) increased to approximately 60 µm in the dilute alloys.
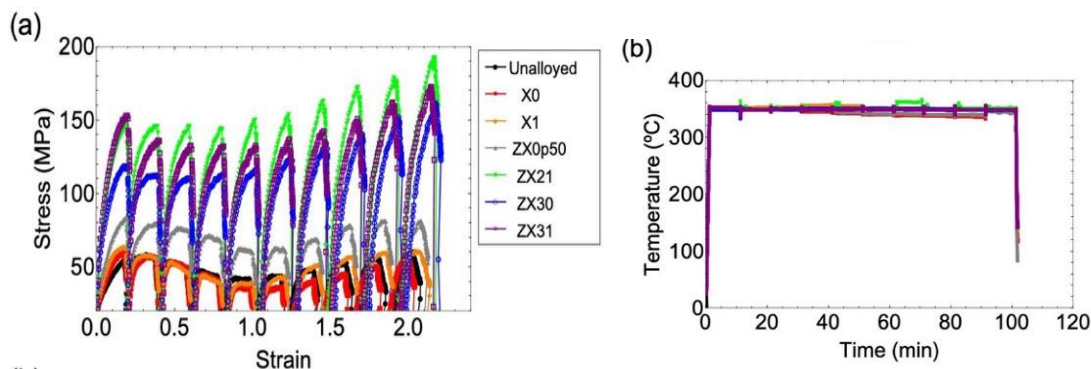

Figure C4.1: Gleeble true stress-true strain plot and (b) temperature profile during testing Gleeble testing for the seven specimens. (Source: UM)

The final annealing treatment resulted in more extensive static recrystallization (SRX) in the three higher Zn ternary alloys as shown in Figure C4.2. The grain size increases slightly in the ZX30 alloy (which contains the lowest wt.% Ca of the ternaries) from 20 µm to just under 30 µm, while the grain diameter in ZX21 appears to decrease from 25 µm in the deformed condition to 12 µm in the annealed condition.

The higher Zn ternary alloys all exhibited comparatively weak textures in the deformed state. The addition of Ca alone did not change the texture evolution from that observed in unalloyed Mg in this study. The Zn content had a much stronger effect on the texture evolution than the Ca content. The behavior of ZX30 and ZX31 are quite similar, despite the higher Ca content in ZX31. In contrast, ZX21 and ZX31, which vary in composition by ~1 wt.% Zn, responded differently to both TMP and the post-deformation annealing treatment. Evidence of DDRX was observed in the microstructures of all three ternary alloys, although this mechanism is not associated in a significant change in texture.

It should be noted that only the alloys with microstructures consisting of a large fraction of highly misoriented grains underwent a change in texture during annealing. Others have tracked the texture evolution during static recrystallization at 400ºC in hot-rolled Mg-0.91 wt.% Zn -0.52 wt.% Ca alloy and also observed texture reduction, which they attributed to more randomly oriented RX grains consuming more strongly textured deformed grains. An increased Zn addition also retarded recrystallization during processing. The deformed ZX21 specimen had a significant fraction of low misorientation grains in the as-deformed state, while the 3.2 wt.% Zn alloys had far fewer recrystallized grains.
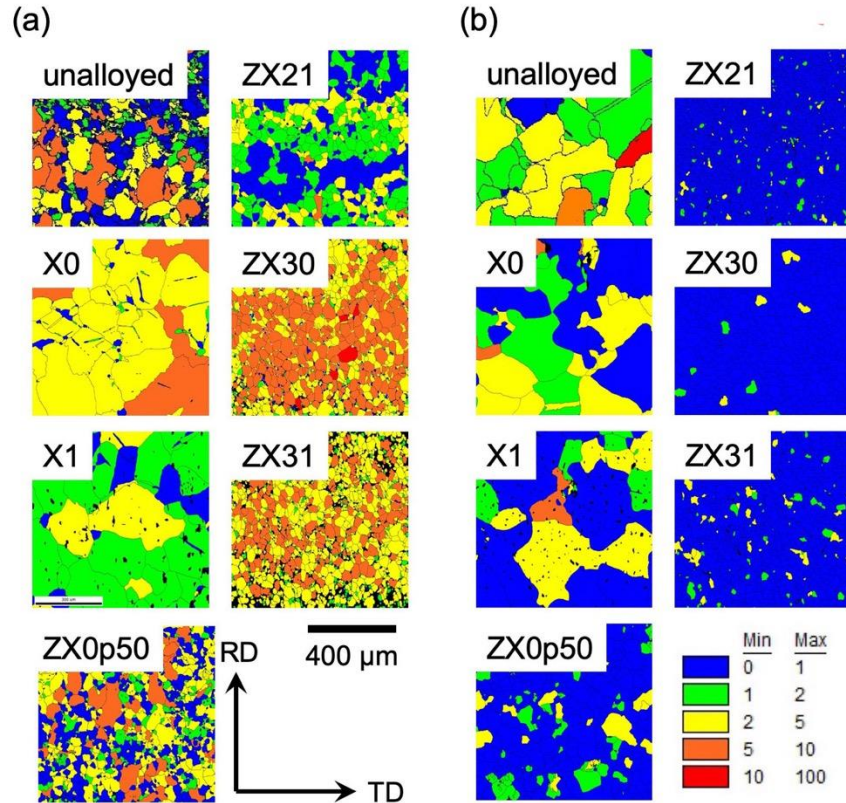
Figure C4.2: EBSD GOS maps of the samples in the (a) as-deformed and (b) annealed conditions. All maps cover an area of 800 µm x 800 µm. (Source: UM)

C4.2.3 Effect of Total Strain (Number of Passes)
Both texture and grain size were reduced with an increasing number of passes at a strain of 0.2/pass. Deformation promotes the nucleation of randomly oriented RX grains, which nucleate preferentially within twins and along grain boundaries. As the grain size is refined, twinning decreases, but RX grains continue to nucleate along the increasing grain boundary area. The randomly oriented RX grains grow slightly during annealing, which leads to a reduction of the basal-deformation texture as they occupy a larger fraction of the microstructure.

C4.2.4 Effect of the Intermediate Annealing Step
In the alloy study, the weakest final textures were achieved in the samples with the lowest fraction recrystallized and the largest spread in grain misorientations. Slower recrystallization kinetics, in that case, achieved through solute drag, promoted weaker recrystallization textures in Mg-Zn-Ca alloys. The longer intermediate annealing treatment did lead to a stronger basal texture than the 10-minute intermediate anneal during processing, but still produced a relatively weak basal deformation texture (<5 MRD). The longer intermediate anneal also permitted some grain growth, and the increased grain size allowed for more twinning activity during deformation.

C4.2.5 Effect of Strain Rate
Strain rate is expected to affect both the dynamic and static recrystallization kinetics and therefore it will influence texture development in the Mg-Zn-Ca alloy system. A strain rate of 1/s produced an undesirably strong basal texture in the ZX30 alloy with the 10-pass schedule. In some additional ZX30 samples, this high strain rate resulted in strain localization and non-uniform deformation. The intermediate strain rates produced the weakest textures after annealing.

C4.2.6 Static Recrystallization in 10-Pass ZX30

A final annealing treatment of 350ºC for 30 minutes was shown to lead to a significant change in texture in the "10-pass" ZX30 (and ZX31) samples. A microstructure consisting of primarily of equiaxed grains is likely fully recrystallized. At 300ºC, with treatments less than 30 minutes, the grain boundaries are serrated and irregular and the microstructure consists of both small, likely RX grains, and larger irregular grains. The structure is more equiaxed for treatments 30 minutes and greater, though some irregular grains still exist at 30 minutes. At 350ºC, that transition to a more equiaxed structure occurs by 10 minutes. Based on optical microscopy alone, it appears that full RX occurs by 60 minutes at 300ºC and 15 minutes at 350ºC. This is used to guide the EBSD metrics for quantifying RX.

A summary of the % RX calculated using GOS during post-deformation annealing in the 10-pass ZX30 samples is shown in Figure C4.3. The solid lines are rough predictions based on a Johnson-Mehl-Avrami-Kolmogorov recrystallization model. The estimated fraction recrystallized at 60 minutes falls below the predictions at both temperatures. This is likely a consequence of grain growth as larger grains tend towards larger GOS values as optical microscopy suggests nearly complete RX after 60 minutes of annealing at both of these temperatures.
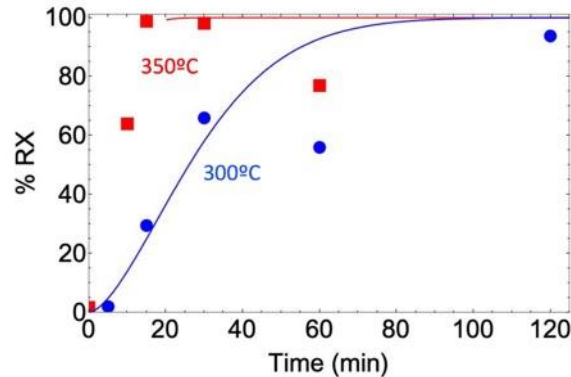

Figure C4.3: Progression of recrystallization (%RX) in annealed 10-pass ZX30 samples calculated using GOS. (Source: UM)

A comparison of the % RX in 10-pass ZX30 samples annealed at 300ºC demonstrated that since grain average misorientation (GAM) is step-size dependent, only EBSD scans collected with a 1.2µm step size were considered. The GAM method of characterization leads to an unreasonably high %RX in the as-deformed condition based on optical microscopy. However, GAM measurement indicates that complete (100%) recrystallization occurs after 60 minutes at 300ºC.

In order to better observe the early stages of recrystallization, higher resolution EBSD scans were collected in the as-deformed condition and after 5, 15 and 30 minutes at 300ºC. Given the smaller area covered, and the inhomogeneity in the microstructure before full recrystallization, these scans should not be considered fully representative of the microstructure. IPF maps of these scans are shown in Figure C4.4. Little evolution is seen after 5 minutes at 300ºC. After 15 minutes the smaller, more randomly oriented grains begin to dominate the microstructure. After 30 minutes, the grain size is more uniform and the lack of color gradients and a decrease in the fraction of un-indexed white pixels demonstrates less misorientation within the grains, one marker of recrystallization.
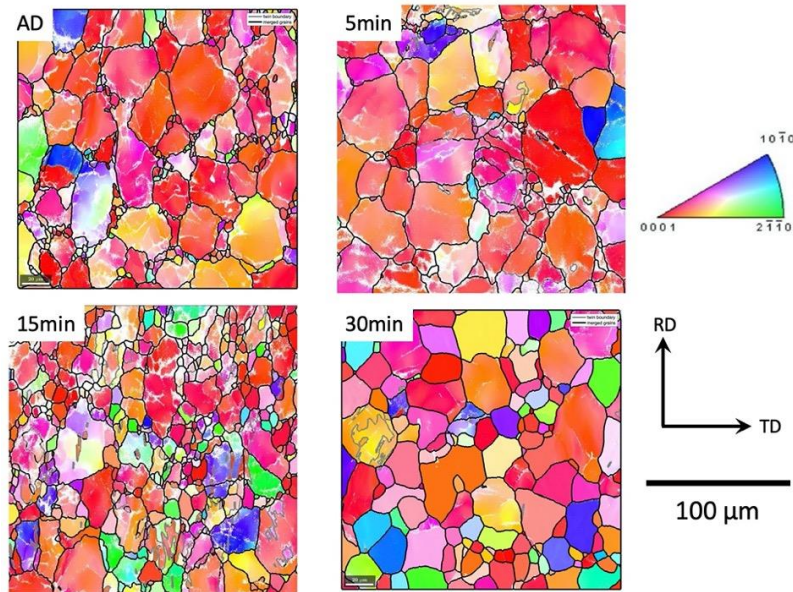
Figure C4.4: IPF maps of the higher resolution EBSD scans showing the evolution of microstructure in 10-pass ZX30 samples during annealing at 300ºC. (Source: UM)

In conventional Mg sheet, texture is often unchanged, or becomes sharper during static annealing. In contrast, the texture has been observed to weaken in Mg-Zn-(Ca, RE) and RE containing alloys. One proposed mechanism for this reduction is that the solutes alter grain boundary energies and mobilities, which may reduce the bias which selects for basal oriented grains during static recrystallization. This study supports findings that the nucleation and growth of randomly oriented RX grains leads to weaker basal textures in Mg-Zn-Ca alloys.

C4.2.7 Process Optimization in ZX21

It was demonstrated earlier that the alloys with 3.2 wt.% Zn (ZX30 and ZX31) had a weaker texture than the ZX21 alloy, however the TMP process used for the alloy comparison had been optimized using the ZX30 alloy. In ZX30 limiting recrystallization and grain growth between passes seems to be essential for producing a weak final texture, and therefore, a reduced deformation temperature and a reduced intermediate anneal were explored for process optimization in ZX21, as shown in Table C4.3. EBSD IPF maps comparing the annealed (350ºC/30 min) microstructures of the 4 TMP schedules used on ZX21 are shown in Figure C4.5.

Curiously, for the 10-pass schedule, the final grain size is larger with a 5 min intermediate anneal than it is when using a 10 min or 15s intermediate anneal. This may be a result of inhomogeneity in the original cast microstructure. The grain size observed using the Ramp schedule is comparable to that observed when using a 5 min intermediate anneal in the 10-pass schedule. The two larger grained ZX21 samples are not fully RX (using GOS) and show bands of higher GOS grains perpendicular to rolling direction.

As intended, shortening the duration of the intermediate annealing step led to a reduction in texture in all of the modified processing schedules. The texture in the annealed state is relatively weak after all four processing schedules. The texture is the strongest in the 10-pass schedule with the 10 min intermediate annealing duration.

Table C4.3: Tests run on the ZX21 alloy.

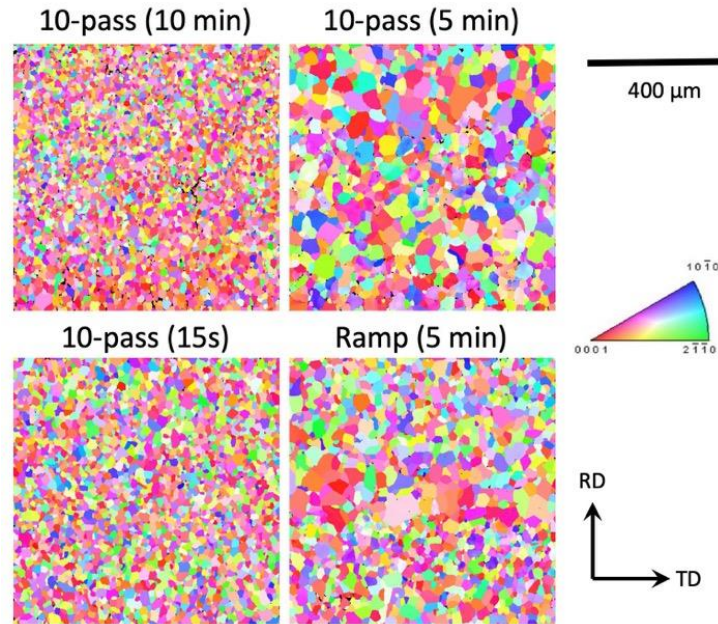| Sample Name	Process Name	# of Passes	Temp (ºC)	Strain per Pass (/s)	Duration of Intermediate Anneal (s)
D30	10-pass	10	350	0.2	600
Q02	10-pass-15s	10	350	0.2	15
300D01	10-pass-300ºC	10	300	0.2	600
5D06	10-pass-5 min	10	350	0.2	300
RampD04	Ramp	12	350 to 325	0.05 to 0.25	300

Figure C4.5: EBSD IPF maps of ZX21 samples comparing different processing routes after the final annealing step. The duration of the intermediate anneal is given in the parentheses. (Source: UM)

C4.2.8 Texture and Formability in Mg Sheet Alloys

The formability and texture of several Mg alloy sheets were characterized in support of other USAMP project Tasks. Basal pole figures for the four different batches of EFP are shown in Figure C4.6. Although the maximum intensity in the basal pole figures were all quite low for Mg alloy sheets (3 or less MRD), there were significant differences in the distribution of the intensity. Based on texture alone, EFP Batch #1 would be expected to be the most formable as it has the lowest texture intensity, and the c-axis of the majority of the grains is tipped down away from the sample normal, allowing for activation of basal slip in through thickness deformation. EFP Batch #2 has only a single peak in the center of the basal pole figure, meaning the majority of grains in the sheet are oriented such that their c-axis is aligned with the sheet normal. This undesirable texture was demonstrated to result in poor formability but does result in decreased planar anisotropy.

The texture in EFP Batch #3 exhibits basal peak splitting in only the TD, a texture that allows for easier activation of basal slip with through-thickness deformation, but results in anisotropy within the plane of the sheet. The EFP Batch #4 material exhibits a texture between that of Batch #1 and Batch #3, but more similar to Batch #3 with respect to the intensity of the TD-split peaks.
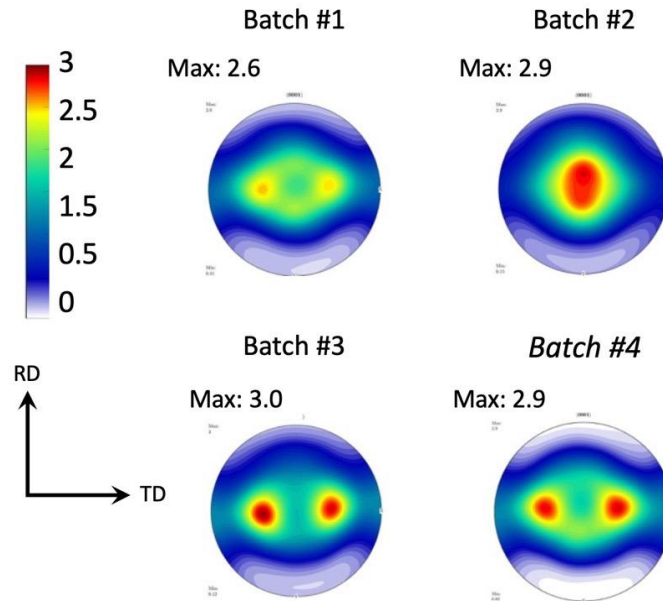
Figure C4.6: Basal pole figures describing the texture in the four batches of EFP used in this project. (Source: UM)

Room Temperature Dome Height (Erichsen cup) Testing
Erichsen cupping tests were conducted on ZEK100 and sheets from three EFP batches at room temperature using a sheet clamping force of 10 kN, a deformation rate of ~5.6mm/min, and using graphite lubrication on the tool. Tests were concluded when cracking was visually observed, which also correlates to a drop in the force-displacement curve. The Erichsen dome height was calculated as the displacement at which the force dropped. Results are summarized in Table C4.4:.

Table C4.4: Summary of Erichsen dome height tests on ZEK100 and EFP.

Alloy	Mean Erichsen Dome Height (mm)	Standard Deviation (mm)	Crack Orientation
ZEK100	6.7	0.1	All parallel to TD
EFP Batch 1	6.2	0.6	No strong preference in orientation
EFP Batch 2	4.6	0.4	All parallel to RD
EFP Batch 3	6.5	0.4	All parallel to RD

Elevated Temperature Deep Draw Testing
Elevated temperature deep draw tests were conducted on the ZEK100 (1.6 mm thick), EFP Batch 1 (1.2 mm thick), and EFP Batch 3 sheets. Due to the low draw heights achieved at 100ºC, room temperature tests were not conducted. Circular blanks 65 mm in diameter were punched from the sheets. Tests were conducted with an Erichsen Universal Sheet Metal Testing Machine Model 142-40 with a 32 mm outer diameter punch. This work used a blank holding force of 10 kN and a punch displacement rate of ~ 6 mm/min (lower than that used for the forming tasks). For the deep draw test, the blank, die, and tooling (aside from the punch) are heated externally to the desired temperature. Once the desired temperature was reached, the assembly was held at that temperature for 10 minutes at which point it was transferred into the sheet formability machine and the test was initiated as quickly as possible. No lubrication was used. Tests were terminated when the load dropped due to the formation of a crack or unusual force/displacement behavior was observed. At least three repeats were done for each condition. The results are summarized in Table C4.5. The average draw refers to the total sheet displacement, not the displacement of the punch.

Table C4.5: Results from deep draw testing in EFP and ZEK100.

Alloy	Temperature (ºC)	Ave. Draw (mm)	Standard Deviation (mm)
EFP-Batch 1	100	8.3	0.5
	200	15.2	1.9
	250	21	7.8
EFP-Batch 3	200	24.6	7.6
ZEK100	100	8.9	1.0
	250	11.0	0.5

The full draw (30 mm) was almost achieved in some of the EFP Batch #3 specimens at 200ºC and in the EFP Batch #1 specimens at 250ºC, but sample-to-sample variation was high in these materials. The maximum draw height before cracking at 100ºC in EFP Batch #1 was significantly less (8.3 mm). At the higher temperature, ZEK100 exhibited lower deep drawability than the EFP Batch 1 (11 mm) but the draw depths at 100ºC were comparable. Representative comparisons of the cups at different temperatures used are shown in Figure C4.7. For the low formability conditions, failure occurred near the location of the maximum bending radius. In several of the high temperature EFP tests, no cracks formed; the tests were terminated when the force-displacement curve showed hardening behavior which suggested the edges of the sheet would eventually fracture. This was done to limit debris in the sheet testing machine.
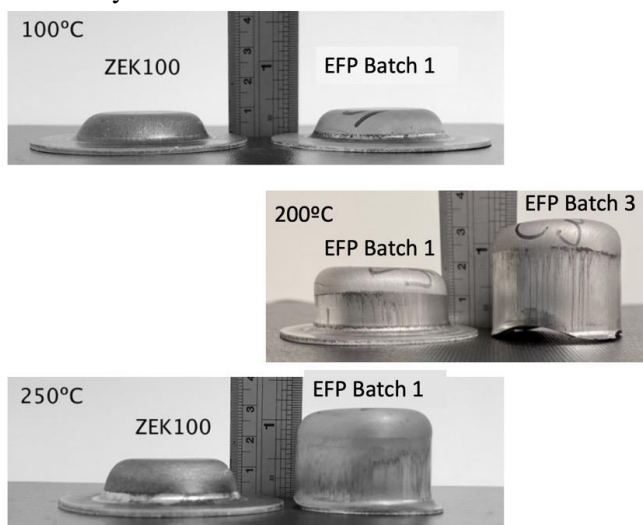

Figure C4.7: Comparison of deep draw cups from ZEK100 and EFP batches at various temperatures. (Source: UM)

The ZEK100 sheet requires more force to deform than the EFP Batch #1 at the same temperature. As expected, both alloys are softer at the higher temperature. The two batches of EFP show similar force-displacement behavior at 200ºC.

Characterization of USAMP Experimental Alloy 2 Sheet Samples Prepared by POSCO
Visual inspection of these sheets revealed some regions with cracking. The surface exhibited multiple features that appeared to be inclusions but are likely marks from the sheet sticking to the rolls (Figure C4.8a). Optical and scanning electron microscopy of the sheets revealed a high density of particles in strings elongated along the rolling direction (Figure C4.8b).
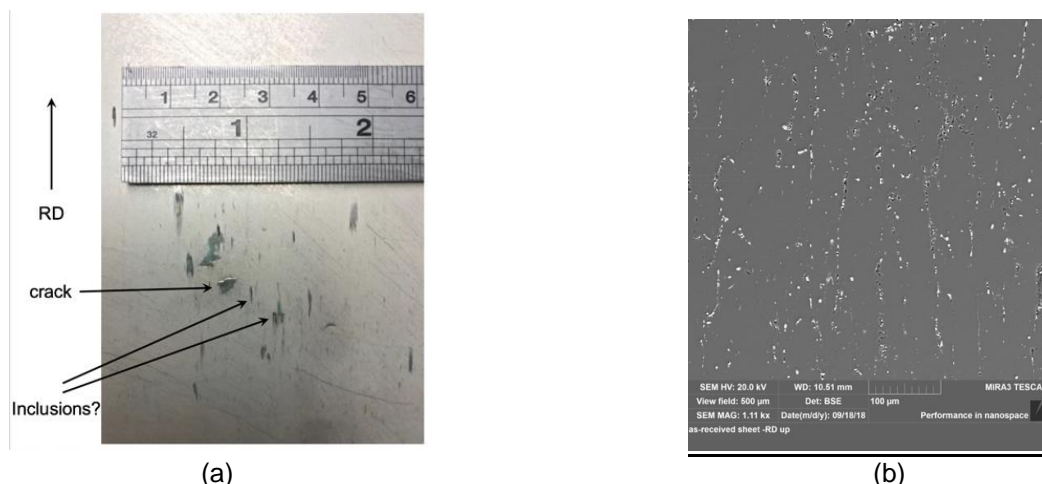
Figure C4.8: (a) Surface defects on as-received Alloy 2 sheet, and (b) SEM image of as-received sheet. RD is vertical (Source: UM)

C4.3 CONCLUSIONS AND RECOMMENDATIONS

Desirable spread basal textures with a low texture intensity were produced in Mg-Zn-Ca sheet alloys through a combination of a 10-pass deformation schedule and a final recrystallization annealing treatment. Calcium contents of at least 0.1wt.% are required to produce the desired textures and Zn content strongly affected the texture in the as-deformed and annealed conditions. The three higher Zn ternary Mg-Zn-Ca alloys (ZX21, ZX30, and ZX31) showed a significantly reduced basal texture intensity in the as-deformed condition (max ~ 4 MRD) compared to the unalloyed and Mg-Ca binaries and the low Zn ternary (ZX0p50) (max intensities > 12 MRD). Annealing for 30 minutes at 350ºC did not alter the strong texture in the dilute alloys nor did static recrystallization appreciably change the as-deformed texture in the ZX21 alloy. Significant basal texture evolution was observed during static recrystallization in the ZX30 and ZX31 alloys. The final weak texture of these two alloys exhibited a desirable annular structure, with the c-axis tipped from the normal direction which is a desirable texture for improved formability. Increasing the Ca content from 0.1 to 0.3wt.% did not lead to any appreciable differences in texture but did lead to an increase in secondary phase particles.

While the high Zn ternary alloys show promisingly weak textures, it is important to note that improper processing can lead to strong basal textures in these "good" alloys as well. Increasing the strain rate from 0.5/s to 1/s lead to a much stronger basal texture in the 10-pass ZX30. A longer intermediate annealing step led to increased basal texture intensities as well.

Limiting static RX and grain growth until the final annealing treatment is essential to producing a weak texture. A high strain rate increases SRX kinetics allowing for increased recrystallization during the intermediate annealing passes. A longer intermediate annealing treatment allows for recrystallization and potentially grain growth to occur. While limiting SRX during processing lead to improved textures, processing needs to promote DRX. This work demonstrates that the small, likely DRX grain have random orientations and that they exist through processing from the original deformation pass to the last. To optimize texture, it is important to control their nucleation and growth. In contrast to the RX grains, the deformed grains tend to have a more basal orientation. During annealing, the volume fraction of the deformed grains decreases, leading to the decrease in basal texture intensity observed in the Mg-3.2Zn-Ca alloys. In the Mg-Zn-Ca system annealing leads to texture reduction rather than proliferation of the basal texture due to modified recrystallization kinetics.

C5. Alloy 2 and Alloy 2 Plus Design and Development
(Ohio State University – Principal Investigator: A. Luo)

C5.1 SUMMARY

The formability of magnesium can be improved via fine grain structure and random texture to enable some room-temperature (RT) forming operations. A new sheet alloy, Alloy 2 Plus, has been developed based on thermodynamic calculations and experiments to optimize composition and homogenization, and rolling schedules to maximize formability-enhancing solutes in solution with minimum intermetallics beyond that needed for grain size control. The alloy developed demonstrated excellent ductility (31% tensile elongation) and RT formability (7.8 mm Erichsen Index) and a strength of 159 MPa in solution-treated condition (T4). The alloy also demonstrates a high yield strength (270 MPa) upon post-forming aging treatment (T6). Key to the development was the multi-stage homogenization process of the designed chemistry to sequentially dissolve intermetallics for maximum supersaturation. The homogenized alloy showed no edge-cracking during rolling. The excellent combination of strength and formability of the Alloy 2 Plus is comparable to 6000 sheet aluminum alloys and shows potential for room temperature forming for automotive applications. Detailed discussion of this work may be found at https://data.lightmat.org/project/.

C5.2 KEY ACCOMPLISHMENTS AND RESULTS

C5.2.1 Alloy 2 Development
Based on CALculation of Phase Diagram (CALPHAD) modeling approach, Mg-2Zn-0.3Ca-0.2Ce-0.1Mn ("Alloy 2"), was designed to offer more balanced strength and ductility. Conventional homogenization processes (at temperatures below the alloy's solidus to avoid incipient melting) are inefficient in maximizing solute concentrations in the Mg matrix since the low diffusivities of the alloying elements cannot completely dissolve secondary phases from the as-cast microstructure at these low temperatures. CALPHAD simulation was used to design a new homogenization process (multiple isothermal stages with final stages at temperatures higher than the alloy's solidus) for the new alloy, to achieve complete dissolution of the alloying elements without incipient melting. The combination of the new alloy design and thermomechanical process (TMP) provided an excellent combination of strength and ductility at room temperature for Alloy 2.

Figure C5.1a shows the calculated solidification path of USAMP Experimental Alloy 2, based on the classical Scheil model. It shows that primary Mg phase will form at 642°C, followed by various intermetallics. Based on this and diffusion simulation results, a new homogenization schedule, designated as H510 and shown in Figure C5.1b, was designed with four isothermal stages (275°C for 4h, 375°C for 12h, 420°C for 2h, and 510°C for 1h) to sequentially dissolve each intermetallic phase without incipient melting. A conventional homogenization profile (H390) was designed with one isothermal stage at 390°C for 48 hours, for comparison with the new homogenization profile. Figures C5.2a-c show that H510 is more effective than H390 in dissolving the second phase particles in as-cast Alloy 2.

Figure C5.3 shows the tensile properties of Alloy 2 sheet with the two homogenization profiles followed by the same rolling and annealing process, and the results are also summarized in Table C5.1. The results show that the new homogenization profile produces excellent strength and ductility for Alloy 2. The Alloy 2 sheet samples in the as-rolled condition exhibit high yield strength (~269 MPa) and good elongation (~9.4%). Additionally, Alloy 2 sheet is heat-treatable, providing excellent elongation (~29%) and reasonable strength (157 MPa) after only 10 min of annealing from the as-rolled condition.
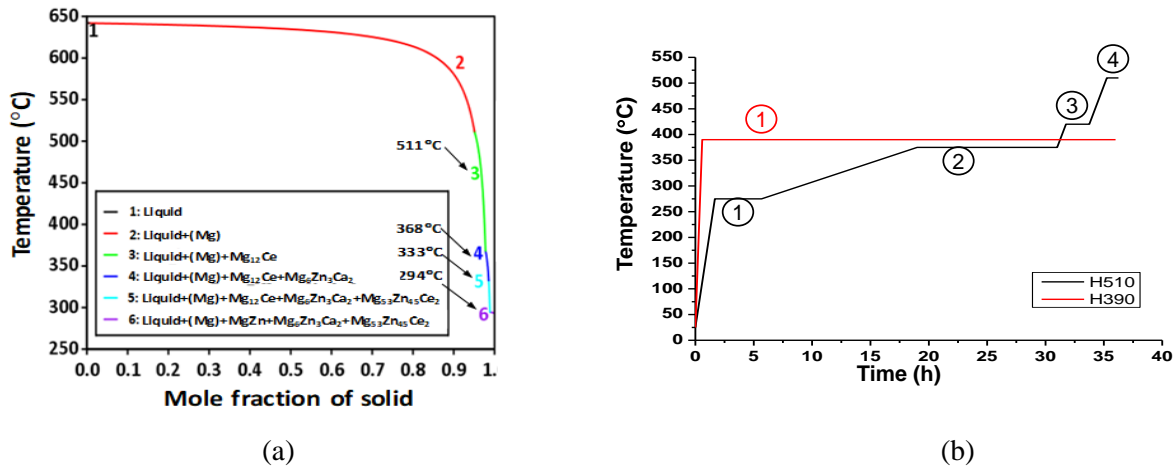
(a)

(b)

Figure C5.1: (a) Calculated solidification path; and (b) Multi-stage homogenization profile (H510) and conventional homogenization profile (H390) designed for Alloy 2. (Source: OSU)

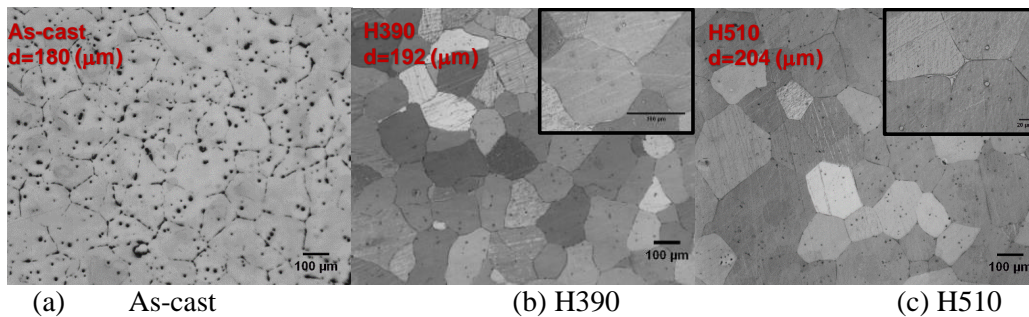(a)   As-cast

(b) H390

(c) H510

Figure C5.2: Optical micrographs of Alloy 2: (a) as-cast condition; (b) after H390; and (c) after H510 homogenization treatments. (Source: OSU)

Table C5.1: Room-temperature tensile properties of Alloy 2 processed under different conditions. Note that R400 denotes 400°C pre-heat prior to each rolling pass; A350 denotes annealing at 350°C; and AR denotes as-rolled condition.

Condition	Yield strength (MPa)	Ultimate tensile strength (MPa)	Elongation to failure (%)
H510-R400-AR	269±1	290±4	10±2.4
H510-R400-A350-10min	157±5	236±3	29±2.0
H390-R400-AR	223±4	253±6	8±3.0
H390-R400-A350-10min	148±3	228±3	22±3.3

The electron backscatter diffraction (EBSD) inverse pole figure (IPF) map in Figure C5.4a shows the microstructure of Alloy 2 after rolling followed by annealing at 350°C for 10 minutes. Figure C5.4b shows a corresponding image quality map overlapped with large angle grain boundaries. The average grain size of Alloy 2 before rolling is about 126 μm as measured from EBSD. The combination of rolling and annealing yields significant grain refinement to about 5.4 μm, which contributes to both high strength and high ductility. The texture intensity (Figure C5.4c) is reduced indicating a weak basal texture (MRD=2.71) in the alloy. A high density of evenly distributed Mn and $Mg_6Zn_3Ca_2$ precipitates (Figure C5.4d) also contributed to strengthening.
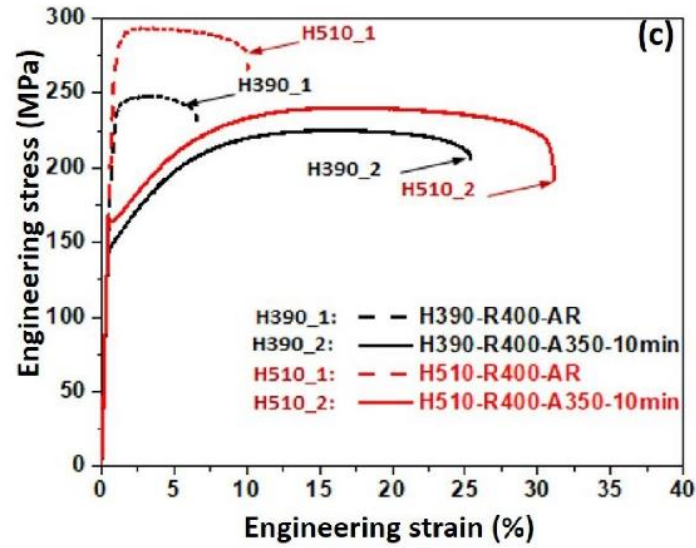
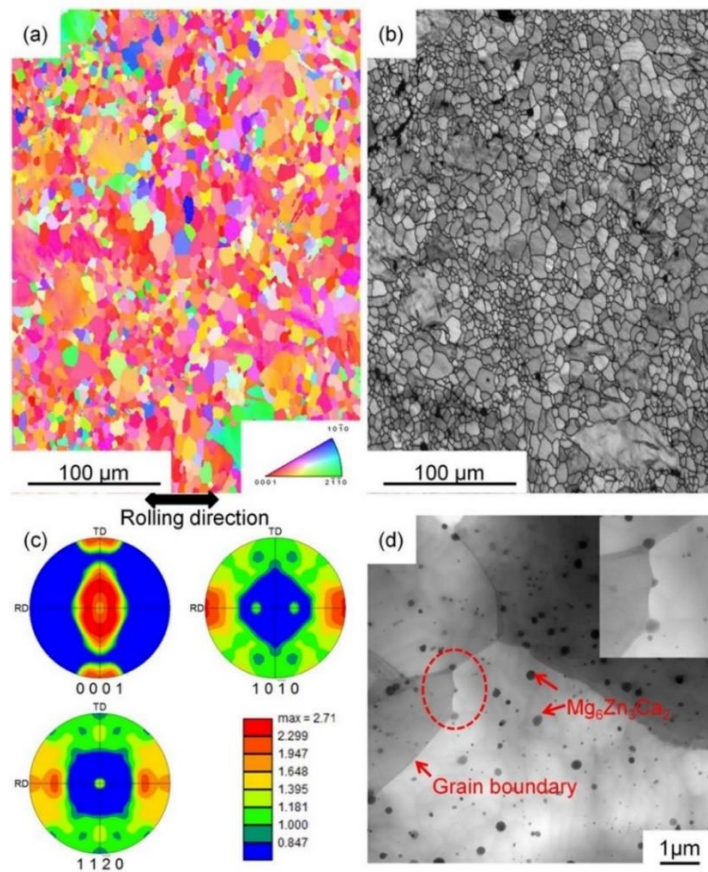Figure C5.3: Tensile curves of Alloy 2 at room temperature. (Source: OSU)

Figure C5.4: Microstructure characterization of Alloy 2 after annealing at 350°C: (a) EBSD IPF map; (b) image quality map overlapped with grain boundaries with misorientation angles larger than 15° (black lines represent large angle grain boundaries); (c) texture pole figures; and (d) BF-STEM. (Source: OSU)

C5.2.2 Alloy 2 Plus Development

Although Alloy 2 shows greater ductility than AZ31B alloy, it has similar room-temperature (RT) formability, Index Erichsen (IE) value of 6.5 mm (using a 20 mm diameter hemispherical punch on 1 mm sheet samples), as ZEK100 (6.7 mm) and EFP (6.2 mm) alloys. Alloy 2 Plus, Mg-1.0Zn-1.0Al-0.5Ca-0.4Mn-0.2Ce, was designed to further improve its RT formability and age-hardening response. In changing from Alloy 2 to Alloy 2 Plus, 2% Zn was replaced by 1% Zn and 1%Al, and Mn content was increased from 0.1% to 0.4%. The reason for introducing Al and increasing Mn content is highlighted in Figure C5.5, which shows that the Al-Mn atomic pair has the strongest affinity and could form crystalline Al_8Mn_5 phase. Other atomic pairs with negative mixing enthalpies may form some clusters without forming crystalline precipitates during aging treatment.

Solidification analysis of Alloy 2 Plus showed that the primary Mg phase will form at 638°C, followed by various intermetallics. See Figures C5.6a and C5.6b. Figure C5.6c is the equilibrium phase fraction vs. temperature plot for Alloy 2 Plus, and shows a solidus temperature of 450°C. This is much lower than the 638°C calculated for non-equilibrium solidification.

Similar to H510 for Alloy 2, a new homogenization profile (designated as H480) was designed with four isothermal stages (320°C for 4 h, 360°C for 4 h, 440°C for 52 h and 480°C for 1 h) to sequentially dissolve the intermetallic phases without incipient melting. See Figure C5.6d.
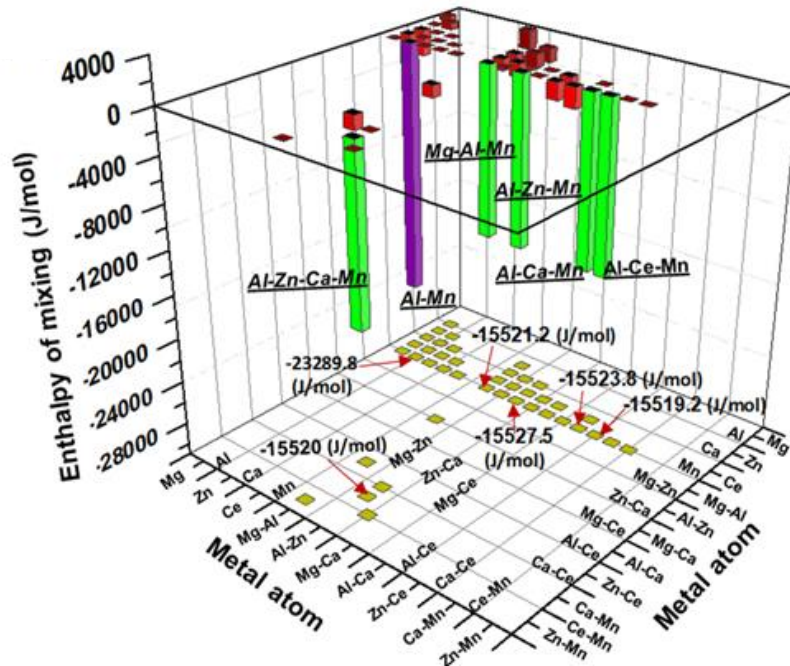

Figure C5.5: Projection of mixing enthalpy of various equiatomic pairs in Mg (HCP) matrix. (Source: OSU)
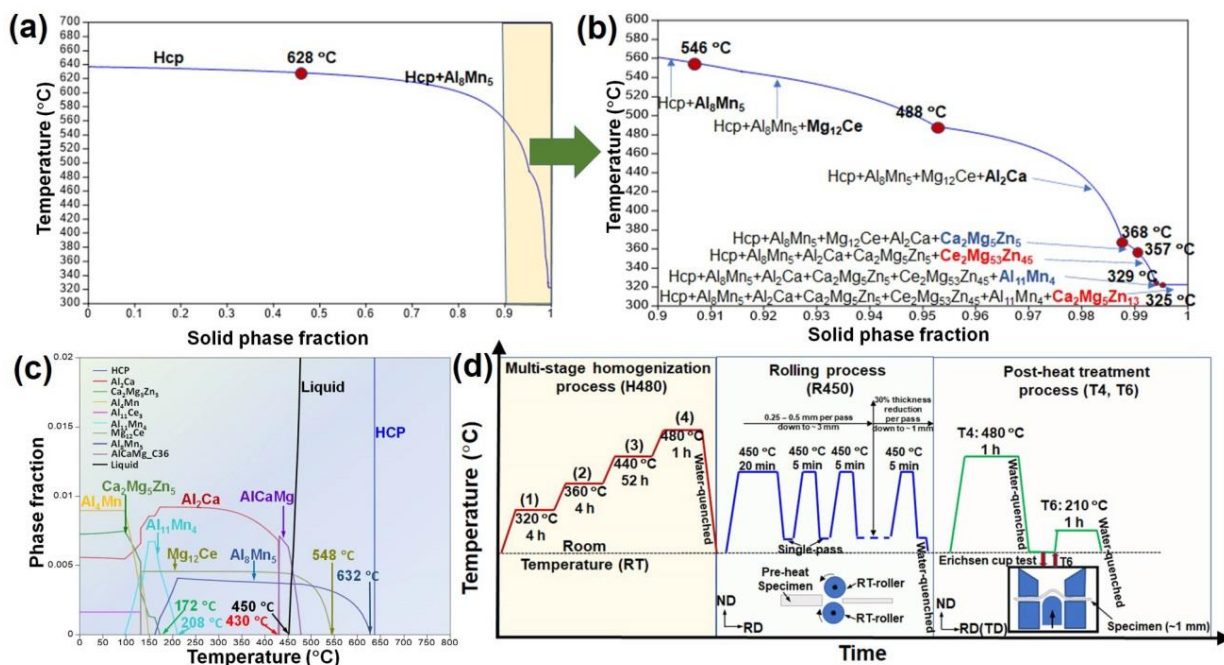
Figure C5.6: (a) Calculated solidification path for Alloy 2 Plus using the Scheil model, and an enlarged region near the end of solidification is shown in (b); (c) equilibrium phase fraction vs. temperature calculations; and (d) thermomechanical processes for producing Alloy 2 Plus sheet alloy. (Source: OSU)

Figure C5.7a shows the calculated solute distributions of solutes Al, Zn, Ca, Ce and Mn in Mg matrix in both the as-cast (AC) condition and the H480-homogenized condition, based on diffusion simulation using DICTRA. The results suggest that the new multi-stage treatment is very effective in dissolving solute elements. The diffusion coefficients (of Al, Zn, Ca, Mn and Ce solutes in Alloy 2 Plus) vs. temperature in Figure C5.7b show an exponential relationship. For example, the diffusion coefficients of the solutes at 480°C are about 10 times higher than those at 400°C, indicating significantly faster homogenization potential. Specifically, Al and Mn have the lowest diffusion coefficients among all alloying elements in Mg, which explains why Al_8Mn_5 is the most difficult phase to be dissolved during solution treatment. Figures C5.7c and C5.7d and show optical micrographs of Alloy 2 Plus in the as-cast condition and after H480 homogenization treatment, respectively. The second phase particles near and along the grain boundaries are essentially dissolved after homogenization. However, a small number of residual particles, mostly Al_8Mn_5 and few Al_2Ca as identified by TEM, are still visible in Figure C5.7d.

Microstructure of Solution-Treated Alloy 2 Plus
Figure C5.8a shows the microstructure of Alloy 2 Plus after rolling process R450 followed by a post-forming solution treatment and water quenching (Figure C5.6d). The average grain size is significantly refined to about 9.6 μm. The pole figure results in Figure C5.8b show a weak split basal texture with a maximum intensity of 3.3 MRD. The maximum intensity of basal poles is tilted by about ±40 degrees away from the normal direction (ND) and towards the transverse direction (TD). Such fine grain size and weak texture of the solution-treated Alloy 2 Plus sheet should contribute to high ductility and formability.

Formability and Mechanical Properties of Alloy 2 Plus
Figure C5.9 compares Erichsen cup test results of the most formable magnesium sheet alloys at room temperature, with solution-treated Alloy 2 Plus showing the highest formability, i.e., IE value of 7.8 mm compared to 6.5 mm for Alloy 2. Figure C5.10a shows the age hardening curve of Alloy 2 Plus sheet alloy at 210°C. Hardness increases from 56 HV as solution treated to 78 HV as peak aged in only 1 hour.

Figure C5.10b displays the tensile stress vs. strain results tested from the solution-treated and peak-aged samples. The solution-treated Alloy 2 Plus sheet offers a decent yield strength (YS) of 159 MPa and an ultimate tensile strength (UTS) of 253 MPa, with an exceptionally high elongation of 31%.
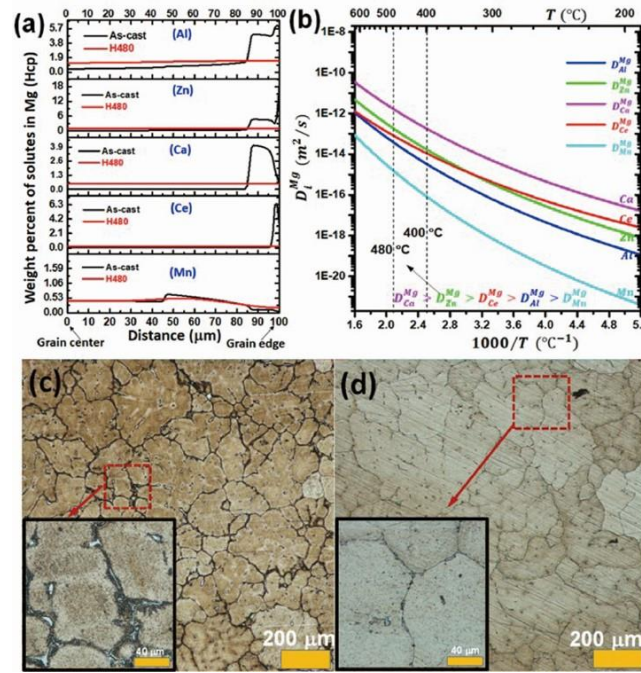
Figure C5.7: (a) Diffusion modeling results of Al, Zn, Ca, Ce and Mn solutes in Mg; (b) solute diffusion coefficients in Mg; optical micrographs of Alloy 2 Plus (c) as-cast; and (d) after H480 homogenization. (Source: OSU)
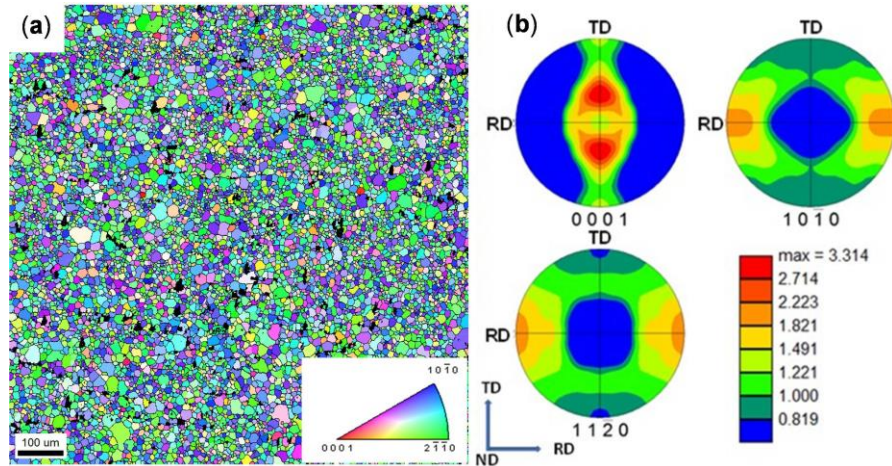

Figure C5.8: EBSD microstructure of Alloy 2 Plus after solution-treatment at 480°C for 1 hour: (a) EBSD IPF map; (b) texture pole figures showing basal pole splitting along TD, and maximum MRD of 3.31. (Source: OSU)

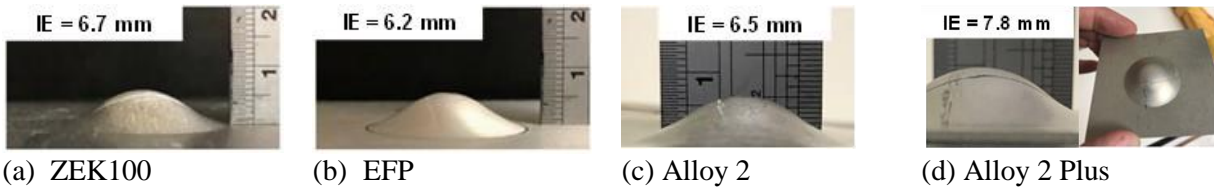(a) ZEK100   (b) EFP   (c) Alloy 2   (d) Alloy 2 Plus

Figure C5.9. Formability (Erichsen test results) at room temperature. (Source: OSU)
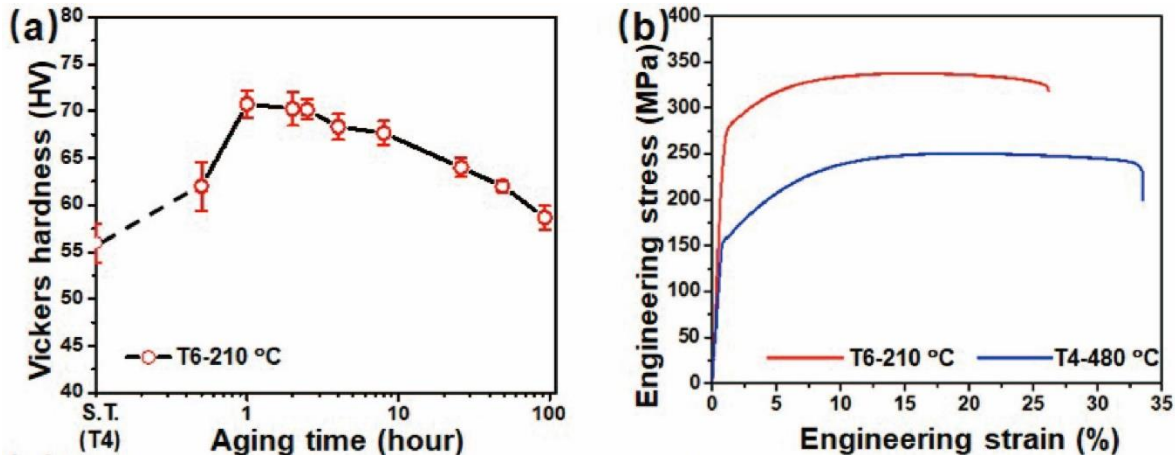

Figure C5.10: (a) Age hardening response at 210°C; and (b) tensile curves from the solution-treated and peak-aged Alloy 2 Plus samples. (Source: OSU)

After a short aging treatment, the YS and UTS of Alloy 2 Plus are greatly increased to 270 MPa and 332 MPa, respectively, and the elongation drops only slightly, to 26%. The Alloy 2 Plus sheet provides excellent formability in solution-treated condition, similar to that of 6000 series Al alloys (7.6 mm for 6061-O and ~10 mm for 6016-T4). Post-forming, an artificial aging (T6) can significantly increase the yield strength with only a slight reduction in ductility. The aging process utilized herein (~1 h at 210°C) can be achieved or adjusted to the automotive body paint bake process.

Figure C5.11 plots Index Erichsen value vs. yield strength at RT for various alloys. Compared to commercial AZ31B alloy, ZEK100, EFP, and Alloy 2 all show improved room-temperature formability, but with slightly reduced yield strength. However, the new sheet alloy, Alloy 2 Plus, offers both excellent ductility (31% tensile elongation) and RT formability (7.8 mm Erichsen Index) in the solution-treated condition, and an extraordinary high yield strength (270 MPa) in the peak-aged condition. That is comparable to 6000 series sheet aluminum alloys, and clearly shows potential for room temperature forming of automotive applications.

Microstructure of Age-Hardened Alloy 2 Plus
Figures C5.12a and C5.12b show scanning tunneling electron microscope (STEM) imaging for the T6 microstructure of Alloy 2 Plus, where no visible crystalline precipitate phases were found, except for the nano-size Al_8Mn_5 rods which already existed in the solution-treated samples. This again indicates that Al and Mn solutes have the strongest affinity in Alloy 2 Plus to potentially form crystalline phases during aging. Although the Al-Mn pair is thermodynamically favored to form crystalline phases during aging, no visible precipitates were observed in the microstructure, Figure C5.12b. Therefore, it is speculated that the significant enhancement of YS and UTS after T6 treatment is due to the formation of solute clusters as shown in Figure C5.12c, with a pinning effect on the basal <a> dislocations.
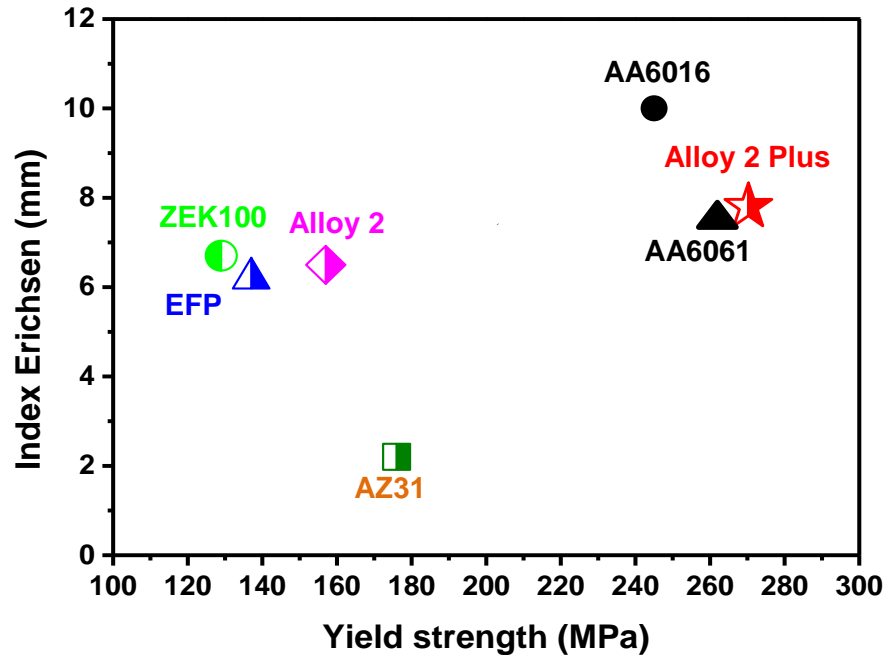
Figure C5.11: RT formability (Index Erichsen values) vs. YS of various alloys. For the age-hardening Alloy 2 Plus, AA6061, and AA6016 alloys, the IE was measured in the solution-treated condition, but YS was measured in peak-aged condition. (Source: OSU)

| (a) | (b) | (c) |
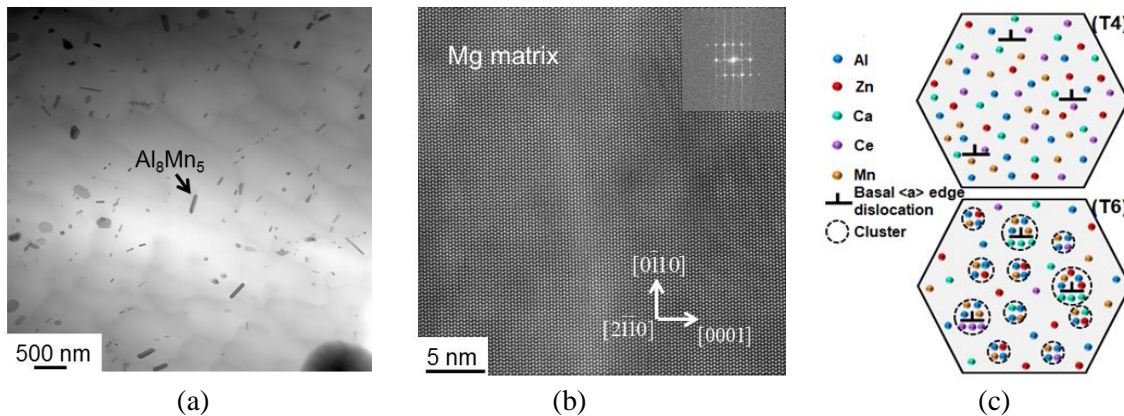
Figure C5.12: (a) and (b) Microstructure of Alloy 2 Plus after aging at 210°C for 1 hour: (a) bright field STEM image; (b) atomic resolution HAADF-STEM image; (c, top) Schematic showing dissolved solute atoms and basal dislocations in solution-treated material; (c, bottom) Schematic showing solute atoms segregated to basal dislocations and also in small clusters in peak-aged material. (Source: OSU)

C5.3 CONCLUSIONS AND RECOMMENDATIONS

1. ICME tools were used to successfully design a new magnesium alloy composition and thermomechanical processing parameters for homogenization, rolling, solution treatment, and artificial aging.

2. The resulting Alloy 2 Plus sheet (Mg-1.0Zn-1.0Al-0.5Ca-0.4Mn-0.2Ce) exhibits high RT formability in the solution-treated condition, and high strength in the peak-aged condition. The performance is similar to 6000-series aluminum sheet alloys, and therefore suggests opportunity for use of Alloy 2 Plus in lightweight panels.

C6. Alternate Rolling Schedules to Enhance Formability
(Oak Ridge National Laboratory – Principal Investigator: M. Govindarajan)

C6.1 SUMMARY

The key to achieving near-room temperature formability in magnesium alloy sheets will depend on the ability to decrease the intensity of the basal crystallographic texture, which is typically found in such rolled sheet, and promote a more random texture. Oak Ridge National Laboratory has developed a rolling process with the capability to control temperatures and rolling velocities, which has previously been used to tilt the basal texture along the rolling direction in Mg alloy AZ31B. The goal of this task was to develop the best process for warm rolling the new Mg alloy compositions developed in this project. Rolling trials were conducted on USAMP Alloy 2 and Alloy 2 Plus ingots using the shear (i.e., asymmetric) rolling mill at ORNL. Results show that Alloy 2 and Alloy 2 Plus could be rolled to large thickness reductions at 275°C while the edge quality of rolled Alloy 2 Plus was better than that of Alloy 2. In contrast to using ingot preheat alone, where rolling had to be conducted at 360°C, rolling could be accomplished at much lower temperatures when both the ingots and the rolls were heated. Within the limited processing paths evaluated, spreading of basal poles was observed in the presence of asymmetric rolling with reductions in texture intensities observed along certain processing paths. Further comprehensive mapping of the effect of processing paths on texture evolution during rolling is required to identify the most promising processing window. Detailed discussion of this work may be found at https://data.lightmat.org/project/.

C6.2 KEY ACCOMPLISHMENTS AND RESULTS

A major limiting factor in achieving low-temperature formability in Mg alloys is the development of basal texture during traditional symmetric rolling and recrystallization processes used in the fabrication of Mg-alloy sheet. Prior work has also shown that static recrystallization and grain growth in alloys such as AZ31B result in an increase in the intensity of the basal texture, thus reversing any texture modification achieved through processes such as asymmetric rolling. Although limited work on AZ31B has shown only modest tilting of the basal texture, the synergistic effects of composition modifications (rare earth additions for example) and rolling process (symmetric/asymmetric) is promising.

C6.2.1 Homogenization
Several ingots of USAMP Alloy 2 and Alloy 2 Plus were received from The Ohio State University in the as-cast condition. Initial ingot dimensions were 110 x 110 x 18 mm. Two ingots of Alloy 2 and one of Alloy 2 Plus were multi-step homogenized in a flat-bed infrared furnace (Table C6.1).

Table C6.1: Summary of processing parameters of Alloy 2 and Alloy 2 Plus.

Processing\Alloy		Alloy 2		Alloy 2 Plus
Homogenization	(1)	275°C, 4h	(1)	320°C, 12h
	(2)	375°C, 12h	(2)	440°C, 32h
	(3)	420°C, 2h		
	(4)	510°C, 1h		

C6.2.2 Rolling Trial #1
The ingot that was about 18 mm thick was cut into three 5 mm thick slices. This slice that was about 110 mm wide was then cut into three strips of 35 mm wide. Reductions per pass from 5% to 15% were attempted to ensure that large overall reductions could be achieved with a minimum number of passes. Preheat times of 15 min to 30 min were experimented with, resulting in relatively long times to perform multiple experimental trials, thereby limiting the process window that could be sampled. Results from this

experimental matrix showed reductions of ~12% at a preheat temperature of 360°C resulted in acceptable rolling behavior with limited edge cracking and no surface cracking. Rolling experiments with Alloy 2 Plus resulted in much better quality rolled sheets with minimum edge cracking. Final experiments were performed with only Alloy 2 Plus.

C6.2.3 Rolling Trial #2

The aim of these experiments was to use either symmetric only or a combination of symmetric and asymmetric rolling to achieve ~1 mm final thickness while starting with a thickness of ~ 5 mm. A slice of ~110 x 110 x 5 mm was rolled using passes of ~12% reduction to achieve a thickness of ~ 1.65 mm. Figure C6.1 shows the rolled sheet at this stage. This sheet was then cut into two pieces ~ 53 mm wide (half width). One of these two pieces was then selected and cut into two pieces normal to its longest direction. One of the two pieces was subsequently used for symmetric rolling to ~1.25 mm thick while the other piece was used for asymmetric rolling using dissimilar sized rolls (Figure C6.2), but the same preheat temperature and reductions/pass. The final thickness of the symmetric rolled sheet was 1.27 mm, and that of the asymmetric rolled sheet was 1.16 mm. See Figure C6.3. Note that the asymmetrically rolled sheet shows some bending due to the two surfaces being rolled at different linear velocities. This bending can be reversed during shear rolling, but was not attempted in this work, so that the effect of shear rolling only on the properties and texture could be evaluated.

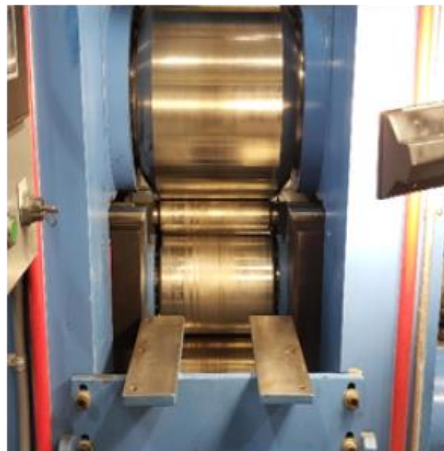Figure C6.1: Rolled Alloy 2 Plus sheet, 1.65 mm thick, 110 mm wide. (Source: ORNL)

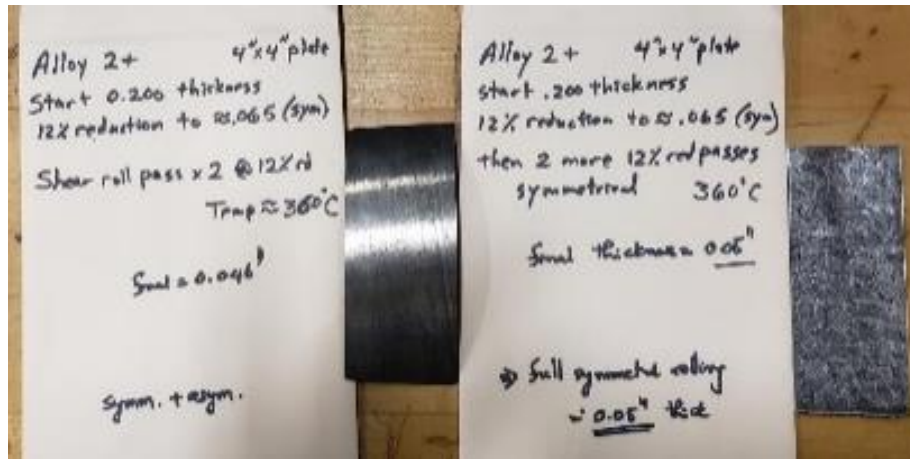Figure C6.2: Shear rolls. (Source: ORNL)

Figure C6.3: Image of sections of symmetric plus asymmetric rolled sheet (left) and symmetric rolled sheet (right) sent to OSU for analyses. (Source: ORNL)

C6.2.4 Rolling Trial #3: Symmetric and Asymmetric Rolling with Shear Rolling Mill

Rolling trials were conducted on Alloy 2 and Alloy 2 Plus ingots using the shear rolling mill available at ORNL after appropriate homogenization treatments. Table C6.2 shows a summary of selected rolling parameters used for rolling trials.

Table C6.2: Summary of various process conditions used for rolling trials

Temperatures	Velocity ratios	Reduction	Passes
135°C 275°C	1:1 (symmetric) 1:2 1:4	10%-73% (Total reduction)	Single pass Multi-pass

Figure C6.4 shows that both Alloy 2 and Alloy 2 Plus could be rolled to large reductions at 275°C. Edge quality of Alloy 2 Plus was better than that of Alloy 2. It was observed that symmetric rolling at 275°C with a targeted ~35% reduction in thickness resulted in cracking along the center of the rolled piece in Alloy 2 but the piece could be successfully rolled using asymmetric rolling. Thus, asymmetric rolling was beneficial in targeting larger reductions, especially in Alloy 2 Plus, and provided the desired weak basal texture (MRD = 5.9) with a tendency towards a random texture (Figure C6.5).

Figure C6.4: Alloy 2 and Alloy 2 Plus sheets rolled to large reductions at 275°C. (Source: ORNL)
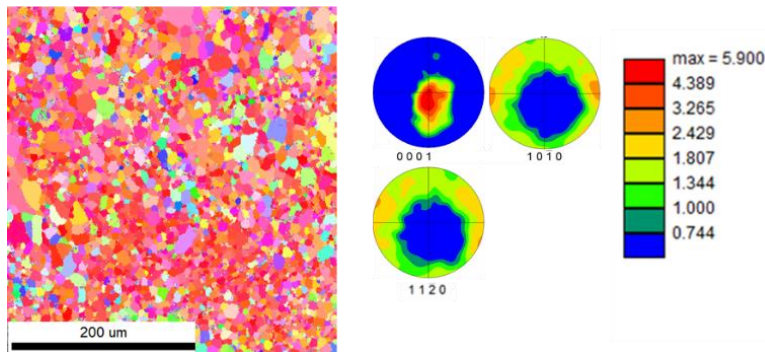
Figure C6.5: EBSD image and (0001), (1010) and (1120) pole figures from Alloy 2 Plus asymmetric rolled at 275°C (1:1.2, 56%) showing almost complete recrystallization. (Source: ORNL)

C6.3 CONCLUSIONS AND RECOMMENDATIONS

1. Developmental alloys (Alloy 2 and Alloy 2 Plus) were successfully rolled using warm rolls and using different velocity ratios. Rolling could be accomplished at much lower temperatures (275°C vs. 360°C) with heated rolls than with alloy preheating only.

2. Asymmetric rolling was critical in achieving larger reductions in Alloy 2.

3. Basal pole distributions were broader and a decrease in texture intensity (to MRD = 5.9) was observed in the asymmetrically rolled samples.

4. Observation of dynamic recrystallization after asymmetric rolling was correlated with a decrease in texture intensity, but further work is required to separate contributions from asymmetric rolling.

C7. Mechanical Testing, Material Properties, and FLDs
(PNNL – Principal Investigator: A. Rohatgi)

C7.1 SUMMARY

This work was performed at Pacific Northwest National Laboratory (PNNL) and funded through the DOE-VTO LightMAT program in support of the USAMP project. The goal of the research was to perform mechanical characterization of Mg sheet alloys that were identified by USAMP as candidates for stamping the demonstration automotive door inner and outer panels. The resulting data was then provided to project partners for modeling and other tasks within the LCMS project.

The experimental work was performed in two main stages comprising tensile testing and formability testing, and both employed the stereo-digital image correlation (DIC) technique to capture the deformation behavior at high spatial and temporal resolution. Tensile testing involved extensive characterization of Mg EFP sheet as a function of temperature, strain-rate and orientation, as well as a limited set of elaborate tests on Mg ZEK100 alloy sheet at room-temperature. Formability testing involved room-temperature and elevated temperature limiting dome height (LDH) tests on Mg EFP under different strain states.

The results from tensile tests on Mg EFP demonstrate its anisotropic behavior is more pronounced at higher strain-rates or at lower temperatures. Further, for any given test temperature and orientation, strain-rate seems to have a significant effect on its tensile stress-strain behavior. Capturing anisotropy and strain-rate effects were essential prerequisites for developing new material cards that otherwise lack these dependencies. Evidence of micro-yielding plasticity was also observed at low strains at which most metals and alloys would otherwise be considered elastic.

These results, complemented with detailed DIC deformation data, were key to developing new and improved material cards that were used to simulate warm stamping of the door outer panel, door inner panel, and the cross-form stamping. As such, the material cards and consequent simulations were key deliverables of the project that were enabled by this experimental task. Detailed discussion of this work may be found at https://data.lightmat.org/project/.

C7.2 KEY ACCOMPLISHMENTS AND RESULTS

C7.2.1 Mechanical Properties Testing of ZEK100 and EFP
The objective of this task was to determine the mechanical properties of the Mg-alloy sheets in tension.

Tension Tests on ZEK100
The objective of these tests was to determine the evolution of symmetry axes upon tensile testing and use the resulting data to develop a model along the lines of prior work on steel. The testing approach comprises "primary" and "secondary" specimens. The primary specimens were designed to enable multiple secondary specimens (ASTM-E8 sub-size geometry) to be machined from their gauge length region. For a given test condition, the primary tension sample was oriented at an angle 60° to the original ZEK100 sheet rolling direction (RD). The primary tension specimens were pre-strained (2% and 6%), unloaded, and subsequently, secondary tension samples were extracted from the pre-strained region and at various orientations, relative to the original loading axis of the primary specimen. In addition to the primary + secondary tests, conventional tensile tests on the as-received sheet were also performed to evaluate anisotropy. All tests were performed at room-temperature at an initial strain-rate of $5x10^{-4}$/s.

Results:

The key results of these tests confirm the tensile stress-strain behavior of the as-received Mg ZEK100 sheet under current test conditions is quite anisotropic with the material having the highest and lowest yield strength in RD and TD directions, respectively. Figures C7.1a and C7.1b show the results from the primary and secondary tension tests. Figure C7.1a shows an example of the stress-strain curves of the secondary tension specimens. Figure C7.1b shows the 0.2% offset yield stress of the secondary tension specimens as a function of the orientation angle at two levels of pre-strains and for primary specimen orientation of 60°. The data in Figure C7.1b shows that the yield strength varies in a sinusoidal-like manner as the sample orientation is systematically varied about the primary loading direction. Such behavior is hypothesized to be associated with evolving texture and twinning and highlights the importance of modeling the evolution of the yield surface with strain.
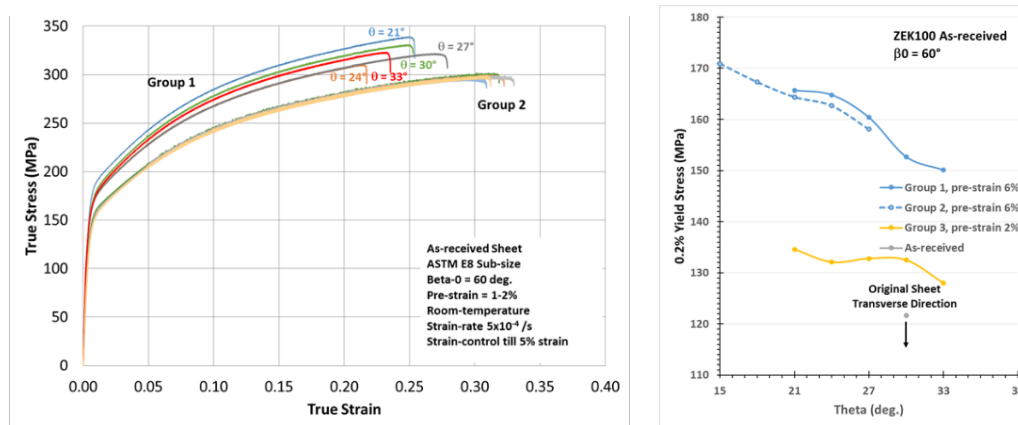

Figure C7.1: Results from room-temperature tension experiments on Mg ZEK100 (a) Stress-strain curves of secondary specimens. (b) Dependence of yield stress of secondary specimens as a function of their orientation relative to primary specimen's loading axis. (Source: PNNL)

Tension Tests on Mg EFP

The objective of these tests was to understand the strain-rate dependence and in-plane anisotropy of Mg EFP under tensile loading. The resulting data will enable development of accurate material models and stamping simulations that may capture strain-rate and anisotropy effects during stamping. Tensile specimens of Mg EFP (USAMP Batch #1) were tested at elevated temperatures in air. The test matrix comprised three temperatures (150°C, 200°C and 250°C), four strain-rates (0.004, 0.01, 0.1 and 0.5/s) and three in-plane orientations (0°, 45° and 90°). A minimum of three specimens were tested at each test condition. Supporting room-temperature tension tests were also performed on Mg EFP, typically at 0.01 or 0.001/s, to ascertain the extent of anisotropy and to develop a general understanding of its behavior (e.g., yield stress, work-hardening, ductility). Strain during elevated temperature tests was measured by the stereo-digital image correlation (DIC) technique, and by mechanical extensometer or stereo-DIC for room-temperature tests.

The need to accurately model the sheet material's stamping behavior required the plastic stress-strain curves to be appropriately calculated, especially during elevated temperature testing due to non-uniform deformation at large strains. Thus, the specimen axial strain for elevated temperature tests was calculated in two main ways: The virtual extensometer approach and the necked-region approach. Using the virtual extensometer feature of the Vic-3D™ software, virtual initial gauge lengths of 1", 2" or 3" were created during DIC data processing and the specimen axial strain was defined as the average axial strain over the respective virtual gauge lengths. Although the virtual extensometer approach is suitable to plot axial strain for homogeneous deformation, it may not the best approach once the specimen begins to neck and

the deformation is localized. Thus, the "necked-region" approach to measure specimen axial strain was implemented to consider strain localization. First, the region of eventual necking failure was identified in the DIC images. A rectangular box-shaped "area-of-interest," centered over the failure region and 0.5 mm axial height x full width of the DIC-processed region, was defined. The axial strain value for each time step was then defined as the average axial strain within this box region.

Results:

For the tension samples on Mg EFP, the non-uniform deformation (and necking) and peeling off of the speckle pattern paint near the necked region were typical of elevated temperature tested samples. The strain in each engineering stress-strain curve was plotted using the virtual extensometer and necked-region methods. If the specimen deformation is relatively homogeneous, the stress-strain curves are identical irrespective of the strain calculation method. However, once the necking becomes severe (e.g., after ~0.25-0.3 strain), the stress-strain curves deviate from one another and the behavior depends upon the strain calculation method.

Figure C7.2 shows a collection of true stress-strain curves for Mg EFP (USAMP Batch #1) at 200°C as a function of strain-rates and in-plane orientations. The data shows a significant increase in the flow stress with increasing strain-rate. A similar strain-rate dependence was observed at other temperatures as well. The data also shows that the strain-rate has a significant effect on the initial work-hardening rate for all the orientations with the work-hardening rate increasing with increasing strain-rate until a limit is reached after a strain of ~0.15. Finally, the anisotropy (i.e., flow stress dependence on in-plane orientation) is more pronounced at the higher strain-rate and at lower temperature.
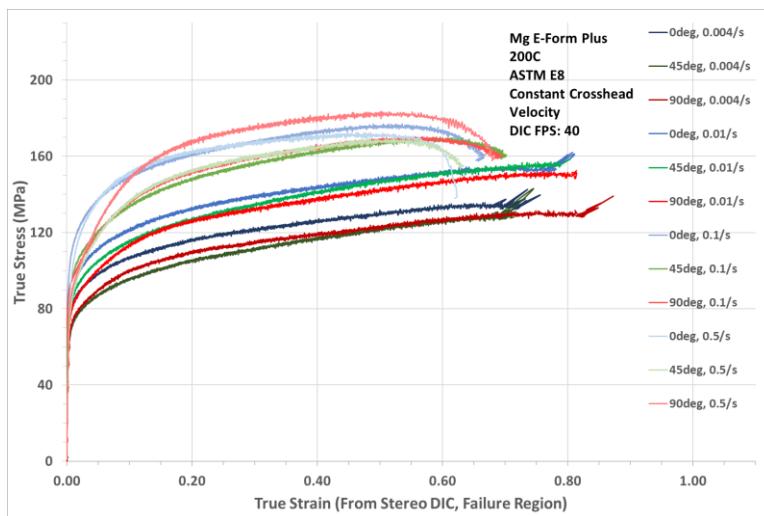
Figure C7.2: True stress-strain for Mg EFP (Batch #1) at 200°C as a function of strain-rate and orientation. (Source: PNNL)

In addition to the elevated temperature tension tests described above, a limited number of room-temperature tension tests were performed on Mg EFP and evidence of micro-yielding plasticity was observed. Upon careful examination of the initial loading curve, Mg EFP is seen to undergo micro-yielding at a stress of ~50 MPa corresponding to a strain of ~0.1%. See Figure 7.3a. Figure C7.3b shows another test (0.001/s, RD) where the sample was unloaded at ~0.2% and subsequently reloaded. Upon unloading, the data indicated a permanent plastic strain of 0.02% suggesting that micro-yielding involved plasticity in what would otherwise be considered as the elastic loading regime. This micro-yielding behavior was further investigated in other sub-task using beam-line experiments to determine which slip systems were responsible for this behavior.

Figure C7.3: Room-temperature engineering stress-strain curve for Mg EFP (Batch #2) highlighting the phenomenon of micro-yielding. (a) Full stress-strain curve with the inset showing a magnified view at low strains with evidence of micro-y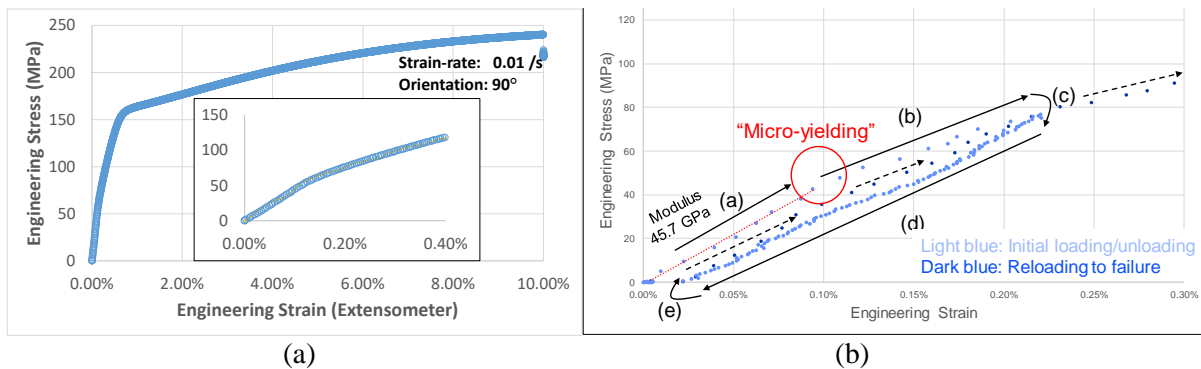ielding at ~0.1% strain. (b) Stress-strain curve showing the initial loading (path a-b), unloading (path c-d) and reloading (path e) during the tension tests to study micro-yielding occurring at low strains. (Source: PNNL)

C7.2.2 Experimental Forming Limit Diagram (FLD) Determination

The objective of this task was to help determine if the Mg EFP sheet alloy has sufficient formability to be stamped into the target automotive components (door inner and door outer) identified by USAMP for this project. In the first step, the "limiting direction" for Mg EFP i.e., the in-plane direction with least formability, and plane-strain formability (i.e., FLD_0) were determined through room-temperature LDH tests. In the second step, elevated temperature (200°C and 250°C) LDH tests were performed in the limiting direction to determine the FLD_0. An Interlaken[TM] LDH test machine with a 4" diameter hemispherical punch and an elevated temperature capable die-set were used. Testing was performed at a punch speed of 5 mm/s and stereo-DIC technique was used to measure surface strains (using Vic-3d[TM] software). Various lubricants (e.g., boron nitride, oil, Teflon sheets, and Fuchs Renoform 1102) and specimen geometries (e.g., rectangle, dog-bone shape, etc.) were used to minimize friction effects and enable specimen fracture at the dome apex location.

Results of Forming Limit Measurements in Mg EFP Batch #1

Three Mg EFP samples were tested at room-temperature under equi-biaxial strain condition in the LDH. The lowest major strain (~12.4% true strain), just prior to fracture, was observed in the sample (Figure C7.4a) where the crack orientation was along RD. Hence, the direction 90° to the RD, i.e., transverse direction (TD) was identified as the limiting direction and subsequent experiments to determine FLD_0 were performed in the TD orientation.

Three samples were tested at room-temperature in the LDH under plane-strain condition and in the limiting direction. The samples showed a similar major true strain of ~14% FLD_0) in the major direction (TD) while the minor true strain was ~-1.3% on average. Although, Mg EFP was expected to have "high" formability, its room-temperature FLD_0 (~14%) is insufficient for the stamped door design selected for this project (estimated ~35%). Thus, elevated temperature LDH tests were performed to determine FLD_0 (at 200°C and 250°C).

In initial attempts, a rectangular plane-strain specimen geometry (as used for room-temperature LDH tests) in combination with boron nitride lubricant was found to be unsuitable to ensure sample failure at the dome apex. Consequently, non-rectangular specimen geometries, such as "dog-bone" type and those similar to the ISO 12004 standard were fabricated and tested. However, irrespective of the geometry and

lubricants (e.g., boron nitride, Teflon films, Fuchs Renoform, etc.), these samples did not fail at the apex. For example, Figure C7.4b shows a dog-bone geometry sample tested at 200°C that failed with a single crack along the rolling direction. Although the failure location was closer to the apex relative to that in rectangular geometry specimens, the strain state near the crack was not one of plane strain, as evidenced by a large, non-zero minor strain (e_{xx} = -11.33%). Therefore, the FLD_0 could not be determined with the out-of-plane configuration used in LDH.
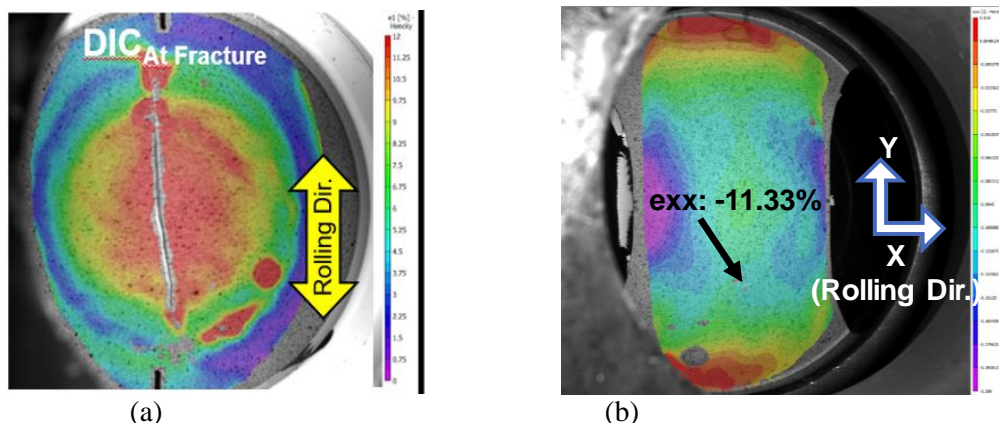

| (a) | (b) |

Figure C7.4: Images of an LDH tested EFP (a) equi-biaxial sample at room-temperature, overlaid with DIC strain contours showing crack orientation upon fracture; (b) plain-strain sample at 200C with a "dog-bone" geometry, showing minor (e_{xx}) Hencky strains adjacent to the crack. (Source: PNNL)

To determine FLD_0 for Mg EFP, USAMP contracted with FADI-AMT LLC who developed a test method using an in-plane configuration. Note that for this report, the terms FLD (forming limit diagram) and FLC (forming limit curve) will be used interchangeably to denote the same data. To achieve a plane strain condition, FADI-AMT optimized a custom sample geometry (PST-III6) that was pulled in tension at three temperatures (150°C, 200°C and 250°C) in the TD orientation. Testing was performed using a standard electromechanical test frame with custom grips and heating chamber. A standard 2-camera system was used for optical non-contact strain measurements (for 3D DIC).

DIC post-processing analysis was used to extract the FLC points as shown in Figures C7.5a-c. Surface strains (major vs. minor) were computed and FLC points were extracted per the ISO-12004 standard, using the section-based method. Also, FLC points were extracted via the time-dependent approach providing ample points to extrapolate the FLD_0 using the linear best fit method, as shown in Figure C7.6. Note that FLD_0 increases from 0.33 at 150°C to 0.64 at 250°C.

(a)   (b)   (c)
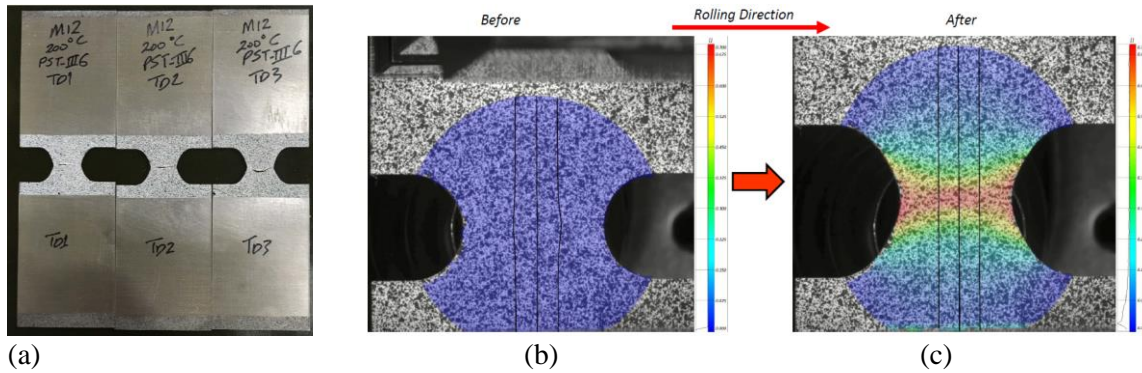
Figure C7.5: FLC test specimens PST-III6 Mg-EFP (USAMP Batch #1) (a) Custom sample geometry test specimens (b) Sample with three section imposed in a vertical orientation before test, (c) Sections and strain map after deformation. (Source: FADI-AMT)
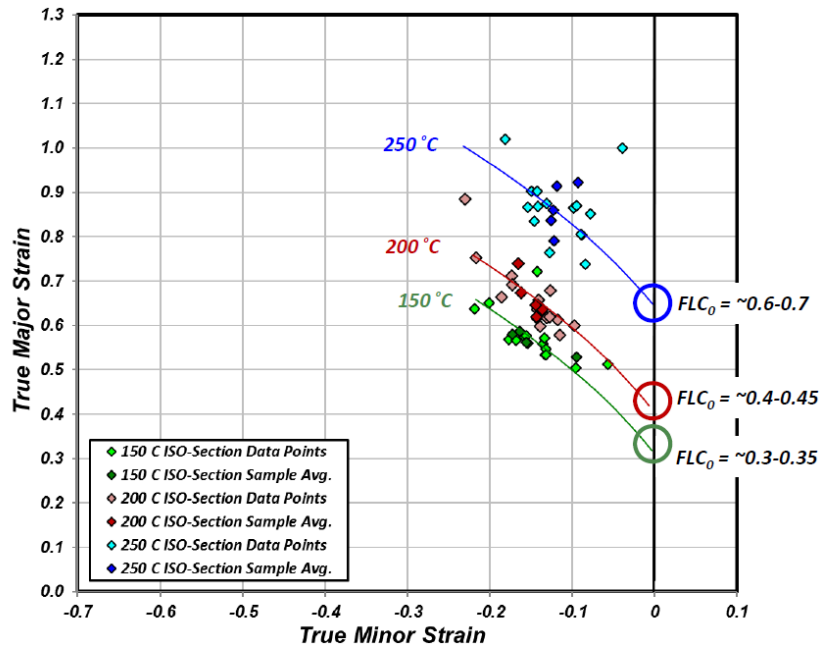
Figure C7.6: Forming limit chart for Mg EFP Batch #1 showing extracted FLC points and extrapolated FLC_0 at three temperatures (150°C, 200°C and 250°C). (Source: FADI-AMT)

C7.3 CONCLUSIONS AND RECOMMENDATIONS

The scope of this work was to perform mechanical characterization of Mg alloy sheets and provide the necessary data that could serve as input for the modeling effort. A test matrix was executed consisting of over one hundred tests requiring ~1TB data storage – all experimental data is available in a DataHUB folder. Under the test conditions employed in this research, the following conclusions can be drawn:

1. For elevated temperature tension loading of Mg EFP sheet, the strain-rate has a significant effect on the initial work-hardening rate for the orientations tested: For a given test temperature, the initial work-hardening rate increases with increasing strain-rate up to a strain of ~0.15/s; with further straining, the work-hardening rate is roughly similar across the strain-rates.

2. The anisotropy (i.e., flow stress dependence on in-plane orientation) in Mg EFP sheet is more pronounced at the higher strain-rates and at lower temperatures.

3. For room-temperature tension loading, Mg EFP shows clear evidence of micro-yielding plasticity at strains as low as ~0.1% that would otherwise normally be considered as elastic loading regime for most metals and alloys.

4. Preliminary room-temperature tension testing on Mg ZEK100 suggest an evolution of the symmetry axis with loading akin to that reported in literature for steel.

5. For room-temperature LDH testing, the transverse direction in Mg EFP sheet was found to be the limiting direction and the corresponding plane-strain formability (FLD_0) was measured to be ~14%. This level of FLD_0 is too low to stamp the door at room-temperature.

6. For elevated temperature LDH testing, the FLD_0 could not be determined as the sheet samples tended to fail away from the plane-strain location i.e., the dome apex. (Similar experimental issues were encountered in parallel efforts by other project team partners as well. The problem was solved by deforming the sample in in-plane configuration as opposed to out-of-plane configuration used in LDH).

C8. Continuum-Level Constitutive Model for Magnesium Deformation
(UPenn – Principal Investigator: J. Bassani and
InalTech Inc – Principal Investigator: K. Inal)

C8.1 SUMMARY

The University of Pennsylvania and InalTech team focused on developing Integrated Computational Materials Engineering (ICME) methods coupled with experimental studies and data tools to simulate thermomechanical processing for improved and cost-effective formability. A continuum model was developed for textured Mg polycrystalline sheet materials that deform by slip and twinning mechanisms for use in simulations of warm forming. Primary features of the anisotropic elastic-plastic model account for the continuous evolution of (i) anisotropic yield stresses (e.g., yield strengths in the principal directions of anisotropy), (ii) overall hardening under arbitrary strain paths, (iii) strength differentials (e.g., tension/compression asymmetries), and (iv) the evolution of the material symmetry axes (i.e., the orientation of the orthotropic triad that characterizes the symmetry of the polycrystalline texture). Major research outcomes are accurate and robust, continuum-level thermo-elastic-plastic constitutive models that are coupled with finite element implementations for improved simulations of large and complex deformations of textured Mg sheet materials.

The approach was to couple, as much as possible, with existing FEA simulation tools that are widely used in the automotive industry. The commercial finite element software LS-DYNA was chosen as the platform for these developments. LS-DYNA has several built-in anisotropic material models but only for fixed axes of anisotropy. One such anisotropic plasticity model that can incorporate strength differentials was built on the work of Cazacu et al. [2006], which LS-DYNA denotes MAT233. But like all the built-in models, MAT233 cannot describe the rotation of material symmetry that is known to strongly affect forming limit behavior. The team used a two-step task strategy: (1) Determine the material parameters required to populate the material input card for MAT233 which required specifying more than 30 material parameters and (2) Extend the Cazacu et al. [2006] model to include the evolution of material symmetry using crystal plasticity theory, which had never been done. The resulting new material model is designated as MAT233+. For both tasks, since deriving all the necessary parameters from experiments was prohibitive, a multi-scale framework was adopted to determine many of the input parameters including those that characterize microstructural evolution in phenomenological plasticity. To characterize the evolution of material symmetries associated with the rotation of the principal axes of anisotropy, the team adapted the Bassani and Pan [2012] model developed for cubic polycrystals and successfully used for modeling a class of steel alloys and by Kohar et al. [2019] for aluminum alloys.

The deliverable LS-DYNA material models are calibrated for the EFP Batch #1 material at 200ºC and at a nominal strain rate of 0.01/s. Following steps summarize the procedure for the development and calibration of MAT233 and MAT233+ material models, with the required inputs to LS-DYNA:
1. Identify needed experimental measurements, consisting of uniaxial stress-strain data and EBSD.
2. Build a crystal plasticity (CP) model with the initial texture given by the EBSD data.
3. Calibrate CP model to uniaxial stress-strain responses.
4. Generate multi-scale data using CP simulations.
5. Implement finite element modeling framework.
6. Calibrate the MAT233+ user material model.

An example of new simulation capabilities using the user material model (UMAT) MAT233+ in conjunction with LS-DYNA is shown below in Figure C8.1. The graphic depicts the effective plastic strain distribution superimposed on the deformed geometry for cross-form stamping of an EFP sheet. Detailed discussion of this work may be found at https://data.lightmat.org/project/.
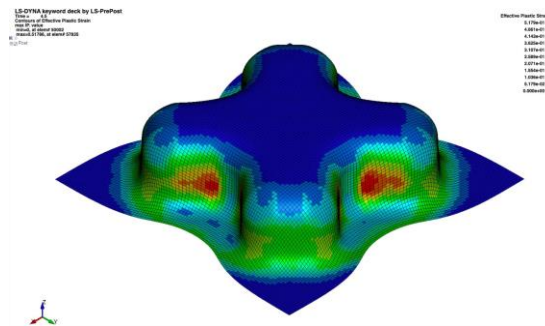
Figure C8.1: A successful cross-form simulation using new material model (UMAT) MAT233+. (Source: InalTech)

C8.2 KEY ACCOMPLISHMENTS AND RESULTS

A major project goal was to accurately simulate the limits to forming associated with the stamping of geometrically complex parts, e.g., an inner door panel, which requires accurate material models that account for the influence of anisotropy and microstructural evolution, which is known to directly affect strain localization. A new phenomenological anisotropic elastic-plastic model was developed for textured Mg polycrystalline sheet materials deforming by crystallographic slip and twinning. For non-uniform deformations, such as those found in forming a car door panel, the evolution of those properties is complex and continuously varies throughout deformation processing of components.

The thermomechanical behavior of Mg sheet materials is complex, because they are highly textured, HCP polycrystals, with highly anisotropic single-crystal constituents that undergo temperature-dependent multi-slip and multi-twinning deformation mechanisms. To develop accurate phenomenological material models for macroscopic simulations, the UPenn/InalTech team adopted a strategy that coupled experiments (utilizing data obtained from other investigators in the project) and polycrystalline simulations. This multi-scale approach proved essential to augment data needed for the continuous local rotations of the anisotropic material symmetries resulting from texture evolution that was not readily available from experiment, due to both time and cost constraints. The approach led to a key outcome from this project: the first-ever successful development of thermomechanical constitutive models for Mg alloys, in particular for EFP. Prior to this work, existing capabilities that utilize commercial finite element software, including user-defined material models, were limited to *fixed* axes of anisotropy that cannot account for the evolution of texture in "off-axis" straining, i.e., when the principal axes of strain are not aligned with the orthotropic axes of material symmetry. Overcoming this limitation is a major outcome of the USAMP's research that significantly advances the state-of-the-art in magnesium sheet technology.

C8.2.1 Building the Material Models
Through the course of the project, several Mg alloys were investigated, including efforts to develop new alloys, but eventually the decision was made to primarily base the overall project on the POSCO EFP material. The model is therefore calibrated for the EFP Batch #1 sheet material at 200ºC and at a nominal strain rate of 0.01/s.

To develop accurate ICME capabilities for large-scale, macroscopic simulations (i.e., for an entire door stamping operation), a strategy was adopted that coupled experiments (from other investigators in the project) and polycrystalline simulations. This multi-scale approach proved essential to augment data needed for the continuous local rotations of the anisotropic material symmetries resulting from texture evolution that was not readily available from experiment. This latter approach, which the UPenn/InalTech

team had successfully adopted in earlier work on FCC aluminum alloys (Kohar et al., 2019), led to a key outcome from this project: the first-ever successful development of thermomechanical constitutive models for Mg alloys, in particular for EFP. Particular attention was given to material anisotropy and the asymmetry of flow that results from twinning. The newly developed model for Mg polycrystals which accounts for the evolution of texture is a major outcome of USAMP's research that significantly advances the state-of-the-art in magnesium sheet simulation technology.

Experimental Measurements

The key experimental data required as input for the multi-scale approach to develop thermo-elastic-plastic constitutive models were: (i) the initial ESBD measurement and (ii) uniaxial stress-strain curves for several orientations of the tensile axis relative to the RD. Stress-strain curves were generated at PNNL (see Figure C8.2) for three directions of the tensile axis: 0° (RD), 45° (DD) and 90° (TD) at a temperature of 200°C and a nominal strain-rate of 0.01/s. Digital image correlation was utilized to measure strain.
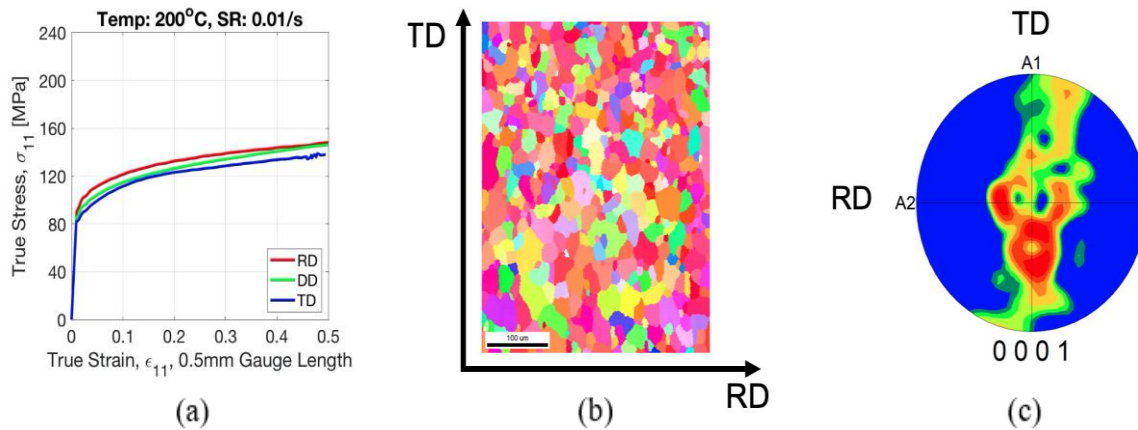

Figure C8.2: Experimental data for EFP Batch 1 sheet material: (a) stress-strain curves at 200°C and strain-rate of 0.01/s for the tensile axis in RD, DD and TD direction, (b) EBSD measurement, and (c) pole figure. (Source: PNNL)

C8.2.2 Build a Crystal Plasticity (CP) Model with the EBSD

Typically, a 2D EBSD is sufficient to represent the microstructure of sheet material. A Taylor-type magnesium CP formulation that captures twin volume fraction evolution is used to model the EFP sheet.

C8.2.3 Calibrate CP Model to Uniaxial Stress-Strain Responses

Experimental data displayed a distinct difference in the hardening rates in the different directions. This difference is caused by the microstructural dependence of the extension twinning mechanism that results from the sheet texture. This means that at least two different experiments are required for calibration to capture this phenomenon. The strategy uses the RD and TD stress-strain responses for calibration. The stress-strain response in the DD direction is then predicted and used as a verification.

A comparison of the CP model with experiments is shown in Figure C8.3 – it highlights predicted stress-strain curves in the DD direction, which involves significant texture evolution and validates the CP model. In particular, the effects of twinning and differential hardening are accurately captured in the CP model. Therefore, the fully validated CP model can be used to generate *virtual* data that is required for MAT233+, which accounts for the evolution of texture via the rotation of the material symmetries.
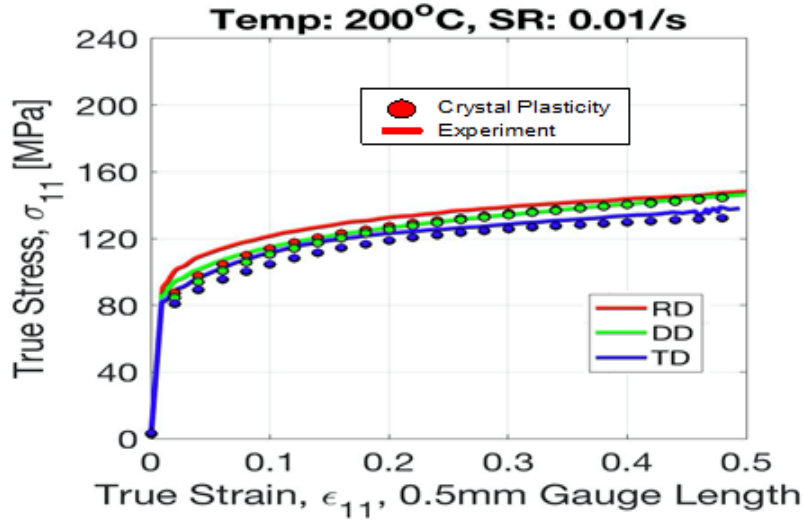
Figure C8.3: The experimental data (solid curves) and the fit from the CP model (circles) for the RD (red), DD (green) and TD (blue) directions of the initial tensile axis. (Source: InalTech)

C8.2.4 Multi-Scale Data Generation using CP

Different strain paths are simulated to produce data on material symmetry rotations that are required to calibrate MAT233+. Accordingly, the initial texture along RD was rotated in 15° increments before simulating uniaxial tension, as shown in Figure C8.4.
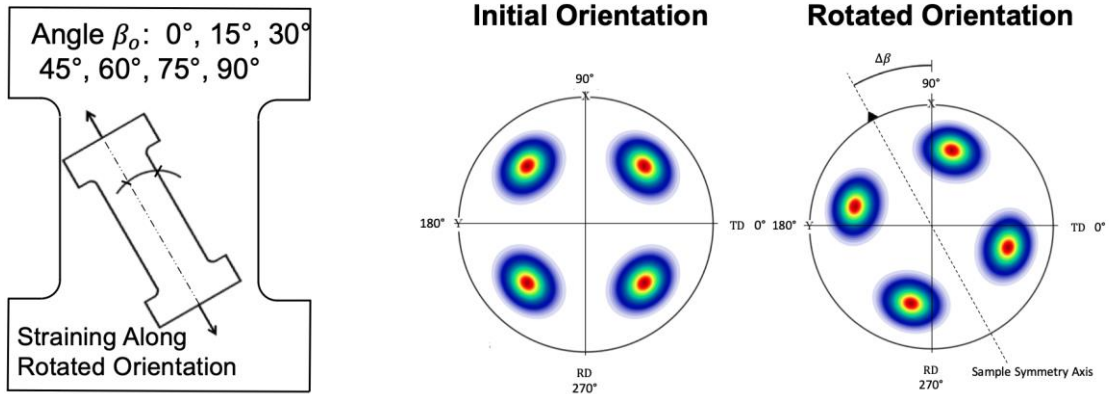
Figure C8.4: Off-axis uniaxial tension simulations from CP model. The initial angle of the tensile axis β_o is incremented in 15° intervals to generate virtual data for the MAT233+ phenomenological model. (Sources: PNNL and InalTech)

The results from the CP simulations (see Figure C8.5 below) that fully specify the rotation of the othotropic axes for in-plane tensile stressing of the EFP material were used to determine the spin function η_3 required for MAT233+. Recall that only η_3 enters the model under plane-stress conditions. Note that is an important distinction in the material symmetry rotations for the Mg alloy as compared to the results for a steel alloy. In the latter case, there are just 2 stable orientations that result from uniaxial stressing at any angle in the plane of the sheet. In contrast, for the EFP Batch 1 material, there are 4 stable orientations, a behavior that, to the USAMP's knowledge, has not been seen before. Therefore, the simple representation for η_3 is not sufficient. An enhanced functional form was proposed for that spin function, which is likely a characteristic of Mg alloy sheets and is another key outcome from this project.
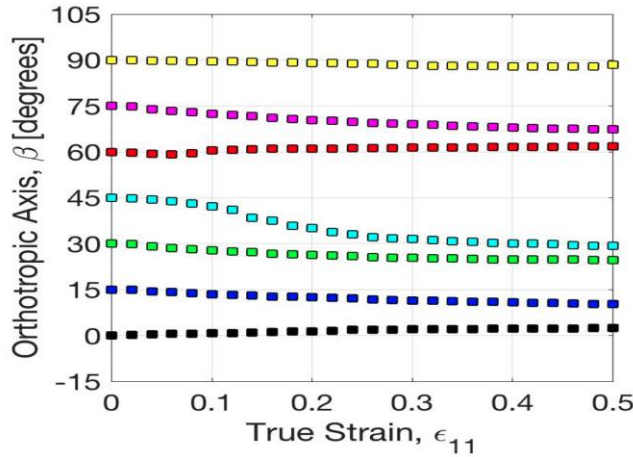
Figure C8.5: Simulations for the rotation of the material symmetry axes from the CP model for EFP. (Source: InalTech)

C8.2.5 Numerical Modeling Framework

A phenomenological plasticity framework was implemented into the yield function proposed by Cazacu-Plunkett-Barlat [2006]. This framework accounts for microstructural evolution through continuous rotations of the orthotropic symmetry axes, as shown in Figure C8.6. It involves a single transformation model with tension-compression asymmetry. A total of nine coefficients (including asymmetry and yield surface exponent) are required for calibration. A UMAT subroutine was written by InalTech, since LS-DYNA does not include anisotropic models that allow rotations of the material symmetries.
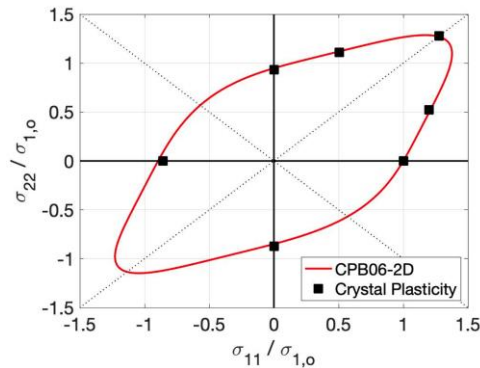
Figure C8.6: Normalized CPB yield surface calculated from the data generated from the CP model which agrees well with the CP predictions. (Source: InalTech)

C8.2.6 Calibration of MAT233+ Material Card

To develop the MAT233+ material card required for the UMAT subroutine, "virtual experiments" were generated from the CP model, given the initial texture and predicted texture evolution. This included stress-strain curves for different texture axis orientation, microstructure evolution, and calculation of yield surfaces. A modified Swift hardening model was adopted. Excellent agreement between the MAT233+ and CP predictions is seen as indicated by the solid lines in Figure C8.7.
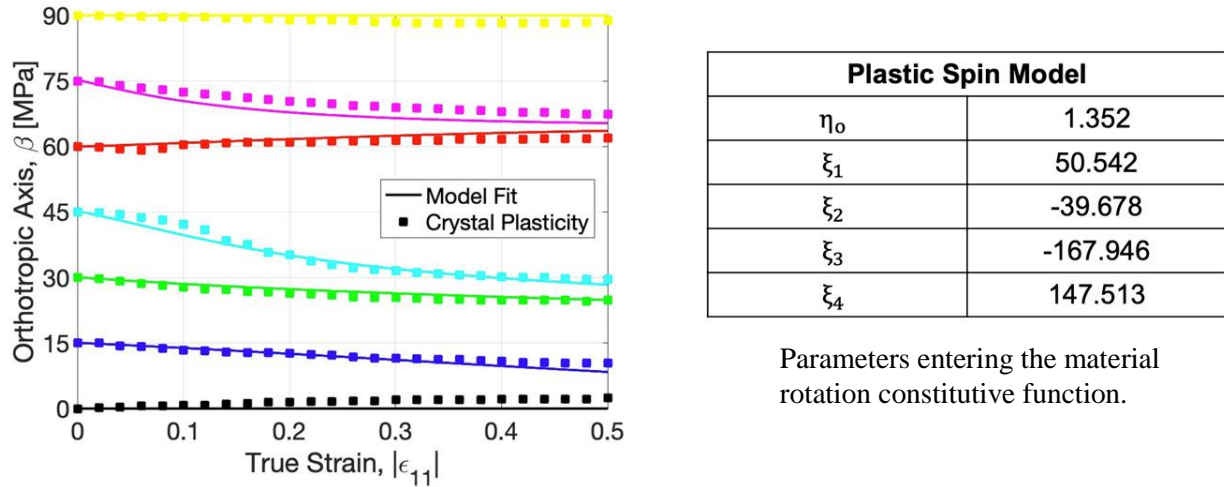

Plastic Spin Model	
η_0	1.352
ξ_1	50.542
ξ_2	-39.678
ξ_3	-167.946
ξ_4	147.513

Parameters entering the material rotation constitutive function.

Figure C8.7: Predicted rotations from the MAT233+ model and comparisons with the CP simulations. (Source: InalTech)

C8.3 CONCLUSIONS AND RECOMMENDATIONS

ICME methods have been developed that are coupled with experimental studies and data tools. Phenomenological elastic-plastic constitutive models for textured polycrystalline sheet materials undergoing deformation-induced microstructural evolution have been successfully constructed and implemented in the commercial finite element program LS-DYNA, which is widely used in the automotive industry. The goal is to be able to accurately simulate thermomechanical processing of magnesium alloys to achieve improved formability. Both slip and twinning mechanisms have been accounted for, where the latter gives rise to strength differentials (tension-compression asymmetries) that were beyond existing modelling capabilities for macroscopic simulations that include the effects of texture evolution. This is a significant advancement.

To develop accurate ICME capabilities for large-scale, macroscopic simulations (e.g., for an entire door stamping operation), the UPenn/InalTech team successfully adopted a strategy that coupled experiments and polycrystalline simulations. This multi-scale approach proved essential to augment data needed to model, in particular, the continuous local rotations of the anisotropic material symmetries resulting from texture evolution, which was an important objective of this sub-task. A key outcome from this project was the first-ever development of macroscopic thermomechanical constitutive models for Mg alloys, in particular for EFP, for use in large-scale simulations of deformation processes. The newly developed model for Mg polycrystals significantly advances the state-of-the-art in magnesium sheet technology.

The full implementation of the Mg alloy sheet material model in LS-DYNA required writing a UMAT, a user provided subroutine, that has been made available to Vehma, who have undertaken studies of the stamping of the inner door panel. These models will be made available to the broader community. A demonstration of the improved simulation capability is shown for cross-form stamping (refer to the graphic in the Summary section above).

C8.4 REFERENCES (specific to this report section)

1. Bassani, J. and Pan, H., "A phenomenological model for microstructural evolution during plastic flow," *Comptes Rendus Macanique,* vol. 340, pp. 369-377, 2012.

2. Cazacu, O., Plunkett, B. and Barlat, F., 2006. Orthotropic yield criterion for hexagonal closed packed metals. *International Journal of Plasticity*, *22*(7), pp.1171-1194.

3. Kohar, C.P., Bassani, J., Brahme, A., Muhammad, W., Mishra, R.K. and Inal, K., 2019. A new multi-scale framework to incorporate microstructure evolution in phenomenological plasticity: theory, explicit finite element formulation, implementation and validation. *International Journal of Plasticity, 117,* 122-156.

C9. Formability Testing to Determine the FLC_0 for Mg EFP (FADI-AMT LLC – Principal Investigator: F. Abu-Farha)

C9.1 SUMMARY

This sub-task on additional testing of EFP Batch #4 at elevated temperature for three strain paths was added towards the end of the project, after the USAMP reviewed the outcomes of multiple crystal plasticity based finite element cross-forming simulations performed by InalTech (see Section C8) using the new MAT233+ card and compared the results with the Argus strain map of the cross-form.

Both major strains and minor strains were analyzed, and key differences between simulation and experiment (for displacement 47.5 mm) were identified. InalTech offered several possible explanations to account for the differences in simulation correlation:
1. The CP model is developed for constant temperature and strain rate (200°C, 0.01 /s), and there is lack of any thermal softening.
2. The relatively coarse mesh (6 mm compared to 1.5 mm and 3 mm) may have missed capturing localized strain which may be higher during forming, and then relaxation may have occurred at the end of the forming which caused cracking observed in the experimental cross-form part, even though the strain map does not show it.
3. Lack of twinning – Twinning will become more pronounced as the temperature decreases during the experiment.

It was concluded that while simulations with both MAT233 and 233+ cards identified and correlated with areas of the cross form with highest strains, the models are unable to explain why the simulation results do not predict the fracture areas. A corresponding study of door panel fractures surfaces performed by FADI-AMT concluded that there are no significant differences in thinning behavior between rolling direction and transverse direction.

InalTech recommended additional material testing and data gathering be done which would help support new simulation runs and model calibrations, and thereby augment the team's knowledge on the FLDs for EFP sheet. The observed that based on the findings in literature, increasing the strain rate seems to be decreasing the formability for calcium/cerium-added Mg alloys. This is contradictory to everything known so far, especially for materials with positive strain rate sensitivity (like the EFP Mg alloy).

The USAMP contracted with FADI-AMT to perform custom formability testing on EFP Batch #4 sheets with digital image correlation (DIC) to generate FLDs from 3 points: uniaxial tension, plane strain tension and balanced biaxial tension, in order to develop accurate FLCs for the material at 200°C and at three different strain rates as outlined below. These test results may correlate better when exploring different time-steps for peak strain values which may also explain the strain levels and fracture locations. The formability (i.e., FLD_0) of EFP Batch #4 sheet at 200°C decreases from 0.42 to 0.18 as the strain rate of testing increases from 0.01 to 1.0 /s. FADI-AMT's test data is available at https://data.lightmat.org/project/.

C9.2 KEY ACCOMPLISHMENTS AND RESULTS

The sheet formability of Mg EFP Batch #4 was evaluated experimentally at 200°C and three strain rates (~0.01, 0.1 & 1 /s). The standard approach for formability testing with a hemispherical punch (Nakajima per ISO 12004) does not work for Mg sheets at ~200°C by simply using heated dies and punches; non-uniform temperature distribution and excessive friction both led to significant offsets in strain paths and failure location (per previous test results reported in Section C7).

Therefore, a custom testing approach was used here to ensure temperature uniformity and eliminate frictional issues. The three main loading paths on a forming limit diagram were achieved as follows:

1. Uniaxial Tension (UT): pull tests of custom dog-bone samples (high length to width ratio)

2. Plane-Strain Tension (PST): pull tests of custom samples (high width to length ratio)

3. Balanced Biaxial Tension (BBT): pneumatic bulge testing through a circular die insert

All three types of tests were performed isothermally at 200°C within an environmental chamber to achieve uniform temperatures across the test samples as well as the tooling. UT and PST tests were performed using custom pulling grips that rely on shoulder loading to prevent slippage and permit testing at intermediate strain rates. Both, conventional 3D DIC and high-speed 3D DIC were used in order to generate sufficient number of images for evaluation. The ISO 12004 section-based approach was used to extract the FLC points from all tested samples.

The generated FLC points as well as the projected FLC lines (one per strain rate) are shown below in Figure C9.1. Large scatter was noted with this material despite doubling the number of tests per condition (increased from 3 to 6 replicates in most cases), and despite the high degree of test control (both mechanical and DIC). For comparison, FLC testing via the Nakajima approach was performed on the same material at 23°C. The results shown below reveal the same high levels of scatter, which is unusual for such a sheet metal given the high quality of stress/strain curves that were obtained for this material. Based on these results, it is possible to draw some conclusions as follows:

1. For this batch, FLC_0 at 200°C and a strain rate of ~0.01/s is ~0.42 (with a deviation band as high as ±0.07), which is at least as good and potentially better than previously tested batches (i.e., Batch #1 and #3) of this same Mg alloy.

2. Formability limits drop with increasing strain rate (note how FLC_0 drops to ~0.18 as strain rate approaches ~1 /s).
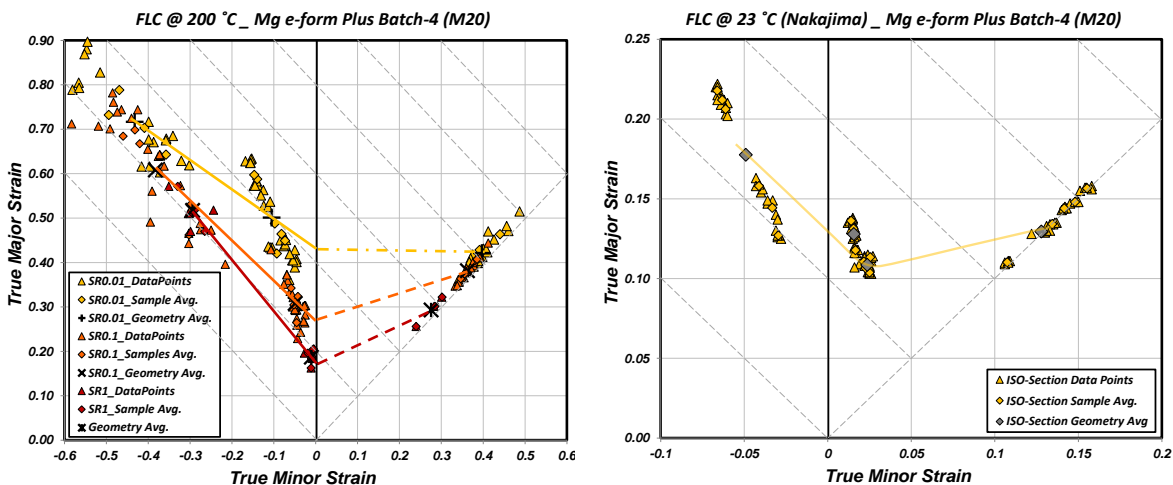
Figure C9.1: FLC points generated for EFP Batch #4 sheets at 200°C as well as the projected FLC lines (left) and at 23°C (right). Whereas the 200°C data were collected at strain rates of 0.01, 0.1, and 1 /s, the 23°C data were collected at 0.01 /s (Source: FADI-AMT).

Both sets of tests run at room and elevated temperature show high levels of scatter – the scatter was highest for the UT loading case. Interestingly, the uniaxial tension curves were extremely repeatable for all three strain rates, as shown below in Figure C9.2. This indicates that the scatter in the FLC data is

either driven by (1) non-homogeneity of strain localization in the material, or (2) the way FLC points are extracted (i.e., algorithms for extracting FLC points).
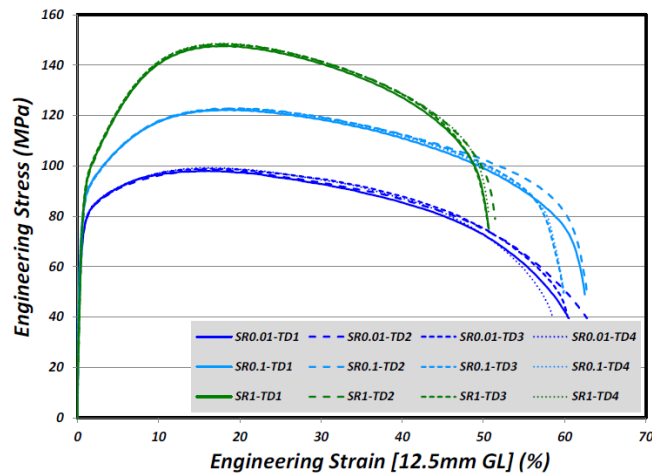
Figure C9.2: Uniaxial tension curves were highly repeatable for all three strain rates at 200°C. (Source: FADI-AMT)

Considering explanation (2) above, this is the same approach used extensively before with many materials and it is typically robust and only leads to scatter due to material non-homogeneity. The fact that uniaxial tension and plane-strain tension sample were used here (rather than the conventional Nakajima samples) could play a role, but FADI-AMT pointed out that the same scatter was noted in the Nakajima testing at room temperature, and thus, all of these items combined lead one to believe that this response is primarily driven by the material itself.

C9.3 CONCLUSION AND RECOMMENDATIONS

1. The formability (i.e., FLD_0) of EFP Batch #4 sheet at 200°C decreases from 0.42 to 0.18 as the strain rate of testing increases from 0.01 to 1.0 /s.

2. Future studies need to determine the root cause of the large degree of scatter in the measured strains at fracture seen at both 23°C and 200°C FLD testing. Reducing the scatter would enable automotive engineers to design stampings which more fully utilize the lightweighting potential of EFP sheet.

Chapter D. Task 3: Sheet Coatings, Lubricant Development and Evaluation

TASK INTRODUCTION

Task 3 activities fell into three general areas: Coil Pretreatments, Stamping Lubricants, and Paint Shop Cleaners and Pretreatments. These are discussed below in the order in which they would occur in the automotive manufacturing process. The goal of these efforts was to facilitate forming and minimize corrosion, and do so with minimal added cost.

D1. Coil Pretreatment with Non-Metallics
(Henkel – Principal Investigator: C. Thomas)

D1.1 SUMMARY

Henkel Surface Technologies was tasked with developing a magnesium coil pretreatment process to protect magnesium coil from oxidation after production through storage and forming. To that end, Henkel screened and optimized several Henkel cleaners, etchants, and pretreatment products and processes, narrowing in on the best performer, as evaluated by humidity corrosion resistance and elemental surface analysis.

Initially, Henkel's coil pretreatment process was optimized for ZEK100 sheet the surface of which, as determined by scanning electron microscopy (SEM) and glow discharge optical emission spectroscopy (GD OES) analysis, was found to be heavily oxidized. Several Henkel deoxidation and/or etch products were screened at varying concentrations, temperatures, and exposure times where the product selection criteria included effective removal of oxidation and low smutting, and sufficient deposition of pretreatment components.

EFP Batch #2 sheet was received in 2018, and the coil pretreatment development process was repeated for this alloy. The surface had very little oxidation and therefore required adjustment of deoxidation parameters of the prior established process. Conversely, the supply of EFP Batch #3 (received still later) was found more oxidized, thereby requiring deoxidation optimization and implementation into the pretreatment process for this batch. Henkel worked collaboratively with AET throughout the development process to ensure EFP with pretreatment Process D would not prevent successful welding.

Bend testing was performed to evaluate the durability of Henkel Process D coating during the forming process. Bent panels were subject to humidity with no visible increase in oxidation detected. Humidity Testing exposing Xtalic zinc coating vs. Henkel Process D coating was performed to compare their corrosion resistance performance. Both experimental pretreatments fell short of the performance compared to the control, galvanized steel.

To evaluate potential increase in corrosion in areas exposed to structural adhesive, Lap Shear adhesive joints for corrosion testing were assembled, e-coated and subjected to 30 days of ASTM B117 salt spray testing. No apparent weaknesses in the adhered area were detected. In addition, the improved corrosion resistance of EFP panels with Henkel Process D was apparent.

In conclusion, this investigation showed the application of Henkel products can improve corrosion resistance of ZEK100 and EFP sheet magnesium and is feasible for use on automotive OEM body components. Detailed discussion of this work may be found at https://data.lightmat.org/project/.

D1.2 KEY ACCOMPLISHMENTS AND RESULTS

D1.2.1 Objective and Approach
Henkel's reponsibility for sheet coatings (Task 3 in Figure A1) was to apply surface treatment to the magnesium alloys investigated in this project, meeting technical requirements for adhesion and corrosion performance. Henkel agreed to cut, pretreat, and distribute to project subrecipients 300 pretreated ZEK100 panels during BP1 followed by 380 pretreated EFP magnesium panels during BP2.

Henkel coil pretreatment systems were screened by testing currently available Henkel Mg pretreatment coating systems, over ZEK100 and EFP alloy sheets, evaluating for critical properties, and selecting the best performer.

D1.2.2 Pretreatments for ZEK100
Seventy 1216 mm x 1019 mm sheets of ZEK100 magnesium alloy were received by Henkel from USAMP in August 2017, and were cut into smaller panels, generally 102 mm x 152 mm, in preparation for cleaning and pretreatment screening trials.

Material Surface Characterization
To make an informed selection of cleaning and etching products, the surface of the ZEK100 magnesium alloy was analysed using glow discharge optical emission spectroscopy (GD OES) and scanning electron microscopy (SEM). GD OES analysis revealed a magnesium oxide/hydroxide layer 200-300 nm thick.

The SEM images show multiple irregularities on the surface and a ridged surface profile. It is suspected the ZEK100 sheet received had been stored for many years without mill oils or other surface protections and oxidized in storage.

Deoxidizing ZEK100
The thick oxide layer required removal to effectively apply the subsequent pretreatment. Several Henkel deoxidizers were selected and screened, and the processing optimized. The before and after photographs, included below (Figure D1.1), show a distinctive change in color and luster after deoxidation.

Screening and optimization of Henkel pretreatments was performed with ZEK100 during January and February 2018. Marginal progress was made based on successful deoxidation of the metal surface and deposition of passivating/barrier pretreatment as determined by humidity testing and GD OES depth profile analysis. With the arrival of the EFP sheet, development work on ZEK100 sheet was suspended.

D1.2.3 Pretreatments for EFP
Two hundred forty 550 x 500 mm sheets of EFP magnesium alloy were received from USAMP in March 2018. The sheets were cut into smaller panels for cleaning and pretreatment tests. To make an informed selection of Henkel cleaning and etching products, the EFP sheet surface was analyzed using GD OES and SEM. The GD OES depth profile showed a very clean surface with low oxidation at less than 10 nm. The SEM images showed a ridged surface profile with minimal surface pitting or other irregularities.

Surface Etch and Pretreatment
An etched metal surface is generally more accepting of pretreatment deposition. An etching cleaner bath or separate deoxidizing bath, prior to pretreatment, can be used and both types were screened for effectiveness. The goal is to activate the metal surface with minimal necessary etch while avoiding additional oxidation. A 3 to 5 second immersion in an acid-based Henkel cleaner/etchant was effective. The magnesium was then rinsed, and a Henkel thin film coil pretreatment was applied using a roll coater. Finally, the panels were held horizontally and dried in a 150°F oven for approximately 5 minutes. This

new process was named pretreatment C. EFP sheet samples having this pretreatment were evaluated for humidity corrosion resistance (see Figure D1.2) and adhesive lap shear strength (Table D1.1).

Figure D1.1: ZEK100 sheet before (left) and after (right) deoxidation (Source: Henkel)

D1.2.4 Distributing EFP

In July 2018, pretreatment C was applied to 200 EFP panels (600 mm x 300 mm) and distributed to other project team members: Fuchs, Quaker, PPG, and AET. Pretreated panels were randomly selected and analysed using GD OES depth profiling to determine the coating weights of passivating/barrier components. The average coating weights of Components A and B were 28 mg/m^2 and 0.4 mg/m^2.

Figure D1.2. EFP panels after 24-hour humidity exposure. (left) Control panel (solvent cleaned only). (right) Panel having Henkel pretreatment C. (Source: Henkel)

Table D1.1. Lap shear strength of EFP panels: Control (solvent clean only) and Henkel pretreatment C.

Parameter	Control	Pretreatment C
Mean Lap Shear Strength	18.58 MPa (2694.98 PSI)	15.71 MPa (2278.24 PSI)
Failure Mode	Mixed mode- Primarily adhesive failure	

D1.2.5 Process Improvement
Most of Henkel efforts in September 2018 focused on improving the pretreatment process to better remove organic contaminants such as fingerprints and smudge marks seen on some pretreated material. This effort was approached by separating the cleaning/etching bath into an alkaline cleaning bath following by an acid etching bath. The targeted etch range of 0.2-1.0 g/m^2 was achieved. Additionally, this product deposited Component A (proprietary to Henkel), a passivating/barrier component, with a coating weight approximately 60% greater than that in pretreatment C (aka Process C). This new clean/etch/deposit process was named pretreatment D (aka Process D).

D1.2.6 EFP Magnesium-Welding Screening by AET
EFP coupons with Henkel pretreatment D were supplied to AET for welding evaluation. AET observed low performance, prompting further investigation. The organic component of pretreatment D was suspected to be creating the poor welding results. Process E was developed that would deposit the protective/passivating component without the organic component. AET performed a subsequent evaluation comparing weldability of processes C, D and E. Process D gave the best results.

D1.2.7 Lap Shear Strength Testing
Triplicate sets of EFP samples were prepared using 25.4 mm x 102 mm coupons of both untreated solvent-wiped substrate and substrate pretreated with pretreatment D. Structural adhesive Teroson EP 5089 (designed for metal bonding) was applied to the 12.5 mm lap using spacer beads to give 0.25 mm adhesive thickness. The samples were heat cured 170°C for 37 minutes then cooled for 30 minutes before testing shear strength using at a speed of 13 mm/min at an average temperature of 23°C. Results are shown in Table D1.2. Lap shear strength is highest for the control sample, lower for D, and lowest for E.

Table D1.2. Lap Shear Strengths

	Control	"D"	"E"
Mean Lap Shear Strength	16.42 MPa	11.49 MPa	10.31 MPa
Failure Mode	100% Adhesive Failure With Residue	100% Adhesive Failure With Residue	100% Adhesive Failure With Residue

D1.2.8 Bend Testing
Bend testing was performed to evaluate resistance to cracking of the pretreatment during forming. A modified version of the "Standard Test Methods for Mandrel Bend Test of Attached Organic Coatings, ASTM D522M-17 Test Method B" was performed on 102 x 152 mm EFP panels by bending them over a 3/8th inch diameter cylindrical mandrel. The procedure was modified because the test calls for bending fully painted panels over increasingly small diameter cylinders and visually inspecting for paint cracking. Pretreatment D is on the nanoscale coating, so cracking is not visible to naked eye. The smallest available cylinder diameter was used. Subsequent evaluations, including FE-SEM analysis, confocal microscopy, and humidity testing, were performed with the bent panels. Humidity testing at 100% RH and 100 °F for 24 hours resulted in no apparent increase in oxidation for the bent material (see Figure D1.3).

Confocal microscopy was performed to measure the surface roughness parameters on the control and bent panels. The bent panel is slightly rougher than the control panel. FE-SEM analysis of the bent and unbent panels revealed a moderate amount of cracking on the surface of the bent panel. No flaking or loss of adhesion were apparent.

EFP pretreated with Henkel Process D

EFP pretreated with Henkel Process D

EFP -As received (no pretreatment)

Figure D1.3: Bend test panels after 24-hour humidity exposure (Source: Henkel)

D1.2.9 Pretreating and Distributing EFP

In February and March of 2019, approximately 200 panels of EFP material, in varying dimensions, pretreated with Process D, were distributed to other project team members. See Table D1.3.

Table D1.3. Distribution of Process D pretreated EFP panels.

Team Member	Date	Quantity	Panel Dimensions
Fuchs	February 28, 2019	10	203 mm x 305 mm
Quaker	March 1	10	203 mm x 305 mm
PPG	February 14	100	102 mm x 152 mm
AET	February 14	80	203 mm x 305 mm

Additionally, in March 2019, 10 pieces of 120 x 120 mm sheets of EFP material pretreated with Process D were shipped to support Erichsen Cup Draw testing. In July 2019, 470 x 470 mm EFP panels pretreated with process D were shipped to EWI, Fuchs, and Quaker to support cross-form testing.

D1.2.10 Application to Mini-Doors

Task 3 organizations collaborated in producing a "mini door" that has coil pretreatment (Henkel), forming lubrication (Quaker or Fuchs), welding (AET), pretreatment and paint (PPG). In November 2019, Henkel deoxidized and applied pretreatment D to EFP panel sections of the "mini-door" to be distributed to the appropriate lubricant supplier. Table D1.4 shows the size and quantity of material prepared.

Table D1.4: Mini-door coupons distribution for lubricant application.

Lubricant	# of Mini Doors Coupons	
	4" x 12"	3.25" x 3.125"
Quaker	4	4
Fuchs	4	4

Henkel deoxidized and applied Process D pretreatment to approximately 100 pieces of 8" x 12" EFP panels and shipped them to Task 3 members for subsequent lubricant application and/or testing.

D1.2.11 Humidity Test

In December 2019, EFP samples with Henkel pretreatment D were tested side-by-side with EFP samples having Xtalic Zn, and electrogalvanized steel panels as controls, in a modified version of ASTM D 2247 "Standard Practice for Testing Water Resistance of Coatings in 100 % Relative Humidity". The testing was performed in Henkel's 100 % RH chamber at 100°F for periods of 24, 48 and 72 hours. The samples were tested in triplicate, with untreated cut edges. The coupons were visually evaluated and photographed. GD OES surface analysis was performed to measure surface oxidation.

After 24 hours of 100 % humidity exposure, EFP panels with Henkel pretreatment D show a slight change in luster and color change (Figure D1.4) where spotty areas of darker color are apparent. GD OES analysis showed an oxide layer of approximately 400 nm. Xtalic Zn-coated magnesium appears darker in color with white areas that are rough in texture. GD OES analysis in the light grey area of the panel shows very little oxidation, where the dark grey area has nearly 1000 nm of oxidation. Electrogalvanized steel panels are visibly darker in color, and GD OES shows an oxidation depth of about 1000 nm.
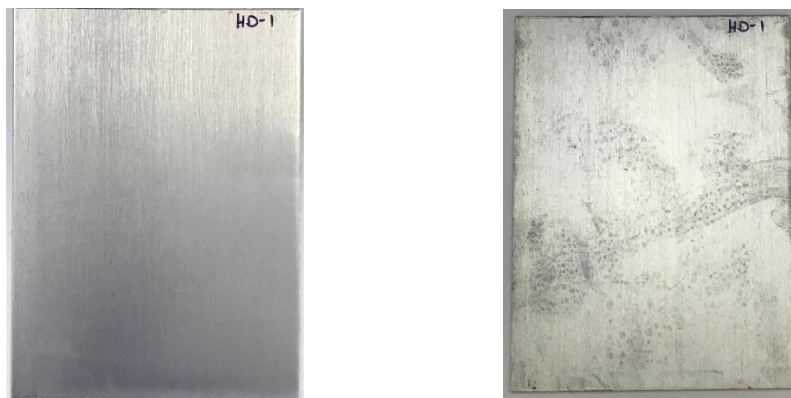

Figure D1.4: EFP panels with Process D coil pretreatment. (left) Before humidity exposure. (right) After 24 h humidity exposure. (Source: Henkel)

After 72 hours of humidity exposure, appearance of EFP panels with Henkel pretreatment D changes considerably, and GD OES surface analysis supports this observation, showing oxidation increase to approximately 1800 nm. Xtalic zinc-coated panels have a speckled appearance including areas that are very dark and spots of white. Galvanized steel panels appear dark in color and have a similar level of oxidation as after 24 hours. This evidence suggests EFP magnesium with either Xtalic zinc coating or Henkel pretreatment D falls short in providing corrosion protection of galvanized steel. Both Henkel Process D and Xtalic zinc coating had changes in surface texture that may be difficult to correct, creating challenges for use in the Class A areas of an automobile. In conclusion, both Henkel pretreatment D and Xtalic zinc treatment provide short-term protection, but it is limited.

D1.3 CONCLUSIONS AND RECOMMENDATIONS

1. The heavily oxidized ZEK100 magnesium alloy was successfully deoxidized and pretreated using Henkel products. Further characterization and testing of this material were suspended when EFP magnesium alloy was made available. The optimized Henkel pretreatment Process C was tested.

2. Persistence of surface defects noticeable after application of pretreatment Process C led to a modification in the cleaning stages to remove organic deposits. An updated Process D was tested.

3. Variability in lap shear results and inconsistent welding results over pretreated EFP, as observed by AET, may indicate variability in surface conditions and indicate a need for further investigation and possibly optimization of pretreatment application.

4. Henkel coil pretreatment Process D includes deoxidizing and cleaning products that effectively remove magnesium oxides/hydroxide followed by pretreatment that increases corrosion resistance in 100% humidity testing and salt fog testing.

5. Coil pretreatment should be applied immediately after the Mg alloy sheet is produced to avoid conditions where excessive oxidation may occur.

D2. Coil Pretreatment with Aluminum and Zinc Coatings
(Xtalic Corporation – Principal Investigator: R. Hilty)

D2.1 SUMMARY

The overarching goal of the coatings task of this project was to provide a corrosion protective surface which is amenable to upstream and downstream processing of magnesium sheet in automotive applications. Xtalic succeeded in developing a zinc plating capability for large scale sheet samples which shows good performance in welding, lubrication, paint-type electrocoating, forming and handling.

Xtalic has advanced the state of the art in nanostructured aluminum plating from ionic liquids. The plating process has been scaled to larger sheet sizes, 5 x 10 cm, and demonstrated to be able to go larger. Al-Mn and Al-Zr alloys were plated and shown to be hard and strong. In some cases, higher alloy dosages led to amorphous content which can produce brittle behavior in forming test simulations. Al-Mn and Al-Zr coated sheets show strong corrosion performance in ASTM B117 salt spray conditions, exceeding 336 hours in duration. With the additional application of paint-shop style electrocoating, the aluminum coatings endure more than 1200 hours of salt spray without corrosion. Xtalic further developed methods to reduce the cost of the aluminum plating technology through qualification of lower cost anode materials, longer plating bath life and a lower cost bulk supplier of the electrolyte chemistry.

During the course of the project, the objectives shifted towards a lower cost option. Xtalic developed a zincation/zinc plating process for magnesium sheet as a way to provide activation prior to aluminum plating. The zincation coating was top coated with an electroplated zinc layer in order to boost the thickness and enhance performance. The zinc-only corrosion performance is adequate to meet the needs of surviving handling and transportation between the Mg sheet coil producer and the forming shop. Further, welding tests on the zinc-only coating showed strong performance. As a result of this strong performance and the potential for lower cost, the USAMP management team redirected the project effort towards a zinc-only solution.

The zinc-only option required development and qualification of a corrosion performance specification. In collaboration with Henkel, Xtalic has qualified a heat/humidity test method used to ensure quality of the coated sheet stock. Xtalic scaled the zinc plating option to larger scale using the capabilities of an existing pilot plating line. Sheet samples as large as 19 x 26 inches could be plated on the line with good quality. The process can be scaled to roll to roll plating operation if needed.

Xtalic coated samples for downstream task members. Zinc coated Mg sheet samples were produced at Xtalic and sent to AET for welding studies, PPG for electrocoating studies, Henkel for corrosion testing, and Fuchs and Quaker for lubricant application and testing. Xtalic also produced mini-door samples using the zinc process and 13 panels of 19 x 19 inch cross-form test panels for formability testing.

The technology developed here has advanced the state of the art in corrosion protection of magnesium sheet stock. This technology is ready for commercialization in rack plated parts and could easily be adapted to roll to roll plating. Samples produced for downstream testing consistently showed good responses, including welding, corrosion testing, lubricant application, forming, and paint-shop pretreatment. The zinc coated sheet showed the best option for lower temperature forming of Mg sheet. A zinc-based coating solution provides good performance with a small thickness applied and would be a good choice for commercial applications. Detailed discussion of this work may be found at https://data.lightmat.org/project/.

D2.2 ACCOMPLISHMENTS AND RESULTS

D2.2.1 Key Objectives

The project deliverables and plan for performance addressed four main objectives:

1. Performance specification: Work with USAMP members to finalize the desired performance specification for the corrosion coating.

2. Prototype plating development: Develop prototype plated parts which show good adhesion and meet initial performance standards in screening tests.

3. Plating cost improvement: Evaluate options to further reduce cost of plating using ionic liquids, in particular, exploring options to control or reduce water contamination susceptibility.

4. Prototype part sampling and testing: Manufacture prototype parts to prove feasibility of the manufacturing system and the performance of the coated magnesium sheet. Provide plated sheet test coupons to other project team members throughout the project to aid others in developing lubricants, formability, and post-forming corrosion treatments.

D2.2.2 Background and Approach
The primary objective of this sub-task was to produce a coating method that will provide substantial improvement in corrosion resistance for Mg sheet in coil applications. Baseline testing of the Mg alloys showed that the performance in the uncoated state is poor. Samples of ZEK100 and AZ31B were exposed to ASTM B117 salt fog for 48 hours and the parts corroded significantly even without the added driver of a galvanic couple. Figure D2.1 shows the extensive corrosion on the ZEK100 sample after just 48 hours of salt spray exposure. Figure D2.2 shows a similar response from Mg alloy AZ31B.
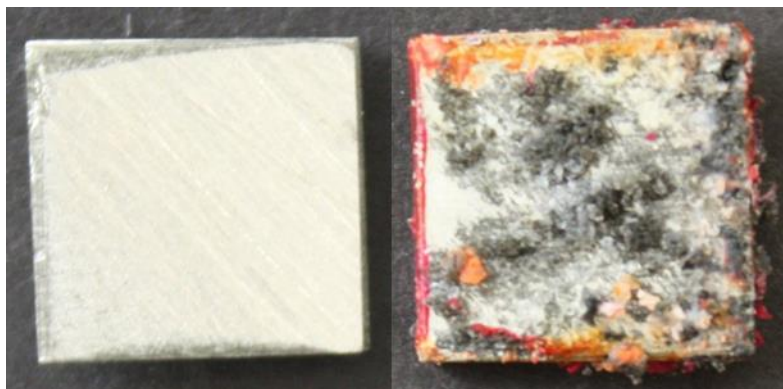

Figure D2.1: ZEK100 Mg sheet samples, 50 x 50 mm. (left) As-received sample and (right) after 48 hours exposure to ASTM B117 salt fog. (Source: Xtalic)

D2.2.3 Performance Specification
As magnesium sheet use is rather new to the automotive industry, there are no existing performance criteria against which the performance of the coating could be measured. A summary of the performance specifications Xtalic defined for magnesium sheet use is shown in Table D2.1. The first five lines represent the rapid test methods available to assess performance at Xtalic. The G85 test method and 40ºC/100% RH methods were executed at outside labs.

Figure D2.2: AZ31B samples, 15 x 50 mm. (left) As-received and (right) after 48 hours of ASTM B117 salt fog. (Source: Xtalic)

Table D2.1: Performance specification for the coating.

Test	Test Method/Duration	Pass/Fail Criteria
Adhesion	Cross-hatch scratch and tape	No peeling or delamination
Adhesion	Bend to break	No peeling or delamination
Appearance	Visual exam	Smooth and uniform
Thickness	Cross-section	Dependent on corrosion performance
Corrosion-Salt	ASTM B117 Salt fog, 1000 hrs.	Rejected-too severe
Corrosion-Acidified Salt	ASTM G85, Annex 2, 30 weeks	Rejected-too severe
Corrosion-Heat/Humidity	40ºC, 100%RH, up to 48 hours	No porosity corrosion of base metal; minor discoloration is acceptable due to surface oxidation

Xtalic collaborated with Henkel to finalize a corrosion aging test. This test is a heat/humidity test (40ºC/100%RH) where parts are exposed up to 48 hours and inspected for evidence of corrosion. This test aligns well with the type of test used for galvanized steel typically used in automotive applications.

### D2.2.4. Prototype Plating Development
The objective of this sub-task was to develop prototype plated parts which show good adhesion and meet initial performance standards in screening tests. The original goal of the project was to use a coating based on plated aluminum, specifically electroplating aluminum from ionic liquid electrolytes. This processing method provides flexibility to produce Al rich alloys with improved properties. Corrosion is a key performance metric requiring an alloy optimized for corrosion potential. In this case, the aluminum may be alloyed with Mn, Zr or Cr. The alloying element can be added in various ranges, but generally from 3 to 11 atomic percent. While other alloying additions are possible, these three are the most appropriate for corrosion control. However, in no case is the alloy expected to be anodically protective of the Mg substrate.

D2.2.5 Activation Development
Mg sheet is a highly reactive sheet material. The native oxide layers on the surface must be removed before plating in order to ensure a metal-to-metal interface and adequate adhesion between the layers. Xtalic researched a method to directly activate the Mg substrates in ionic liquid. In the case of aluminum alloys, the native oxide can be removed *in situ* by applying a negative potential (i.e., make the Al the anode) while in the plating bath. This strips the oxide from the surface leaving nascent metal. The polarity is then reversed, and the surface is plated with adherent metal. Despite various attempts, the surface of the Mg alloys would not homogeneously activate using this procedure.

Xtalic tested an alternate approach to replace the native oxide with some other reaction product which can be more easily removed in the plating bath. Ammonium fluoride was found to react with magnesium

oxide to form MgF_2 but this could not be easily removed in plating. An alternate approach may be to create an acetate layer on the surface of the Mg according to the reaction:

$$MgO + 2CH_3COOH \rightarrow Mg(CH_3COO)_2 + H_2O$$
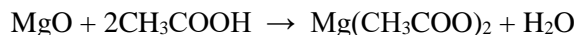
The acetate layer can dissolve in the ionic liquid, revealing a pure metal surface for plating. Xtalic was successful in producing the acetate layer and the reaction could occur outside of the glovebox environment. However, the Mg metal is reacting with the ionic liquid and producing a black layer which reduces adhesion.

Replacing the oxide layer with a layer of zinc will eliminate the Mg reactivity issue. Xtalic started from a traditional zincation formulation, then modified it to control the reaction kinetics. During immersion conversion to Al (in IL) or to Zn (in aqueous solution) it is important to avoid creating islands of Al or Zn in contact with exposed Mg. This leads to strong galvanic corrosion and prevents the formation of continuous coating. There are two steps to the process, activation and zincation. The activation and zincation use a proprietary fluoride-based process. This process produced a uniform zinc layer on top of the Mg, as shown in Figure D2.3.
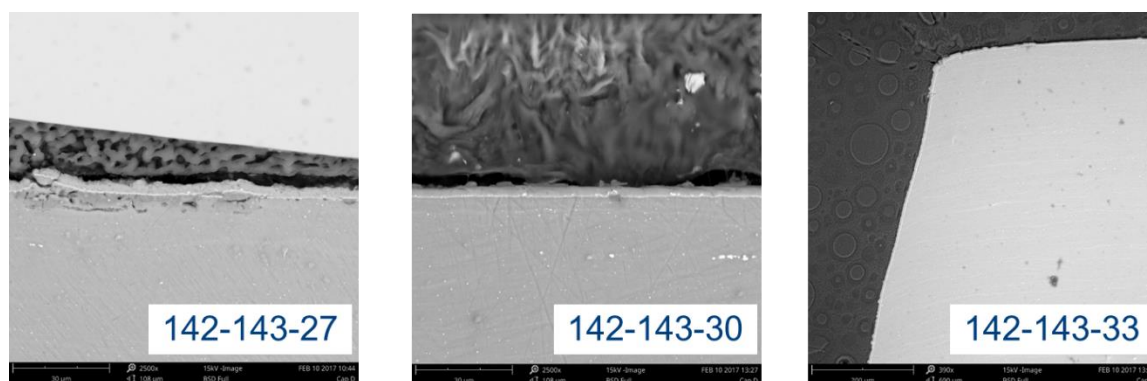

Figure D2.3: Zincation layers on Mg. The zinc layer shows good adhesion and coverage. (Source: Xtalic)

Nano-Al Coating Development
The zincated layers can subsequently be coated with nano-Al layers to the desired thickness.
This same zincation approach was then applied to an alternate alloy, AZ31B. This alloy did not respond well to the original zincation process. An adjustment to the formulation allowed for uniform zincation coverage with subsequent Al plating. A double zincation process, where the first zincation is acid etched then reformed as a secondary process, was effective in improving the coverage across the sample.

The process was further extended to WE43 Mg alloy but was unsuccessful. To date, modifications to the process have been unable to produce viable results. Further work will be required to activate this alloy, but efforts were halted as the alloy was deemed out of scope for the project. The zincation layer is generally very thin, less than 1 μm. Zinc plating layers can be thicker (a few microns). Zincated parts were subsequently coated with a nano-aluminum alloy (Al-5at.%Zr) which provides desired color and corrosion resistance. Xtalic pulse plated 15 to 30 μm of alloy onto the zincated Mg then exposed the parts to ASTM B117 salt spray for various periods.

Zincated Al-Zr plated samples of ZEK100 were salt spray tested and examined after 24 hours and showed some darkening of the Al alloy coating, as shown in Figure D2.4. Continued exposure to 96 hours produced a similar result. Extending further to 120 hours, the evidence of corrosion was unmistakable, as shown in Figure D2.4. Once the coating has been breached the galvanic couple between the Al and Mg

alloys drives rampant corrosion. It is clear from this set of experiments that the coating is adherent but needs to be thicker and must not pit, which would lead to rapid failure.
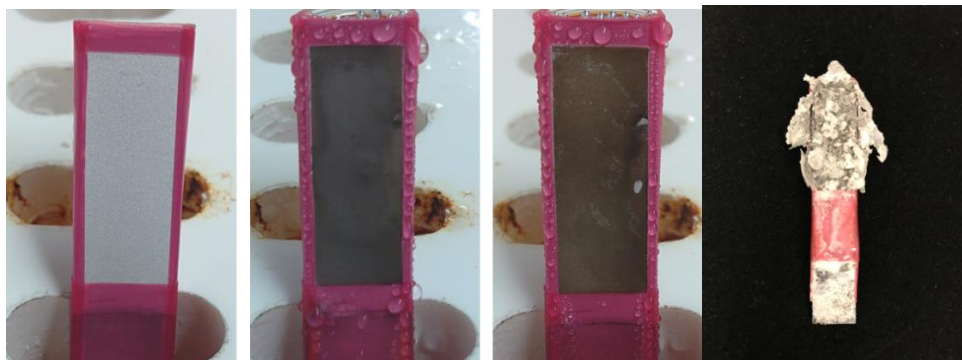

Figure D2.4: ZEK100 plated with ~15µm of Al-Zr, masked with tape (purple) and exposed to ASTM B117: (a) as plated, (b) 24 hours, (c) 96 hours, (d) 120 hours of salt spray exposure. (Source: Xtalic)

EFP Batch #1 samples were plated and shown to be much higher quality than previous substrates, with better coating and overall performance. Figure D2.5 shows the samples of EFP with 3 samples coated with Al-Mn and subjected to 360 hours of salt spray. Through 360 hours there was no evidence of pitting corrosion. Samples of EFP size 1 x 5 cm were coated with zincation, zinc plating followed by 30 µm of nano-Al alloys were sent to PPG for coating. PPG applied some initial tests of a proprietary pretreatment and electrocoat treatments to the samples. E-coated samples were exposed to ASTM B117 salt spray with check-ins every 100 hours.
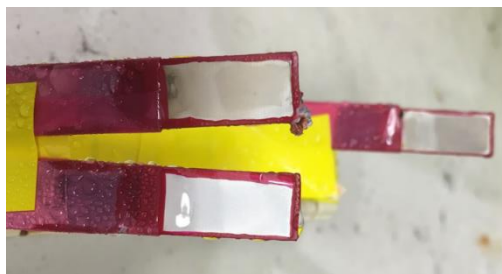

Figure D2.5: Al-Mn coating on EFP material after 360 hours of salt spray testing. (Source: Xtalic)

Table D2.2: Sample testing of PPG coatings applied to nano-Al on EFP substrates

Sample	Plans
1. PPG Chem Clean	Section to look for Al loss during cleaning
2. PPG Pt1 pretreat	Section to look for Al loss during cleaning
3. PPG Pt1 pretreat + e-coat	B117 salt spray
4. PPG Pt2 pretreat	Section to look for Al loss during cleaning
5. PPG Pt2 pretreat + e-coat	B117 salt spray

Samples 3 and 5 (PPG over nano-Al over Zn over EFP) showed no evidence of corrosion at all checkpoints during testing (168, 366, 500, 800, 1000, 1500, 2000 hours). This is very encouraging for potential final finish applications requiring strong corrosion control. Xtalic scaled the sample size for nano-Al plating for larger samples. Xtalic plated 22 samples with the stack of Zn/Zn/Al-Mn over EFP. These parts show good appearance with generally smooth deposit across the part. 25 samples of nano-Al over Zn over EFP were delivered to AET for welding studies. The nano-Al on these samples was nominally 30 µm thick.

A forming tool was designed and built as shown in Figure D2.6, using a sphere which forms a dome into the sheet. Uncoated EFP material was used to qualify the tool. Formability testing on Al-Mn and Al-Zr coatings showed that the bare EFP material or EFP with Zn-only coating showed better formability. The nanostructured Al coatings are hard and strong but can lead to cracking of the surface under extreme formability testing. Therefore, nanostructured Al alloys were abandoned from the development effort due to the cracking challenges (which were surmountable), but also due to the higher cost impact on Mg alloy.
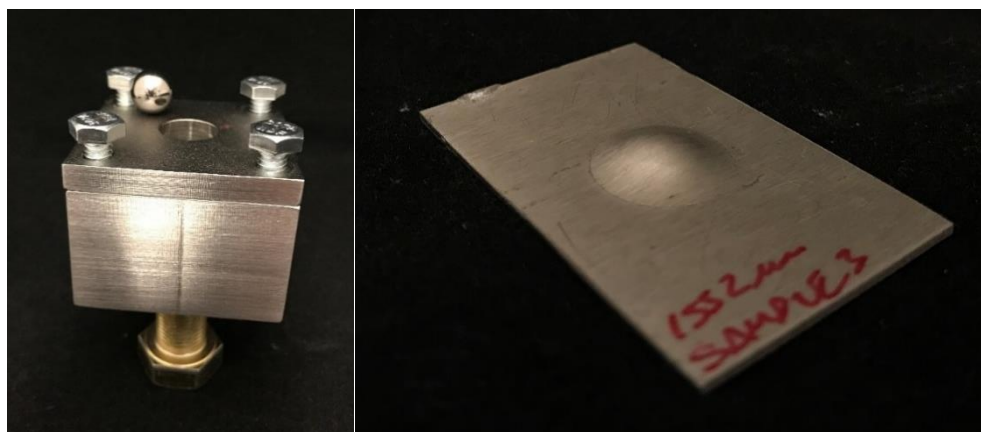

Figure D2.6: Formability tester with a 12 mm sphere (left) and a proof-of-concept test on EFP. (Source: Xtalic)

Zn-Only Coating Development
At the request of the USAMP project team, the development forward on this project focused on scaling up the aqueous based Zn plating process for further testing by downstream users of the project. Xtalic scaled the zinc plating onto a pilot production line, which includes larger tank sizes. Each of the plating baths and cleaning tanks were cleaned and made up with fresh chemistry. The zinc plating tank can accommodate a 19 x 26 inch panel. After initial testing on 7 x 26 inch sheets of EFP Batch #3 with success, Xtalic plated several sheets in the full 19 x 26 inch size to verify the thickness and quality of the plated part. Thickness was measured by optical and electron microscopy on cross-sections taken from various points on the large sheet. Plating quality was confirmed using visual inspection, tape test for adhesion, and 24-hour exposure to 40ºC/90% RH. The color is generally uniform and there can be some slight thickness build on the very edge of the sample. In a production setting, the roll-to-roll sheet can be shielded to make the coating completely uniform across the sheet.

D2.2.6. Plating Cost Improvement
The objective of this sub-task was to evaluate options to further reduce the cost of plating using ionic liquids-in particular exploring options to control or reduce water contamination susceptibility.

Ionic Liquid Cost
A significant concern for the cost of the plating solution is the fundamental cost of the ionic liquid electrolyte. While the electrolyte is not directly consumed in the plating process, some losses occur either through drag-out after plating or bath loss due to manufacturing error or bath breakdown. Xtalic identified and qualified an alternate source for the EMIM:Cl ionic liquid which can manufacture in significantly larger batch quantities. This provides two potential benefits: 1) scale up potential for larger quantity manufacturing and 2) cost reductions due to economy of scale for making the ionic liquid. Quality control analysis of the incoming EMIM:Cl determined that it will need to be purified before use due to low level metallic contamination. Most non-Al metals in the ionic liquid can be removed through dummy plating, a process where low current plating is used to preferentially deposit more readily reducible metal species. The contamination of Fe, Zn and Ga could be problematic to plating. Fe is the

slowest to be removed from the bath while Ga and Zn are generally eliminated after the first dummy treating process. Parts plated under known and repeated conditions as the dummy plating progressed showed that the color of the samples changed as the bath became purer. The color can be quantified using the L* a* b* color map system where L represents the brightness of the deposit.

Raw Material Cost
A potential cost driver for the plating process is the cost of raw materials required to build the plated layers. The plating process uses an aluminum based ionic liquid and a consumable aluminum anode. During the plating process, the oxidation/reduction process leads to dissolution of the aluminum anode material, which replenishes the aluminum concentration in the ionic liquid. 4N aluminum (99.99% pure Al) or better is typically the anode material but substantially increases the cost of the metals. For low-cost commercial purity anodes, Xtalic acquired samples of AA1350. This is specified at 99.5% Al and is a low-cost material but can have impurities of Fe and Cu. The 1350 alloy has been fabricated into an anode and qualified as an anode material.

Plating Bath Life
A significant element which drives cost of ionic liquid plating is the plating bath life. Over time, the plating bath can begin to perform poorly due to contamination, buildup of contaminants or breakdown products. In traditional aqueous electrolytes, the most common cause of poor performance is the introduction or breakdown of organic products in the bath. These can be removed through carbon treatment. This approach is not possible in ionic liquids because the ionic liquid itself is organic. Bath life is measured in units of amp-hours/liter. Good performance would be 5000 amp-hours/liter or more. Xtalic also researched that stability of ionic liquid in an environment which includes oxygen but remains controlled for water. While water is known to react with ionic liquid, air stability is unknown and operating in an air environment (such as a Li-ion style dry room) would significantly reduce cost and ease the commercialization pathway. Xtalic created a test where a quantity of new plating bath was built then split into aliquots for storage in an air environment that is free of moisture. FTIR and visual examinations suggest changes to the ionic liquid. Cyclic voltammetry testing of 4 aliquots shows a small shift in the deposition potential of the Al as the bath ages.

D2.2.7 Prototype Part Sampling and Testing
The objective was to manufacture prototype parts to prove feasibility of the manufacturing system and the performance of the coated magnesium sheet. Xtalic provided plated sheet test coupons to other project team members for evaluations.

At the early stages of the project, Xtalic focused on providing a nanostructured aluminum solution for coating on magnesium sheet. Xtalic provided samples of aluminum alloys over zinc over Mg sheet up to 50 x 100 mm in size to AET, PPG and Henkel. Once the project focus shifted to a coating solution focused on zinc, all sampling efforts also shifted to zinc coatings only.

Holes were drilled into the sheets to facilitate electrode connection during plating. (In a production environment, a contact roller would be used to make electrical contact and as such, no holes would be needed.) The 13 sheet samples were delivered to Fuchs, Quaker and EWI as requested. Full size sheets, 19x26 inches, were plated with Zn, and samples were provided to other project team members as follows:
- AET: 100 pieces of 150 x 150 mm (6 x 6 inch) plus 10 pieces 305 x 432 mm, for welding studies;
- Fuchs: equivalent of 1000 pieces of 75 x 30 mm samples, plus four mini-door panels;
- Quaker: equivalent of 1000 pieces of 75 x 30 mm samples, plus four mini door panels; and
- Henkel: 6 Zn coated samples, nominally 4 x 6 inches, for heat/humidity testing.

D2.3 CONCLUSIONS

1. In partnership with Henkel, Xtalic chose a 40ºC/100%RH test method to evaluate the corrosion that might be expected between manufacture of the Mg sheet coil stock and stamping/forming of the automotive component.

2. Xtalic developed an entirely new, proprietary pretreatment and zincation plating process for magnesium sheet. The process has proven to be well suited for EFP alloy, producing a coating of a few microns thick zinc layer that is well adhered and meets corrosion requirements.

3. Xtalic also further developed and demonstrated the capability to coat magnesium sheet with nanostructured Al alloys, specifically Al-Mn and Al-Zr alloys. These nanostructured alloys survive ASTM B117 salt spray testing in excess of 336 hours as bare aluminum alloys over magnesium.

4. The corrosion performance of a coated magnesium sheet is highly dependent on the quality and integrity of the coating. Due to the high galvanic potential between magnesium and virtually all other metals, any damage or imperfections in the coating can lead to rapid corrosion of the substrate.

5. Significant reductions in the plating cost of nanostructured aluminum alloys on magnesium sheet may be achieved as follows:
    1. Use of a high-volume supplier of the electrolyte.
    2. Changes in the incoming raw material inspection criteria to account for difference in purity levels and a purification process.
    3. Full utilization of the life of the plating bath, as verified by FTIR scanning, L*a*b* colorimetry and SEM topographical studies of the plated surfaces.

6. Zinc-only coating is expected to be a relatively low-cost process for coil coating of magnesium sheet.

D3. Development of Forming Lubricants Having Water Base
(Fuchs – Principal Investigator: P. Bosler)

D3.1 SUMMARY

The goals of this sub-task were to develop water-base lubricants which would be attractive for use in warm-blank, cold-die stamping of magnesium parts at temperatures (a) up to 250°C and (b) up to 100°C. In addition to facilitating stamping of the part, lubricants should be easy to apply, not leave residue on parts or tooling, and be compatible with both upstream processes (such as coil pretreatments) and downstream processes (such as joining and painting). Fuchs' approach was to develop a dry film lubricant which would be applied to sheet blanks prior to heating for the 250°C stamping, and a wet lubricant which could be applied to the tooling for the 100°C stamping. The former was based on the Forge Ease AL 278 ("Fuchs 278") dry-film lubricant which performs well in forming of heated aluminum blanks, but may exhibit poor wetting, and, after heating, could carbonize on parts and become difficult to clean. The latter was a water-based synthetic that remains "oily" as a film even after the water content is evaporated. It was designed to perform best when wet.

Lubricant development was conducted using small strips of aluminum and magnesium alloys in sliding contact with steel in a heated laboratory tribology tester. Results included coefficient of friction (COF) as functions of sliding speed and temperature. Performance of new lubricants were compared with that of the benchmark Fuchs 278. Cleanability and weldability tests were conducted by other project team members.

After developing and evaluating 5 candidate lubricant developments, Fuchs testing revealed that two candidates were appropriate for the project:
- A modified version of Fuchs 278, called Renoform 1102 ALWF ("Fuchs 1102"). In this dry-film product, the company replaced a polymer with a synthetic ester to reduce charring and added a super wetter to improve sheeting.
- Renoform 2502 ALWF ("Fuchs 2502") – a water-based synthetic that remains "oily" as a film even after the water content is evaporated. It was designed to perform best when wet.

Fuchs 1102 lubricant performed well in 200°C tribology tests, Erichsen cup draw tests, and cross-form stamping trials. However, it fell short in the stamping trials of actual door panels, which experienced consistent splits. Use of the benchmark Fuchs 278 lubricant rather than Fuchs 1102 allowed for unsplit door panels to be stamped. Detailed discussion of this work may be found in Fuchs' final report at https://data.lightmat.org/project/.

D3.2 KEY ACCOMPLISHMENTS AND RESULTS

D3.2.1 Initial activities - Selecting Candidate Lubricants and Most Effective Tribology Tests
1. Selected Fuchs 278 (a water-based emulsion with dispersed additives) as an initial benchmark lubricant due to successful history with aluminum warm forming (AA5xxx and AA 6xxx), some history as wet *and* dry application, and various temperature ranges (100°C to 350°C). However, improvements were mandated due to characteristic buildup on tooling.

2. Developed two initial test formulas based on substantial screening of additives, discussions with raw material suppliers, and testing to determine ingredient compatibility, solubility and/or emulsifying characteristics. These are Renoform 10 ALWF ("RF10"), replaced organic material from Fuchs 278, (tight emulsion, contains boron nitride) and Renoform 25 ALWF ("RF25"), (inorganic material formula, solution, contains boric acid).

3. Reviewed several sets of tribology equipment for use in determining performance on low-ductility soft metals in a stamping environment. The following pieces were tested using both new candidate lubricants on aluminum alloy AA 6082: Strip Draw (SLT), Twist Compression (starvation testing), Falex Pin and V-Block, Cup Draw, and Anton Parr Rheometer (tribometer). Ultimately, the Anton Parr tribometer was determined to provide best initial tribology results. It provides coefficient of friction results for lubricants run in a wet and a dry condition at test temperatures up to 300°C.

4. Initial comparative testing of lubricants was done on the Rheometer using AA6082 because magnesium sheet was not yet available from the USAMP LCMS program. The lubricants were comparatively tested neat (undiluted) and diluted 4:1 (20%). Figure D3.1 depicts the basic concepts of the Anton Parr Rheometer and the two conditions (dry and wet).
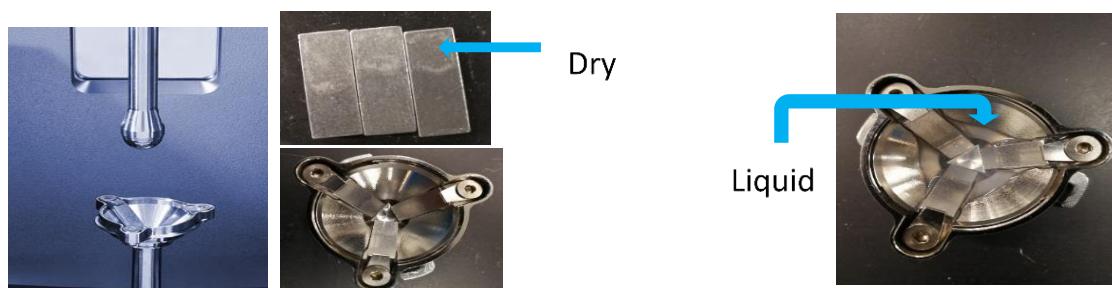

Figure D3.1: Photographs of Rheometer, including steel ball and sheet metal test strips. (Source: Fuchs)

Test results

Tribology testing indicates coefficient of friction rating as follows:
- When products were run neat and as a dry film heated to 200°C, lubricants performed in the following order best to worst: RF10> RF25> 278
- When products were run diluted 4:1 as a dry film and heated to 200°C, products performed in the following order best to worst: RF10> 278 > RF25.
- When comparing the neat lubricant to 4:1 diluted lubricant in a dry condition and heated to 200°C the products performed in the following manner best to worst: All 3 lubricants performed better diluted with water than run neat
- When products were run neat, wet and at ambient temperature, they performed in the following manner best to worst: RF10> RF25>278. (Increased COF for all lubricants compared to respective dry film runs)

Neat lubricants – dry-film, heated to 200 C

4:1 dilutions dry-film, heated to 200 C

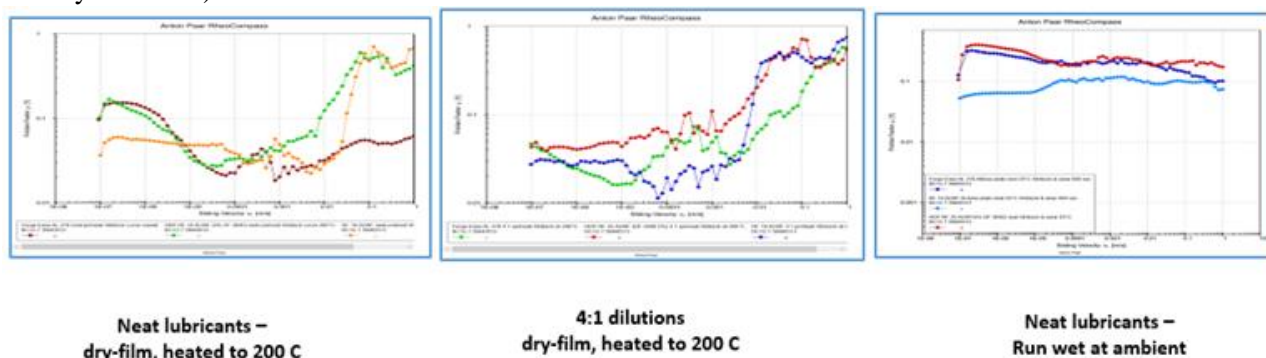Neat lubricants – Run wet at ambient

Figure D3.2: Plots of COF as functions of sliding velocity in rheometer. (Source: Fuchs)

Fuchs then undertook the following actions to improve the lubricant candidates for this project:
- Eliminate boron nitride as an ingredient
- Improve wetting characteristics
- Reduce carbonization at high temperatures
- Resulting developed products: Fuchs1102 and Fuchs 2502

Tribology tests were run on the rheometer that compared the COF results against the benchmark, Fuchs 278, and three candidate lubricants at 200°C and ambient.
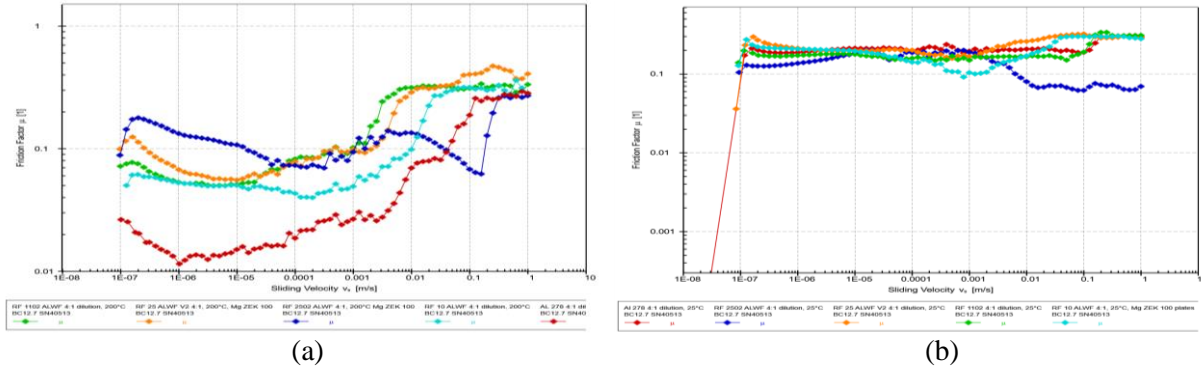

| (a) | (b) |

Figure D3.3: Plot of COF as function of sliding velocity for five lubricants diluted to 20%. (a) 200°C, dry films. (b) 25°C (ambient), wet. (Source: Fuchs)

The COF was lower at 200°C for all lubricants. It should be noted that at this temperature, all lubricants but Fuchs 2502 turned into a dry film. At ambient, all lubricants were run in a wet state. From these results, Fuchs1102 and Fuchs 2502 were determined as best candidate lubricants for the USAMP project:
- Fuchs 1102 exhibited features like the benchmark lubricant, Fuchs 278, it performed well as a dry film. Unfortunately, it did not perform well in a wet state.
- Fuchs 2502 performed well in a wet state. In case application to dies rather than to blanks became a preferred method, Fuchs 2502 was also selected for further study.

D3.2.2 Lubricant Testing on Magnesium
The following approach was used:
1. POSCO EFP blanks were cut to size to fit the Anton Par rheometer.
2. Three lubricants (278, 1102, 2502) were tested at 4:1 (20%) dilution.
3. Panel sets were coated with each respective lubricant and allowed to dry.
4. Of the dry coated panels, one half was run at 100°C and the other half was run at 200°C.
5. The results were compared for these tests and also with to previous results from Mg ZEK100.
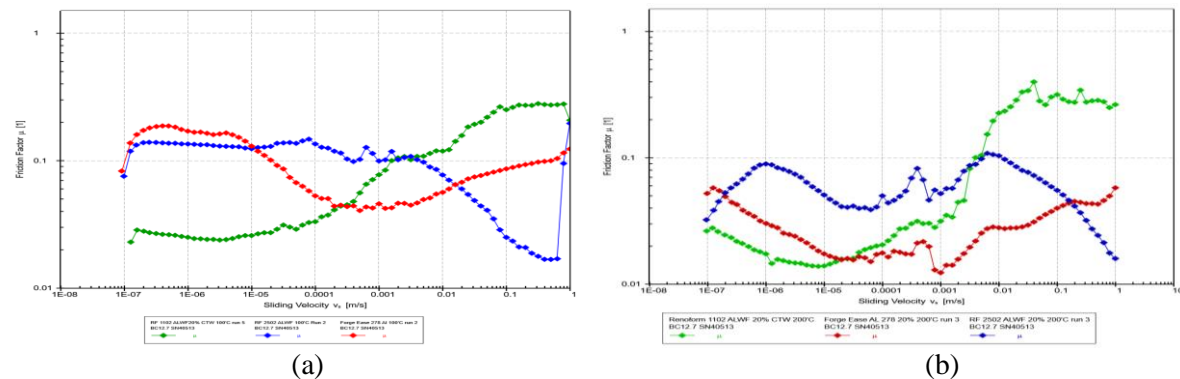

| (a) | (b) |

Figure D3.4: Lubricant results on POSCO EFP run at (a) 100°C and (b) 200°C. Red♦ 278. Green♦ 1102. Blue 2502. (Source: Fuchs)

Test Results
1. All lubricants exhibited a lower coefficient of friction (COF) when run at 200°C
2. The consistency of COF of each lubricant exhibited differences at the two temperatures.
   - At 200°C, the COF of 278 and 1102 climbed significantly with time and increasing velocity.
   - At both 100°C and 200°C, the COF of 2502 remained relatively consistent and even improved as time and velocity increased.

The tribology results with POSCO EFP were compared to previous results using Mg ZEK100, as described below.

D3.2.3 Comparing ZEK100 and EFP Performance
Two magnesium alloys were proposed by the project group: POSCO EFP and ZEK100. Fuchs evaluated its lubricant formulations on both materials at heated conditions.
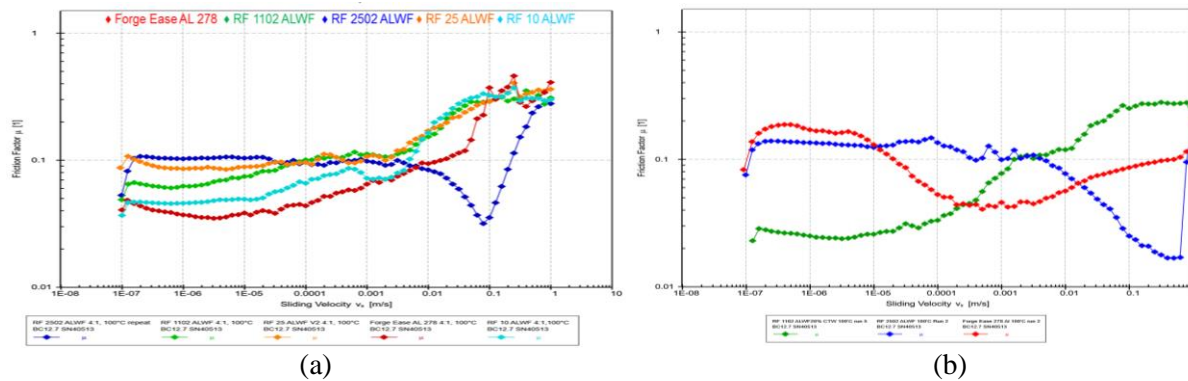

(a)   (b)

Figure D3.5: Lubricant results on (a) ZEK100 and (b) EFP sheets at 100°C. Red♦ 278. Green♦ 1102. Blue 2502. Light blue RF10. Orange RF25. (Source: Fuchs)
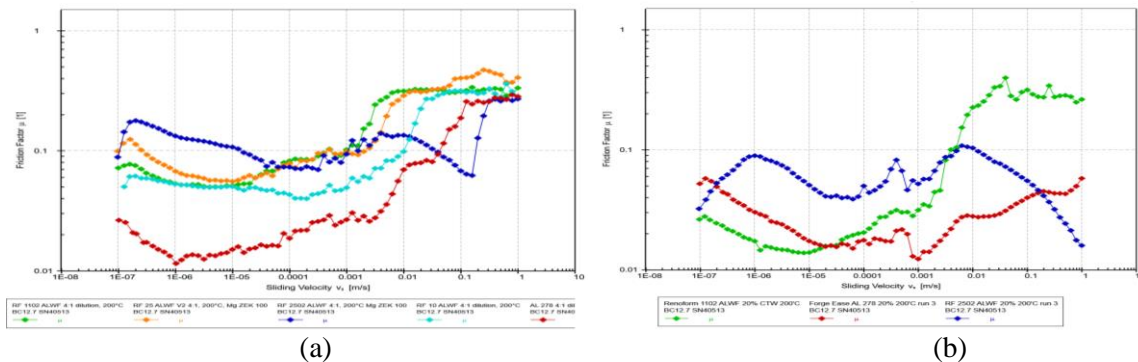

(a)   (b)

Figure D3.6: Lubricant results on (a) ZEK100 and (b) EFP sheets at 200°C. Red♦ 278. Green♦ 1102. Blue 2502. Light blue RF10. Orange RF25. (Source: Fuchs)

Test Results
1. Worst to best performance of each lubricant was similar with each magnesium alloy.
   - RF 2502 ALWF -> FE AL 278 -> RF 1102 ALWF
2. The general performance (based upon lowest COF) was noticeably better with POSCO EFP than with ZEK100.
   - Oxidation of EFP was significantly less than ZEK100 and may have contributed to improved formability.
3. The consistent test results with both magnesium alloys help validate the lubricant choices.

D3.2.4 Comparing Lubricant Performance on POSCO EFP with and without Pretreatment

The lubricity performance on POSCO EFP without Henkel's pretreatment was compared to its performance on this material with the pretreatment. At both, 100°C and 200°C, no difference in performance was exhibited.
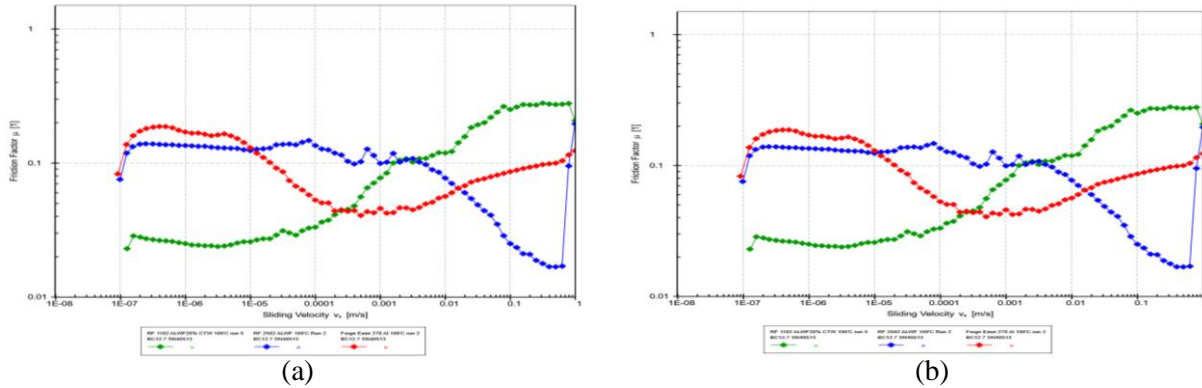

(a)   (b)

Figure D3.7: Lubricant results at 100°C on EFP sheet (a) without pretreat and (b) with Henkel pretreat. Red♦ 278. Green♦ 1102. Blue 2502. (Source: Fuchs)

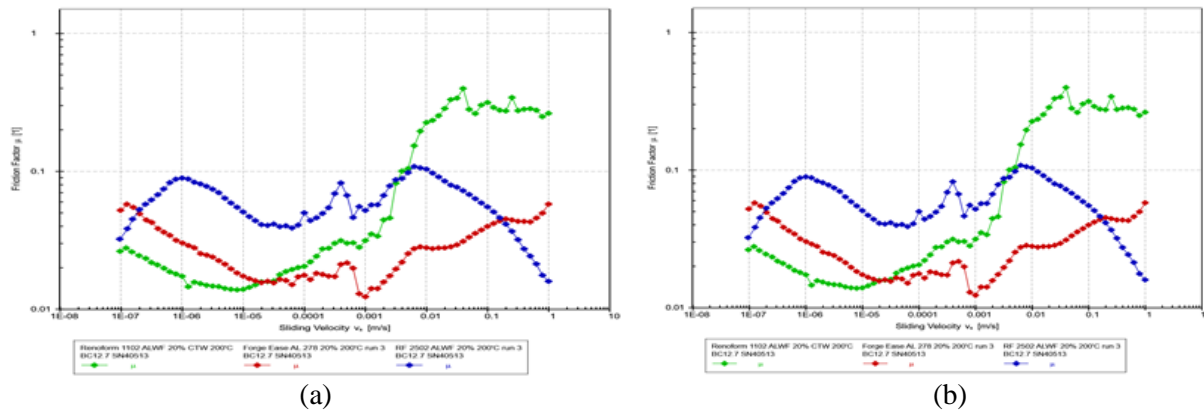(a)   (b)

Figure D3.8: Lubricant results at 200°C on EFP sheet (a) without pretreat and (b) with Henkel pretreat. Red♦ 278. Green♦ 1102. Blue 2502. (Source: Fuchs)

Test Results

The Henkel pretreatment appears to have no effect on lubricant performance.
- At 100°C, Renoform 2502 ALWF provides the lowest coefficient of friction.
- At 200°C, Forge Ease AL 278 provides the lowest coefficient of friction. At this temperature, Renoform 2502 ALWF provides slightly less lubricity.

D3.2.5 Warm Cup Draw Testing and Cross-Form Stamping at EWI

Fuchs coated blanks of EFP, both with and without coil pretreatments, with Fuchs 1102 lubricant, allowed them to dry, then sent to EWI for cup drawing and cross-form stamping trials. The purpose of these trials was to determine process windows (i.e., combinations of temperature and blank holding force which yield acceptable formed parts) and help down-select a lubricant for use in door panel stamping trials. Results of these trials are presented in section G1 of this report. They established 200°C as the preferred forming temperature and showed larger process windows for the Fuchs 1102 lubricant compared to the Quaker lubricant.

Test Results and Summary:
Fuchs' tribology testing demonstrated best results with Fuchs 1102 when run as a dry film. Subsequent cup draw testing and simulation production stamping at EWI appeared to corroborate these results. In comparison with a Quaker oil-based lubricant, the Fuchs lubricant appears to provide better formability.

D3.2.6 Door Outer Panel Stamping Demonstrations
In December 2020, Vehma's stamping partner Promatek, ran stamping tests on a door outer panel using EFP blanks coated with Fuchs 1102, and experienced splits near the draw beads. Promatek then applied the original benchmark lubricant, Forge Ease AL 278 diluted 3:1with alcohol to improve wetting, to blanks and experienced better stamping results. The part continued to exhibit splitting, but less.
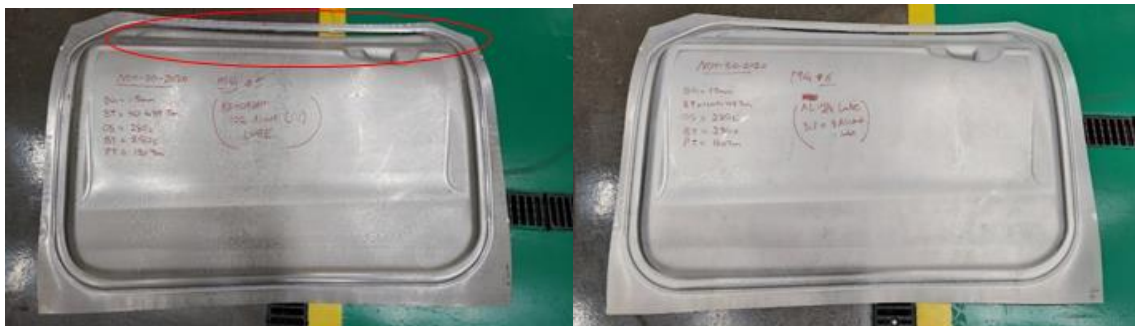

Figure D3.9: Door outer panels stamped using EFP alloy and (a) Fuchs 1102 lubricant diluted to 50% with water and (b) Fuchs 278 lubricant diluted to 25% with alcohol. (Sources: Fuchs and Vehma)

Promatek modified the die by lowering the draw beads to allow for easier metal flow. After the die modifications, the following lubricants were tested (Each respective lubricant was applied to blanks, allowed to dry, heated to ~ 250°C, then submitted to the stamping press):
- Fuchs 278 diluted 3:1 with alcohol
- Fuchs 278 diluted 2:1 with water
- Fuchs 1102 diluted 1:1 with water

Panels were successfully formed using blanks lubricated with Fuchs 278 diluted with water or alcohol. Blanks coated with Fuchs 1102 performed better (smaller splits) but did not form a split-free part.

D3.3 CONCLUSIONS AND RECOMMENDATIONS

1. Fuchs 278 dry-film lubricant applied to magnesium blanks facilitates the warm-blank (250°C), cold-die, stamping of complex automotive parts, such as door inner panels.

2. Fuchs 1102 was developed from Fuchs 278 to improve the wetting and reduce carbonization of the residue. It exhibited good performance in terms of coefficient of friction, compatibility with high temperature, cleanability, and other post process steps, but did not work as well as Fuchs 278 in stamping.

3. Fuchs 2502 wet lubricant exhibits good tribology test results even at ambient temperatures, and should be considered for application to the die in warm-blank, cold-die, stamping of Mg. Alternatively, it could be applied to a pre-heated blank as that blank is transferred into the die.

4. The formulation of Fuchs 278 should be modified to improve the wetting characteristics of the product, reduce the carbonized effect to the residue at elevated temperatures (which may necessitate additional cleaning processes), and reduce any potential build-up in dies. Initially, the use of Thermal Gravimetric Analysis would help to determine the depletion of ingredients at specific temperatures.

D4. Development of Forming Lubricants Having Oil Base
(Quaker Houghton – Principal Investigator: D. Hellen)

D4.1 SUMMARY

Quaker Houghton was tasked with developing effective, low-cost lubricants for forming magnesium alloys at forming temperatures under 100°C, and also up to 250°C. The lubricants developed must be compatible with various magnesium alloy sheets, and with downstream automotive body shop and paint shop processes. The development strategy focused on screening commercially available formulae for performance, then modifying to improve. Candidate formulae were subjected to a series of tests designed to stress the lubricant, including lubricity, lubricant thermal stability, metal reactivity, corrosion resistance in humid environments, cleanability, and weldability. Lubricant evaluation was conducted on Mg sheet substrates of: ZEK100, EFP, and EFP with Henkel pretreatments C and D.

This work resulted in a neat lubricant, QUAKERDRAW 450 MAG ("Quaker 450"), which meets the project scope. The lubricant provides a reduction in the coefficient of friction of tool steel on magnesium alloys at elevated temperatures comparable to standard automotive cold forming lubricant coefficient of friction levels. Quaker 450 is stable and compatible with the magnesium alloys utilized in this project and the pretreatments developed during the project by task participants. The developed lubricant was found to be cleanable from the magnesium alloys used during the project in a representative automotive cleaning process, and compatible with a representative automotive paint system. Additionally, the lubricant offers corrosion protection between forming and paint processes and can be welded through with standard automotive weld schedules.

Quaker 450 was shown to enable warm drawing of EFP magnesium 50 mm diameter cups at temperatures as low as 180°C, and stamping of 470 mm square cross-forms down to 200°C. A matrix of coefficient of friction tests were completed to support forming modeling project work. A design of experiment formability evaluation trial was explored during the project to support further improvement of the developed lubricant. Detailed discussion of this work may be found at https://data.lightmat.org/project/.

Terms and Acronyms (specific to this section).

Initial Peak	The COF in a TCT test when the tool first gets up to test speed
RCP	Reciprocating Wear Test, a test for evaluating lubricant performance
TBD	Time to Breakdown, the time it takes for a lubricant to fail in the TCT test
TCT	Twist Compression Test, a test for evaluating lubricant performance
TCT Friction Factor	A factor computed from the TCT TBD, COF, and Initial COF

D4.2 KEY ACCOMPLISHMENTS AND RESULTS

D4.2.1 Technical Approach
Lubricant formulations were evaluated for thermal stability at 100°C and up to 315°C (changed to 250°C after Project Quarter 1, per USAMP directive). The most thermally stable products were further evaluated for metal reactivity, cleanability, corrosion resistance, and lubrication of USAMP-supplied ZEK100 magnesium alloy sheet by RCP and TCT. Additional formula modifications were generated of the best performing lubricant on ZEK100 under the conditions noted above. Formula 1 Modification 3 was selected as the best performing lubricant formulation for ZEK100 at 100°C and up to 250°C.

Once EFP sheets samples became available in mid-2018, Formula 1 Modification 3 was evaluated for use on this alloy. Formula 1 Modification 3 performance on EFP was significantly lower than on ZEK100.

This is likely attributed to both chemical and physical differences between the ZEK100 and EFP sheet samples supplied for testing. ZEK100 sheet samples were noted to be several years old and have a thick corrosion layer on the surface. The EFP samples were noted to be polished with a minimal corrosion layer. Several lubricants were re-evaluated on EFP at 100°C and up to 250°C. Two lubricant formulations were successful in this testing and were selected for use on EFP at 100°C.

Additional lubricant formulations were evaluated for use on EFP at 250°C. The product selection was expanded for this testing and two lubricant formulations were identified as successful lubricants at 250°C, Formulas 2B and 4A. Formulas 2B and 4A were subsequently tested on EFP with Henkel pretreatment C. Formula 4A was found to be successful on both the bare and pretreated metal. Formula 2B was found not offer adequate lubrication on the pretreated surface.

Following positive Project Year 1 lubricant developments focused on ZEK100 alloy, additional lubricant formulations were generated with modification to Formula 4A and evaluated for use on EFP at 250°C. Formula 4C was determined to offer the best lubrication performance on EFP alloy and was given the name QUAKERDRAW 450 MAG ("Quaker 450"). Subsequent testing evaluated corrosion protection of Quaker 450 on EFP and determined the lubricant offers corrosion protection equivalent to current automotive industry standards. Cleanability performance was measured against current automotive industry standards and found Quaker 450 has a slightly longer time-to-water-break-free result that standards. Varnish/oxidation testing was performed at 250°C and 270°C and determined the lubricant is stable at 250°C with no oxidation and can show signs of oxidation when maintained at 270°C after 10-25 minutes. The optimum coating weight of Quaker 450 was evaluated by testing the lubricant from 1.0-3.0 g/m^2 by TCT on EFP with Henkel pretreatment C at 250°C. Higher coating weights offered better lubrication in this evaluation.

EFP with Henkel pretreatment D became available during Project Year 2. The Quaker 450 lubricant was compared on bare EFP, EFP with Henkel pretreatment C, and EFP with Henkel pretreatment D. Testing determined the pretreatments did not significantly impact the lubricant's performance.

Quaker 450 lubricant supported cup-draw and cross-form testing at EWI. Bare EFP blanks, EFP blanks with Henkel pretreatment D, and EFP blanks with Xtalic pretreatment were coated with the lubricant prior to warm forming at EWI. Quaker 450 successfully formed cups and cross-form panels in narrow forming process windows. Expansion of the forming process window is a future goal for lubricant development.

D4.2.2 Comparison to Project Goals to Accomplishments
A lubricant was developed to provide forming lubrication below 100°C and up to 250°C for ZEK100 magnesium alloy, to provide in-process corrosion resistance, and be removable. Another lubricant, QUAKERDRAW 450 MAG, was developed to provide forming lubrication for EFP, provide in-process corrosion resistance, and be removable. Downstream process compatibility was further confirmed by other project participants for cleaning, painting, corrosion and welding. Successful cup forming and cross-form stamping was accomplished with the lubricant in a narrow forming process window.

D4.2.3 Development, Testing, and Evaluation of Candidate Formulations

Thermal Stability Study
A thermal stability study was carried out by Thermogravimetric Analysis (TGA). The samples were run from ambient temperature to 350°C. The results are shown in Figure D4.1. All tested formulations show stability to 100°C. Formulas 013725, 011542, and 013705 (aka Formulas 1, 2, and 3, respectively) are candidates for higher temperature applications, with formula 013725 showing stability up to 350°C.

Lubrication Screening by Reciprocating Wear Test (RCP)
Formulas 1-3 were tested by RCP on cleaned Mg strip at four temperatures between 100°C and 250°C. Products that did well in RCP were selected for additional TCT analysis for lubrication testing under more severe conditions.

Lubrication Screening by Twist Compression Test (TCT)
The lubricant formulations screened by TGA in Project Quarter 1 and tested by RCP in Project Quarter 2 were tested by TCT at both 100°C and 250°C. TCT testing on ZEK100 at 100°C verified that Formulas 1 and 2 were good candidate formulae for further testing (Figure D4.2) which were subsequently tested at 250°C. Formula 1 was further modified into several formulations for improved lubrication performance and evaluated by TCT at both 100°C and 250°C. Formula 1 Mod 3 was identified as the best lubricant at both testing temperatures.
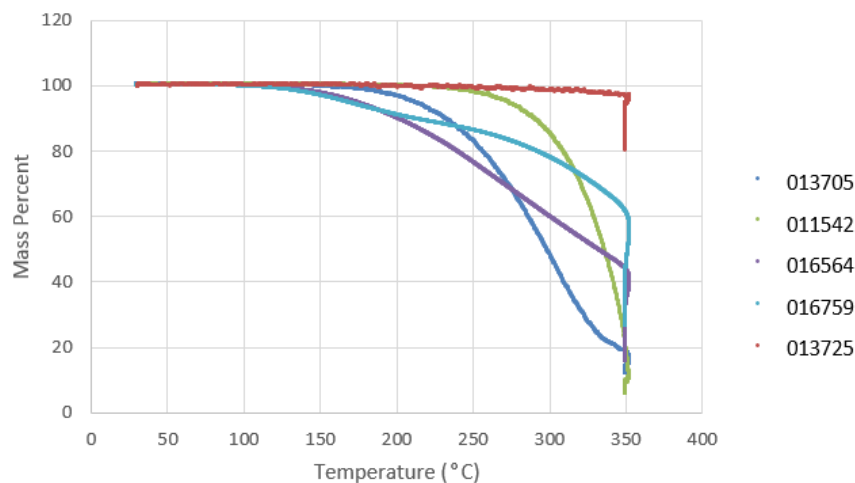

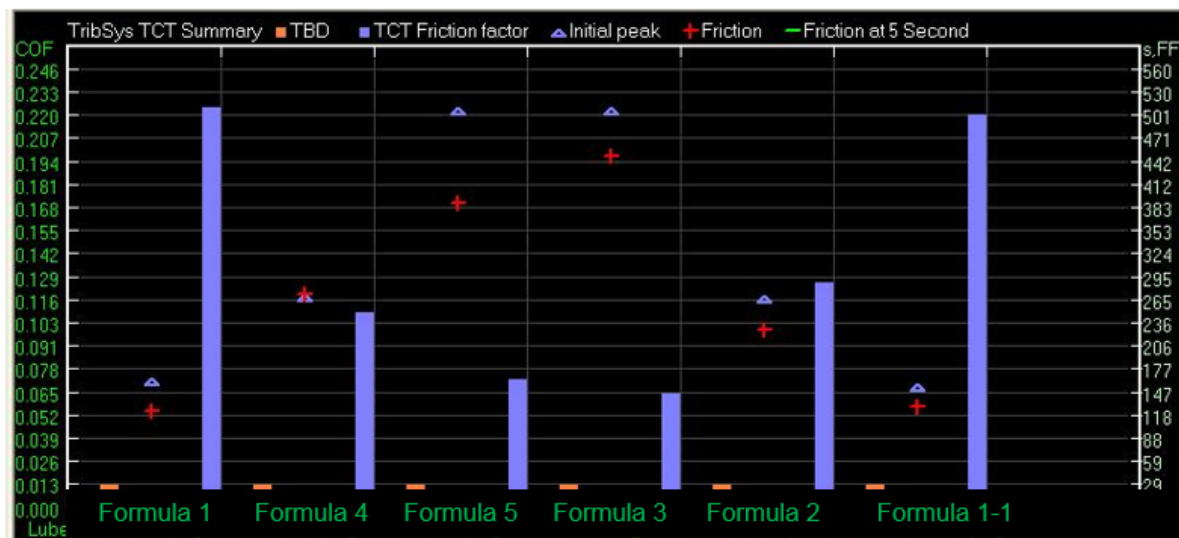Figure D4.1:   Chart showing TGA results for selected lubricant formulae. (Source: Quaker)

Figure D4.2: TCT Analysis at 100°C on ZEK100 at 3,000 PSI. (Source: Quaker)

Short Term Corrosion Resistance by GM 10 Cycle Humidity Testing
ZEK100 coupons were next coated with the Formula 1 Mod 3 lubricant and subjected to GM 10 Cycle Humidity Cabinet testing. Tested references include bare ZEK100 coupons, ZEK100 coupons coated with an internal corrosion preventative standard, and ZEK100 coupons coated with a base naphthenic oil. Very

little corrosion was observed in this test. The bare ZEK100 coupons were the only coupons to exhibit corrosion at 10 days and 15 days. The observed corrosion was minor and did not accelerate significantly between 10 and 15 days. The tested Formula 1 Mod 3 lubricant performed well and provided short term corrosion protection for the ZEK100.

Cleanability Performance of Lubricant on ZEK100 Sheet
ZEK100 coupons coated with the Formula 1 Mod 3 lubricant and were next subjected to a cleanability test to evaluate the lubricant's removability by standard industry cleaning processes, Figure D4.3. A reference lubricant was tested as a standard. Formula 1 Mod 3 performed well in the test and is as cleanable as the tested industry standard.
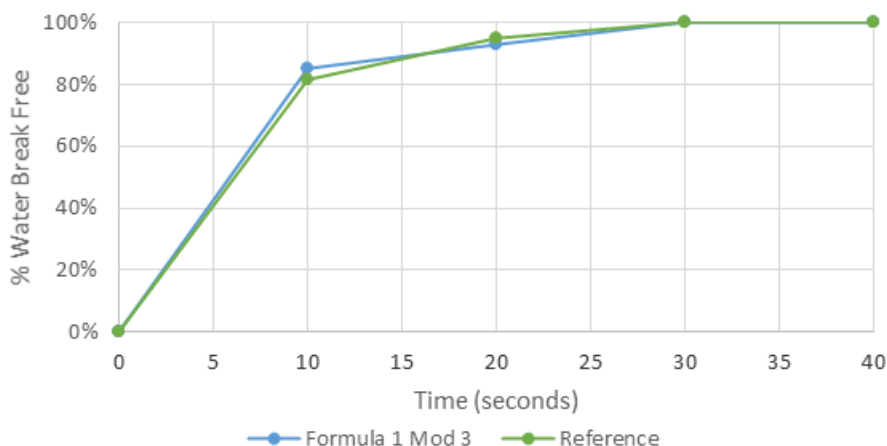

Figure D4.3: Cleanability performance of lubricant on ZEK100 sheet. (Source: Quaker)

Progress in Lubrication Screening by Twist Compression Test (TCT)
The lubricant formulations developed and verified were further tested by TCT at both 100°C and 250°C. TCT testing of EFP at 3,000 PSI and 100°C showed that the lubricant Formula 1 Mod 3 provided adequate lubrication but did not significantly outperform other lubricants as expected. Additional testing was conducted at 6,000 PSI and confirmed that Formula 1 Mod 3 performs differently on EFP than ZEK sheet. Additionally, testing showed that some lubricants that were previously identified as not usable for ZEK100 may be acceptable for use on EFP. Testing was repeated on EFP at 6,000 PSI and 250°C for formulations that are stable at 250°C. Testing at 250°C further confirms that the lubricants reviewed offer significantly different performance on EFP than ZEK100.

The ZEK100 was confirmed by several project partners to have a significant surface oxide layer, while EFP was noted as being 'polished' and verified to have a very thin oxide layer. It was concluded that the surface roughness, oxide layers, and chemistry all play a role in lubricant performance.

Five lubricant formulations were developed in Project Quarter 5 for evaluation exclusively on EFP magnesium sheet at 250°C. Formula 2 is water containing and was evaluated as both a wet film (2A) and a dry film (2B). The remaining formulas contain no water and were evaluated as applied. Formulas 2B and Formula 4A provided satisfactory results on bare EFP at 250°C. The remaining formulations did not provide adequate lubrication under the tested conditions and were omitted from further testing.

TCT testing on EFP with Henkel pretreatment C at 250°C was also completed. Overall, lubrication levels were negatively impacted by the pretreatment as compared to the bare EFP metal. Formula 2B performed poorly by TCT analysis on the pretreated metal, although the raw data indicates that the tool and coupon were kept separated by the lubricant. Formula 4A performed well on the pretreated metal.

Four new lubricant formulations were developed in Project Quarter 6 for evaluation on EFP magnesium sheet with Henkel pretreatment C at 250°C. All formulas developed in this project quarter contain no water and were evaluated as applied.

TCT testing on EFP with Henkel pretreatment C at 250°C was completed with Formula 1 Mod 3, Formula 4A, and new formulas 4C, 4D, & 5A. Formulas 4C, 4D, and 5A are derivatives of Formula 4A for review of additive optimization. Overall, 4C and 4D did not offer a reduction in TCT COF but did increase time to breakdown and TCT factor. Formula 5A both maintained TCT COF and increased time to breakdown and TCT Factor.

Additional testing was completed for additive optimization of Formula 1 Mod 3 and Formula 5A, referred to as Formula 1 Mod 4 and Formula 5B, respectively. Testing showed an additive effect in Formula 5B and a competitive/subtractive effect in Formula 1 Mod 3. Formula 5B was selected for further evaluations for process compatibility and targeted for use in formability trials.

However, the Formula 5 was later removed from testing as it was found to have high-temperature stability concerns. TCT testing was repeated on EFP with Henkel pretreatment C at 250°C with Formula 4A, C, and D. Formulas 4C, 4D, and 5 are derivatives of Formula 4A. Thereafter, Formula 4C was selected for the final formulation and is now known as QUAKERDRAW 450 MAG (i.e., "Quaker 450" in this report).

Additional testing was completed on Quaker 450 to understand the impact of coating weight on the lubrication performance. This testing was completed under the same conditions as the previous testing with coating weight varied form 1.0-3.0 g/m^2. Test results indicate a higher coating weight provides better lubrication with a slight decrease at 2.0 g/m^2.

D4.2.4 Detailed Testing of Quaker 450

Cleanability Testing
Quaker 450 was next compared to two automotive standard products by removability/cleanability testing. The subject lubricants were coated onto the magnesium panel, baked at 270°C for 5 minutes and then aged at 49°C for 7 days to simulate a warm forming operation and subsequent accelerated panel storage. Quaker 450 was found to be cleanable with slightly longer removal times than the two standards it was compared to.

Corrosion Protection by GM 10 Cycle Testing
Quaker 450 was compared to two automotive standard products for corrosion protection by GM 10 Cycle humidity cabinet and was found to protect the metal surface and be comparable to the two standards it was tested against.

Varnish Performance
Quaker 450 was also tested for longer term varnish formation by maintaining coated panels at 270°C while being monitored at 5-minute intervals. Testing shows no lubricant change at 5 minutes and some discoloration/oxidation at 10-15 minutes. Some tested panels generated varnish in as little as 15 minutes while others lasted 20-25 minutes prior to varnishing.

Coil Pretreatment Evaluations
Quaker 450 lubricant was evaluated on EFP sheet with Henkel pretreatment D to compare lubrication performance to previous testing on EFP with Henkel pretreatment C and bare EFP. TCT testing was performed at 250°C for a set time to evaluate the average coefficient of friction over that time. (See Table D4.1) This is an alternate method of friction analysis that can be performed by TCT. The data indicate that the Henkel pretreatment D performs similarly to Henkel pretreatment C and bare EFP with

Quaker 450 lubricant under these test conditions. A higher initial friction peak was noted for EFP with Henkel pretreatment D, but the average coefficient of friction over the set time is comparable to Henkel pretreatment C.

Table D4.1: TCT Analysis at 250°C on Henkel Pretreated (D) EFP at 3,000 PSI

Sample	Initial Peak		Friction		Time to Breakdown		TCT Friction Factor	
	Ave.	Std. dev.	Ave.	Std. dev.	Ave.	Std. dev.	Higher is better	Std. dev.
EFP Bare	0.120	0.060	0.130	0.007	89.06	0.028	696	328.5
EFP with Henkel C	0.140	0.012	0.129	0.003	89.08	0.000	679	64.0
EFP with Henkel D	0.179	0.008	0.132	0.003	89.08	0.000	630	38.1

D4.2.5 Cup Draw Testing

Quaker 450 lubricant contains no water and was evaluated as applied. Cup draw blanks were supplied by USAMP's contractor Edison Welding Institute (EWI) as bare EFP, Henkel pretreated EFP, and Xtalic pretreated EFP. All blanks were coated on one side with Quaker 450 applied at 1.0-2.5 g/m^2 prior to evaluation at EWI. Formed test cups are shown in Figure D4.4 below. All cracked at 150°C. Good cups were drawn at 180-220°C using a binder holding force (BHF) in the 5-22kN range. All Henkel- and Xtalic- pretreated and bare blanks formed without cracking at 200°C and 22kN.

Figure D4.4: Cup draw test samples. EFP sheet blanks with Quaker 450 lubricant applied. (a) 150°C, 2-kN BHF and (b) 200°C, 30-kN BHF. (c) Crack-free and formed to full depth using 220°C, 22-kN BHF. (Source: Quaker)

D4.2.6 Cross-Form Testing

Cross-form blanks were supplied from EWI as bare EFP, Henkel-pretreated EFP, and Xtalic-pretreated EFP. All blanks were coated on both sides with Quaker 450 lubricant. A representative cross-form is shown below in Figure D4.5, illustrating successful forming at 200ºC.
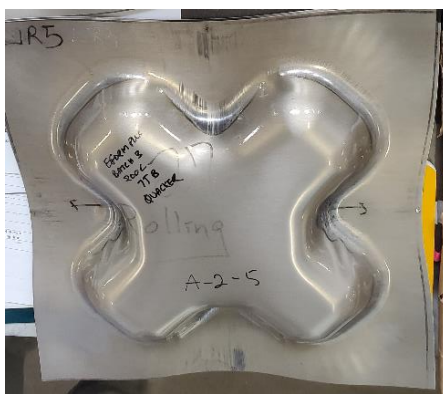

Figure D4.5: Cross-form of bare EFP panel successfully formed with Quaker 450 at 200°C. (Source: Quaker)

D4.2.7 Further Lubricant Development Exploration

Four new lubricity-enhancing additives were evaluated for use in Quaker 450 utilizing a Design of Experiment (DOE) tool. Thirty-one formulations were generated and tested to measure the individual and combined impacts of the additives on lubrication. The formulations were also screened for varnishing performance at 220°C and neat stability. Sixteen of the 31 DOE formulations were stable and their test results are graphed in Figure D4.6. Three new formulations were generated for optimum performance based on the DOE results. These three formulations were then tested against Quaker 450 by TCT at 220°C and 3,000 PSI on EFP with Henkel pretreatment D, Table D4.2, and evaluated for varnishing performance and product stability, as shown in Table D4.3. The Quaker 450 formula outperformed all three DOE lubricant formulas.
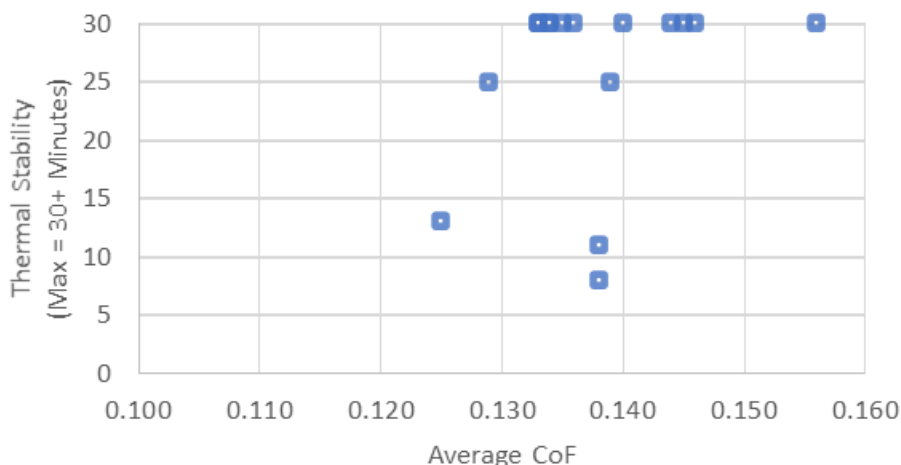

Figure D4.6: Comparison of stable DOE formulations by Thermal Stability and Average COF. (Source: Quaker)

Table D4.2: TCT Analysis at 220°C on Henkel Pretreated (D) EFP at 3,000 PSI.

Sample	Initial Peak		Friction		Time to Breakdown		TCT Friction Factor	
	Ave.	Std. dev.	Ave.	Std. dev.	Ave.	Std. dev.	Higher is better	Std. dev.
450	0.158	0.014	0.136	0.001	30.00	0.000	214	21.4
M1 Formula	0.182	0.010	0.140	0.004	30.00	0.000	202	14.7
M2 Formula	0.199	0.010	0.140	0.004	30.00	0.000	198	14.0
M3 Formula	0.167	0.015	0.143	0.002	30.00	0.000	203	20.8

Table D4.3: Product Stability and Varnishing of Model DOE Formulas.

Formula	Stable Product	Time to Discoloration at 220°C (min)
450	Yes	>30
M1 Formula	Yes	>30
M2 Formula	Yes	>30
M3 Formula	Yes	>30

Coefficient of Friction Testing by Tool Speed and Pressure

Finally, Quaker 450 was tested by TCT on bare EFP against tool steel, with a sliding speed of 20 mm/s, to determine COF. Results were in the range of 0.10-0.13 as shown in Table D4.4.

Table D4.4. TCT data on bare EFP against tool steel with Quaker 450 lubricant.

Temperature	Pressure					
	15 MPa		30 MPa		45 MPa	
	COF	St. Dev.	COF	St. Dev.	COF	St. Dev.
150ºC	0.117	0.019	0.110	0.010	0.101	0.004
200ºC	0.125	0.011	0.108	0.007	0.109	0.001
250ºC	0.126	0.002	0.116	0.006	0.124	0.009

D4.3 CONCLUSIONS AND RECOMMENDATIONS

1. Quaker Houghton developed an oil-based lubricant for use in forming ZEK100 and EFP at forming temperatures in the 100°C - 250°C range. This lubricant, QUAKERDRAW 450 MAG ("Quaker 450"), reduced the COF between tool steel and the magnesium sheets at elevated temperatures.

2. Heated Reciprocating Wear Testing and heated Twist Compression Testing were key to successful development of the Quaker 450 lubricant.

3. Secondary characteristics of Quaker 450 on magnesium sheets were evaluated and found favorable. These include corrosion protection during manufacturing, stain and varnish tendency, cleanability, spot weldability, compatibility with a representative downstream automotive paint system, and others.

4. Quaker 450 is compatible with upstream coil pretreatments developed during the project. It was evaluated in cup draw testing and cross-form stamping and was successful in generating formed cups and cross-form panels, albeit with narrow forming process windows. Future development could focus on reducing the COF at elevated temperatures and providing a broader forming process window.

D5. Paint Shop Cleaners and Pretreatments for Corrosion Resistance
(PPG – Principal Investigator: L. Valdez)

D5.1 SUMMARY

PPG focused on the following research objectives under the sheet coatings development Task 3:
1. Development and Evaluation of cleaner compatibility with magnesium alloys,
2. Development and testing of pretreatments on different magnesium alloys,
3. Pretreatment integration with other coil coatings, lubricants, and joining processes,
4. Optimization of pretreatments on magnesium alloys in multi-metal systems.

PPG developed chromium-free cleaning and pretreatment solutions for both ZEK100 and EFP Mg alloys and completed integration with other components of the project. Significant progress was also made in making the pretreatment processes compatible for multi-metal systems. The contributions of this work addressed the reactive nature of Mg alloy and enabled its use in multi-metal applications. Detailed discussion of this work may be found at https://data.lightmat.org/project/.

D5.2 KEY ACCOMPLISHMENTS AND RESULTS

D5.2.1 Project Objectives
In recent years, there has been a growing interest in using magnesium alloys in different businesses due to advantages such as its low density, high strength-to-weight ratio, and good machinability, but a major drawback to expanded usage is its highly reactive nature. The motivation for this work was to develop metal pretreatment solutions for different magnesium alloys to address this challenge. The task of developing a metal pretreatment was approached holistically by considering the entire process from cleaning and surface preparation, to pretreatment formulation, to sealers and other post-rinses for maximum corrosion protection.

A key goal was to help minimize the cost penalty associated with utilization of Mg sheet body panels by (1) cleaning/pretreating the panels as part of the body-in-white assembly rather than as separate pieces and (2) using materials and processes which work on mixed-metal assemblies (rather than multiple ones which are each specific to a type of metal). A typical pretreatment line sequence is shown in Figure D5.1. For processing galvanized steel car bodies, automotive paint shops have used a caustic cleaner to remove dirt and oils, followed by a zinc/iron phosphate pretreatment to grow crystals which serve to anchor the subsequently applied polymeric e-coat. Together, the galvanization and e-coat help protect the steel against corrosion during the life of the vehicle.
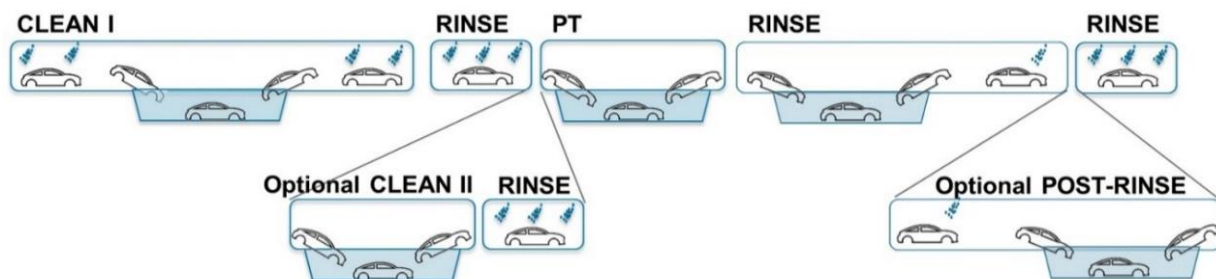

Figure D5.1. A typical automotive pretreatment sequence, prior to electrocoat. (Source: PPG)

D5.2.2 Cleaners and Pretreatments

Table D5.1: Glossary of PPG paint-shop cleaners and pretreatments used in the USAMP study.

Name	Description	pH
Cleaner 1	degreaser	12.11
Cleaner 2	fluorometallic acid	2.5
Cleaner 2A	fluorometallic acid	2.5
Cleaner 2B	fluoride source	2.5
Cleaner 2.1	fluorometallic acid	2.3
Cleaner 2.1A	fluorometallic acid	2.3
Cleaner 2.18	fluorometallic acid	2.3
Cleaner 2.4	fluorometallic acid	2.3
Cleaner 2.21	patent pending	-
Cleaner 2.32	patent pending	-
Cleaner 2.33	patent pending	-
Cleaner 3	acidic deoxidizer	1.5
Cleaner 4	acidic deoxidizer	5.16
Cleaner 4.1	acidic deoxidizer	1.83
Cleaner 5	organic acid	
PT1	fluorometallic acid	4.5
PT2	organophosphate	
PT 2.1	organophosphate	
PT 2.12	organophosphate	

Name	Description	pH
PT 2.13	organophosphate	
PT3	fluorometallic acid	4.6
PT4	fluorometallic acid	4.5
PT5	fluorometallic acid	5
PT6	fluorometallic acid	4.8
PT7	rare earth	3.5
PT8	rare earth	3.5
PT7.4	rare earth	3.5
PT8	rare earth	3.5
PT7.5	rare earth	3.5
PT7.8	rare earth	3.5
PT10.9	rare earth	3.5
PT7.9	rare earth	3.5
PT9	Group IVB/organic	
PT24	phosphate	
PT25	organophosphate	
PT25.1	organophosphate	
PT25.2	organophosphate	
PT25.3	organophosphate	

D5.2.3 Evaluation of Cleaner Compatibility with Magnesium Alloys
This section is focused on the evaluation and analysis of PPG metal cleaners with the different magnesium alloys to understand alloy performance and interactions. This was done by evaluating cleaning effectiveness, pH, and concentration of dissolved magnesium.

Cleaner Evaluation on ZEK100
The goal of this work was to examine cleaners' effectiveness in removing Ferrocote, a common stamping lubricant, and determine the relationship between cleaner pH, dissolved magnesium, and panel surface morphology. This was done by evaluating cleaners with different pH values at different immersion times. The cleaning performance of four different cleaners was evaluated to determine water break performance. The cleaning performance of each cleaner is summarized in Figure D5.2. Cleaner 1 at 120 s immersion time was more effective at cleaning the panel and removing the Ferrocote lubricant than other cleaners.

D5.2.4 Benchmarking and Development of Pretreatments on Magnesium Alloys
This section is focused on the evaluation and development of PPG metal pretreatments with the different magnesium alloys to understand alloy performance and corrosion protection coatings. This was done by evaluating corrosion and adhesion performance of the pretreatment processes.

Initial Pretreatment Evaluation on ZEK100 and EFP
The goal of this work was to evaluate potential pretreatments for corrosion protection properties. ZEK100 panels were exposed to GMW 14872 cyclic corrosion testing for 9 days. Pretreatments 3 and 5 performed better than the other pretreatment processes, as summarized in Figure D5.3.

To further evaluate potential pretreatments, a second cleaner step was added following Cleaner 1 and before the pretreatment. ZEK100 panels were exposed to GMW 14872 cyclic corrosion testing for 15 days. The addition of Cleaner 2 after Cleaner 1 improved corrosion performance. Pretreatment 4 following Cleaner 2 performed better than other pretreatment processes, as summarized in Figure D5.4.
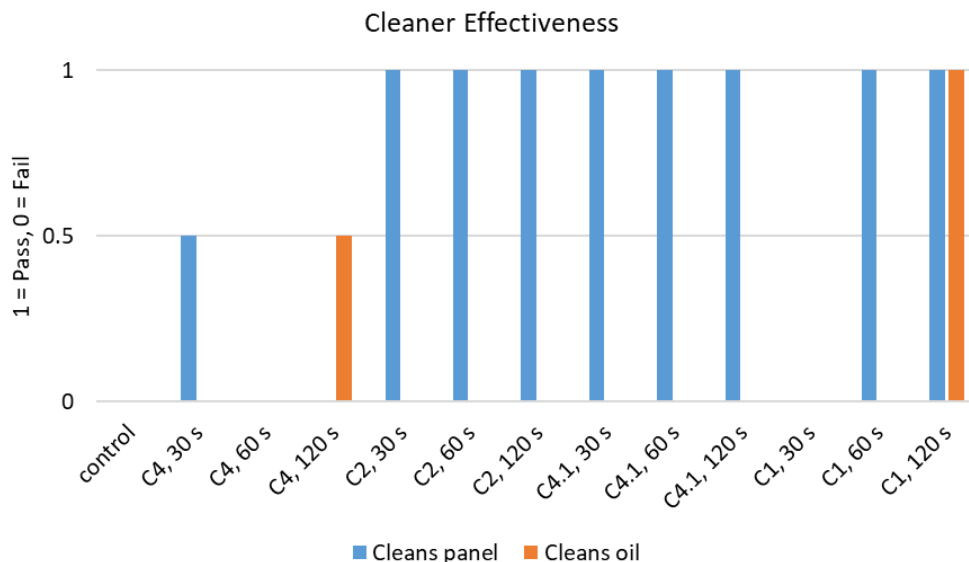

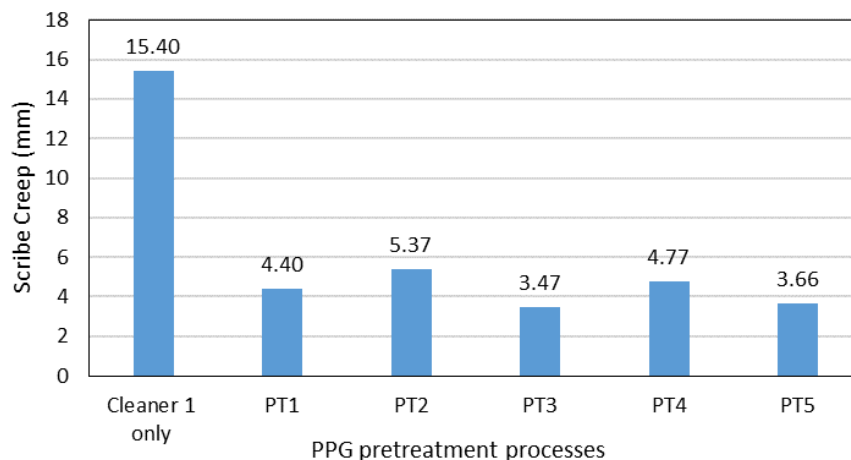Figure D5.2. Evaluation of four cleaners at 30, 60, 120 s immersion times. (Source: PPG).

Figure D5.3. Corrosion performance of ZEK100 after 9 days of cyclic corrosion testing. (Source: PPG)

A kinetic study was performed on EFP to understand the effect of immersion time in Cleaner 2 on corrosion performance. Figure D5.5 shows that most of the corrosion protection is imparted after 1 min immersion in Cleaner 2.

Further Pretreatment Evaluation and Development on ZEK100 and EFP
The goal of this work was to evaluate the pretreatments that were developed for corrosion protection properties. ZEK100 panels were exposed to GMW 14872 cyclic corrosion testing for 20 days. Pretreatments 2, 2.12, and 25 performed better than the other pretreatment processes. Additionally, other promising pretreatment formulations were studied in two separate experiments where ZEK100 panels were exposed to GMW 14872 cyclic corrosion testing for 13 days: Pretreatment 8 performed better than the other pretreatment processes.

Another experiment focused on novel pretreatments was done to evaluate optimized formulations of Cleaner 2. The corrosion performance of EFP and ZEK100 after 3 weeks in G-85 A2 corrosion testing is shown in Figure D5.6. For both alloys, Cleaner 2.18 and 2.4 with and without Pretreatment 1 performed better than the other pretreatment processes.
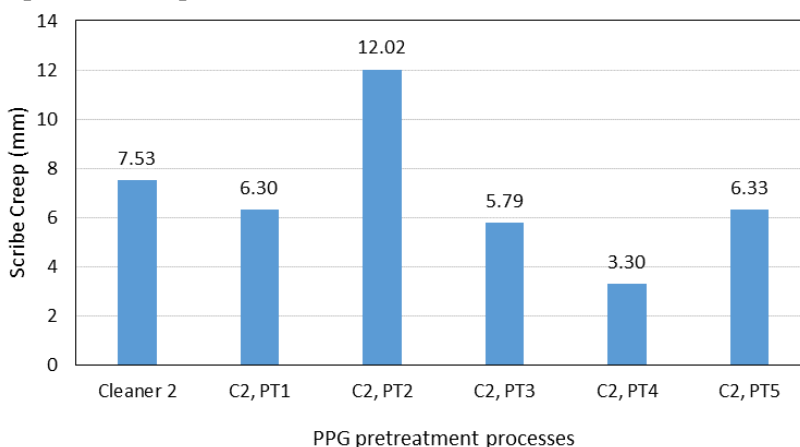

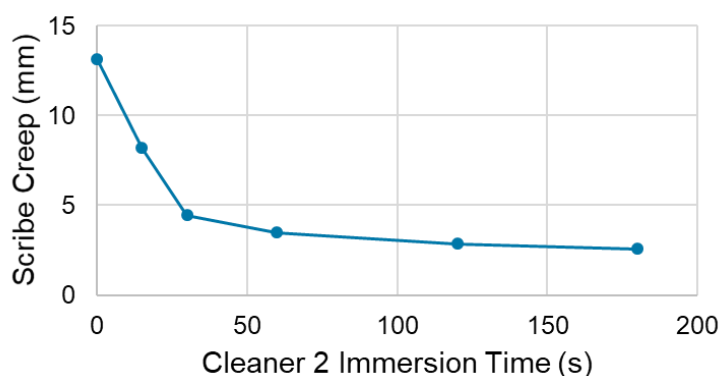Figure D5.4. Corrosion performance of ZEK100 after 15 days of cyclic corrosion testing. (Source: PPG)

Figure D5.5. Plot of scribe creep after 3 weeks filiform corrosion test on EFP. (Source: PPG) Panels were cleaned with Cleaner 1, immersed in Cleaner 2 for the specified duration, then rinsed and dried before electrocoating.
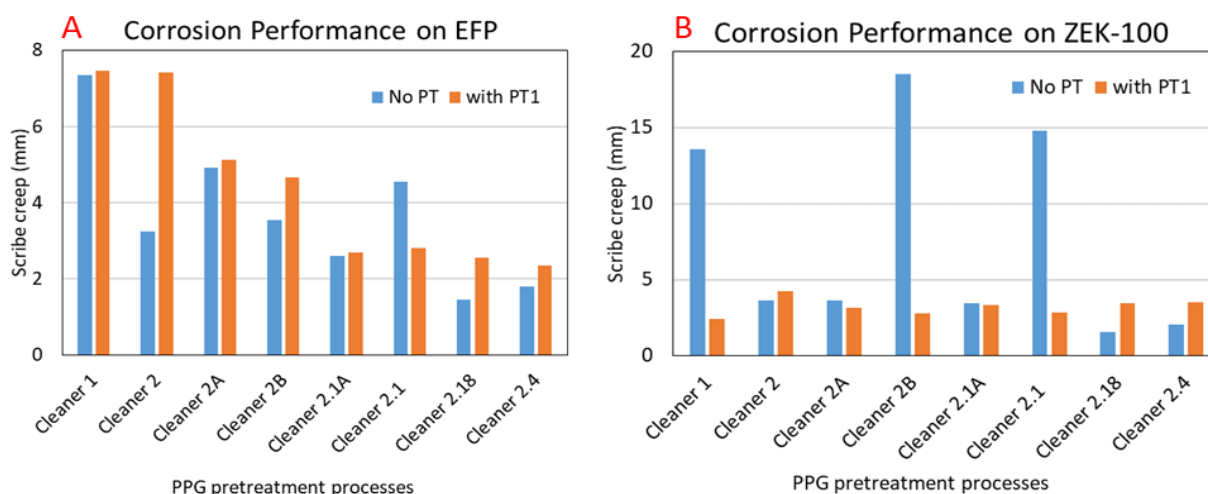

Figure D5.6. Corrosion performance of Mg alloys after 3 weeks of corrosion testing. (Source: PPG)

D5.2.5 Pretreatment Integration with Other Task 3 Coatings and Task 4 Joining Processes

This section is focused on the integration of PPG metal pretreatments with the other components of the project. This was done by evaluating corrosion and adhesion performance of the pretreatment processes following other Task 3 coatings and following the Task 4 joining processes to produce EFP mini-door samples for testing corrosion performance.

Cleaner Effectiveness with Quaker 450 Lubricant

ZEK100 panels coated with a forming lubricant were received from Quaker. Three cleaners were tested for lubricant removal efficacy at three immersion times (30, 60, and 120 s). Figure D5.7 shows that only Cleaner 1 consistently removed the Quaker lubricant to pass the water break assessment.
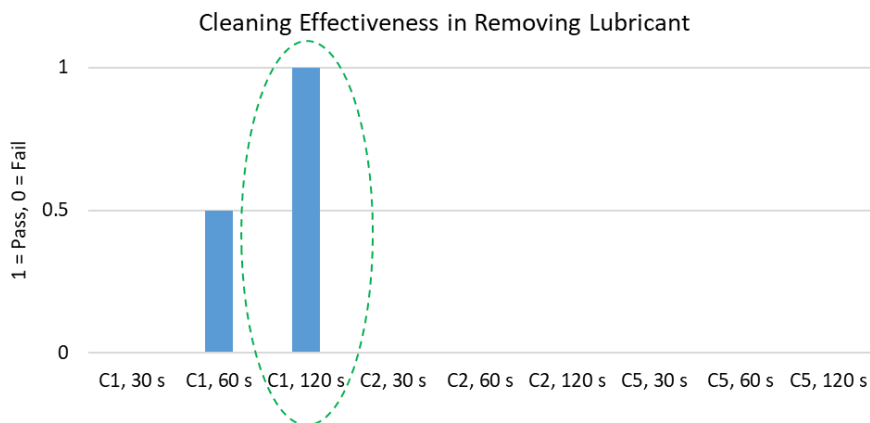

Figure D5.7. Cleaner removal of Quaker lubricant was evaluated with three different cleaners at 30, 60, 120 second immersion times. (Source: PPG)

Compatibility with EFP Panels having a Coil Pretreatment and Fuchs 1102 Lubricant

The goal of this work was to evaluate the compatibility of the top performing PPG cleaning and pretreatment processes on EFP panels having either Henkel or Xtalic coil coating, and Fuchs 1102 lubricant, as well as an as-received EFP panel. Panels were pretreated with either a two or three step process; Cleaner 1 → Cleaner 2.4 → (optional) Pretreatment 8, then e-coated with a standard automotive e-coat and subjected to G-85 A2 filiform corrosion testing for three weeks. Figure D5.8 visually summarizes the corrosion results. The panels treated with Xtalic's zinc plating process showed heavy surface blistering whereas the panels treated with Henkel's coil pretreatment and the as-received EFP panels performed well. The two-step cleaning and pretreatment process appears to provide sufficient protection and would be more desirable than a three-step process.

The dry cross-hatch testing showed a potential benefit to the use of a coil pretreatment and lubricant versus the bare EFP in the case of using Cleaner 1 → Cleaner 2.4 → Pretreatment 8. There may be a slight advantage in wet cross-hatch testing to have the Henkel/Fuchs combination with Cleaner 1 → Cleaner 2.4.
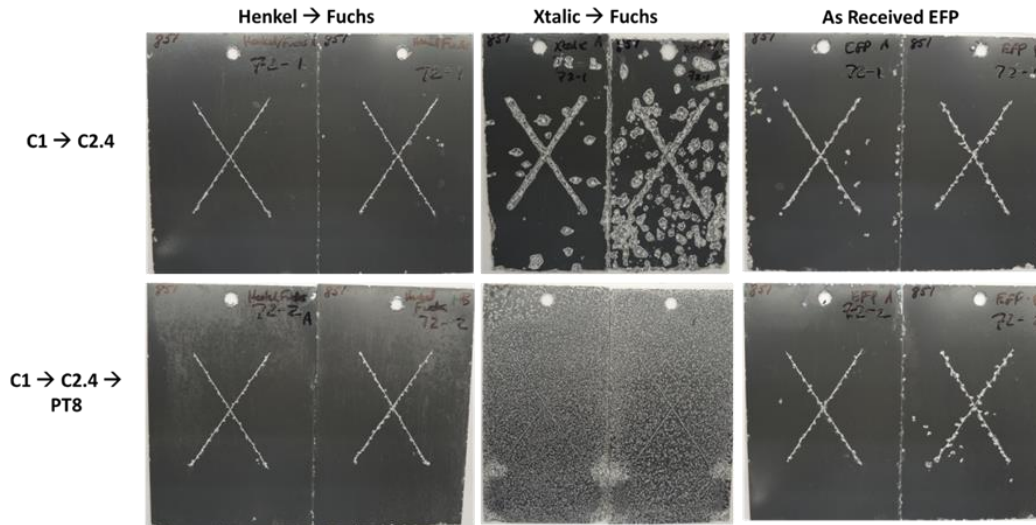
Figure D5.8. Corrosion-tested EFP panels which had been treated with Henkel pretreatment or Xtalic Zn plating, coated with Fuchs 1102 lubricant, cleaned, pretreated, and e-coated prior to testing. (Source: PPG)

Compatibility with EFP Panels having a Coil Pretreatment and Quaker 450 Lubricant
The goal of this work was to evaluate the compatibility of the top performing PPG cleaning and pretreatment processes on EFP panels with either Henkel or Xtalic coil coating and Quaker 450 lubricant, as well as an as-received EFP. The following cleaning and pretreatment processes were evaluated:
- Cleaner 1 → Cleaner 2.4
- Cleaner 1 → Cleaner 2.4 → Pretreatment 8

Panels were exposed to G-85 A2 filiform corrosion for six weeks. There was a loss in performance with the Xtalic/Quaker EFP panels, and were they removed from testing after 3 weeks due to surface blistering, as seen previously with Xtalic/Fuchs EFP panels. The Henkel/Quaker and the as-received EFP panels performed similarly to one another.

Cross-hatch testing was completed. The wet cross-hatch testing showed potential benefit to use of a coil pretreatment and lubricant versus bare EFP in case of using Cleaner 1 → Cleaner 2.4 → Pretreatment 8. There was no difference in wet and dry cross-hatch testing between the Quaker (Henkel/Quaker and Xtalic/Quaker) EFP and the as-received EFP with Cleaner 1 → Cleaner 2.4.

EFP Mini-Door Evaluation
Table D5.2 lists the different top performing PPG cleaning and pretreatment processes that were evaluated on Xtalic/Fuchs, Xtalic/Quaker, Henkel/Fuchs, and Henkel/Quaker EFP panels that were welded, cut, and bent to form mini-doors. The Xtalic EFP mini-doors went through four weeks of G-85 A2 filiform corrosion testing, while the Henkel EFP mini-doors went through ten weeks of G-85 A2 corrosion testing. There was a loss in performance with the Xtalic coil coated EFP panels, which were removed from corrosion testing after four weeks due to surface blistering and perforations through the metal. The Henkel coil pretreatment performed well in up to ten weeks of corrosion testing and did not have perforations through the metal. Figure D5.9 visually summarizes the corrosion results.

Table D5.2. PPG cleaning and pretreatment processes evaluated for EFP mini-door compatibility

Condition	Coil Coating	Lubricant	Cleaning step	PPG Treatment System
1	Henkel	Quaker	Cleaner 1 (C1)	Cleaner 2.4
2	Henkel	Quaker		Cleaner 2.4 → Pretreatment 8
3	Xtalic	Quaker		Cleaner 2.4
4	Xtalic	Quaker		Cleaner 2.4 → Pretreatment 1
5	Henkel	Fuchs		Cleaner 2.4
6	Henkel	Fuchs		Cleaner 2.4 → Pretreatment 8
7	Xtalic	Fuchs		Cleaner 2.4
8	Xtalic	Fuchs		Cleaner 2.4 → Pretreatment 1

D5.2.6 Optimization of Pretreatments on Magnesium Alloys in Multi-Metal Systems

This section is focused on optimization of PPG metal pretreatments for EFP in multi-metal systems and the research was done by evaluating corrosion and adhesion performance of the pretreatment processes on non-joined and joined panels of EFP, cold-rolled steel (CRS), aluminum alloy 6111 (AA6111), and hot-dip galvanized steel (HDGS).

Multi-Metal Compatibility of Non-Joined Metal Panels

In order to evaluate the compatibility of PPG cleaning and pretreatment processes with a multi-metal system, the corrosion performance of several processes was evaluated on non-joined EFP, CRS, AA6111, and HDG samples. The results are summarized in Figure D5.10. The AA6111 panels performed the best, while CRS performed the worst. Out of the pretreatment systems tested, Cleaner 2 or Cleaner 2.4, followed by Pretreatment 1, showed the best performance. Pretreatment 24 followed by Pretreatment 1 was also promising, although variability in the EFP samples was observed.

The adhesion performance of the non-joined samples with the different pretreatment processes was also evaluated. The results for wet cross-hatch testing are shown in Figure D5.11. Out of the pretreatment systems tested, Pretreatment 24 followed by Pretreatment 1 showed the best overall performance, and therefore is recommended to pass wet adhesion testing for all substrates. C2.4 showed good performance on CRS, HDGS, and AA6111, while Cleaner 2.4 followed by Pretreatment 1 showed good performance for EFP, CRS, and HDG.

Multi-Metal Couples Joined using Rivets plus Adhesive Prior to Cleaning

The goal of this work was to determine the level of galvanic corrosion in multi-metal couples of EFP, CRS, HDG, and/or AA6111. The top performing cleaning and pretreatment processes (listed below) were evaluated to select systems that protect all metals. In this work, couples that were joined with adhesive and rivets prior to cleaning and pretreatment were evaluated.

- Cleaner 1 → Pretreatment 1
- Cleaner 1 → Cleaner 2
- Cleaner 1 → Cleaner 2.4
- Cleaner 1 → Cleaner 2 → Pretreatment 1
- Cleaner 1 → Cleaner 2.4 → Pretreatment 1

The pretreatment system for CRS requires Pretreatment 1, while EFP requires treatment with a Cleaner 2 or Cleaner 2.4 type bath for corrosion protection. Hence C2 + PT1 is the most promising solution for mixed substrates thus far.
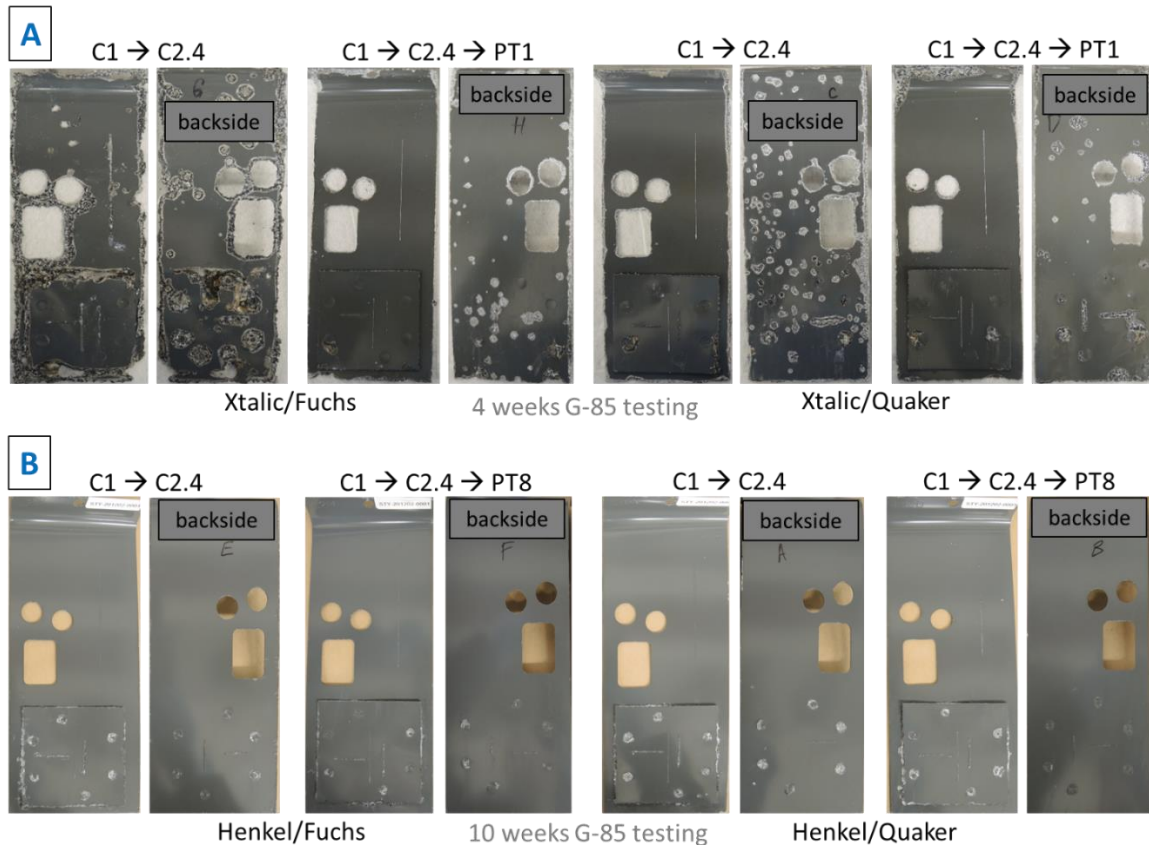
Figure D5.9. EFP mini-doors treated with Xtalic zinc plating (A) or Henkel coil pretreatment (B) and then coated with Quaker or Fuchs lubricant. (Source: PPG) Panels were pretreated with either a two or three step process; Cleaner 1 → Cleaner 2.4 → (opt.) Pretreatment 8 or Pretreatment 1 and then e-coated with a standard automotive e-coat and subjected to G-85 A2 filiform corrosion testing.
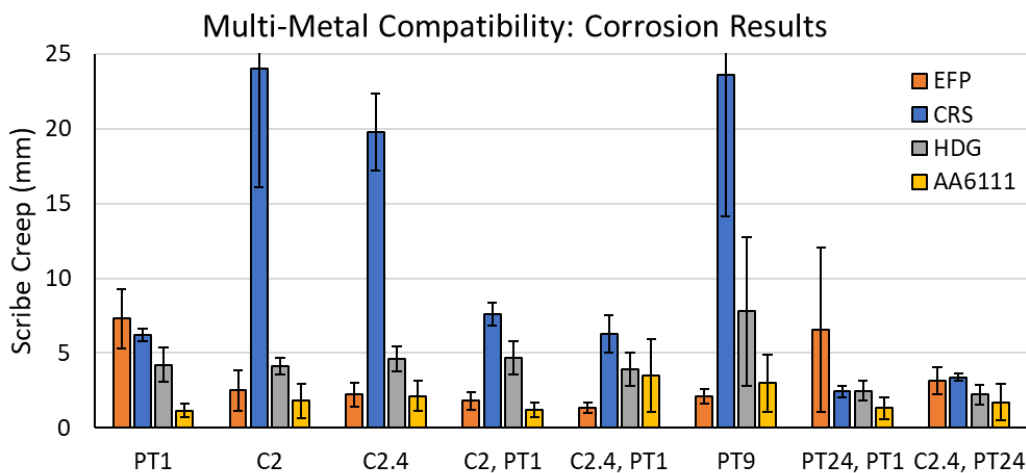

Figure D5.10. Corrosion performance of EFP, CRS, AA6111, and HDGS after three weeks ASTM G-85 A2 corrosion testing. Cleaner 2 or Cleaner 2.4 → Pretreatment 1 and C2.4 → Pretreatment 24 showed promise. CRS showed the most corrosion of all substrates. (Source: PPG)
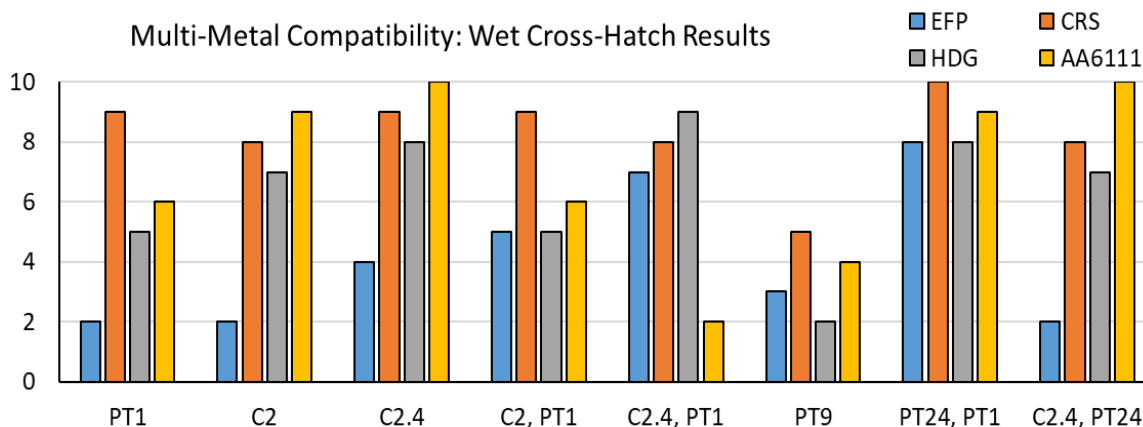
Figure D5.11. Wet cross-hatch adhesion performance of EFP, CRS, AA6111, and HDGS with the different pretreatment processes. Pretreatment 24 → PT1 showed the best performance overall and is recommended to pass wet adhesion testing for all substrates. (Source: PPG)

Optimization of Pretreatment Formulations
Currently, the top performing processes for multi-metal systems involve an additional cleaner and pretreatment. This work aims to *compact* the pretreating process by eliminating the need for a second cleaner and developing one pretreatment that performs well with EFP and other metals. Five cleaning and pretreatment processes were evaluated with EFP and CRS at 120 s, 180 s, and 240 s immersion.

- Cleaner 1 → Cleaner 2.4
- Cleaner 1 → Cleaner 2.21
- Cleaner 1 → Cleaner 2.32
- Cleaner 1 → Cleaner 2.33
- Cleaner 1 → Pretreatment 1

The corrosion performance of the above processes on EFP was evaluated following six weeks of G-85 A2 filiform corrosion testing (See Figure D5.12). EFP performed best with Cleaners 2.4 and 2.21 and had the worst performance with Pretreatment 1. There was little to no change in performance when EFP was pretreated at different immersion times with Cleaners 2.4 and 2.21. The corrosion performance of the five cleaning and pretreating processes was also evaluated on CRS following 30 cycles of GMW 14872 cyclic corrosion testing, a typical test for CRS (See Figure D5.13). CRS panels pretreated with Cleaner 2.21, Cleaner 2.32, and Pretreatment 1 performed best. Based on the results, for better performance on EFP and CRS, Cleaner 2.21 for 180 s or Cleaner 2.32 for 120 s compact processes are recommended.
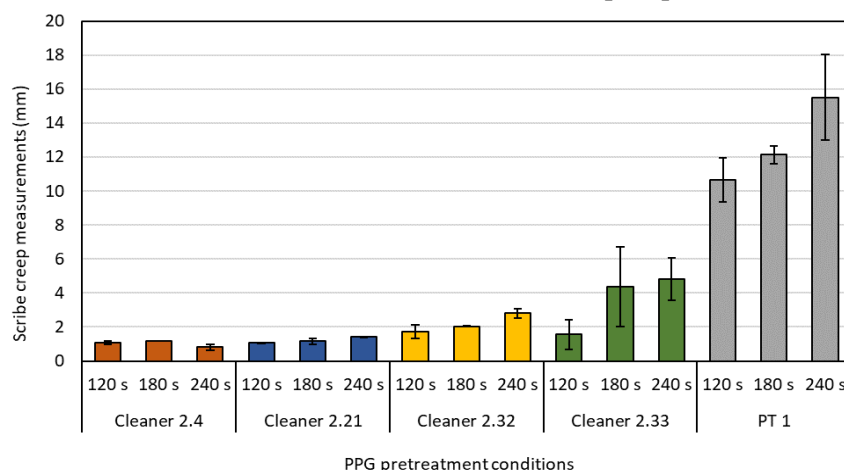

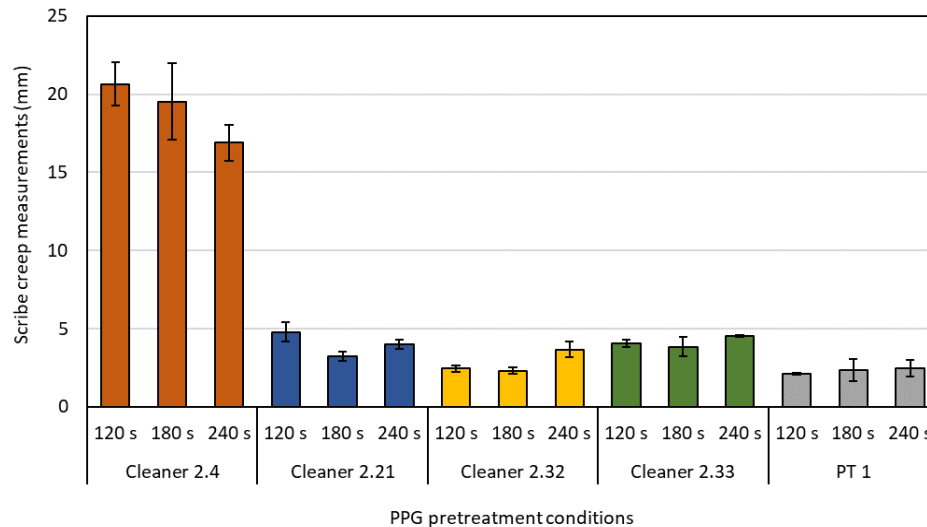Figure D5.12. Corrosion performance of EFP after six weeks of corrosion testing. (Source: PPG)

Figure D5.13. Corrosion performance of CRS after 30 days of cyclic corrosion testing. (Source: PPG)

D5.3 CONCLUSIONS AND RECOMMENDATIONS

The task of developing a cleaner and metal pretreatment prior to paint shop processes was approached by considering the entire process from cleaning and surface preparation, to pretreatment formulation, to sealers and post-rinses for gaining maximum corrosion protection. Key points are summarized below:

1. Cleaner 1, an alkaline cleaner, was much more effective than the acidic cleaners at cleaning Mg panels and removing lubricants. Dissolution of the Mg is not directly related to the bath pH.

2. Pretreatment 2 and Cleaner 2 pretreatments impart good corrosion protection of e-coated ZEK100 and EFP. For both alloys, Cleaner 2.4 was a top performing pretreatment, showing promise as a stand-alone pretreatment.

3. Both two-step and three-step Cleaner 2.4 pretreatment processes were effective in protecting coil-coated and lubricated EFP from corrosion, and in some cases, also improving the adhesion performance.

4. PPG cleaners/pretreatments help afford corrosion protection to welded Mg mini-door samples.

5. Cleaners 2.21 and 2.32 provide sufficient corrosion protection for both Mg and steel, suggesting that multi-metal systems might be processed successfully without increasing the number of steps beyond that currently found in typical automotive paint shops. (i.e., one cleaning step plus one pretreatment step prior to e-coat)

Chapter E. Task 4: Joining Process Evaluation and Development
(AET Integration – Principal Investigator: S. Logan)

E1. SUMMARY

AET's role in Task 4 of this project was to evaluate the capability of commercially available welding processes, and to optimize those processes as necessary, to weld the new USAMP proposed low-cost magnesium alloy EFP sheet material. Specifically, AET investigated resistance spot welding (RSW), friction stir welding (FSW), Arplas resistance projection welding (RPW), and laser welding for suitability to weld 1.17 mm thick EFP sheet Mg to itself. In addition to evaluating the weldability of this material with no coatings, AET also evaluated the weldability of this material with two unique coatings (Henkel Pretreat D and Xtalic Zn) and two unique forming lubricants (Fuchs 1102 and Quaker 450). Furthermore, the bare EFP material provided by POSCO through USAMP was delivered in three batches at different times throughout the project. The two batches evaluated at AET had unique surface characteristics that substantially affected the required weld process parameters for each of these two batches, so two unique sets of process parameters were developed for these two batches of bare material as well.

To establish a baseline for weldability of the new EFP material, AET briefly investigated the weldability of ZEK100 Mg provided by USAMP while awaiting delivery of EFP sheet. However, AET discovered this material had accumulated a thick hydroxide layer (possibly from long-term storage) that prevented any effective RSW evaluation without physically or chemically abrading the hydroxide layer before welding; Therefore, AET ceased work on ZEK100 material early in the project.

In developing the RSW process for EFP, AET investigated several factors such as bulk resistivity of EFP for comparison to commonly used Al and steel alloys, and electrical contact resistance of the bare EFP material (with no lubricant) with five different commercially available electrode cap geometries. These same electrode geometries were also investigated for each of the unique pretreatments without forming lubricants and with each of the two proposed forming lubricants from Fuchs and Quaker. In the end, AET identified that the common commercially available 50-mm radius F-type electrode and the GM proprietary Multi-Ring Domed (MRD) electrode held the best promise for welding all of the unique coating/lubricant configurations with only two unique electrodes. AET then optimized weld process parameters with these two electrode geometries to achieve the widest range of welding currents resulting in welds that met the minimum targeted weld size while not experiencing expulsion or cracking. Furthermore, AET identified that, with one exception, for both of the coil pretreatment choices (Henkel and Xtalic), one weld current range could be developed to successfully weld all three lubricant choices (no lubricant, Fuchs lubricant, and Quaker lubricant) for each coating/electrode combination. Unfortunately, in the case of the bare EFP Batch #3 with no pretreatment, the weld samples coated with Fuchs lubricant required dramatically higher weld current than the no-lubricant choice, so two sets of process parameters would be required in this case.

In developing laser welding processes for EFP, AET developed appropriate process parameters for welding bare EFP with a single spot fiber optic. Although an early preliminary feasibility evaluation was conducted with shielding gas, most of the laser welding process development was conducted without shielding gas. Once an appropriate range of welding process parameters were developed for bare EFP, the process was tweaked as necessary to achieve good welds on coated materials with and without forming lubricants. Due to substantial variation in coating and lubricant thickness, it was difficult to achieve robust welding processes on some of the coated materials, so wobble and defocus techniques were evaluated with the most difficult of these combinations (specifically, Xtalic Zn plating with Fuchs forming lubricant). While these efforts significantly improved the weld quality of this challenging combination, repeatability was still a challenge with all of the coating/lubricant configurations, so AET

also evaluated the TRUMPF BrightLine™ technology that provides greater flexibility for a finer level of optimization for welding unique materials and coatings. With limited trials, this technology was found to be more repeatable and capable of higher weld speeds, although additional process optimization would be required to achieve similar levels of weld quality to those produced without it. Since this technology produced more repeatable results, it was used for laser welding of all mini-door assemblies.

Because it was not clear whether commonly used fusion welding processes, such as RSW and laser welding, would be successful in welding the new Mg alloy (especially with coatings and forming lubricants), AET also investigated linear FSW to a limited extent as it was expected to be a potential back up process in case good welds could not be achieved with the more common fusion welding processes. AET was able to achieve good welds using FSW on both bare EFP and ZEK100 test samples.

AET also evaluated the Arplas resistance projection welding process as a potential process for producing welds for narrow door flanges, but due to technical limitations, opted to move resources from development of the Arplas process to focus more on development and optimization of RSW and laser processes, which are more common in the automobile industry and were proving to be more successful.

Finally, using knowledge gained in RSW and laser welding of the bare and coated EFP materials, AET produced bare and coated "mini-door" assemblies and provided them to PPG for corrosion evaluation of full assemblies in order to supplement the coupon evaluations they had been using to develop their coating processes. Detailed discussion of this work may be found at https://data.lightmat.org/project/.

E2. KEY ACCOMPLISHMENTS AND RESULTS

AET's overall objective for this project was to evaluate up to four commercially available joining methods and develop welding process parameters to join EFP Mg-based alloys in bare and pretreated conditions (with and without forming lubricants), and develop and optimize process parameters for down-selected commercially available welding processes as well as to perform mechanical testing to validate performance of the down-selected and optimized welding processes

E2.1 Materials and Coatings Evaluated
Due to the experimental nature of the project, AET was asked to evaluate several different batches of bare Mg sheet alloy materials, which were delivered from different sources and in different states of condition throughout the project. AET evaluated RSW weldability with several pretreatments that were still under development at their respective suppliers before settling on final chemistries. For example, Henkel originally developed a relatively thick polymer-based coating (Process C) that proved difficult to weld (at least with RSW), so Henkel also provided two new chemistries for AET to evaluate (Processes D and E) before settling on Process D. Similarly, Xtalic initially provided a small batch of their nano-Al pretreatment before being directed by USAMP to switch to the Zn coating in order to improve formability concerns and minimize production cost. AET did conduct some welding evaluations on this material prior to refocusing all efforts to the Zn-coated material.

Also, due to the experimental nature of the pre-commercial EFP alloy developed at POSCO, several batches of the material were produced on different scale-up rolling mills (to address different widths specified by USAMP) and provided to USAMP (and subsequently to AET) at different times and with differing textures and surface conditions. AET did not receive sheet material from EFP Batch #1 or Batch #4 but was provided adequate supplies of Batch #2 and Batch #3. Even though these two batches were essentially the same from a chemistry standpoint, the rolling conditions on these two different mills produced different textures that created differences in forming behavior. The Batch #2 material was very clean with a smooth finish while the Batch #3 sheet had a substantial level of surface oxidation and contamination that resulted in dramatically higher electrical contact resistance, which in turn resulted in

significantly different RSW weld process parameters than those that succeeded on Batch #2. Additionally, since the Batch #3 material was shipped much later than Batch #2, Quaker had already completed their research with Batch #2 and provided material samples to AET. Therefore, AET could evaluate the weldability of Batch #2 material with Quaker lubricant, but not Batch #3 with Quaker lubricant.

Finally, since the forming lubricants were applied by hand, the thickness (and wetness) of the lubricants varied greatly, especially for the Quaker lubricant samples. This resulted in inconsistent weld process parameter evaluation of the lubricated samples, not only from one batch to another, but even on the same coupons. In some cases, this inconsistency resulted in AET developing one set of process parameters that could weld one coating/lubricant configuration successfully on one day but not at all on another day if the material was taken from a different sheet.

Table E1 summarizes the materials, coatings, and lubricants that AET evaluated as well as the types of welding processes that were evaluated for each material/coating/lubricant configuration.

Table E1: Material/batch #/coating/lubricant/welding process evaluations conducted at AET.

Alloy	EFP Material Batch #	Pretreat	Forming lubricant	Weld process				
				RSW		Laser	Arplas	FSW
				AC	MFDC			
ZEK100	N/A	None	None	√	N/A	N/A	√	√
EFP	2	None	None	√	√	√	√	√
			Fuchs	N/A	√	N/A	N/A	N/A
			Quaker	N/A	N/A	N/A	N/A	N/A
	3	None	None	N/A	√	√	√	N/A
			Fuchs	N/A	√	√	N/A	N/A
	2/3	Henkel C	None	√	N/A	√	√	N/A
		Henkel D	None	N/A	√	√	N/A	N/A
			Fuchs	N/A	√	√	N/A	N/A
			Quaker	N/A	√	√	N/A	N/A
		Henkel E	None	√	N/A	N/A	N/A	N/A
		Xtalic Nano-Al	None	√	N/A	N/A	N/A	N/A
		Xtalic Zn	None	N/A	√	√	N/A	N/A
			Fuchs	N/A	√	√	N/A	N/A
			Quaker	N/A	√	√	N/A	N/A

E2.2 Resistance Spot Welding (RSW) Parameters Evaluated

E2.2.1 Bulk Resistance
Bulk resistivity is critical in RSW since it is the effect of the material bulk resistance in combination with the application of current from the welder that creates heat in the metal for welding. AET evaluated the bulk resistivity of EFP and ZEK100 as well as some selected steel and aluminum alloys in order to better understand optimum welding processes for comparison with these better-known materials. AET took five measurements for each material. As can be seen in Table E2, the bulk resistivity numbers of EFP and ZEK100 are actually very close to that of common automotive Al alloys (and even below for ZEK100).

Based on this information, it is apparent that existing knowledge of RSW welding process parameters for Al could provide reasonable guidance for developing RSW processes for RSW ZEK100 and EFP although electrical contact resistance will play a substantial role in these processes as well.

Table E2: ZEK100 and EFP measured bulk resistivity compared to select steel and aluminum alloys.

Material	Thickness (mm)	Grade	Coating	Average Resistivity (μΩ·cm)	STDEV (μΩ·cm)
Magnesium	1.5	ZEK100	Uncoated	5.07	0.052
	1.2	AZ21	Uncoated	7.00	0.155
Aluminum	1.2	5182	Uncoated	6.41	0.043
	1.1	E200 6xxx	Uncoated	6.00	0.065
Steel	1.2	CR240	Uncoated	15.83	0.189
	1.2	CR980DP	Uncoated	33.16	0.526
	1.2	980GEN3	Uncoated	49.55	0.467

E2.2.2 Electrical Contact Resistance
For material with coatings or a high level of surface oxidation or contamination, electrical contact resistance is a critical factor in resistance spot welding since it is the determining factor in heat build-up at the contact surfaces between the two sheets and between the welding electrodes and the sheets. In AET's research, electrical contact resistance plays the largest role in optimizing RSW weld process parameters for each coating/electrode/lubricant configuration. AET measured electrical contact resistance in single sheet and double sheet configurations in accordance with DIN standard procedure DVS2929-1. Single sheet configuration accounts only for the contact resistance between the electrodes and the sheet material being welded, while double sheet configuration also accounts for the contact resistance between the two sheets as well. Compared to the heavily oxidized ZEK100, the measured electrical contact resistance for the new EFP (Batch #2) material with no pretreatments or forming lubricants was substantially lower.

AET also measured electrical contact resistance of pretreated (Henkel Pretreatment C) EFP sheet material in both, single sheet and double sheet configurations, and found the contact resistance of the pretreated samples is substantially higher than that of the bare samples. Additionally, the contact resistance with the MRD type electrode is much lower than that for the radius faced F-type electrode.

The Xtalic Zn-coated samples showed the lowest contact resistance (even lower than bare EFP in the single layer configuration and dramatically lower than bare EFP in the two-layer configurations) while the Xtalic nano-Al coated samples showed lower contact resistance than bare EFP in the two-layer configurations but substantially higher contact resistance in the single layer configuration. As expected, Henkel's pretreatments D and E displayed lower contact resistance than pretreatment C in the double sheet configuration, although E showed unexpectedly higher contact resistance than C in the single sheet configuration. In general, the double layer configuration can be seen as more representative of actual welding conditions than the single layer configuration.

E2.2.3 Electrode Designs Evaluated
Due to the difficulties in achieving consistent welds with the B-type, E-type and F-type electrodes (see Figure E1a) on the Henkel pretreated material, AET also evaluated the GM proprietary MRD (Multi-Ring Domed) electrode for this coating. This particular electrode design, shown in Figure E1b, was developed at GM to weld aluminum and includes a number of grooved rings intended to cut through the oxide layer that typically develops on aluminum (and even to a greater extent on magnesium), so it was thought that

this electrode might be successful in cutting through the polymer-based Henkel pretreatment in order to obtain good electrical contact and produce RSW welds.
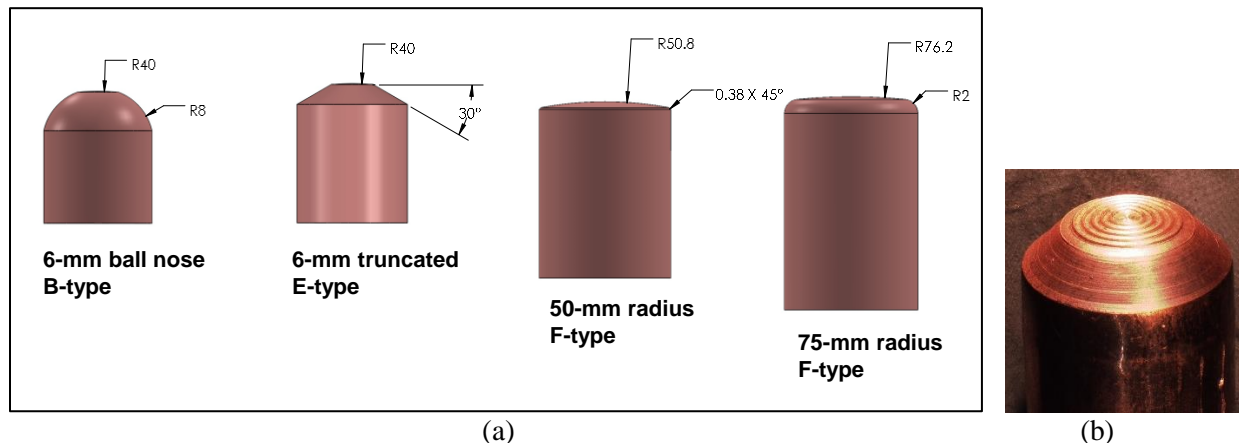

Figure E1: (a) Commonly used weld electrode types evaluated by AET and (b) GM's MRD design. (Sources: AET and GM)

The following summarizes AET's findings:

- The 6-mm ball nose electrode is not as suitable for welding EFP sheet material in the two bare configurations with no lubricant and with Quaker lubricant, while for the Henkel Process D coating, the 75-mm F-type electrode would appear least suitable. Both conclusions were verified during RSW weld process development.
- Increasing the weld force from 800 lbs. to 1,000 lbs. or 1,200 lbs. substantially reduced the double sheet contact resistance regardless of the electrode being evaluated.
- For the F-type electrode, electrical contact resistance (especially for double sheet) is significantly higher with Fuchs lubricant, and similar for Quaker lubricant. For the MRD electrode, resistance is also significantly higher for Fuchs lubricant but is significantly lower for Quaker lubricant.
- For both electrode types, electrical contact resistance is substantially higher for Henkel Process D (especially with the addition of the Fuchs forming lubricant) and substantially lower for Xtalic-Zn compared to bare EFP. For Henkel Process D, the MRD electrode exhibits a comparatively much lower single sheet resistance compared to the double sheet resistance, which could result in easier weldability of this pretreatment for this electrode. Additionally, measured resistance is substantially higher with the Fuchs lubricant regardless of electrode and/or pretreatment selection.
- The electrical contact resistance is far lower for the MRD electrode than the F-type in all cases.

E2.3 EFP RSW Results

E2.3.1 Alternating Current (AC) Weld Process Development

AET successfully RSW welded as-received bare (no pretreatment/coating) EFP (Batch #2) material using alternating current to produce consistent welds with no occurrence of surface melting. Welding process parameters were used to successfully produce welds that were then used for quasi-static shear tension testing. The lower joint strength for EFP compared to ZEK100 is most likely a result of the thickness difference between the two materials-ZEK100 material is 1.5 mm thick while the EFP sheet is only 1.2 mm thick. While AET could weld bare EFP Batch #2 material with a conventional F-type electrode, the newly developed Henkel pretreatment (Process C) created a substantial challenge with this electrode in that the polymer pretreatment would rapidly fuse to the weld electrode tips, dramatically increasing the electrical contact resistance resulting in high levels of porosity, cracking, or expulsion.

A welding schedule was developed for welding Henkel pretreated EFP with the MRD electrode.

E2.3.2 Electrode Life
Consistent with previous experience with other magnesium alloys, RSW of bare EFP Batch #2 sheet material with conventional radius faced electrodes displayed rapid deterioration of weld quality, requiring frequent tip dressing or cap replacement

E2.3.3 Experimental Pretreatment Evaluation
While AET successfully welded the Henkel Pretreat C material with the MRD electrode, the USAMP team was concerned with the requirement to use a proprietary electrode design for welding the coated material. Consequently, Henkel provided AET with material coated with two other formulations. Process D was a polymer-based pretreatment similar to Process C (although the coating was not as thick), while process E used more of an oxide layer rather than polymer. Even though Henkel Process D was easier to weld than Process C, it still presented a challenge for welding with the F-type electrode.

E2.4 Medium Frequency Direct Current (MFDC) Weld Process Development and Optimization
Since most of the automotive OEMS utilize MFDC RSW welding in their plants, AET focused on investigating this type of welding. In addition, to determine if other commercially available (specifically ball nose and truncated nose) electrodes could weld as well as the radius faced F-type and MRD electrodes, AET conducted preliminary MFDC weldability evaluations with these electrodes as well. Weld trials evaluated weld forces ranging from 800-1200 lbs. and weld times ranging between 30 and 60 ms. In these evaluations, none of the electrode types (6-mm ball nose and 6-mm truncated) other than the radius faced F-type and the MRD were successful in producing welds that met the American Welding Society (AWS) recommended minimum weld size (MWS) of $4\sqrt{t}$ (4.4 mm for the 1.2 mm thick EFP sheet) without cracks or expulsion, so AET focused only on the F-type and MRD electrodes going forward. The MRD electrode successfully welded all coating/lubricant configurations, although with the exception of the Henkel Pretreated material, the weld quality and process capability were not always as good as the 50-mm radius faced F-type.

Results of these MFDC weld studies are summarized in Table E3.

Table E3: Preliminary RSW Weld Process Evaluation Summary.

Electrode Type	Bare Batch 2			Bare Batch 3			Henkel Pretreat D			Xtalic Zn		
	No Lube	Quaker	Fuchs	No Lube	Quaker	Fuchs	No Lube	Quaker	Fuchs	No Lube	Quaker	Fuchs
Ball nose	↓	N/A	N/A	↓	N/A	N/A	N/A	N/A	N/A	↓	N/A	N/A
Truncated	↓	N/A	N/A	↓	N/A	N/A	↓	N/A	N/A	↓	N/A	N/A
F-type (50 mm)	↑	↑	↑	↑	N/A	↓	↓	N/A	N/A	↑	↑	↑
MRD	↑	↑	↑	↑	N/A	↑	↑	↑	↑	↑	↑	↑

↑   -   Indicates *"good"* welds were achieved, meeting target $4\sqrt{t}$ (4.4mm for this 1.2 mm thick material) nugget diameter with no expulsion or welding cracks and no interfacial fracture.

↓   -   Indicates *no "good"* welds were achieved meeting the target $4\sqrt{t}$ nugget diameter with no expulsion or welding cracks, and no interfacial fracture.

N/A   -   Indicates that no testing was conducted due to poor results observed in other coating/lubricant configurations or due to lack of material availability

"Good" -   Defined as meeting the MWS with no expulsion

For its optimization studies, AET focused on identifying one acceptable welding current range for each coating/electrode combination that could provide "*good*" welds for all of the three forming lubricant

choices (i.e., no lubricant, Fuchs lubricant, and Quaker lubricant). With appropriate electrode and force selection, AET found that expulsion-free welds meeting the AWS recommended MWS can be produced with simple single-pulse welding schedules.

The typical optimization process included:
- Overlaying weld size data (and identifying if expulsion was observed) and weld currents from studies conducted on each coating/lubricant combination to identify welding current ranges where ***"good"*** welds were achieved for all three lubricants for a given coating/electrode combination.
- Conducting additional welding studies at smaller current increments within the previously identified ranges to determine exactly where any specific coating/lubricant configuration experienced expulsion or failed to meet the target MWS.

Table E4 summarizes welding current optimization efforts for 50-mm radius F-type and MRD electrodes for 1,200 lbs. welding force and 50 ms welding time.

Table E4: MFDC RSW Welding process optimization summary for single pulse welds.

Material Coating	Welding Force (lbs.)	Welding Time (ms)	Electrode Type	Lubricant	Lower Current Limit (kA)	Upper Current Limit (kA)
Uncoated Batch 3	1200	50	50-mm F-type	None	14.4	17.8
			MRD	None	18.0	23.0
				Fuchs	24.2	N/A
Henkel Process D	1200	50	MRD	All	18.8	22.6
Xtalic Zn coating	1200	50	50-mm F-type	All	36.0	39.0
			MRD	All	36.4	37.6

As with the F-type electrode, for uncoated Batch #3 material with MRD electrode, no Quaker lubricant was available, so again the optimization efforts focused on the "no lubricant" and "Fuchs lubricant" combinations. While it was possible to achieve good welds with the MRD electrode for both the "no lubricant" and "Fuchs lubricant" configurations, it was not possible to achieve good welds for both lubricant choices using the same process parameters.

For EFP material coated with Henkel's Process D, it was not possible to obtain good welds with the F-type electrode (or as previously noted, with the 6-mm truncated electrode), so AET focused all efforts on the MRD electrode for welding material with this coating. Interestingly, for this coating, the selection of forming lubricant had little effect on the ability to achieve good welds. The samples with Quaker lubricant did seem to experience significantly less intermittent expulsion than the "no lubricant" and "Fuchs lubricant" configurations. Consequently, the upper welding current limit for this coating was established based on the onset of expulsion in the samples with Quaker lubricant.

For EFP material coated with Xtalic's zinc coating, the electrical contact resistance is substantially lower than even for the uncoated material, so it was easily possible to weld with either the F-type or MRD electrode. In both cases, AET was able to identify potential common welding schedules that would accommodate all three lubricant choices.

E2.4.1 Hot Cracking

While AET was able to develop welding schedules resulting in acceptable expulsion free welds meeting the recommended MWS for all material coating/lubricant combinations, intermittent hot cracking was observed in almost all coating/electrode/lubricant configurations. This hot cracking was not always easily visible in the as-welded condition but was easily seen after cleaning the weld with acetic acid to remove oxides. AET investigated modifying several process parameters to mitigate the occurrence of hot cracking. Shorter welding times resulted in substantially more instances of hot cracking while longer welding times resulted in fewer instances of hot cracking, but a compromise is required between larger weld size and increased instances of hot cracking.

AET also evaluated varying MFDC electrode cooling water flow rate and welding hold time while maintaining a consistent current of 18.5 kA. It appears qualitatively that higher electrode water flow rate combined with shorter welding hold time may reduce the degree of hot cracking for this material and welding process parameters, at least within the limitations of this study. Additionally, it appears that the shorter hold time has greater influence than the increased electrode water flow rate.

E2.4.2 Electrode Life

Starting with a clean electrode cap at 16.0 kA welding current, close to 200 good welds were achieved before the weld diameter dropped below the recommended MWS.

E2.5 Laser Welding (LW)

E2.5.1 Initial Feasibility Study (with shielding gas)

Early in the project, AET contracted Fraunhofer USA Inc. to conduct an initial feasibility assessment of laser welding of bare EFP Batch #2. For this study, Fraunhofer used shielding gas. Seven different laser welding tests were conducted with multiple process parameters being evaluated. A spot size of 400 μm (with comparatively lower speed and power levels and higher shielding gas flow rates) was found to produce the most stable welds, successfully achieving full and partial weld penetrations, although some pores and micro cracks were observed in and outside the weld.

E2.5.2 AET Laser Welding Process Development (without shielding gas)

Figure E2 compares quasi-static joint strength of the best laser welds produced for each coating/lubricant configuration for welds produced at 800W. Clearly, the welds produced on Xtalic Zn coated material, especially with Fuchs lubricant, exhibit lower strength than those produced on bare material or Henkel-coated materials.

To improve the weld quality of the worst of the Xtalic Zn coated configurations, AET evaluated wobble and defocus techniques for welding Xtalic Zn coated material with Fuchs lubricant. Even though AET was able to produce high quality welds with a conventional single spot laser weld process for all coating/lubricant configurations (although Xtalic Zn with Fuchs lubricant required wobble and defocus techniques), the results were not necessarily repeatable. To achieve five good welds for quasi-static shear strength testing, anywhere between 5 and 16 welds were required as can be seen in Table E5. It should also be noted that this repeatability evaluation was conducted prior to the evaluation of wobble and defocus for Xtalic Zn with Fuchs lubricant, so it is possible the results for the Xtalic Zn plated configurations may be improved with the addition of these two techniques.
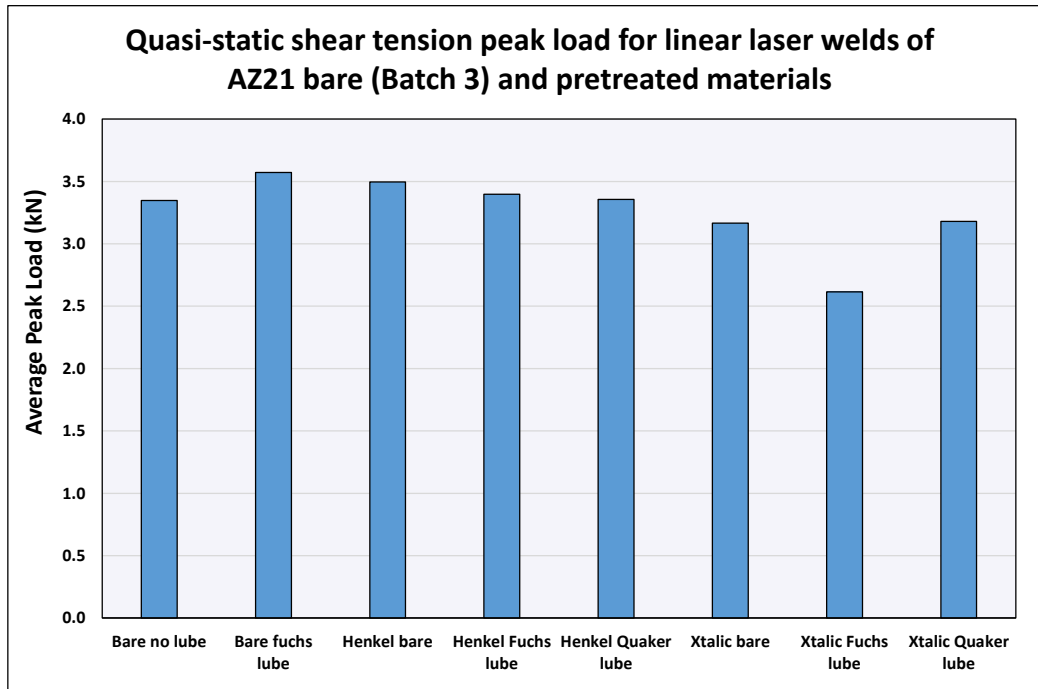
Figure E2: Quasi-static test results for laser welded EFP Batch 3. (Source: AET)

Table E5: Repeatability of single spot laser welding of EFP material.

Repeatability of standard single spot welds without wobble, defocus					
Coating	Lubricant	Weld Power (W)	Attempts	Successful	% Successful
Bare Batch 3	none	800	9	5	55.5%
		1000	8	5	62.5%
	Fuchs	800	8	6	75.0%
Henkel	None	800	10	6	60.0%
	Fuchs	800	9	7	77.8%
	Quaker	800	6	5	83.3%
		1000	5	5	100.0%
Xtalic	None	800	16	5	31.2%
	Fuchs	800	16	5	31.2%
	Quaker	800	7	5	71.4%

Due to material coating variability, AET evaluated the TRUMPF BrightLine™ technology to see if this technology could improve weld repeatability. From limited trials, this technology was found to be more repeatable and capable of higher weld speeds, although additional process optimization would be required to achieve similar levels of weld quality to those produced without this technology. All the laser welds on the deliverable mini-door assemblies were produced with this technology with a 100% success rate.

E2.6 Laser Welding Trials

As shown in Table E6, AET achieved target welds in all coating/lubricant combinations with the 800W single spot fiber laser with 2.5 mm ramp down, and with the 1000W single spot fiber laser with 2.5 mm ramp down for bare Batch #3 sheet with no lubricant and for Henkel Process D with Quaker lubricant. Xtalic-coated specimens required less energy (faster travel speed) than bare or Henkel coated samples, but these samples were more likely to exhibit open pores at the faying surface. Henkel-coated specimens required more energy (slower travel speed), but the welds exhibited fewer open pores and less cracking.

Table E6: EFP Optimized laser weld parameters for single spot laser with no shielding gas.

Coating	Lubricant	Optimum Welding Speed (m/min)			
		Standard laser with 2.5 mm ramp		With wobble	With Brightline
		800 W	1000 W	875 W	800 W
Uncoated Batch 3	None	2.2	4.0	N/A	3.4
	Fuchs	2.8	N/A	N/A	N/A
	Quaker	N/A	N/A	N/A	N/A
Henkel Process D	None	2.6	N/A	N/A	N/A
	Fuchs	2.6	N/A	N/A	3.4
	Quaker	2.4	4.4	N/A	3.2
Xtalic Zn	None	2.8	N/A	N/A	N/A
	Fuchs	3.4	N/A	2.6	4.0
	Quaker	3.2	N/A	N/A	3.8

E2.7 Arplas Resistance Projection Welding (RPW)

The Arplas welding process is a resistance projection weld process that utilizes a long, narrow dimple punch to create a similar long, narrow projection in one of the two welded sheets in order to produce a projection weld that is suitable for narrow automobile flange welding. AET evaluated the Arplas welding procedure using two different commercially available dimple punch geometries developed and provided by Arplas for steel and aluminum welding applications. In Arplas welding, the dimple punch is the feature that forms the projection in order to achieve the projection weld. At this time, Arplas has not developed a geometry specifically for magnesium sheet applications.

Two Arplas welding schedules were developed and evaluated for bare EFP and Henkel Process D, but a key takeaway is that if Arplas welding is to be used with EFP, then substantial additional development work would be required to eliminate forming and welding cracks, or the user may need to choose between having visible surface cracks and substantially lower weld strength.

E2.8 Friction Stir Welding (FSW)

AET briefly evaluated linear friction stir welding on ZEK100 and EFP. Since FSW is a solid-state joining process that does not rely on electrical current and resistance to develop heat and fuse the material, it was expected that this process would be successful in joining the heavily oxidized ZEK100 as well as coated EFP materials expected later in the project. Indeed, even with no attempts to remove the thick ZEK100 hydroxide layer, which created so much difficulty for RSW welding, AET was able to develop process parameters to successfully weld this material.

Once the EFP material became available, AET evaluated friction stir welding. This material did not have a thick hydroxide layer like the ZEK100 material and was not expected to pose any difficulties for FSW, and it did not. AET was able to develop process parameters to successfully weld this material.

It should be noted that FSW pin and shoulder geometry are typically sized for the material thickness with smaller pin and shoulder geometry used for thinner materials. If FSW were to be used with this material in a production process, it may be worthwhile to investigate additional pin and shoulder geometries to optimize weld strength.

E2.9. Fabricated Mini-Door Assemblies

AET produced and shipped 17 "mini-door" assemblies to PPG for corrosion evaluation of complete welded assemblies with features representative of doors. Figure E3 shows the full size mini-door schematic, the full-size welded assembly (prior to hole cutting of the longer panel done at PPG), and close up views of the top and bottom sides of the welded portion of the mini-door assembly. These mini-door assemblies were used for the evaluation of PPG's novel body-shop applied pretreatment formulations and coatings aimed at protecting body-in-white assemblies, as well as bare edges and crevices on assemblies produced from sheet material that had been previously pretreated by either the Henkel process or the Xtalic process. Some of these samples also included residues of forming lubricants from either Fuchs or Quaker in order to simulate a real-world automotive production coating process.

All mini-door assemblies were welded using a combination of RSW and laser welding processes after developing acceptable process schedules to ensure that the two most production-friendly welding processes were being evaluated as well as the corresponding pretreatments and forming lubricants. The MRD electrode was used for RSW welding of all bare and Henkel pretreated assemblies while the 50-mm radius F-type electrode was used for all Xtalic pretreated assemblies. It should be noted that while most of the mini-door assemblies were welded with the same optimized RSW process parameters developed for single pulse MFDC (discussed earlier in the report), for the Henkel Process D with Quaker lubricant combination, the process had to be altered to a multi-pulse MFDC process in order to achieve good welds on these larger panels. Additionally, the laser welds were all produced with the TRUMPF BrightLine™ process since this process was found to be more repeatable.
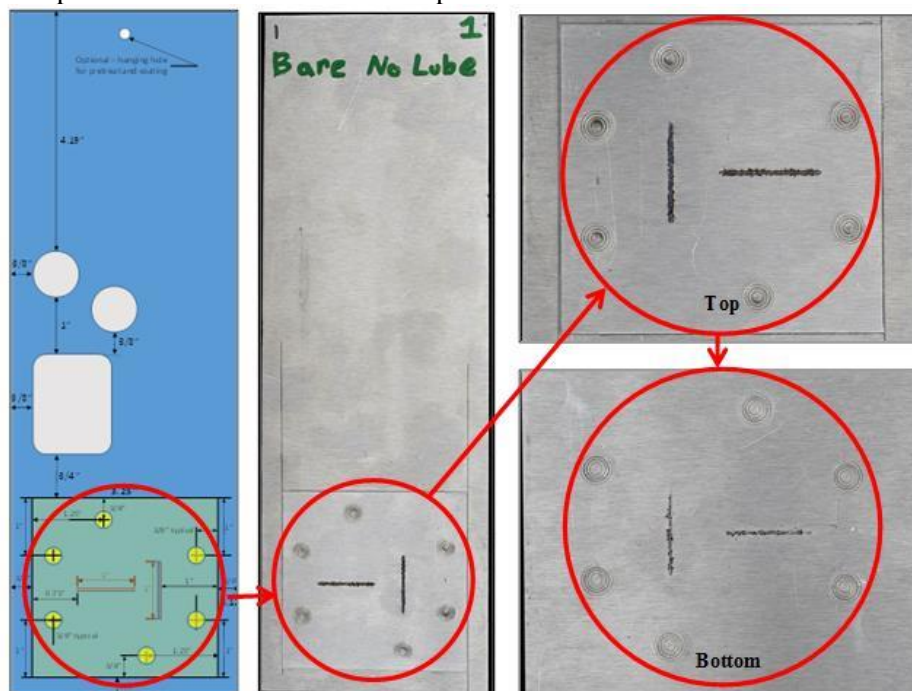

Figure E3: Mini-door assembly schematic (left), full welded assembly (center), and close-up top and bottom views of welded area (right) for bare EFP Batch #3 material with no lubricant.

E3. CONCLUSIONS AND RECOMMENDATIONS

The main accomplishments of Task 4 research by AET Integration included evaluation of RSW, laser, Arplas, and FSW welding processes to determine which processes could be successful in welding EFP material in the bare (uncoated), Henkel Process D, and Xtalic Zn coating configurations without forming lubricants, and with Fuchs and Quaker lubricants. AET focused most of their effort on RSW and laser since these are the welding processes most commonly favored in automotive OEM assembly plants. Welding schedules were developed and documented in AET's final task report. Additionally, AET evaluated Arplas resistance projection welding since this is a newly developing process gaining some favor for welding narrow flanges without requiring a totally new laser body shop. Finally, AET briefly evaluated FSW, which is a solid-state welding process (therefore less likely to be affected by surface coatings or oxidation or the formation of cracks of brittle inter-metallics resulting from the high heat levels of fusion welding), for welding of ZEK100 and bare EFP Batch #2. However, in order to prioritize the project resources on processes that were more likely to be widely used in the automotive industry, the FSW work was discontinued early in the project.

For laser welding, early in the project, prior to establishing an on-site laser welding lab, AET engaged Fraunhofer USA Inc. to conduct an initial feasibility study on bare EFP Batch #2. Fraunhofer employed a shielding gas in their studies and they successfully welded this material using several different process schedules. Later in the project, AET conducted laser welding studies without shielding gas. This turned out to be a greater challenge. Nevertheless, AET was able to successfully weld all of the coating/ lubricant combinations with a single spot optic fiber at 800W power. Although timing and budget constraints prevented AET from optimizing process parameters for all combinations, the results do indicate good direction for potential future optimization efforts. AET was successful in joining all coating/lubricant configurations, except for Xtalic with Fuchs lubricant, with a standard continuous single spot laser weld with a 2.5 mm ramp down to 400W. For Xtalic with Fuchs lubricant, AET produced acceptable welds by adding wobble and defocus techniques to the process. Additionally, TRUMPF's BrightLine^{TM} process technology was evaluated on several configurations and resulting welds were far more repeatable and at higher weld speeds, although additional process optimization, potentially incorporating wobble and defocus techniques along with the BrightLine^{TM} technology, would be required to achieve similar weld quality to those produced without BrightLine^{TM}.

For Arplas welding, which is a unique resistance projection welding process, AET found some significant challenges related to forming cracks when creating the formation in the EFP material. However, once AET was able to form the projections without cracking, then the actual welding process resulted in visible surface cracks as well unless the energy level was reduced substantially below that typically used for steel or Al. Once the energy level was reduced to this extent, then the weld strength was dramatically reduced to a level substantially below that of RSW. Additionally, cross sections at this reduced power level still revealed substantial internal cracks and porosity. Development of a unique dimple punch especially designed for Mg (Arplas' current dimple punch selections were all developed for steels and Al) might help with to achieve better welds with this technology, but development of a new dimple punch geometry was not part of AET's scope of work for this project.

AET only conducted a brief evaluation of linear FSW for bare ZEK100 and bare EFP Batch #2. Not surprisingly, since this is a solid-state process where the substantial oxidation on the surface of the ZEK100, the FSW process was easily able to produce good welds with both ZEK100 and bare EFP Batch #2. Because none of the automotive OEMS is currently using FSW in their assembly plants, AET opted to discontinue development work with FSW.

AET also produced 17 "mini-door" assemblies with RSW and laser welds to support PPG's corrosion studies. The welding processes used for producing these "mini-door" assemblies were mostly those that

had been developed and optimized in previous RSW and laser weld process development work with some modifications (especially, the use of the BrightLine™ technology to improve repeatability of laser welds).

E3.1 Contributions to the State of the Art
AET's key contributions to the state of the art for welding EFP sheet Mg revolved primarily around identifying optimum commercially available RSW electrodes and developing successful RSW welding process parameters and laser welding process parameters to repeatably weld not just clean, bare Mg sheet, but also coated Mg sheet with and without forming lubricants. This is critical since most previous welding studies with Mg sheet have involved cleaning the sheet to remove any coatings or oxidation prior to welding – this step adds to process cost and cycle time, and hence, would not be practical for the high production volumes required by the automobile industry.

E3.2 Key Technology Gaps
The following technological gaps remain for achieving production-scale welding of EFP Mg sheet:

- Eliminating intermittent hot cracking (and even sometimes expulsion) in RSW for all coating/lubricant combinations. Some efforts at AET, such as increased electrode cooling water flow rate and minimizing weld hold time after weld, showed qualitative improvements, but were identified too late in the project to conduct larger scale quantitative studies. Additionally, AET identified that additional forging force applied near the end of the welding process may be able to mitigate hot cracking as well, but AET was not able to evaluate this within the timing of the project. Additionally, the very short welding time for this material (typically, 50 ms) may create a substantial challenge to implementing forging force late in the weld cycle.
- Optimizing laser welding process parameters for all coating/lubricant combinations was not possible within the project timing. Further optimization around the preliminary process parameters (especially when combined with BrightLine™ technology) should be able to substantially improve laser weld quality and repeatability on all desired coating/lubricant combinations.
- Welding with adhesive was not evaluated. Since the addition of adhesive can substantially alter the electrical contact resistance between the two sheets, as well as the thermal conductivity around the weld, then any future projects involving welding of Mg alloys (especially with coatings) should include adhesive as well.
- Due to lack of a dimple punch specifically designed for Mg, AET was unable to develop robust projection formations to really take advantage of the projection welding process of Arplas welding. This may have adversely affected the ability to produce good, crack free welds as well.
- Production of tailor welded blanks (using laser welding, FSW, or both), preferably from dissimilar material thickness is a key technological gap that was never investigated as part of this project. A project including this aspect of welding Mg sheet would be desirable and should include evaluation of forming the tailor welded blanks as well. Forming of tailor welded blank has been shown to be a challenge with Al (due to reduced strength and elongation in the weld zone), so it would be desirable to see if tailor welded blank welding (and subsequent forming) could be successful with Mg.
- Dissimilar welding of Mg sheet, if not necessarily to Al or steel, then at least to other Mg alloys or other coating/lubricant configurations, would be desirable since in a production environment, Mg sheet may be sourced from more than one supplier, and different stamping suppliers may prefer to use different forming lubricants. If using technologies developed in this project, then it would be worthwhile to at least weld EFP with Henkel Pretreat D and Fuchs lubricant to EFP with Henkel Pretreat D and Quaker lubricant or Henkel Pretreat D to Xtalic Zn plate, etc.

Chapter F. Task 5: Produce and Provide Large Sheet

F1. SUMMARY

The principal objective of Task 5 undertaken by USAMP was to acquire magnesium alloy sheets large enough to be able to yield blanks sized for stamping of door inner and outer panels. The task began with the USAMP supplying ZEK100 Mg sheet for baseline evaluations by the team members while awaiting lab-rolled test sheets of samples of new USAMP Experimental Alloys 1 and 2 from POSCO with USAMP-specified alloy constituents. Later, E-Form Plus (EFP) was selected for sourcing medium and wide width sheets due to considerations of meeting project schedule and requirements for large quantities of sheet needed for door panel forming, mechanical property testing, characterization, and corrosion coatings/lubricant studies. Hence, EFP was designated as the USAMP's preferred alloy, and was rolled by POSCO in various mills to provide new sheet material in USAMP-specified widths large enough to produce intermediate test parts (such as cross-forms) and automotive body components. Four batches of EFP medium and wide sheets were delivered to USAMP over the duration of the project.

F2. KEY ACCOMPLISHMENTS AND RESULTS

F2.1. Sheet Acquisition Considerations
The initial goal of the USAMP LCMS Project was to successfully stamp magnesium at ambient temperatures to 100ºC. Towards this goal, the project team adopted an integrated approach by establishing a closed process chain for magnesium alloy sheet acquisition, multiple iterative phases of alloy design/testing through scale-up, and by involving capable suppliers to produce high quality sheets in a pre-commercial industrial environment by implementing alloying, ingot casting, rolling, annealing and stamping guidelines derived from experimental characterization by USAMP's university and National Laboratory partners as summarized below.

At the project kickoff in 2016, it was envisioned that together with the planned multi-thrust sheet approach for formability testing, coating and characterization studies, an iterative robust alloying, rolling and recrystallization process could be designed and implemented to provide USAMP with an automotive grade Mg sheet wide enough to stamp the complex shaped demonstration door components. However, there was only one volume-capable magnesium sheet rolling source in North America with a limited capacity for supplying commercially available sheet Mg alloys suitable for large automobile component applications. The supplier was unable to commit resources towards developing the new alloy and manufacturing it in pilot rolling runs to deliver the 550 mm and 1600 mm width magnesium sheets in the quantities needed for the validation of material and forming models. The USAMP also desired a partner capable of investing in industrial equipment and processes to produce wide width sheets for the demonstration door inner and outer panels. Therefore, USAMP obtained a non-domestic work waiver from DOE to procure these wide width sheets from POSCO (a Korea-based Mg sheet manufacturer), starting with experimental alloys specified by USAMP.

The sheet acquisition strategy for the project was comprised of the following three sub-tasks which are summarized below:
1. Provide AZ31 and/or ZEK100 Mg sheet for baseline evaluations.
2. Provide new proposed sheet material based on alloy development activities in Task 2.
3. Scale up equipment to provide new proposed sheet material in widths large enough to produce automotive body components.

F2.1.1. Provide AZ31 and/or ZEK100 Mg sheet for Baseline Evaluations
General Motors contributed a large batch of ZEK100 Mg sheets soon after Technical Kickoff was held in June 2017, which were used to get the research teams started in developing test protocols, while the USAMP finalized sheet requirements across all other sub-tasks in order to develop the POSCO statement-of-work and determine a schedule for delivery of a non-basal (randomized) textured experimental alloy and wide sheet derived from continuous cast Twin Roll Casting (TRC). Magnesium sheet made by the TRC process is expected to be less expensive than that made by the direct-chill (DC) casting process because fewer reheating and rolling steps are needed to achieve the final desired sheet thickness of 1-3 mm. TRC sheet is cast at just 6 mm thickness, whereas DC slab is 300 mm thick,

Compared to AZ31B, ZEK100 is a relatively new alloy, only available over the past few years. This alloy has displayed improved formability over AZ31B, with increased elongation and reduced anisotropy. However, the enhancements have not been sufficient to substantially reduce the cost of the sheet material, or improve its corrosion performance, or eliminate the need for warm-forming. Moreover, the as-received ZEK100 sheets had significant oxidation layers on their surfaces due to long-term storage at GM. The native oxide layers on the surface needed to be removed before strength testing, coating, joining or plating studies could be undertaken in order to ensure consistency of performance and establish a metal-to-metal interface and adequate adhesion between the layers (in case of plating by Xtalic). Clearly, these two baseline Mg alloys have very different mechanical properties due to the different texture and twinning behavior, and therefore, different forming limits. As reported in Chapter E, from initial resistance spot welding (RSW) trials, AET determined that due to the high contact resistance of the as-received ZEK100 samples, rapid heat generation results in expulsion and poor-quality joints. Using ZEK100 further would require sandblasting or cleaned and deoxidized surfaces. However, friction stir welded (FSW) joints of ZEK100, resulted in a higher peak load due to the larger specific weld area. But (as summarized in Chapter E), in comparison to RSW or laser welding (LW), FSW is not a mainstream or well-understood welding process in production automotive assembly.

Since there was a good amount of data and modelling for AZ31B and ZEK100, based on published data and the USAMP team's experience, the research team evaluated the following additional considerations while identifying data gaps that resulted in a strong case for examining a different Mg alloy sheet for the remainder of the project: strength and ductility levels, in-plane anisotropy of strength and ductility, r-value, tension/compression asymmetry, and crystallographic texture.

F2.1.2. Provide New Sheet Material Based on Alloy Development Activities.
After three quarters of testing and characterization, a decision was reached by the USAMP from sub-awardee feedback to replace the ZEK100 material with E-Form Plus (AZ21) sheets sourced from POSCO, a leading material and technology provider for magnesium rolled products. USAMP contracted with POSCO as a vendor (and not a sub-awardee/co-developer as initially intended), primarily due to (1) POSCO's internal limitations of their strip-casting process (e.g., inability to use Sn as alloying element), and (2) their administrative concerns with accepting USAMP terms and conditions. The USAMP Task 2 team held additional technical reviews before reaching consensus to recommend two new USAMP-specified experimental alloys for POSCO to consider for supply.

In late 2017, USAMP and POSCO finalized a mutually acceptable plan for simultaneously procuring a first batch of EFP (referred to as Batch #1) new Mg sheet material and securing POSCO's support for lab-scale warm rolling trials on the two USAMP-specified experimental alloy compositions cast as ingots by Korea Magnesium Industry (KMI).

Subsequently, alloy design studies were conducted by OSU using CALPHAD modelling and PANDAT (to seek preferred temperature ranges for homogenization and hot work) and the results used by USAMP

to specify and source two 200 kg batches of cast ingots from KMI for POSCO and USAMP's rolling trials and characterization studies by the team:

1. **USAMP Experimental Alloy 1 (Mg-2.98Al-1.01Sn-0.40Mn-0.30Zn):**
   Experimental rolled thin strips were received in March 2018, followed by 180 kg of ingot. As summarized in Chapter C (UF and UM reports), given the low mechanical strength and strong basal texture, this alloy was not investigated further.

2. **USAMP Experimental Alloy 2 (Mg-2.10Zn-0.52Ca-0.42Mn-0.21Ce):** Experimental rolled thin strips were received in July 2018, followed by 180 kg of ingot.

From each Experimental Alloy ingot production by KMI, POSCO was to retain 20 kg ingots for rolling trials at their pilot mill, to supply USAMP with samples of thin strips (~ size 1.2 mm x 100 mm x 400 mm) for further characterization and formability studies by USAMP partners. The as-received alloy composition report from KMI is provided in Table C1.

Upon receipt at GM R&D (the USAMP's designated Mg inventory storage and distribution location for the project), the experimental rolled thin sheet samples of Alloy 1 and 2 were transferred to the UM and OSU for evaluation and characterization studies. Their findings and recommendations are reported in Chapter C of this report, and in more detail in the respective sub-task final reports available on DataHUB.

Alloy 2 Plus: As a result of analysis and TMP trials on Alloy 2 ingots by OSU and later at ORNL, OSU developed and demonstrated a new alloy chemistry, Alloy 2 Plus (Mg-1.0Al-1.0Zn-0.5Ca-0.4Mn-0.2Ce), based on computational thermodynamic calculations. The USAMP evaluated samples of Alloy 2 Plus with EFP in deep-draw cup trials (reported in Chapter C5).

F2.1.3 Scale-up Considerations for New Mg Sheet Material in Wide Widths
The following first three batches of twin-roll cast EFP sheets were sourced in from POSCO to meet the USAMP's scale-up sheet requirements for coating, simulation modeling and formability demonstration studies – the fourth batch of EFP was purchased from successor Pinetree Pos Magnesium (PPM):

1. **POSCO Batch #1:** 50 pcs Mg sheets of EFP (designated B1, size 1.2 x 1580 x 1700 mm), delivered December 2017 to GM R&D.

2. **POSCO Batch #2:** 620 pcs Mg sheets of EFP (designated B2, size 1.2 x 510 x 610 mm), delivered May 2018 to GM R&D.

3. **POSCO Batch #3:** 80 pcs Mg sheets of EFP (designated B3, size 1.2 x 1190 x 1600 mm), with 30 pcs delivered May 2019 to GM R&D, and 50 pcs delivered to Promatek, Toronto, Canada.

4. **PPM Batch #4:** 200 pcs Mg sheets of EFP (designated B4, size 1.2 x 1550 x 1500 mm), delivered September 2020 to Promatek.

For iterative FEA-based simulation modeling of door panel warm-forming in Task 6, the USAMP Data Fit Team (led by Vehma) needed complete datasets on high-strain-rate flow curves for a range of temperatures, as well as thermal, and Coefficient of Friction parameters in order to anticipate formability challenges prior to successful demonstration of the selected door inner and outer panels. Development of these "complete datasets" would only be possible by (a) acquiring a Mg alloy sheet material rolled from a stable, pre-commercial process that is available in sufficient quantities for USAMP's tests, (b) conducting extensive material testing for measuring statistically consistent mechanical properties, and (c) determining the material's formability limits – these were the team's pre-requisites to develop a baseline material card compatible with the LS-DYNA FEA modeling package. The team also determined the modelling technology gaps for a thermo-mechanically formable Mg alloy and recommended that software developer

Livermore Software Technology Corporation (LSTC) was in the best position to enhance the baseline Cazacu[1] material card in LS-DYNA which can better handle the material asymmetry of Mg sheet than other available FEA packages. Vehma agreed to run forming simulations in LS-DYNA if proper guidance was received from LSTC on the enhanced material model. With these additional considerations of extensive property measurement needs for simulation modelling, and recognition of long lead times in procuring new Mg alloy sheet stock, POSCO was the only viable source within the project's timeframe.

Moreover, the team members testing EFP Batch #1 and #2 sheet materials reported the as-received sheet surfaces were much cleaner and smoother than the ZEK100, and free of oxidation. Hence, the task team saw immediate improvements in the EFP Mg alloy sheet's ability to hold coating, as well as noted its superior surface finish and quality. Deep draw cup forming trials were run by the UM to assess warm formability, as shown in Figure F1 below, after which a decision was taken to source additional quantities of the EFP sheet material to meet the project's scale-up requirements for demonstration components.
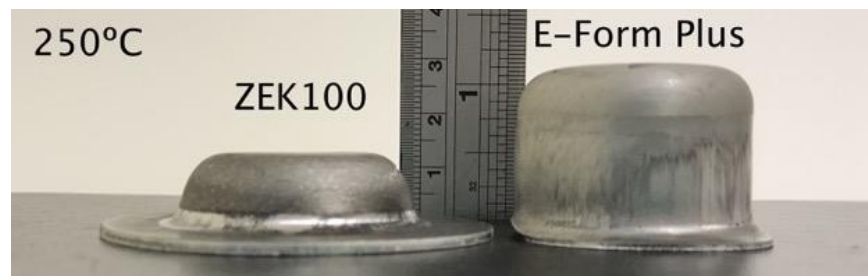

Figure F1: Comparison of deep draw cups at 250ºC. (Source: UM)

As described in report Section C7, PNNL conducted room-temperature quasi-static tension tests on EFP Batch #1 sheet and showed that the as-received sheet is relatively isotropic in its in-plane tensile behavior. The Young's modulus of EFP Mg was similar to that reported in the literature. This relatively isotropic behavior of EFP contrasted with the significantly anisotropic behavior (yield stress and work-hardening) of ZEK100 sheet that PNNL had previously tensile tested in the earlier stages of this project and had major implication on the direction and technical approach taken for development of baseline and enhanced material cards for Vehma's simulation modeling needs.

The USAMP contracted with FADI-AMT for specialized tests on EFP sheets such as: elevated temperature tensile tests with DIC, in-plane compression testing, shear testing, hydraulic bulge testing, heat transfer coefficient determination and strain path testing. The test reports on EFP Batch #1, #3 and #4 were uploaded to DataHUB and were used by UPenn and InalTech for the phenomenological material model, model calibration and cross-form simulation studies (see report Section C8).

Majority of EFP Batch #2 sheets and a portion of Batch #3 sheets were sent to Task 3 and Task 4 sub-awardees to evaluate EFP's potential to meet the USAMP's requirement for coil pretreatments which can survive the downstream forming, welding and paint-shop process for application of corrosion coatings.

In February 2019, POSCO management began re-evaluating the viability of their magnesium sheet product line, and informed USAMP they may no longer be able to produce EFP wide sheets in their rolling mill. With this uncertainty in a stable supply of EFP, the USAMP took steps to acquire additional sheets and to conserve the wide sheets for door forming. Available EFP wide sheets in the 1.2 mm thickness gage were purchased from POSCO, resulting in the delivery of 80 sheets of Batch #3 in May

---

[1] Cazacu, O., Plunkett, B. and Barlat, F., 2006. Orthotropic yield criterion for hexagonal closed packed metals. *International Journal of Plasticity*, *22*(7), pp.1171-1194.

2019. USAMP also developed a backup plan with Vehma to conduct die tuning tryouts with Aluminum 5182-O sheets, prior to using EFP Mg sheets for final forming demonstrations with door panels. USAMP also scaled-down the EFP full-size door panel design parameters to fit PPG's smaller corrosion and coatings test apparatus. Thus, a "mini-door" design was developed, incorporating several features of a full-size door (such as spot-welds, laser weld, cutouts, self-pierce rivets, etc.) to facilitate PPG's corrosion testing as reported in sections D5 and Chapter E.

After POSCO spun-off their magnesium sheet business through startup Pinetree Pos Magnesium (PPM) in Fall 2019, USAMP took delivery of 200 sheets of EFP Batch #4, which were air freighted in small batches in July 2020 (to begin mechanical property tests early), followed by sea freight delivery of the wide sheets to Promatek for door panel forming trials – details of forming trials are in section G3.

F2.2. Batch-to-Batch Variations in EFP Sheet Properties:

During routine tensile tests on as-received EFP by GM R&D and Fadi-AMT, it was determined that these mechanical tests conducted on three different batches of EFP (B1, B2 and B3) sheet samples showed varying degrees of in-plane anisotropy. This issue raised new questions the modeling teams had about the chemistry and processing conditions used for each of the three EFP batches supplied by POSCO. Due to POSCO's announcement in April 2019 of their exiting the magnesium business, it was unclear whether urgent clarifications on these batch-to-batch variations and rolling/heat treat history would be received in a timely manner. Therefore, the USAMP conducted its own independent chemical composition analysis, mechanical testing and microstructural studies to understand these differences in the EFP sheet batches.

GM R&D Laboratory led the alloy composition tests on the three batches of EFP, with support from UM, Henkel and FADI-AMT who also conducted certain material and formability tests. After factoring expected variances across different test labs, USAMP concluded that the batches had identical chemical compositions and met the EFP specification. Figure F2 summarizes these tests, and Table C1 (see report Chapter C) lists the results of chemical analysis on the four batches.

Since POSCO clarified the sheet batches were produced on different rolling mills and at different times, the compositions were not expected to be identical, but were found within the defined tolerances. These measurements of the wt.% of the most important alloying elements are consistent with each other. Post-processing of the stress-strain DIC data for Batches #1 and #3 showed that both curves have similar hardening behavior; thus, test data from both batches were used in to generate the LS-DYNA MAT 233 and MAT233+ material cards.

Test	Test Source	Batches	Sample Size	Samples/ Batch	Parameters	Notes	Test Status
Composition	GM	1, 2, 3	3"x3"	2	Need correct standards for Magnesium	Results show similar compositions meeting EFP specification.	Complete 10/05/2019
Surface and substrate - GDOES	Henkel	1,2,3	1"x1"	2	Surface GDOES and Substrate GDOES	Results show similar composition range and thickness. This technique cannot be used to distinguish batches.	Complete 12/09/2019
EBSD - Texture	U of M	3	1"x1"	1	UofM defined procedure for 1mm²	Batches have different textures: Batch 1: Quad-peak, Batch 2: Near-basal, Batch 3: Split peak	Complete 12/05/2019
Tension - RT	Fadi AMT	1,3	E8	5	0, 45, 90 degrees. Strain rate = 0.004/s	DIC analysis complete.	Complete 10/10/2019
Tension - 200C	Fadi AMT	1,3	E8	5	Tensile specimen Full size E8 DIC & Certification of load cell.	DIC analysis complete.	Complete 10/10/2019
Erichsen Cup (Dome) - RT	U of M	3	100x375 mm	5	Ball Diameter of 25mm	Batch 1 = 6.2 mm Batch 2 = 4.6 mm Batch 3 = 6.5 mm	Complete
Erichsen Cup Deep Draw - 200C	U of M	1,3	65 mm dia	3	Preheated blank and die (not punch)	Batch 1 = 27.0 mm Batch 2 (not tested) Batch 3 = 29.4 mm	Complete
Cross Form Stamping - 200C	EWI	1,3	18"x18"	9	Heated blank, RT tool.	No significant difference in formability.	Complete 8/12/2019

Figure F2: USAMP team studies performed to assess batch-to-batch variations in POSCO-supplied EFP sheets. (Source: USAMP)

Chapter G. Task 6: Forming and Simulation of Medium and Large Parts
(Edison Welding Institute and Vehma International of America)

TASK INTRODUCTION

Forming and simulation of forming of various size parts from EFP sheet at elevated temperatures were done to help select forming temperature, forming lubricant, and binder force, and to identify necessary changes to the door dies, which were originally designed for stamping steel. Strain data from physical parts were compared with simulation results to help validate the material models developed by the Task 2 team. This work is described in the next three sections of this report.

G1. Cup Draw Testing and Cross-Form Stamping Trials
(Edison Welding Institute – Principal Investigator: H. Kim)

G1.1 SUMMARY

Warm forming of mid-size (50-470 mm) shapes were conducted prior to stamping of full-size door panels. Specifically, cylindrical cups were drawn in a heated die, and cross-forms were stamped in un-heated tooling, in order to determine effects of temperature, binder force, lubricant, and coil pretreatment on formability of EFP sheet. Also, the cross-forms were characterized with strain mapping to provide data for use in forming simulations.

Results of the cup deep drawing trials showed the following:
1. Good (no cracks) cups were formed at temperatures of 200°C and 250°C, but not at 150°C.
2. Fuchs and Quaker lubricants had significant benefit in forming.
3. Henkel and Xtalic coil pretreatments did not significantly impact forming of the cups.

Results of the cross-form stamping trials showed the following:
1. More good parts were formed at 200°C and 225°C compared with 175°C.
2. Fuchs and Quaker lubricants had a positive impact on formability of the parts.
3. Henkel and Xtalic pretreatments also had a positive impact on formability of the parts.
4. Major and minor strains were measured successfully using a grid method.

Detailed task reports by EWI may be found at https://data.lightmat.org/project/.

G1.2 KEY ACCOMPLISHMENTS AND RESULTS

G1.2.1 Deep Drawing of Cups with EFP Sheets

Experimental Methods
Deep drawing of cups was done at EWI-Columbus using an Erichsen Universal Sheet Metal Testing Machine and the B2 Cup Test procedure. Test blanks of 100-mm diameter, 1.2 mm thick EFP sheet having various combinations of coil pretreatments and lubricants were heated individually along with the die, and then drawn into 50-mm diameter cups with an unheated punch. Cups were categorized as Good (No Crack) or Bad (Crack) after 30 mm of punch stroke. Blank temperature and blank holding force were varied in the ranges 150-250°C and 0-50 kN, respectively, to determine conditions yielding Good cups.

The coil pretreatments used were Henkel process D, Xtalic Zn, and none/Bare. The lubricants used were Fuchs Renoform 1102 ALWF, QUAKERDRAW 450 MAG, and none (Control). These are described in Chapter D of this report. For brevity, the two lubricants are referred to below as "Fuchs 1102" and "Quaker 450". They had coating weights of 0.5-0.8 g/m^2 and 1.0-2.5 g/m^2, respectively.

Results of Deep Drawing of Cups:
Examples of the Good and Bad cups are shown in Figure G1.1. The typical crack locations are in the cup wall near either the punch nose or the die entry radius.

Figure G1.1: Examples of Good (left) and Bad (right) drawn cups. (Source: EWI)

Forming process windows for blanks lubricated with Fuchs 1102 and Quaker 450 lubricants are shown in Figures G1.2 and G1.3, respectively. With either lubricant, cups formed successfully at 200ºC but not at 150ºC. At 250ºC, cups formed successfully only with the Fuchs 1102 lubricant.
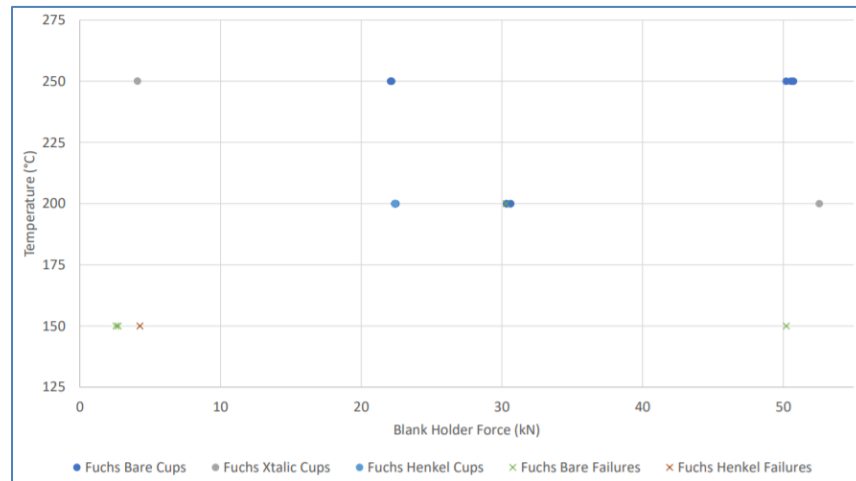

Figure G1.2: Forming process window for EFP blanks with Fuchs 1102 lubricant, based on cup drawing. (Source: EWI)
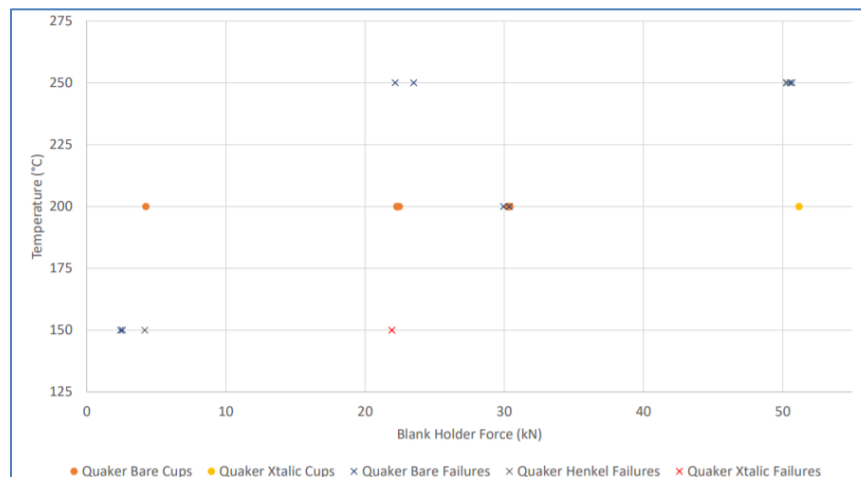

Figure G1.3. Forming process window for EFP blanks with Quaker 450 lubricant, based on cup drawing. (Source: EWI)

Conclusions from Deep Draw Cup Testing:
The following conclusions can be made from the cup draw formability tests:
1. Cups tested at 150°C experienced low formability. No cups were fully formed.
2. Cups tested at 200°C experienced high formability for both Quaker and Fuchs lubricants.
3. Cups tested at 250°C experienced lower formability with Quaker compared to Fuchs lubricants.
4. Coil pretreatments improved formability at higher blank holder forces.

G1.2.2 Cross-form Stamping Trials with EFP Magnesium Sheets

USAMP also contracted with EWI to study the sensitivity of the process parameters to material formability, and to recommend a warm forming process window. The data provided by this work was used to establish correlations between FEA and physical testing. The objectives were to determine the warm forming process window (temperature and blank holding force) for EFP magnesium sheet material and to obtain the detailed experimental data of strain distribution and blue-light scan to correlate with the forming simulation results.

Experimental Methods
Physical testing on EWI's warm forming test cell was conducted with an unheated cross-form test die and heated blanks. Forming depth was set to 2.03 in. to sufficiently challenge the material formability. The limits of the EFP material (i.e., wrinkling if the blank holding force is too low, and splitting if the blank holding force is too high) were determined and subjected to process variation, for stamping temperatures of 175°C, 200°C and 225°C. Blanks were lubricated by the respective suppliers (Fuchs and Quaker Houghton) several days before the stamping trial. Stamping was done with 2 inch/s punch speed.

The following coil pretreatments-lubricants combinations were applied to both sides of EFP sheets:
1. Xtalic Zn: Electrolytic zinc over electroless zinc. Total thickness of 5µm.
2. Henkel process D: Chrome-free conversion coating containing organic and inorganic components. Total thickness of 100-300 nm.
3. Fuchs Renoform 1102 ALWF (3:1 mix ratio): Synthetic water-based product which contains inorganic ingredients and synthetic esters. Coating weight of 0.5-0.8 g/m^2. Applied with a sponge brush. Referred to as "Fuchs 1102" throughout this report.
4. Quaker QUAKERDRAW 450 MAG: A neat oil with inorganic lubricants. Coating weight of 1.0-2.5 g/m^2. Applied with a brush. Referred to as "Quaker 450" throughout this report.

Results of Cross-Form Stamping Trials
Examples of Good (acceptable) and Bad (unacceptable wrinkles) CF stampings are shown in Figure G1.4.

Figure G1.4: Examples of (left) Good and (right) Bad EFP cross-forms stampings. (Source: EWI)

The forming windows for Fuchs and Quaker lubricants used to stamp EFP cross-forms are shown below in Figure G1.5 and Figure G1.6.
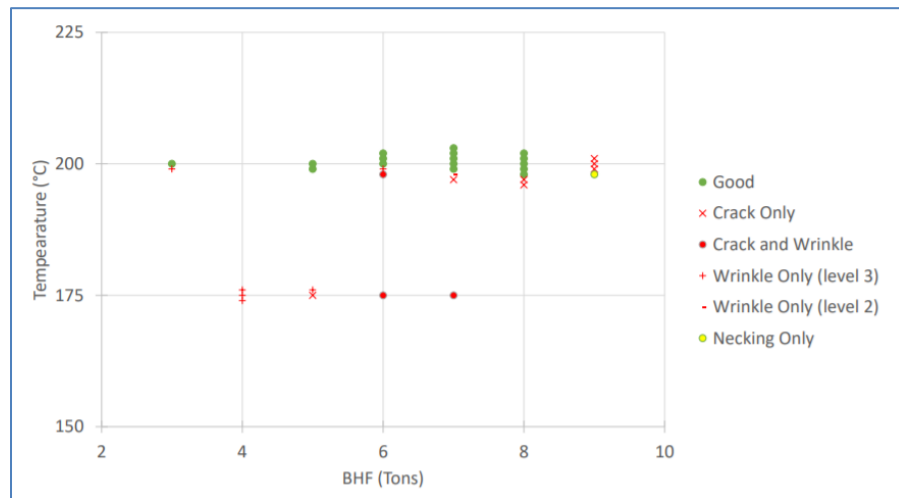

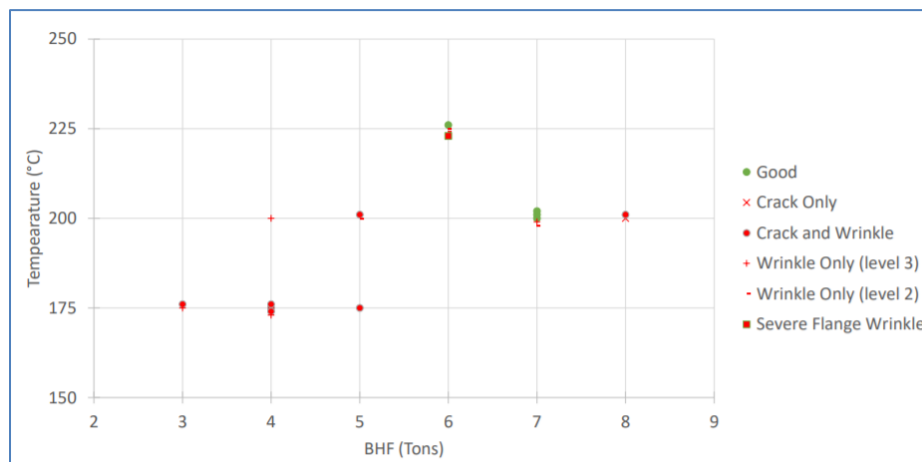Figure G1.5: Forming process window for EFP cross-forms with Fuchs lubricant. (Source: EWI)

Figure G1.6: Forming process window for EFP cross-forms with Quaker lubricant. (Source: EWI)

Argus strain images were captured for one Good cross-form stamping as shown in Figure G1.7 below to correlate with simulation studies.

Key Conclusions from Cross-Form Stamping Tests:
1. This work was successful in measuring and providing the strain data for simulation correlation.
2. 200°C was found the most preferred forming temperature for the cross-form part at a forming depth of 2.03 in.
3. Fuchs and Quaker lubricants both improved formability considerably.
4. Henkel and Xtalic coil pretreatments improved formability marginally.
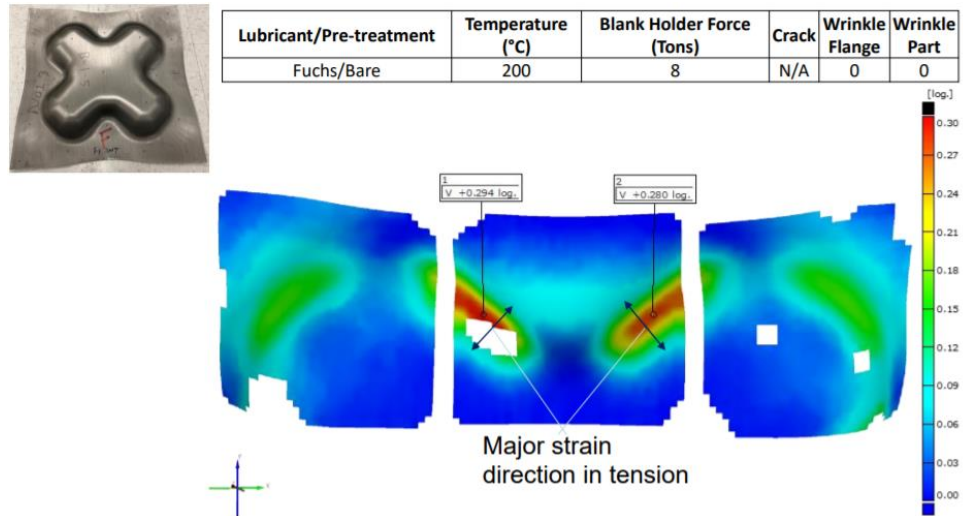5. Material variation influenced the quality of forming.

Lubricant/Pre-treatment	Temperature (°C)	Blank Holder Force (Tons)	Crack	Wrinkle Flange	Wrinkle Part
Fuchs/Bare	200	8	N/A	0	0

Figure G1.7: Argus true strain maps of a good cross-form part stamped from EFP. (Source: EWI)

G1.3 CONCLUSIONS

The following conclusions may be drawn based on the combined results of drawing of cups and stamping of cross-forms with EFP sheet:

1. The optimum forming temperature is 200°C, which should be used for the door forming trials.
2. Fuchs and Quaker lubricants significantly improve formability.
3. Henkel and Xtalic pretreatments do not hinder formability but provide marginal improvement.
4. Material variation does have influence on formability.
5. Strain measurements were successfully done using Argus gridding technique for correlation with FEA simulation results.

G2. Forming Simulation and Correlation
(Vehma International of America – Principal Investigator: A. Srilatha)

G2.1 SUMMARY

Warm forming simulation activity started with the cross-form stamping using LS-DYNA material cards MAT233 and MAT233+ as well as the new crystal plasticity model and correlating those simulations to the Argus scan from the experimental parts. The MAT233+ material model included the rotation of the symmetry axis and resulted in a measurable improvement in the match between simulation and experimental results, while the crystal plasticity simulation validated the accuracy of the material cards. Correlation information and settings from the cross-form simulations were used to perform the door outer and inner panel simulations that guided the initial die modifications to allow the successful stamping of the door inner and outer panels. Detailed discussion of this work by Vehma may be found at https://data.lightmat.org/project/.

G2.2 KEY ACCOMPLISHMENTS AND RESULTS

G2.2.1 Experimental Approach
Vehma used material cards provided by the USAMP project team to conduct warm forming simulations of the cross-form part, the door inner panel and the door outer panel. The subtasks performed were:
1. Forming simulations and correlation of cross-form panels
2. Forming simulations of door outer & inner panels
3. Door outer & inner die modifications

G2.2.2 Cross-Form Simulation and Correlation
The simulation software being used prior to the start of this project was not able to effectively handle the asymmetric behavior of magnesium alloys at warm forming temperatures. USAMP and Vehma worked with LSTC to modify the LS-DYNA software to include tables for temperature and strain rate. LSTC provided both training and revised software to Vehma. The MAT233 material card was used for cross-form simulations to calibrate and prepare for scale-up to door panel simulations. The MAT233+ material card was also used for cross-form simulation; however, unlike the MAT233, it was excluded from the door forming analysis to meet project timing. MAT233+ relied on the development of the phenomenological model which was not complete at the time the door simulation commenced, thus the MAT233+ simulation was used only for comparisons to measure the improvement gained when including the evolving symmetry axis. The simulations were compared to the Argus scan from the experimental cross-form stamping shown in Figure G2.1.

Figure G2.1: Warm-stamped cross-form, approximately 470 mm square. (Source: EWI)

Due to the plastic behavior of the material model, the strain values did not correlate between Argus measurement and simulation; however, the locations of the major strain did show adequate correlation, meeting the criteria that is typically required for automotive component production. Since the adaptive mesh feature was not available on the developer version of software used in this project, the simulations were performed for two finite element mesh sizes, 3 mm and 6 mm (See Figure G2.2). At the larger mesh size, the MAT233 model shows a peak major strain location that does not match the Argus scan, while the MAT233+ simulation is a significant improvement showing a peak major strain location that does match. For the smaller mesh size, both simulations show major strain locations matching the Argus scan and the MAT233+ results in a slight improvement in the peak value. For the minor strains, the simulations all predicted a smaller peak value and different location of the peak compared to the measured data, as shown in Figure G2.3.
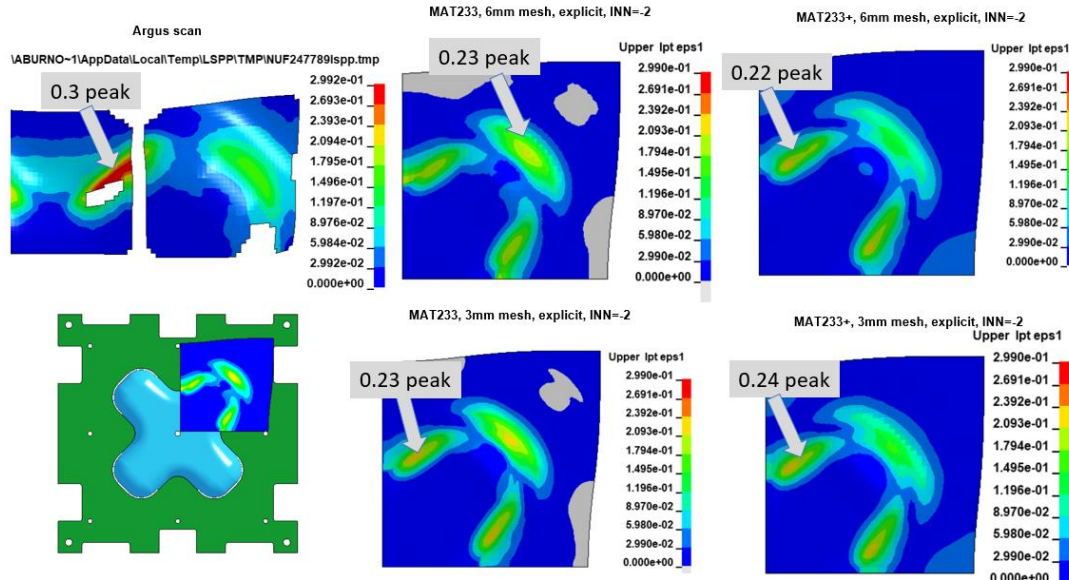

Figure G2.2: Comparison of Argus and MAT233/233+ major strains. (Source: Vehma and InalTech)
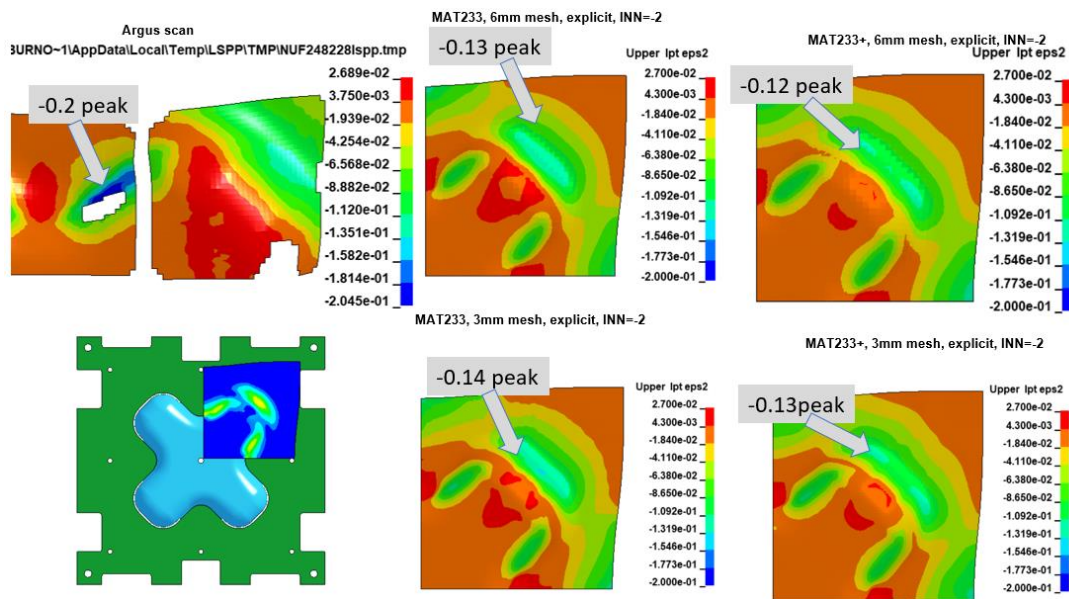

Figure G2.3: Comparison of Argus and MAT233/MAT233+ minor strains. (Source: Vehma and InalTech)

The strain values at various points of the cross-form panel were obtained and compared to the corresponding locations in forming simulations. These points were then plotted relative to the forming limit curve as shown in Figures G2.4 and G2.5. The experimental strains and simulation strains were in the safe region when compared to the FLC curve. The areas that were prone to splitting during the experiment were FLD-safe.
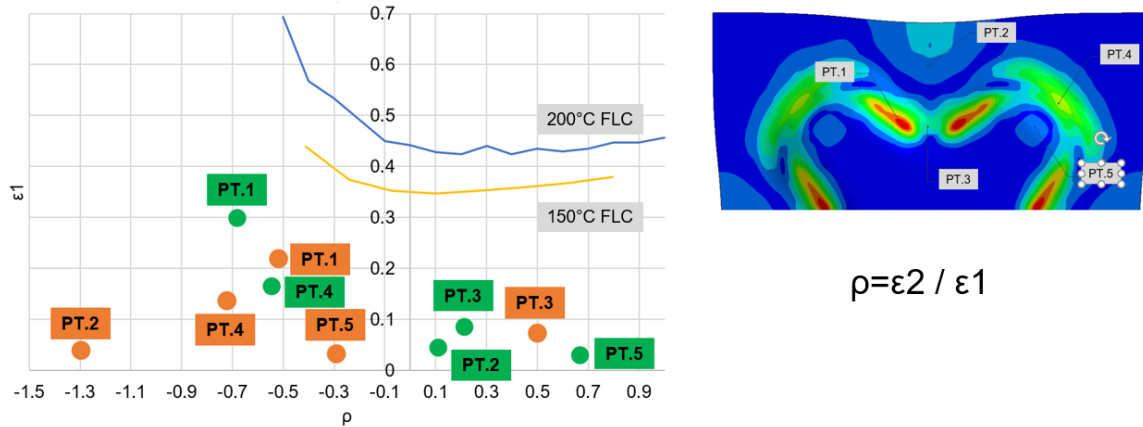

Figure G2.4: Plots from simulations with MAT233+ card compared with Argus scan and FLD map. (Source: Vehma and InalTech)
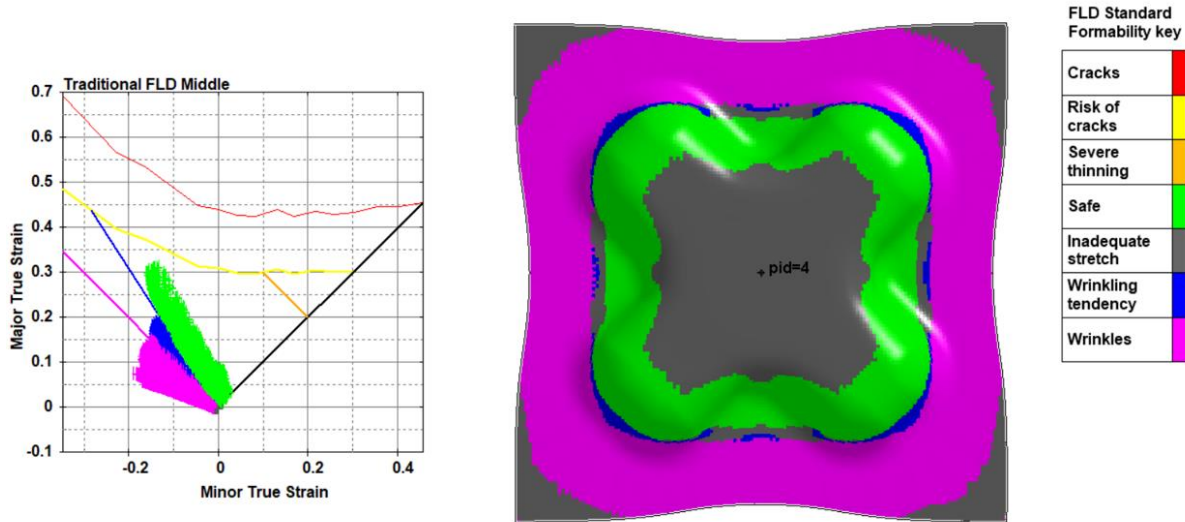
Figure G2.5: Simulations from MAT233+ compared with FLC for 200°C. (Source: Vehma)

G2.2.3 Cross-form Simulation Using the Crystal Plasticity Model

InalTech performed a simulation of the cross-form part using the crystal plasticity model developed in this program. Due to the large amount of computational processing power required to do this simulation (one run required 5 days with 192 processors), it is not practical for commercial part development, but was completed as an additional step to validate the previous LS-DYNA simulations. The results from the CP simulation bolstered the correlation activity yielding a similar strain map and peak minor strain compared to the simulation using the material card MAT233+, as shown in Figure G2.6.

Figure G2.6: Comparison of Argus Scan to MAT233+ and Crystal Plasticity Simulations (Source: Vehma and InalTech)
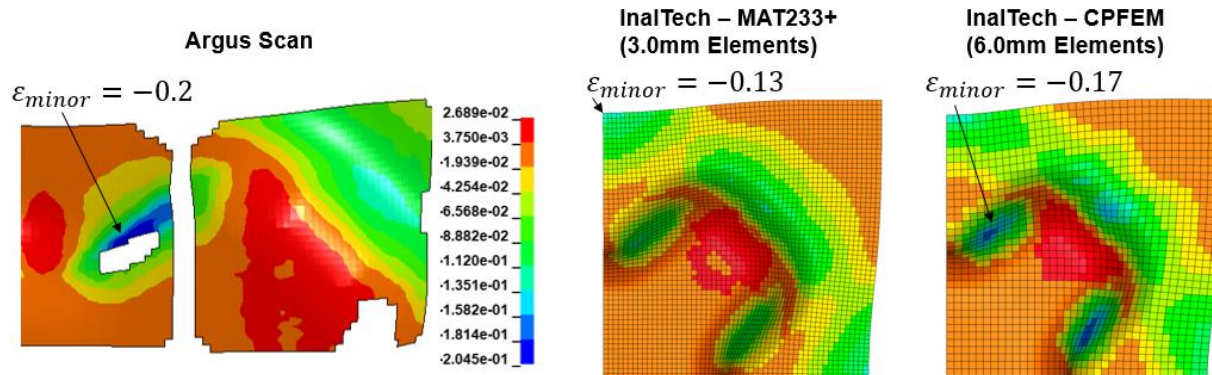
G2.2.4 Fracture Analysis

Although the forming simulation correlated to the Argus scan, it was questioned why the scan did not show fracture level strain at the area where several of the cross-form parts split (Figure G2.7). It was suspected that the strain in that area was much larger during the initial stages of forming and then relaxed near the end of the stamping operation. To verify the hypothesis, InalTech simulated the cross-form part analyzing the strain at defined time-steps but found no evidence of the strain approaching the forming limits at any point in time.

For further examination, USAMP engaged FADI-AMT to characterize fracture surfaces on four warm-stamped door outer panels which cracked or split near draw beads during the stamping process (Figure G2.7). The goal of this brief study was to understand the plastic deformation and fracture processes, and effects of temperature, orientation, and batch by taking careful thickness measurements near the cracks/splits and also by "cross-sectional metallography" of sections at the splits. This study concluded that there is no significant difference in thinning behavior between the rolling and transverse directions. Due to the short time remaining towards the project closeout, only thinning measurements were made, but a planned scanning electron microscope (SEM) study of these fracture surfaces could not be conducted.
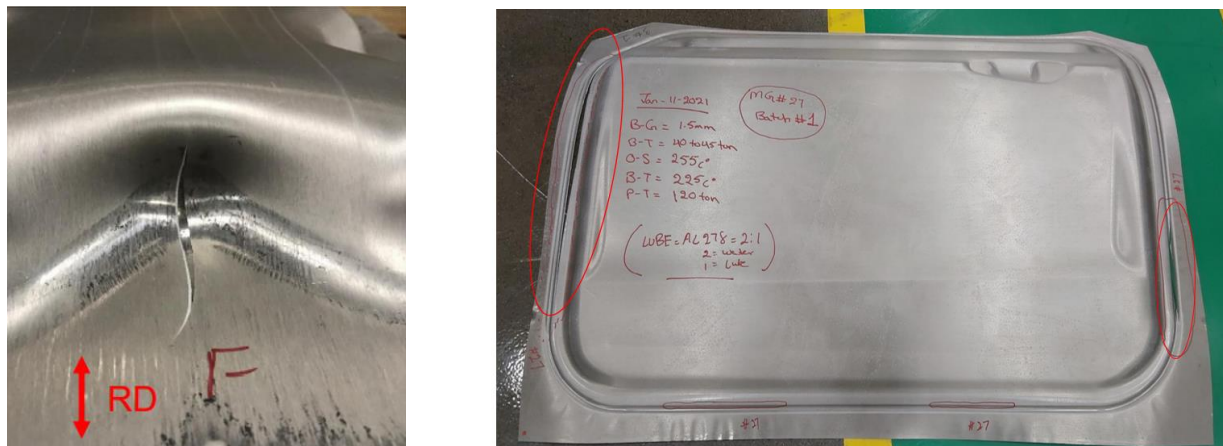

Figure G2.7: Split cross-form part (left) and split door outer panel (right). (Source: FADI-AMT and Vehma/Promatek)

G2.2.5 Door Panel Forming Simulations

Vehma performed the door outer and inner panel forming simulations using the MAT233 material card and the best setting from the cross-from simulations. Low levels of class-A surface strains were achieved

on the door outer panel. The door inner nominal panel had FLD failure areas where strains exceeded 40%. Die modifications were suggested based on forming simulations for both, door outer and inner panels in order to achieve quality parts (see Figures G2.8 and G2.9).

| (a) | (b) |
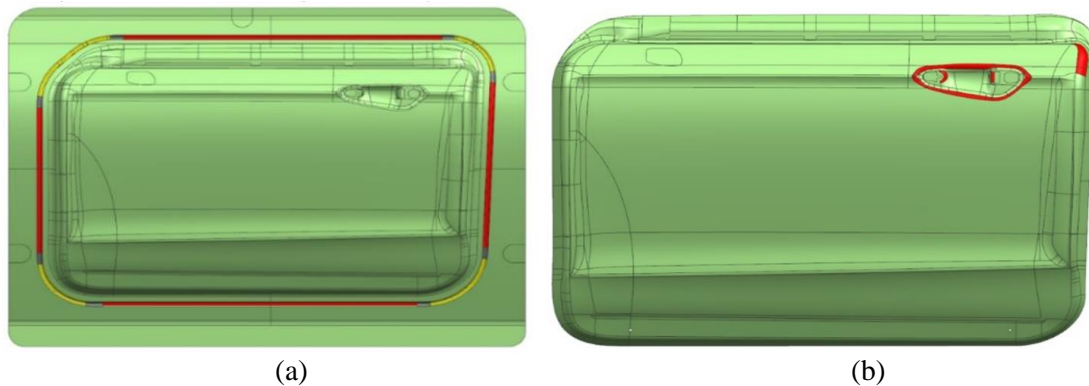
Figure G2.8: Door outer die modifications based on forming simulations. (a) Red indicates draw bead height increased by 1.0 mm, yellow indicates draw bead height decreased by 2 mm. (b) Radii are increased in the areas indicated by red. (Source: Vehma/Promatek)
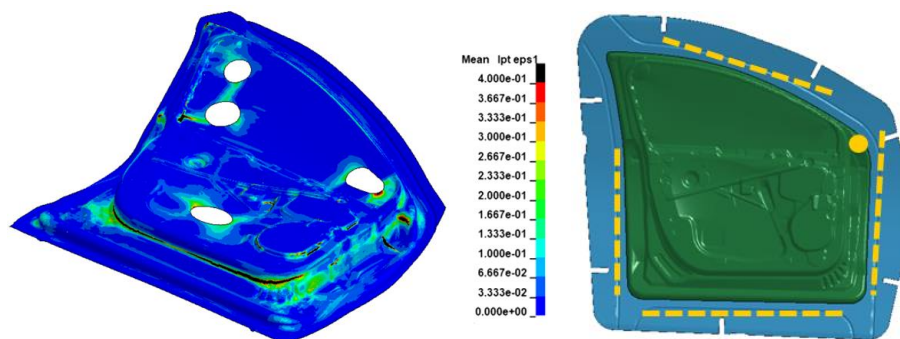
Figure G2.9: Door inner strain plot and draw bead change areas. (Source: Vehma/Promatek)

The draw bead height reductions on the door inner die helped with tool closing in the forming simulation, as extensive splits were occurring with strains exceeding 40%. Remaining areas of splits had to be rectified by product modifications, shown in Figure G2.10. Subsequent door inner forming simulations yielded the strain plot shown in Figure G2.11. Remaining minor splits, if occurring, were agreed upon by the USAMP team to be fixed during physical stamping trials by grinding in necessary areas.
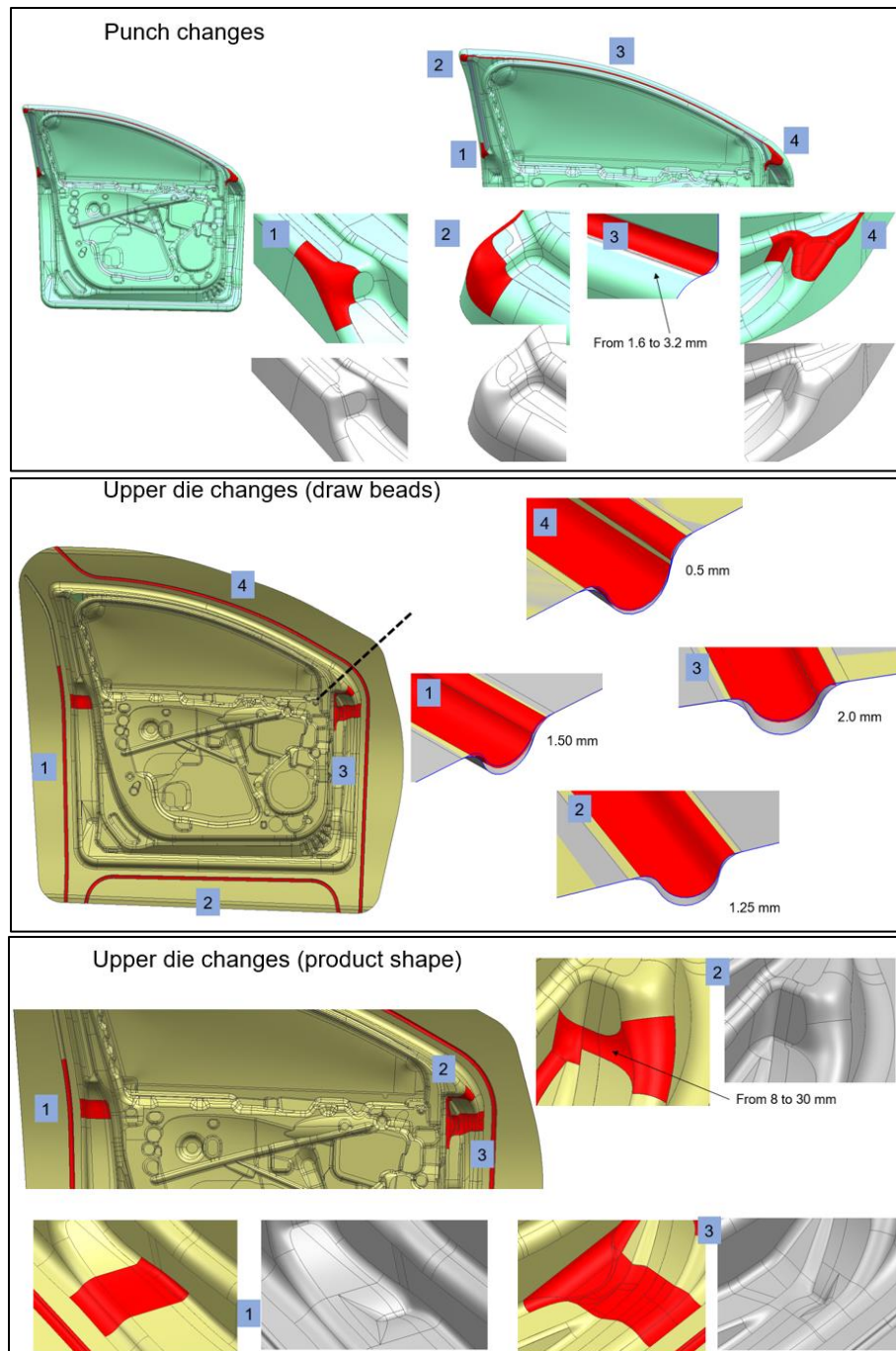
Figure G2.10: Door inner die modifications based on forming simulations. (Source: Vehma/Promatek)
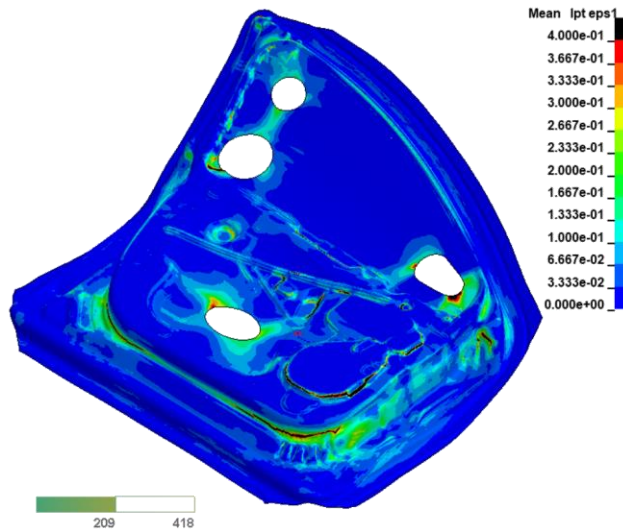
Figure G2.11: Door inner strain plot after product modifications. (Source: Vehma)

G2.3 CONCLUSIONS

1. The MAT233 material card developed in this program showed production level correlation of the major strain map to the Argus scan of the cross-form stamping when the simulation was performed at the smaller mesh size.

2. MAT233+ is a user defined material model that captured the evolving symmetry axis unique to magnesium sheet and demonstrated a measurable improvement by accurately predicting the peak strain location, especially at the larger mesh size.

3. Crystal plasticity simulation of the cross-form part successfully captured the local strain portioning and localized deformation observed during the experiments and validated the accuracy of the LS-DYNA simulation.

4. The information from the correlation study was successfully applied to the door inner and outer simulations that guided the modifications to the stamping dies that ultimately created automotive quality door panels.

G3. Door Panel Stamping Trials
(Vehma International of America – Principal Investigator: A. Srilatha)

G3.1 SUMMARY

Stamping trials were conducted at Promatek (Vehma's contractor in Toronto) to develop processes for one-stage, warm-blank/cold die, stamping of 1.2 mm EFP Mg blanks into Ford Fusion door inner and outer panels. Blanks were coated with diluted Fuchs lubricants 278 or 1102, allowed to dry, heated in an electric oven, robotically transferred to a press, and stamped at temperatures up to 250°C. The dies had been modified from their steel-panel-specific designs based on Mg forming simulations, as discussed in section G2 of this report. Further modifications (i.e., reduction in height of draw beads and increase in radii of product features) were required to form split-free panels. Ten outer panels and sixteen inner panels of good quality were stamped using water-diluted Fuchs 278 blank lubricant and a blank temperature of 250°C. Use of the 1102 lubricant and/or a lower temperature resulted in panel splits. Detailed discussion of this work by Vehma and Promatek may be found at
https://data.lightmat.org/project/.

G3.2 KEY ACCOMPLISHMENTS AND RESULTS

G3.2.1 Forming Cell Setup
Promatek's forming cell consisting of a press, an oven for blank heating, a robotic transfer system, and un-heated tooling is shown in Figure G3.1. This forming cell was used to explore the impact of blank shape, blank temperature, and lubricant on the Mg blanks for forming inner and outer door panels. The goal of the trial was to develop robust procedures to produce door inner and outer panels of acceptable quality with no splits or wrinkles. The blank shape was optimized during the forming trials.
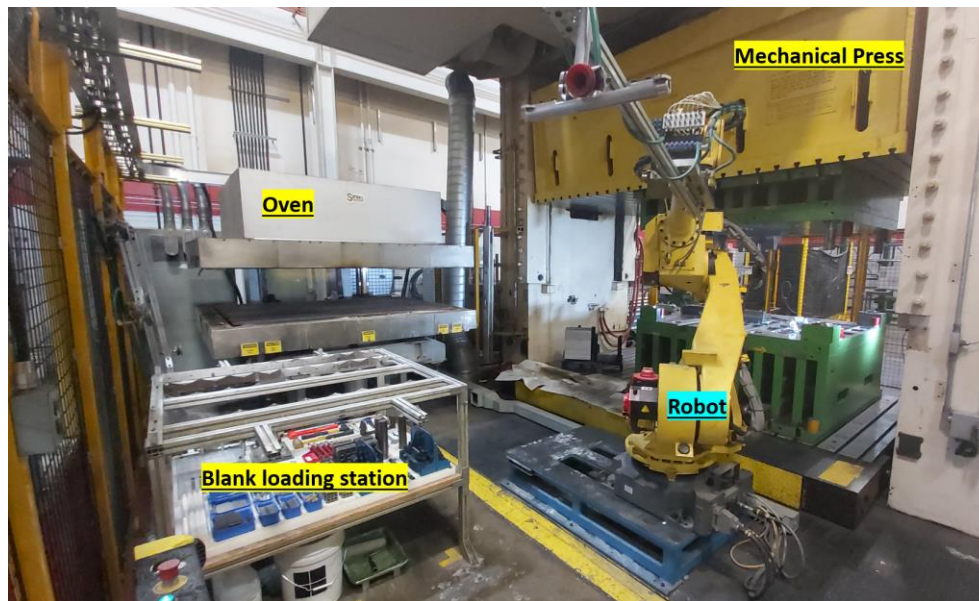
Figure G3.1. 3 Forming cell setup at Promatek. (Source: Promatek)

G3.2.2 Effect of Forming Temperature and Lubricant
The effect of forming temperature and choice of lubricant showed similar trends for both outer and inner door panel stampings. Panels with acceptable quality were formed at an elevated temperature of 250°C. When the blank temperatures were reduced to 225°C and lower, splits were observed in the panels. Similarly, Fuchs 278 lubricant, which was used with either water dilution or alcohol dilution (per Fuchs

recommended dilution ratios), produced good quality panels whereas Fuchs 1102 lubricant used with the same forming conditions (Tables G3.1 and G3.2) produced splits, as shown in Figures G3.2 and G3.3.
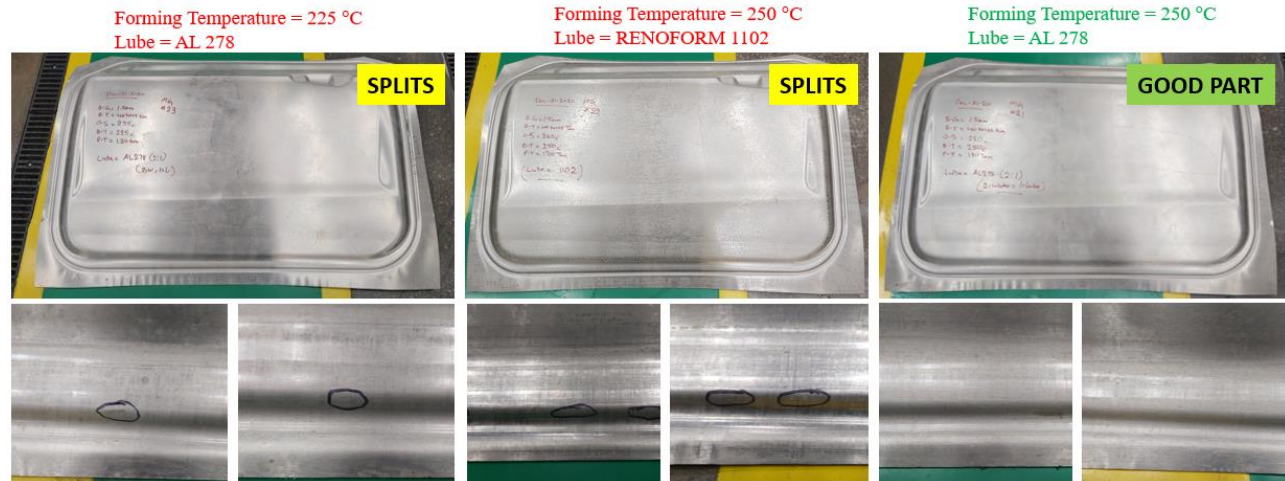
Figure G3.2: Door outer forming results illustrating effects of temperature and lubricant selection. (Source: Promatek)

Table G3.1:   Door outer forming process parameters.

Door Outer Forming Process Parameters	
Binder Gap	1.5 mm
Binder Tonnage	40 to 45 Ton
Binder Pressure	500 Psi
Press Tonnage	120 Ton

Figure G3.3: Door inner forming results illustrating effect of temperature and lubricant selection. (Source: Promatek)

Table G3.2. Door inner process parameters

Door Inner Forming Process Parameters	
Binder Gap	1.3 mm
Binder Tonnage	50 to 66 Ton
Binder Pressure	600 Psi
Press Tonnage	400 Ton

G3.2.3 Door Outer Forming Trials

The door outer panels were stamped after the dies were modified based on forming simulations. Initially, splits occurred alongside the side and top beads, as shown in Figure G3.4. The bottom beads had no splits. Further trials were conducted by gradually reducing the bead heights off the sides and top of the door panel, thereby reducing the splits. Combining the lessons learned from forming temperature variables and the lubricant choice produced better results. A final bead reduction of 1.2 mm off the sides and 1.5 mm reduction in top and bottom beads, with a forming temperature of 250°C and Fuchs 278 water-diluted lubricant, enabled a split-free door outer panel to be successfully formed, as shown in Figure G3.5. Ten acceptable quality door outer panels were made using EFP Batch #4 sheet blanks.

Initial Forming Process Parameters	
Binder Gap	1.5 mm
Binder Tonnage	40 to 45 Ton
Binder Pressure	500 Psi
Oven Setting	230°C @ 85s
Blank Temperature	200°C
Press Tonnage	120 Ton
Lubricant	RENOFORM 1102
Bead	No change

Figure G3.4: Door outer: Badly split initial tryout stamping and associated process parameters. (Source: Promatek)

Final Forming Process Parameters	
Binder Gap	1.5 mm
Binder Tonnage	40 to 45 Ton
Binder Pressure	500 Psi
Oven Setting	280°C @ 85s
Blank Temperature	250°C
Press Tonnage	120 Ton
Lube	Al 278 (2=W, 1=L)
Bead	1.2mm off the sides/1.5 mm of top and bottom

Figure G3.5. Door outer: A good quality panel and associated final forming process parameters.

Results of the door outer stamping trials were different from the cross-form stamping trials in terms of blank temperature and lubricant requirements to achieve un-split panels. Whereas cross-forms were successfully stamped (at EWI) at 200°C using the Fuchs 1102 lubricant, door outers required 250°C and the Fuchs 278 lubricant to avoid splitting. Two factors which may be contributing to these differences are (1) lack of drawbeads on the cross-form die and (2) large radii on corners in the cross-form die.

G3.2.4 Door Inner Forming Trials

The lessons learned from door outer trials for effect of temperature and lubricant was used in door inner trials. The initial stamping trials of door inner panels had extensive splits alongside the side bead, multiple minor cracks on product features, and the panel showed significant wrinkles (see Figure G3.6).

Initial Tryout Process Parameters	
Binder Gap	1.6 mm
Binder Tonnage	40 to 65 Ton
Binder Pressure	500 Psi
Oven Setting	280ºC @ 85s
Blank Temperature	250ºC
Press Tonnage	195 Ton
Lube	Al 278 (2=W, 1=L)

Figure G3.6: Door inner: Initial tryout stamping with splits and wrinkles, and process parameters. (Source: Promatek)

The process parameters and blank shapes were varied, and multiple trials were conducted to significantly improve (i.e., reduce) the splits and wrinkling. The minor cracks were eliminated by meticulously hand grinding areas of splits on the dies to soften up product features that created the splits, as shown in Figure G3.7. A good quality door inner part (Figure G3.8) was stamped at a blank temperature of 250°C and with Fuchs 278 water-diluted lubricant. Vehma manufactured 16 acceptable quality door inner panels with EFP Batch 4 material.
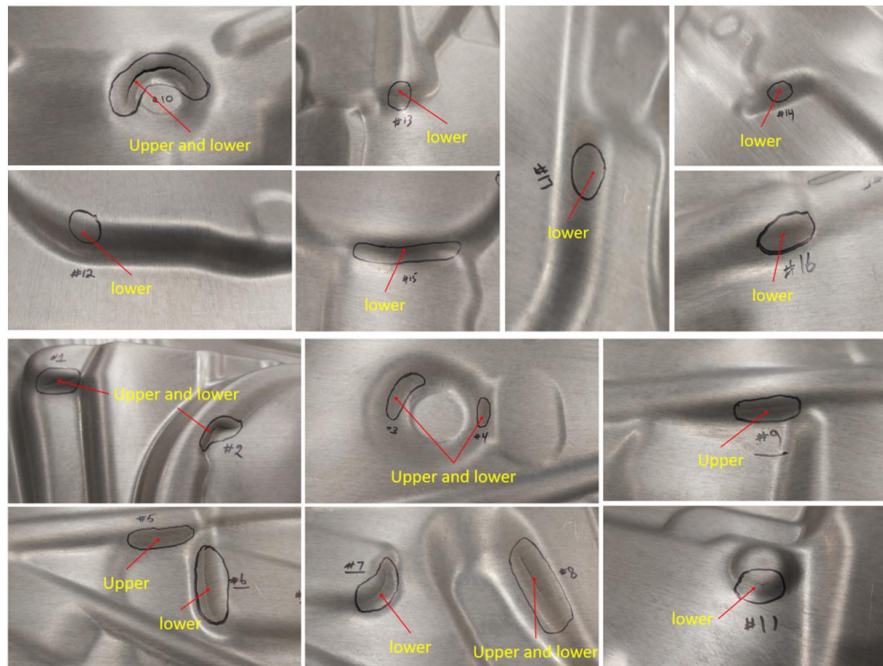
Figure G3.7: Areas on door inner die that were ground to eliminate splits. (Source: Promatek)

Final Forming Process Parameters	
Binder Gap	1.3 mm
Binder Tonnage	50 to 66 Ton
Binder Pressure	600 Psi
Oven Setting	285 C @ 85s
Blank Temperature	250 C
Press Tonnage	400 Ton
Lube	Al 278 (2=W, 1=L)

Figure G3.8: Door Inner: A good quality part and final forming process parameters. (Source: Promatek)

G3.3 CONCLUSIONS AND RECOMMENDATIONS

1. Door panels of acceptable quality were successfully stamped in un-heated dies using EFP Mg blanks at 250°C. Use of lower blank temperatures resulted in panels splitting.

2. Use of Fuchs 278 lubricant (diluted with water, applied to blanks and allowed to dry before stamping) facilitated panel stamping better than did Fuchs 1102 lubricant.

3. Compared to the original die geometry for stamping steel door panels, it was necessary to modify the dies for warm stamping of Mg sheet. Specifically, the heights of draw beads were reduced, and the radii of product features were increased in order to avoid splits.

4. Potential future work should include development of forming lubricants which (a) allow for forming at temperatures below 250°C and (b) eliminate the need for panel cleaning after forming.

Chapter H. Task 7: Demonstrate Performance of Magnesium Door via CAE
(Vehma International of America – Principal Investigator: A. Srilatha)

H1. SUMMARY

Vehma's goal in Task 7 was to perform the computer-aided design (CAD) and computer-aided engineering (CAE) simulations required to analyze the performance of the 2013 Ford Fusion side door, for which the door outer and inner panels were manufactured from Mg sheet alloys instead of the original steel sheet materials, and reinforcements were made of aluminum. The analyses were performed for two Mg alloys, EFP, from which door panels were stamped in Task 6, and ZEK100-O. (The latter was commercially available as Elektron 717™ from Luxfer Magnesium Elektron several years ago). This work was fully virtual and did not include physical testing of an assembled door. The performance of the door assembly was analyzed for the following automotive engineering requirements:

1.   Stiffness and Modal
2.   Denting and Oil Canning
3.   Check over and Sag
4.   FMVSS 214 S-Static Pole Analysis
5.   Mass Comparison with Steel Door

The simulated side door achieved all requirements at a mass of 10.18 kg using a 1.2 mm EFP inner and a 1.1 mm EFP outer stamping. The Mg door panels achieved a 62% mass saving relative to the steel baseline panels. Detailed discussion of this work may be found at https://data.lightmat.org/project/.

H2. KEY ACCOMPLISHMENTS AND RESULTS

H2.1 Performance Analysis Procedure

This Task commenced with the 3D CAD design of the door contributed by Ford, the Bill of Materials for which is provided in Figure H1. Abaqus and Nastran software were then used to simulate the door performance based on Mg alloy materials properties obtained from both, experiments tests and suppliers, and to affect design changes to achieve the desired results. The door assembly performance was simulated based on Ford Test Procedures and compared to Ford targets, to obtain a real-world measure of the outcome. In this document, most quantitative results are replaced by a Pass/Fail scale to protect Ford proprietary information.

The needed stress-strain data for EFP was obtained by tensile testing coupons cut from cross-form warm-stamped samples (produced by Task 6; see Figure H2). The remaining needed EFP parameters (density, elastic modulus at RT, Poisson's ratio at RT) were obtained from other project Tasks and used to generate the desired EFP Batch 3 CAE material properties. The needed material properties for ZEK100-O were obtained from the producer, Luxfer Magnesium Elektron. See Table H1.

Door performance was analyzed for ZEK100-O and EFP alloys, optimizing sheet thicknesses and placement of Nitto patches on the inside of the outer panel (see Figure H3) until the door satisfied all the desired performance targets mentioned above. The ZEK100 material required the inner panel to be 1.2 mm thick and the outer panel 1.0 mm. A Nitto patch was needed only for enhancing static stiffness. EFP material required an inner panel 1.2 mm thick and the outer panel to be 1.1 mm. A Nitto patch was needed for static stiffness and dent resistance. The EFP outer panel must be up-gauged to 1.1 mm for dent resistance due to its lower yield strength.
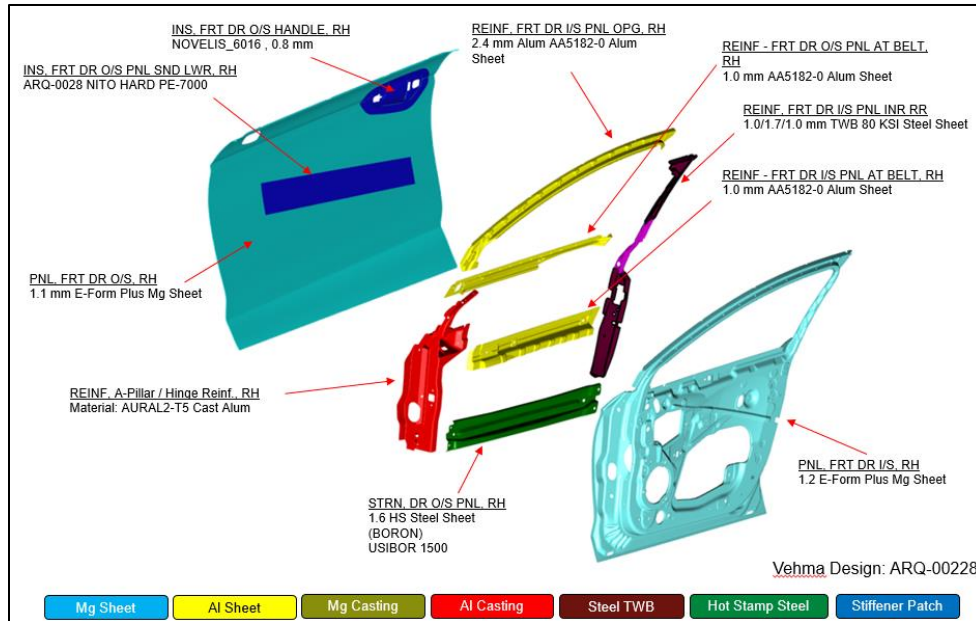
Figure H1: Door CAD Bill of Material. (Source: Vehma)
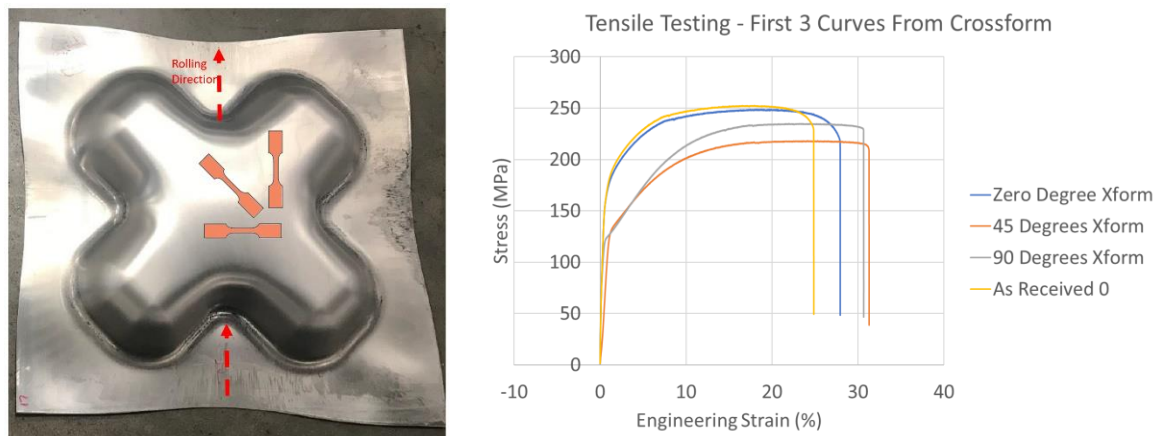
Figure H2: (a) Warm-stamped cross-form (470mm square), showing the approximate size and locations of the tensile samples excised. (b) Stress-strain curves for warm-stamped EFP, Batch #3. The curve for 90-degree sample orientation was used for CAE. (i.e., tensile sample perpendicular to rolling direction). (Source: Vehma)

Table H1: Material Properties used in performance analysis simulations.

Material	Density (Ton/mm3)	Elastic modulus (MPa)	Poisson ratio	Yield Stress (MPa)
ZEK100-O (E717-O)	1.75E-09	44000	0.27	165
EFP	1.76E-09	42000	0.3	120
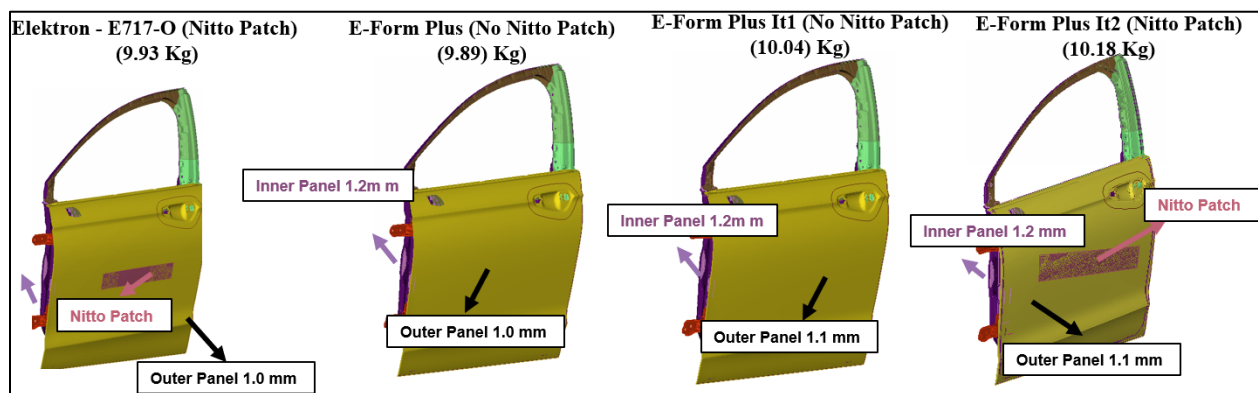
Figure H3: Analyzed Door Models. (Source: Vehma)

H2.2 Stiffness & Modal Analyses
The stiffness of beltline, door frame, and outer panel were analyzed for specific load values applied at specific locations on the door, per the test procedure. Door resonance mode, inner panel mode, and outer panel mode were studied. As mentioned above, a Nitto patch was needed for both ZEK100-O and EFP to enhance static stiffness.

H2.3 Dent Resistance and Oil Canning
In this test, a lateral load is applied to the outer panel by a rigid object or a wooden disc with specific boundary conditions. For ZEK100-O material, Nitto patches were not needed, and the outer panel needed to be only 1.0 mm for dent resistance. For EFP, the outer panel needed to be 1.1 mm thick for dent resistance, as well as requiring Nitto patches to obtain the best possible outcome.

H2.4 FMVSS 214 S-Static Pole Analysis
In this test, a rigid barrier provides an inward load on the door (see Figure H4), testing the crush resistance of the door assembly. The plastic strain experienced by the inner panel near the bottom of the latch increases in EFP, compared to ZEK100-O, due to the lower yield stress. This causes the drop in intermediate crush compared to ZEK100-O material (see Figure H5). Regardless, both materials meet the requirement of initial and intermediate crush resistance.
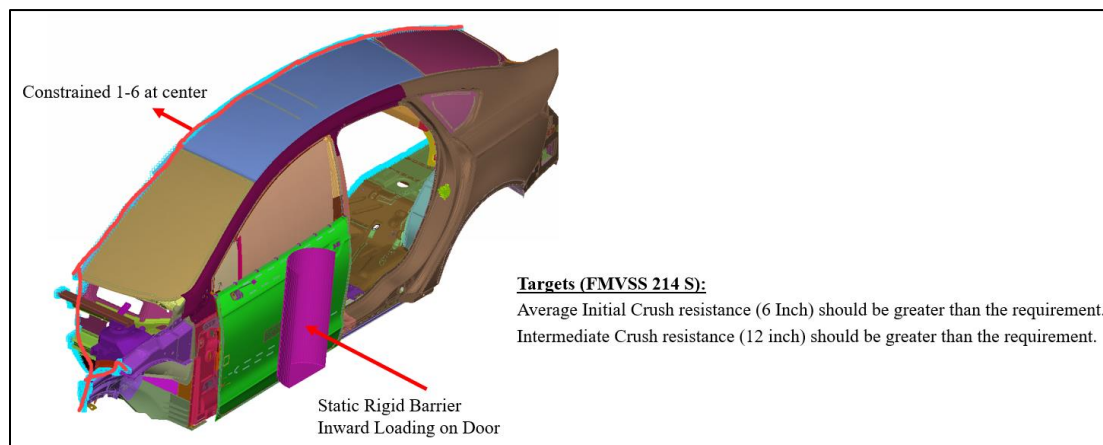

Figure H4: Static Pole Model Setup & Target. (Source: Vehma)
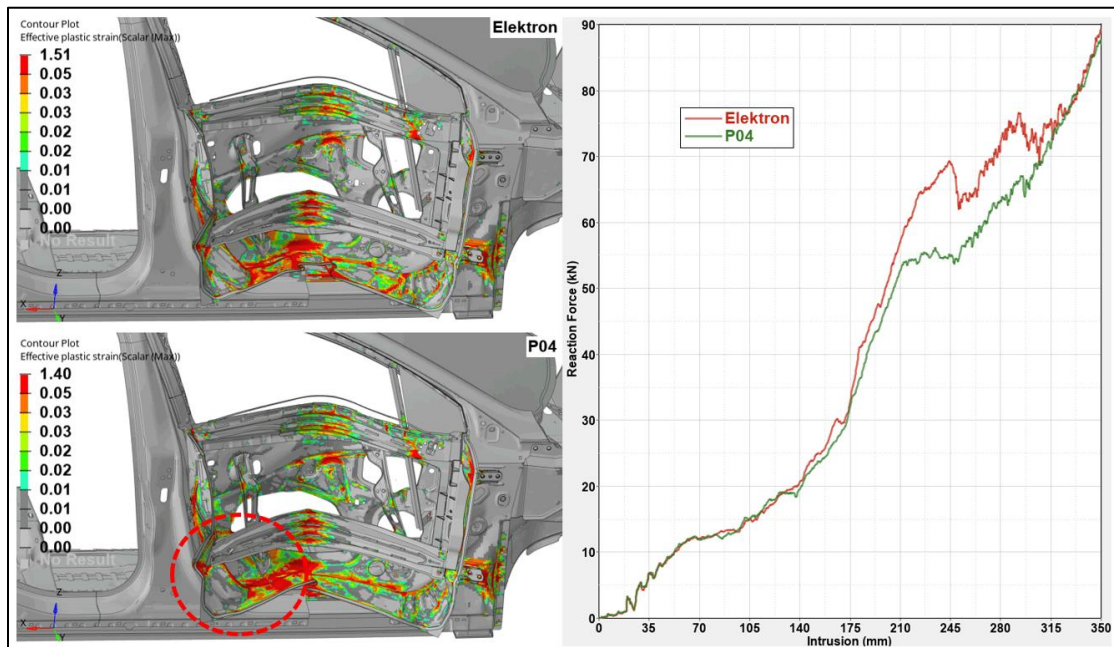
Figure H5: FMVSS 214S Results. In chart on right, the green line is for EFP and the red is for ZEK100. (Source: Vehma)

H2.5 Mass Comparison

Table H2 provides a mass comparison of the Fusion inner and outer door panels made in steel and magnesium. The mass saving of these two panels (plus Nitto patch) in magnesium is 63% (6 kg) compared to the steel panels.

Table H2: Steel vs. Magnesium Door Panels Mass Comparison

Parameter	Steel	ZEK100-0	EFP	Unit
Density	7.831	1.75	1.76	g/cc
Inner Thickness	0.75	1.2	1.2	mm
Inner Mass	5.332	1.906	1.917	kg
Outer Thickness	0.65	1.0	1.1	mm
Outer Mass	4.073	1.400	1.549	kg
Nitto Patch	0	0.070	0.140	kg
Combined Mass	9.405	3.377	3.607	kg
Savings	0	64	62	%

H3. CONCLUSIONS

CAE analyses were performed for Stiffness and Modal, Denting and Oil Canning, Check Over and Sag, and FMVSS 214 S-Static Pole, for a side door design based on the 2013 MY Ford Fusion baseline, but with magnesium inner and outer panels and aluminum reinforcements. All engineering requirements were met at a door mass of 10.18 kg using a 1.2-mm thick EFP inner and a 1.1-mm thick EFP outer stamping, and a Nitto patch. The Mg alloy door panels achieve a 62% mass saving relative to the steel baseline panels. With no Nitto patches to enhance stiffness, the outer stamping needs to be 1.25 mm thick and the mass saving is reduced by 150 g (to 60%). If ZEK100-O were to be used instead of EFP, the outer panel could be down-gaged to 1.0 mm, with a resulting mass saving of 64% compared to the steel panels.

Chapter I. Conclusions and Recommendations for Future Work

I1. CONCLUSIONS

This broad-scope USAMP-led research project has achieved its objective of demonstrating lower cost magnesium sheet alloys, while accelerating knowledge and technology advances in three thrust areas:

1. Demonstrated a virtual development framework for new Mg sheet alloys with leading edge modeling techniques that range from design and characterization to their deployment into complex automotive manufacturing systems and developing the business case.
2. Achieved the practical understanding of Mg sheet alloys with the development of detailed material property data at elevated temperatures, and their implementation in computational modeling tools for validation with forming of both intermediate size parts and at scale via the demonstration automotive door panels.
3. Improved rolling and joining processes, protective pretreatments, high-temperature lubricants, and demonstrated compact processes for corrosion coatings to enable greater use of existing Mg alloy sheet materials.

The UF identified the roles of Ca and Zn in solution after thermomechanical processing under DSA and non-DSA conditions, and subsequent static recrystallization, on texture evolution of dilute Mg-Ca and Mg-Ca-Zn alloys. This research was undertaken to design alloys which have the texture benefits of rare-earth additions but without containing rare earths. The Mg-Ca-Zn alloys represent promising RE–free alloys for production of low–cost magnesium sheets for the automotive industry. The UM's work consisted of a systematic study of how both alloying and processing influence texture in Mg-Zn-Ca ternary alloys and resulted in the creation of a large database linking processing with microstructure and texture. This database will serve as a foundation for establishing models for static and dynamic recrystallization kinetics, allowing for the development of ICME models to predict texture evolution.

In addition to several binary and ternary Mg sheet alloys investigated, the project has resulted in a laboratory-scale demonstration by OSU of a new sheet alloy, Alloy 2 Plus. Its composition and processing were developed using an ICME approach. This patent-pending Alloy 2 Plus offers both, excellent ductility (31% tensile elongation) and RT formability (7.8 mm Index Erichsen) in the solution-treated condition, but with a high yield strength (270 MPa) upon post-forming aging treatment (T6). The excellent combination of strength and formability of this new magnesium alloy, comparable to those of 6000 series sheet aluminum alloys, clearly shows potential for room temperature forming of automotive panels. ORNL explored scale-up of the thermomechanical processing via shear rolling studies.

The UIUC work in ICME contributed in several ways: (1) development of predictive models of effects of solute chemistry on deformation in magnesium – i.e., the first-principles computation of solute interactions with a variety of line defects associated with different plastic deformation modes enabled the parameterization of predictive models of strength with solute chemistry, temperature, and strain-rate; (2) suggested routes for development of alloy chemistry of magnesium alloys with improved formability – i.e., predictive models were combined with thermodynamic databases to identify optimal solute selections; and (3) increased computationally efficient routes to map out the solute energy landscape for other alloy systems – this was the first application for so many deformation modes and the majority of the periodic table.

Two PNNL teams characterized EFP and validated the ICME predictions from solute energy calculations with DFT studies/characterizations for driving formability studies and measurement of primary and secondary mechanical properties, using the constitutive model for textured Mg-alloy which was completed. PNNL provided strain-rate dependent tensile behavior that was incorporated in the new

material card at stamping-relevant elevated temperatures. The stress-strain data showed a significant dependence of work-hardening over the two-orders of magnitude strain-rate range used in experimental studies. Additionally, this work produced detailed DIC-based deformation data that was essential to accurate finite element modeling. PNNL also performed in-situ experiments in a beam-line to elucidate fundamental dislocation behavior and slip-systems activation associated with micro-yielding. Such knowledge could explain the post-yield work-hardening and microstructural evolution.

While it was concluded that an ideal texture for Mg sheet is entirely dependent on alloying and thermomechanical process conditions in rolling, a pathway was shown where elevated temperature forming mitigates the texture and anisotropy effect. USAMP has thus, achieved its stated goal to develop and apply computational modeling to predict viable alloy chemistries, as well as produced and evaluated new RE-free alloys, and texture randomization without using strip-casting technology. The goal of the multi-scale modeling effort undertaken by InalTech and UPenn was to be able to accurately simulate thermomechanical processing of magnesium alloys to achieve improved formability. Both slip and twinning mechanisms have been accounted for in these new models, where the latter gives rise to strength differentials (tension-compression asymmetries) that were beyond existing modeling capabilities for macroscopic simulations that include the effects of texture evolution. This is a significant advancement.

Based on formability evaluations of USAMP-developed Experimental Alloys 1 and 2, it was determined that the significant alloy and processing modifications needed would not fit within the project schedule. Hence, USAMP procured four batches of EFP in medium width and wide width sheets in order to meet the project's substantial sheet requirements for material characterization and implementation in the ICME-driven modeling and simulation studies, as well as development of sheet protective coatings and process windows for production stamping. Comprehensive material testing and characterization of commercial EFP alloy was performed at both ambient and elevated temperatures under realistic strain levels as part of a continuum modeling approach for simulation of the cross-form and door inner and outer panels. The test data were utilized in new crystal plasticity material models, and two new LS-DYNA material cards (MAT 233 and MAT 233+) were developed for modeling component formability over a range of forming temperatures, strains, and FEA mesh sizes.

Fuchs and Quaker Houghton, in parallel efforts, developed lubricants for use in forming ZEK100 and EFP magnesium alloys at forming temperatures of up to 100°C and up to 250°C. Quaker developed a neat lubricant, QUAKERDRAW 450 MAG (aka "Quaker 450"), which met the project goal by providing a reduction in the coefficient of friction between tool steel and magnesium alloys at elevated temperatures. However, forming experiments indicated Quaker 450 has a narrower forming window compared to Fuchs' Renoform 1102 and Forgease 278, which were evaluated in door panel forming.

The USAMP evaluated medium-scale and large-scale formability of E-Form Plus and successfully stamped cross-form parts at 200°C, and large door panels at 250°C using coating and lubricants developed in this project. Vehma utilized LS-DYNA simulation results and learnings from the cross-form stamping trials to modify the door inner and outer dies and successfully manufactured door panels of acceptable quality for a complex material like EFP. The stamping process used the Fuchs AL278 water-based lubricant at a forming temperature of 250°C to deliver 10 door outer panels and 16 door inner panels of acceptable quality.

The coatings research thrust demonstrated low-cost coil applied pretreatments and resulted in novel formulations and corrosion coatings for protecting sheet assemblies, as well as evaluated numerous blends of warm-forming lubricants for scale application in component warm forming. Xtalic developed a new, proprietary coil pretreatment using nano-structured aluminum that was applied to EFP, and later demonstrated a (lower cost) zinc plating process for magnesium coil protection. The process has proven to be well suited for EFP materials producing a coating of a few microns thick zinc layer that is well

adhered and meets corrosion requirements. Henkel's new coil-applied pretreatment Process D includes deoxidizing and cleaning products that effectively remove magnesium oxides/hydroxide followed by pretreatment that was shown to increase corrosion resistance in 100% humidity testing and salt fog testing. In corrosion studies for simulated BIW assemblies, PPG showed that the processes using two cleaning steps and a pretreatment step can adequately protect rivet- and adhesive- joined and un-joined EFP, AA6111, HDGE, and CRS substrates in the same line prior to paint-shop operations. PPG developed paint shop corrosion coating systems which are effective for E-Form Plus and mixed-metal assemblies. The novel cleaning solutions were optimized to provide a compact process for treating Mg sheet and assemblies along with AA6111 and CRS.

AET's joining studies with ZEK100 and EFP resulted in three welding process schedules and joint quality attributes for resistance spot welding, laser welding and Arplas welding using EFP applied for Mg-Mg sheets and fabricate 'mini-door' components for corrosion studies. RSW processes were developed to successfully weld both bare and coated EFP sheet to itself. Laser welding processes, both, with and without shielding gas, were also successfully developed. Sheets with all combinations of coating and lubricant were able to be laser welded without shielding gas, and only one combination required the use of wobble and defocus techniques. Arplas welding was plagued by cracking and low joint strengths.

Finally, USAMP's technological advances were applied on the Mg-intensive door design to estimate the aggregated impact on the cost of producing Mg sheet-intensive door assemblies – the Mg door cost is significantly under the $5.50/kg saved cost target for several scenarios of coil production cost. The initial cost drivers analysis found that magnesium assemblies are more expensive because material and assembly costs relative to baseline steel designs outweigh gains from lower mass and part count. The material costs are primarily driven by high raw material costs. Primary magnesium produced using the Pidgeon process is about half as expensive as that produced using the electrolytic process. Camanoe's process-based cost modeling comparison of producing the magnesium door to the steel door showed that the Pidgeon magnesium door's lightweighting cost of $4.26/kg saved was under the project target of $5.50/kg, whereas the electrolytic magnesium scenario had a lightweighting cost of $6.60/kg. The cost of the coated magnesium alloy sheet and its associated uncertainty is a key driver of the results. This includes scenarios whether the primary magnesium is Pidgeon or electrolytic, the cost of alloying, and the twin-roll casting conversion cost. A 10% change in material costs leads to approximately a 5% change in total door costs for both the magnesium and steel designs. A 10% decrease in the cost of electrolytic magnesium would lead to it being within the project lightweighting cost target of $5.50/kg saved.

While the larger parts in the Chrysler magnesium-intensive door design are cost-competitive, the smaller parts have relatively large lightweighting costs, and the aluminum casting is heavier and significantly more expensive than the equivalent three steel parts. This indicates that warm forming and aluminum casting may not be cost effective for small magnesium parts, and there is significant opportunity to optimize the magnesium door design with alternative solutions for these small parts.

This USAMP project has substantially accelerated the time-to-market for new sheet product and potentially wide scale implementation for low-cost Mg automotive sheet components by (1) providing the resources to pull forward the underlying technical developments required for commercialization, and (2) initiating pre-commercial partnerships for advancing material qualification studies.

I2. RECOMMENDATIONS FOR FUTURE WORK

The cost of lightweighting a door assembly with Mg sheet was determined to be between $4.26 - $6.60/kg saved for a mass savings of 9 kg compared with steel. This range is driven mostly by the price of the coated sheet and encompasses the $5.50/kg target provided by DOE. The cost penalty for lightweighting can only be optimized if the entire door is designed predominantly for magnesium within the confines of

a mixed material solution, which remains the task of individual OEMs and their design approaches. Alloy development, which was a cornerstone of this project, identified some chemistries that demonstrated non-basal slip. However, some atomistic calculations were constrained to binary systems due to the computational methodologies available. Further work should involve more complex interaction models to enable ternary alloy calculations with associated better thermodynamic databases to understand when two solutes might promote higher solubility. In general, the Mg-Ca-Zn system was identified as most promising and needs further optimization to understand the effect of chemistry and processing on promoting negative strain rate sensitivity leading to pronounced dynamic strain aging. This phenomenon provides the appropriately oriented grains after recrystallization that have the preferred texture for non-basal slip. The interplay between strain rate, number of rolling passes, and recrystallization time and temperature on texture needs robust mathematical processing models validated with carefully controlled experiments. In this regard, developing virtual microstructures becomes a powerful approach to understand plasticity in computational space and also needs validation with experiments. A promising lean alloy (Alloy 2 Plus) containing 1.0Zn-1.0Al-0.5Ca-0.4Mn-0.2Ce was developed using computational thermodynamics and based within the constraints of the above observations. This alloy exhibited high RT formability and high strength. Further work is needed to incorporate the mechanisms of dynamic strain aging and recrystallization to further improve its formability and suggest alloy modifications. Asymmetric rolling, a promising approach for promoting non-basal texture with its unique thermomechanical processing, should be extended.

Improving formability models will remain important considering the pronounced effects of strain-rate and initial work-hardening rate. The strategy of coupling experiments with the polycrystalline microstructure for high fidelity simulations still needs pristine mechanical property data at various temperatures along various strain paths and at various strain rates. This needs to be coupled with continued improvements to the model to better account for anisotropy of Mg and the evolving texture to better model the sheet that has limited formability. Improved material cards are needed to cover the broad temperature- and strain-ranges encountered in forming the door panels. The challenging vision for determining material cards by integrating the plastic behavior of individual grains in 3D remains an overarching goal that will bring in a next generation of precision to formability modelling, and needs to be continued.

While OEMs will be tasked with scale-up of the various lubricants and pretreatments developed, the influence of variability in surface conditions on their efficacy needs further understanding. Single-step lower-cost pre-coatings that can provide corrosion protection in mixed materials designs are greatly needed to avoid individual treatment of panels after forming. The zinc coatings identified are an important contribution from this study. Lubricants that provide a wide process window and that do not need cleaning after forming still need to be ensured, since otherwise they add much cost in high volume production compared with coatings that do not interfere with the current paint shop bill of process and only get cleaned in the paint shop process. While joining by various methods was broadly demonstrated to be feasible for the magnesium sheet, the influence of residual lubricant and the use of adhesive before joining still needs understanding and validation.

An important observation which could limit magnesium sheet use was variability in properties observed that could be traced back to the presence of second-phase particles and the microstructure produced during sheet forming. This remains critical to be addressed by the sheet manufacturers, else components and their shapes will be designed to the minimum properties leading to either higher mass solutions or with parts that are not desirable. Finally, panels with Class A painted surfaces still need validation.

Appendix 1: Collaborating Organizations

The USAMP-LCMS Project involved 25 organizations and over 100 researchers. About a quarter of the participants were technical staff from the three USAMP member OEMs – remaining three-quarter team members were from tier suppliers, academic sub-recipients, national laboratories and project vendors/service providers.

Project Participants	Type
U.S. Dept of Energy EERE/Vehicle Technologies Office (VTO)	Sponsor
U.S. Dept of Energy National Energy Technology Laboratory (NETL)	Sponsor/Contracting Office

USAMP LLC (U.S. Council for Automotive Research):
    FCA US LLC
    Ford Motor Company
    General Motors Holdings LLC
	Awardee/Sponsor

AET Integration Inc.	Sub-Recipient
Camanoe Associates	Vendor
Edison Welding Institute	Vendor
FADI-AMT LLC	Vendor
Fuchs Lubricants Company	Sub-Recipient
Henkel Corporation	Sub-Recipient
InalTech Inc.	Vendor
Korea Magnesium Industry	Vendor
LightMAT – Pacific Northwest National Laboratory	Consortium
LightMAT – Oak Ridge National Laboratory	Consortium
Livermore Software Technology Corporation (LSTC)	Vendor
M-Tech International LLC	Vendor
Ohio State University	Sub-Recipient
POSCO	Vendor
Pinetree Pos Magnesium (PPM)	Vendor
PPG Industries, Inc.	Sub-Recipient
Quaker Houghton Chemical Corporation	Sub-Recipient
Transphere, Inc.	Vendor
University of Florida	Sub-Recipient
University of Illinois	Sub-Recipient
University of Michigan	Sub-Recipient
University of Pennsylvania	Sub-Recipient
Vehma International of America, Inc.	Sub-Recipient
Xtalic Corporation	Sub-Recipient

Appendix 2: Publications Generated

1. Hilty B., "Nanostructured Al-Alloy Coatings for Corrosion Protection of High-Strength Al and Mg Alloys" proceedings of the TMS 2018 Symposium, "Surface Engineering for Improved Corrosion Resistance."

2. Bong HJ, Hu, X., Sun, X., Ren Y., "Mechanism-based Constitutive Modeling of ZEK100 Magnesium Alloy with Crystal Plasticity and In-situ HEXRD Experiment," Acta Materialia, 2018.

3. Carter, J., "Challenges and Opportunities for Implementing Magnesium in Automotive Applications," Keynote presentation at the 11th International Conference on Magnesium Alloys and their Applications, 24-27 July 2018, Beaumont Estate, Old Windsor, UK.

4. Bong HJ, Hu X., Sun X., Ren Y., "Mechanism-based Constitutive Modeling of ZEK100 Magnesium Alloy with Crystal Plasticity and In-situ HEXRD Experiment," International Journal of Plasticity, 2018, https://doi.org/10.1016/j.ijplas.2018.09.005

5. Bong HJ, Hu X., Sun X., Ren Y., Mishra R., "Crystal Plasticity Based Constitutive Modeling of ZEK100 Magnesium Alloy Combined with In-situ HEXRD Experiments," Journal of Physics: Conference Series 1063 (1), 012031.

6. Fellinger MR, and Trinkle DR, "Solute-dislocation Interactions in Mg from First Principles: <c+a> and Twinning Dislocations with Flexible Boundary Conditions," oral presentation at TMS Symposium on Physical Metallurgy: Computational Thermodynamics and Kinetics, San Antonio, TX, March 2019.

7. Shi R, Miao J, Li Z, and Luo A, "A New Magnesium Sheet Alloy and its Multi-stage Homogenization for Simultaneously Improved Ductility and Strength at Room Temperature," Scripta Materialia 171 (2019), pp 92-97.

8. Cuadrado W, and Manuel MV, "Connecting Dynamic Strain Aging to Deformation Processing in Magnesium-Calcium-based Alloys," oral presentation at TMS Annual Meeting, February 23-27, 2020, San Diego, CA.

9. Shi R, Miao J, Avey T, Luo A, "A New Magnesium Sheet Alloy with High Tensile Properties and Room-Temperature Formability", Scientific Reports, 2020, 10, (1), 1-10, https://doi.org/10.1038/s41598-020-67161-9.

10. Buccholz K, SAE Vehicle Engineering Technology e-Newsletter, 11/19/2020, "USCAR Broadens Its Research Footprint," Weblink: https://www.sae.org/news/2020/11/uscar-broadens-its-research-footprint. (This article documents an interview with USAMP Project Leader Randy Gerken).

11. Sachdev A, "Lightweighting with Magnesium Sheet," a virtual oral presentation at Inauguration of Global Magnesium Industrial Research Center (GMIRC), Suncheon City, Korea, December 10, 2020.

12. Berman TD and Allison JE, "Relating Texture and Thermomechanical Processing Variables in Mg-Zn-Ca Alloys," Magnesium Technology. 2020 Proc, TMS, J.B. Jordon, V. Miller, V. Joshi, and N.R. Neelameggham, eds., Springer International Publishing, 2020, 175-180.

13. Berman TD et al., "Relating Texture and Thermomechanical Processing Variables in Mg-Zn-Ca Alloys," oral presentation at 2020 TMS Annual Meeting & Exhibition, San Diego, CA, February 26, 2020.

14. Luo AA, Shi R, Miao J, Avey T, "Review: Magnesium Sheet Alloy Development for Room Temperature Forming", JOM, 2021, 73, pp 1403–1418, https://doi.org/10.1007/s11837-021-04616-y.

15. Zhao D, Shi R, Evans RP, Luo AA, Xie KY, "On the Exceptionally High Ductility of Mg-2Zn-0.3Ca-0.2Ce-0.1Mn Alloy," Materials Science and Engineering A, 2021, 819, 141484, https://doi.org/10.1016/j.msea.2021.141484.

16. Berman TD, "Preparing Magnesium Alloys for Electron Backscatter Diffraction, poster -presentation at 2020 TMS Annual Meeting & Exhibition, San Diego, CA, February 24, 2020.

17. Berman TD and Allison JE, "Texture and Microstructure Evolution in Thermomechanically Processed Mg-Ca and Mg-Zn-Ca Alloys," oral presentation at 2021 TMS Annual Meeting & Exhibition, virtual, March 17, 2021.

18. Berman TD and Allison JE, "Coupling Thermomechanical Processing and Alloy Design to Improve Textures in Mg-Zn-Ca Sheet Alloys," JOM, 73, 1450-1459. (2021).

19. Berman TD and Allison JE, "Evolution of Texture and Microstructure in Mg-Zn-Ca Sheet Alloys during Thermomechanical Processing," oral presentation at 12th International Conference on Magnesium Alloys and their Applications, virtual, June 16, 2021.

20. Berman TD and Allison JE, "Texture Evolution in Mg-Zn-Ca Alloys," oral presentation at the PRISMS Center Annual Workshop, virtual event, August 6, 2021.

21. Valdez L, Allen K, Harris R, and Rock R, "Novel Magnesium Pretreatment Coatings Offering Excellent Corrosion Protection," oral presentation by PPG Industries at American Coatings Association Conference, June 2021.

22. Sachdev A, "Advances in Magnesium Alloys for Automotive Applications," oral presentation at 12th International Conference on Magnesium Alloys and Their Applications, virtual event, June 15-18, 2021.

23. Ghaffari B, "An ICME Approach to Development of a Low-Cost Magnesium Sheet Component for Automotive Applications," invited plenary presentation at 6th World Congress on ICME (ICME 2021), November 14-18, 2021.

Appendix 3: Subject Inventions and Patents

(1) The Ohio State University reported the following Subject Invention as part of Closeout submissions:

1. T2020-044, Inventor: Alan Luo, "A High-Strength and High-Ductility Magnesium Sheet Alloy for Room-Temperature Forming Applications" – Application progress is below:
    - U.S. Provisional Application No. 62/908,077, filed September 30, 2019
    - PCT application No. PCT/US/2020/053065, filed September 28, 2020
    - PCT publication No. WO 2021/067782 A1, published on April 08, 2021

(2) PPG Industries disclosed via iEdison 13 Subject Inventions, each individually identifiable by the assigned T-number. Out of the 13 disclosed inventions, seven were included in patent application filings and three are in the process of being filed. Letters of recession were filed for the remaining three disclosed inventions. All 13 inventions were reported in PPG's October 2021 closeout submission and their current status is provided below:

Patent Applications Filed:

1. PCT/US2020/045656 Control of Etching by Cleaner Composition and Organic Pretreatment for Magnesium Substrate (Includes T-115306).

2. PCT/US2020/045629 ChemDeox 395 as a Pretreatment-enhancing Cleaner on Magnesium Alloy (Includes T-115308, T-115816, T-118158, and T-118162).

3. Application #63/228,756 One-step Multimetal Pretreatment for Mg and Steel (Includes T-120644) – combined with T-124614 below.

4. Application #63/228,756 Compact pretreatment for both Cold-Rolled Steel and Magnesium (Includes T-124614) – combined with T-120644 above.

Patent Applications in Preparation:

5. T-117692 Peroxide-free Cerium Pretreatment of Magnesium Substrates for Longer Bath life.

6. T-122068 Cerium Pretreatment with Oxidizer Coupling on E-Form Plus Magnesium.

7. T-119012 Corrosion Protection of Mg Alloys via Orthophosphonic Derivative Based Pretreatment.

Recession Letters Filed:

8. T-117830: Corrosion and Adhesion Improvement of ZB 1.5 on Mg Substrate with a Pre-electrocoat Bake – Recession 9/14/2020

9. T-118530: Improvement of Mg Substrate Corrosion Performance with an Si-containing Organic Pretreatment - Recession 10/23/2020.

10. T-122794: Unique Treated Magnesium Substrate Using ChemDeox 395 and Nupal 435 – Recession 2/11/2021.

This page left intentionally blank